Flexoelectricity in Liquid Crystal Materials

Akhshay Singh Bhadwal

A thesis submitted in partial fulfillment of

the requirement of Nottingham Trent University

for the Degree of Doctor of Philosophy

This research programme was carried out

in collaboration with Merck Chemicals Ltd , Southampton, UK

Department of Physics and Mathematics

Nottingham Trent University

Nottingham, United Kingdom

December 2020

Declaration

This work is the intellectual property of the author, and may also be owned by the research sponsor(s) and/or Nottingham Trent University. You may copy up to 5% of this work for private study, or personal, non-commercial research. Any re- use of the information contained within this document should be fully referenced, quoting the author, title, university, degree level and pagination. Queries or requests for any other use, or if a more substantial copy is required, should be directed to the owner(s) of the Intellectual Property Right.

Acknowledgment

First and above all, I would like to thank my supervisor, Professor Carl Brown, for his kind and expert supervision. Much of my problems seem to go away in meetings with Carl. Thanks a lot for your unwavering patience and selfless support throughout my Ph.D. A big thanks to our liquid crystal genius Ian Sage, I have learned a lot from you over these years and I feel privileged to have this opportunity to work with you, thanks for sharing your extensive knowledge. Thanks also to my co-supervisor Demos Koutsogeorgis for introducing me to thin film research and for his support during the project. I would also like to thank my industrial supervisors Rachel Tuffin and Hassan Arasi and their colleagues (Owain Parri, Mark Goebel, Joe Sargent, Sarabjot Kaur) at Merck UK, both for the research meetings and supply of liquid crystals. Thanks to Dr. Leo Weegels, Dr. David Wilkes (Merck, Germany) for showing keen interest in our liquid crystals microfluidics research and providing me an opportunity to work on short term industrial projects. My sincere gratitude to Professor Nigel Mottram for providing me much needed theoretical support. Despite of his busy schedule, Nigel always finds time for me. Thanks to my dear friend, Andrew Edwards for being my mentor in the lab.

I wish to express my thanks to all my colleagues and past member of the group for their encouragement and support. Thanks to all the wonderful friends I made at NTU, without your support this would have been a lonely ride. Finally, thanks to my parents and family for their support and love. I hope to make you all proud.

Dedicated To

To the fantastic four of my life,
and all the sacrifices they made for me

Contents

iv

5   Influence of flexoelectricity on alternating HAN structures and free surface wrinkles   156

List of Figures

List of Tables

Abstract

With the maturation of the soft matter physics-based system, liquid-crystal (LC) materials research is undergoing a resurgence. Devices based on nematic class of liquid-crystal materials are now being used beyond the field of displays with applications ranging from the field of spectroscopy, microscopy to biology. This burgeoning interest in nematic liquid crystals-based devices requires systematic understanding of both static and dynamics of nematic director under influence of various external and internal forces. This thesis reports the realisation, investigation, and elucidation of three distinct and original dynamic switching geometries within a nematic liquid crystal layer that was subject to an applied electric field. The elastic forces associated with the time-dependent nematic director distortions within the layer, and the coupling to the relative strength and direction of anchoring at the boundaries, were key critical factors in governing the detailed switching response for all of these geometries.

In the first geometry, the nematic layer was subject to externally driven Poiseuille flow whilst the A.C. electric field was applied orthogonal to the layer. Switching was investigated for both planar alignment, with the easy direction parallel to the flow, as well as homeotropic alignment at the solid confining plates, in both cases as a function of the flow rate and the electric field strength. For planar alignment, flow-controlled switching between distinct nematic director distortion modes was demonstrated and elucidated, where the modes involved were the $n = 0, 1, 2$ flow perturbed analogues of the $sin(n\pi z/d)$ director distortion modes, using nomenclature from the zero flow classic Fréedericksz transition perturbation analysis.

In the second geometry, the nematic layer was subject to hybrid planar and homeotropic alignment respectively at the lower and upper solid confining plates. This symmetry

breaking provided a topological defect line within the layer which was manipulated via a spatially periodic in-plane A.C. electric field. Precisely field controlled linear in-plane transport and motion of dispersed colloidal micro-particle was demonstrated, mediated by the A.C. electric field-induced dynamic evolution of the tortuous shape of the topological defect line.

In the final geometry, the nematic layer was subject to hybrid planar and homeotropic alignment respectively at the lower and upper surface. A spatially periodic in-plane A.C. electric field creates a period stripe array of alternating mid-layer tilt orientations separated by parallel substantially linear tilt walls that contained topological defect lines. Modulating the polarity of an applied D.C. electric field in the device demonstrates the polarity dependent movement of the intervening tilt walls, as well as the accompanying topological defects as a result of electrostatic coupling to the flexoelectric polarisation. This flexoelectricity induced defect movement was studied in a positive nematic layer with a solid confined and free upper surface. The behaviour described above, in case of the free upper surface, is accompanied by a polarity dependent phase changes in the periodic wrinkling deformation at the free surface.

This page is intentionally left blank

Chapter 1

Introduction to Liquid Crystals

1.1   Liquid crystals

Science has always been occupied by serendipitous discoveries. Out of many such events

is the discovery of *liquid crystals* (LCs). For long, the matter was classified into three

distinct phases (solid, liquid, gas), depending on the order of constituent atoms and their

mobility (degree of freedom). However, this classification is not always correct; there

exist a class of materials that shows phase, intermediate between solids and liquids known

as a *liquid crystalline* phase or a mesophase. The discovery of liquid crystalline phase

is credited to an Austrian botanist named Friedrich Reinitzer who found the existence

of two melting point in cholesteryl benzoate [1], at first melting point these cholesteric

compound melts to form a hazy liquid followed by the formation of a clear liquid at

second melting point. Unlike isotropic liquids where orientational and positional order

is missing, different classes of liquid crystals possesses a combination of symmetries

leading to the formation of different sub-phases in liquid crystals. A detailed description

of the classification of liquid crystals is discussed in de Gennes *et al.* 1995 [2]. In this

thesis, we will focus on thermotropic calamitic (rod-shape) liquid crystals, in particular,

nematic type of calamitic liquid crystals. Other sub-phases of thermotropic calamitic

liquid crystals including nematic type liquid crystals is shown in Figure.1.1.
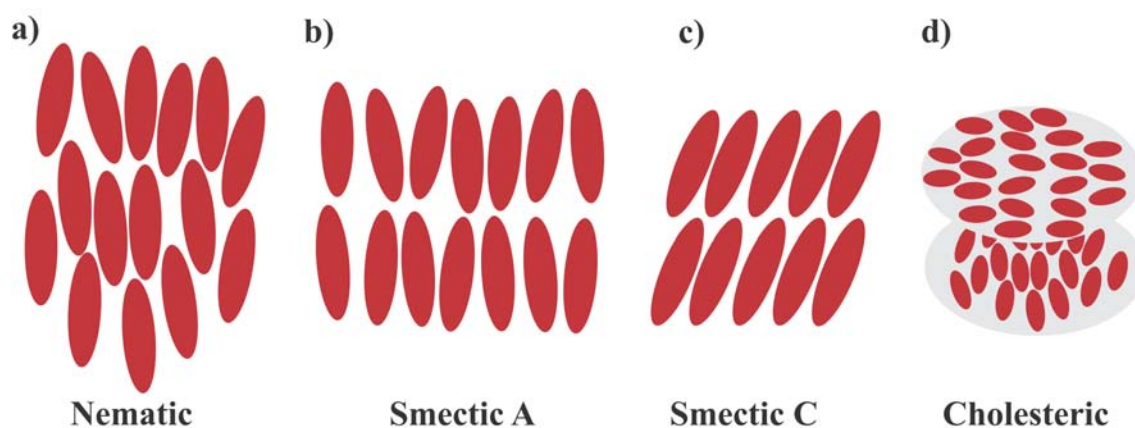
Figure 1.1: Calamitic phases of liquid crystals.

1.1.1   Anatomy of a nematic liquid crystal

Before discussing various physical properties of nematic liquid crystals, let us understand the basic anatomy of the nematic liquid crystal molecule. A single nematic molecule has a rod-like molecular design consisting of a moderately rigid core region commonly made up of aromatic or heterocyclic units. This core region can encompass mobile charges, which can be polarised preferentially along the different axis of the core in an applied electric field and plays a crucial role in determining the physical properties of liquid crystals. This core region can be surrounded by flexible hydrocarbon chains on both the ends with presence/absence of a side group or a single hydrocarbon chain with or without terminal permanent dipole group at one end. Thus, engendering a rod-like chemical architecture. Figure. 1.2 shows plausible molecular design for nematic liquid crystals molecules. Now onwards for simplicity, we would represent above discussed molecular architectures and their mixtures as a single entity having a rod-like shape (represented by the filled core in Fig. 1.2) consisting of mobile charges.
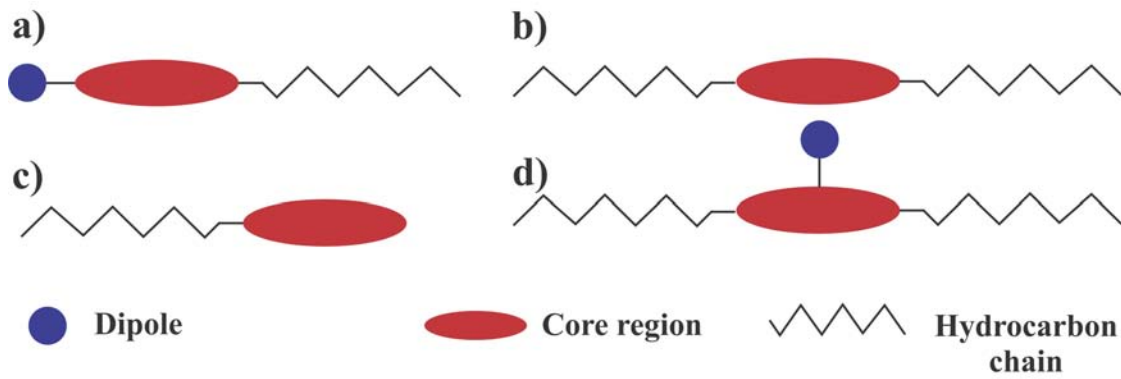
Figure 1.2: Idealized schematic of plausible molecular architectures for nematic liquid crystals.

1.1.2 Order parameter Liquid crystals

As discussed above order plays a crucial role in the distinction of liquid crystals. The Nematic liquid crystal is the simplest example where a molecule on an average aligns towards a preferred orientation direction denoted by the **n**-director, where **n=-n** in an ordinary nematic liquid crystal. The nematic scalar order parameter (S), provide a quantifiable value to determine the extent of orientational order in liquid crystals, i.e., the degree to which the molecules align with the n-director (taking a snapshot in time and averaging over space, or looking at a single molecule averaged over time). The Order parameter (S) is given as an ensemble average of the second order Legendre polynomial (Eqn. 1.1).

$$s = \frac{1}{2}\langle 3cos^2\theta - 1 \rangle \tag{1.1}$$

Where S is order parameter and θ is the angle between the molecular axis of an individual molecule and the **n**-director. For a perfect system where all the liquid crystals molecules align in the direction of **n**-director, the order parameter is found to be 1 whereas for isotropic liquids S=0, due to the non-existence of a preferred direction in the system. Figure 1.3 (a-c) represent different states of order parameters. It should also be noted that the order parameter also varies as a function of temperature within the nematic phase

3

temperature range. Figure 1.4 represents a change in order parameter of 5CB with temperature below clearing temperature (T_c). A union of ordering of the anisotropic nature of constituent molecules in liquid crystals collectively defines the anisotropic behaviour in physical properties (optical, dielectric, viscosity, and many more) of liquid crystals.
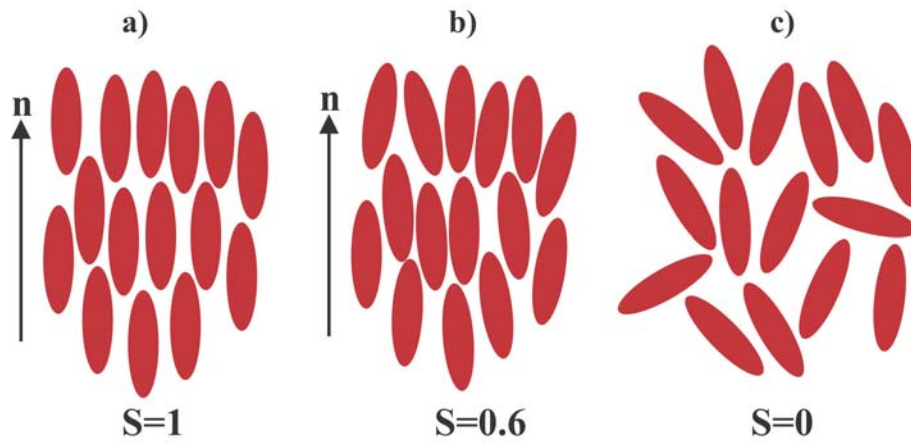
Figure 1.3: Order parameter corresponding to a) perfect orientational order b) Orientational order in a nematic LC, and c) Lack of orientational order in isotropic liquids.
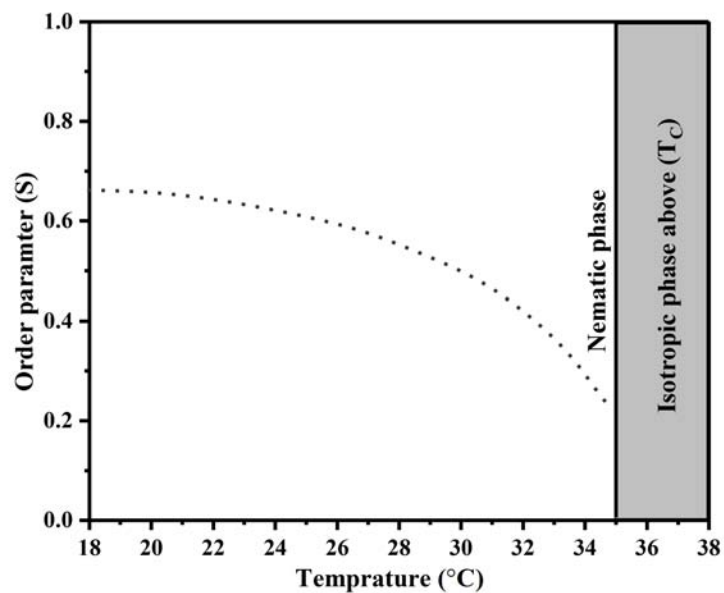
Figure 1.4: Schematic of the order parameter variation with temperature for 5CB.

1.1.3 Anisotropy in Liquid crystals

1.1.3.1 *Optical Anisotropy*

Optical anisotropy in a material arises due to the variation in the extent of polarisability (α) of the material along different directions. In order to better understand the origin of this phenomenon in materials (solids and liquid crystals). Let us consider an electromagnetic wave (light) traveling along the (x-direction) through a material for example liquid crystals. In this scenario, the electric field ($\underline{E}$) associated with the light wave can be represented as equation (1.2):

$$\underline{E} = \underline{E_0}e^{-i(\omega t - kx)} \tag{1.2}$$

Here, $\underline{E_0}$ represents the magnitude and direction of polarization, t represents time, ω angular frequency, k is the wave vector ($k = 2\pi/\lambda$). Now when an electromagnetic wave (light) travels through the material there will be an interaction of the electric field with electrons in the materials and the resultant of this interaction will alter the wave propagation, leading to the modification of wave vector ($k = 2\pi n/\lambda_{air}$) [3]. Hence if we have a material with a variation of polarisation in different directions, the refractive index of this material depends on the direction of light. The refractive index (n) is related to the dielectric permittivity at the frequency of the wave by $n = \sqrt{\varepsilon}$. However, please note that frequency values for light waves is approximately around 5×10^{14} Hz [4] and at these value ε can vary from its low-frequency values.

Due to the directional dependence of polarisability many solid materials like calcite ($CaCO_3$), quartz (SiO_2) also exhibit optical anisotropy. The birefringence of a material is given as (Eqn.1.3):

$$\Delta n = n_e - n_o \tag{1.3}$$

Where n_e and n_o is extraordinary and ordinary refractive index having the light wave

propagating parallel and perpendicular to the optical axis (Fig. 1.5 b).
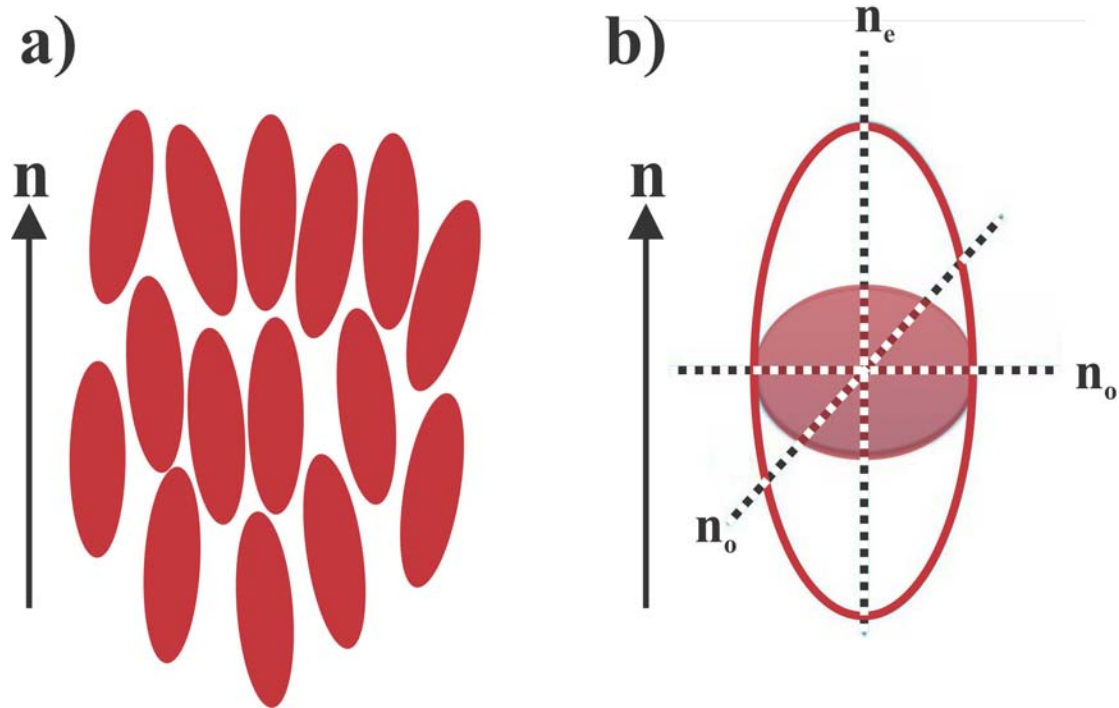
Figure 1.5: a) Nematic n-director, b) optical indicatrix of refractive index.

In calcite crystal, n_o=1.65504 and n_e=1.48490 at a wavelength of 643 nm giving a $\Delta n =$ 0.17014 [5]. This phenomenon doesn't exist in isotropic liquids where $\Delta n = 0$ due to lack of order and temporal fluctuations of molecules. However, in the case of nematic mesophase optical anisotropy can be easily manifest due to extent of nematic ordering and the anisotropy in polarisability ($\alpha_\parallel$ and $\alpha_\perp$) of mobile charge carrier present in the core of the nematic molecule. For example, 4-Pentyl-4-cyanobiphenyl (5CB) at a temperature of 25.2°C have, $n_o = 1.91$ and $n_e = 1.59$ at a wavelength of 400 nm [6].

1.1.3.2 *Dielectric Anisotropy*
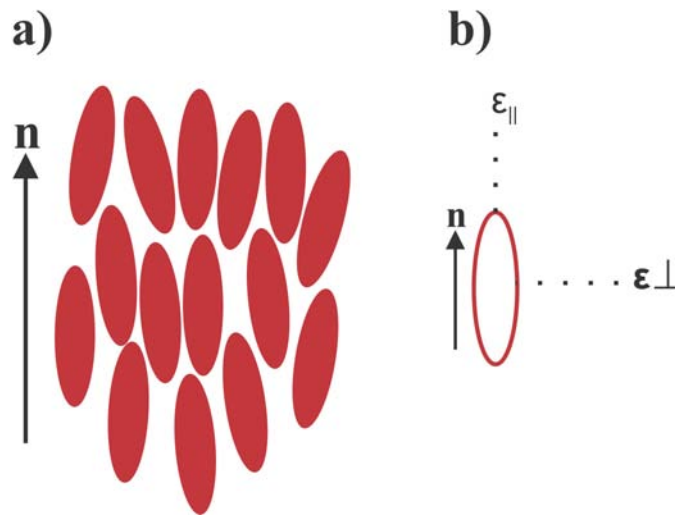
Figure 1.6: a) Ensemble of liquid crystals **n** denotes director orientation b) Dielectric anisotropy in nematic liquid crystal (unfilled ellipse represent a region of anisotropic nematic material).

Dielectric anisotropy plays a crucial role in liquid crystal based displays as most of the nematic liquid crystals used in display screens are voltage-driven; thus, it determines the electro-optical response of the screen. By analogy to optical anisotropy where you got two different refractive indexes (n_e and n_o) along different directions of n-director in case of dielectric anisotropy, we get two different dielectric permittivities ($\varepsilon_{\parallel}$ and $\varepsilon_{\perp}$), where $\varepsilon_{\parallel}$ is, permittivity parallel to the n-director and $\varepsilon_{\perp}$ is permittivity perpendicular to n-director (Fig. 1.6). Due to this variation in permittivities, we get dielectric anisotropy ($\Delta\varepsilon$) given as (Eqn. 1.4):

$$\Delta\varepsilon = \varepsilon_{\parallel} - \varepsilon_{\perp} \tag{1.4}$$

The value of $\Delta\varepsilon$ can be positive or negative depending on the type (molecular structure) of nematic liquid crystals.

It should be noted that at optical frequencies dielectric anisotropy depends upon nematic ordering and anisotropy in polarisability ($\alpha_\parallel$ and $\alpha_\perp$). However, at low frequencies depending upon the molecular structure of nematic, there will be an additional contribution from molecular structure towards bulk polarisation for example in nematic liquid crystals having polar molecules you will observe induced as well as orientational polarisation arising from the orientation of permanent dipoles. Hence, considering the orientational polarisation of polar liquid crystal molecule, the enhanced value of $\Delta\varepsilon$ is given by Maier and Meier equation 1.5 [7]:

$$\Delta\varepsilon = \frac{NhF}{\varepsilon_0} + \left\{ \Delta\alpha - \frac{F\mu^2}{2k_BT}\left(1 - 3cos^2\beta\right) \right\}S \qquad (1.5)$$

Here, N is the molecular number density, F and h account for the anisotropic interactions leading to the local electric field, ε_0 is permittivity in vacuum, β is the orientation relative to the long principal axis, S is order parameter, $\Delta\alpha$ is molecular polarisability anisotropy, μ is dipole moment, k_B is Boltzman constant, and T is the temperature. A common example of nematic liquid crystal having polar group is 5CB (idealized structure given in fig.1.1a) whose dielectric anisotropy $(\Delta\varepsilon) = 14.2$ at ambient laboratory conditions. Other liquid crystals having $\Delta\varepsilon$ ranging from -8 to +100 have also been synthesized [8]. Electric field-induced re-orientation liquid crystals for both positive $(+\Delta\varepsilon)$ and negative $(-\Delta\varepsilon)$ is given in figure. 1.7.
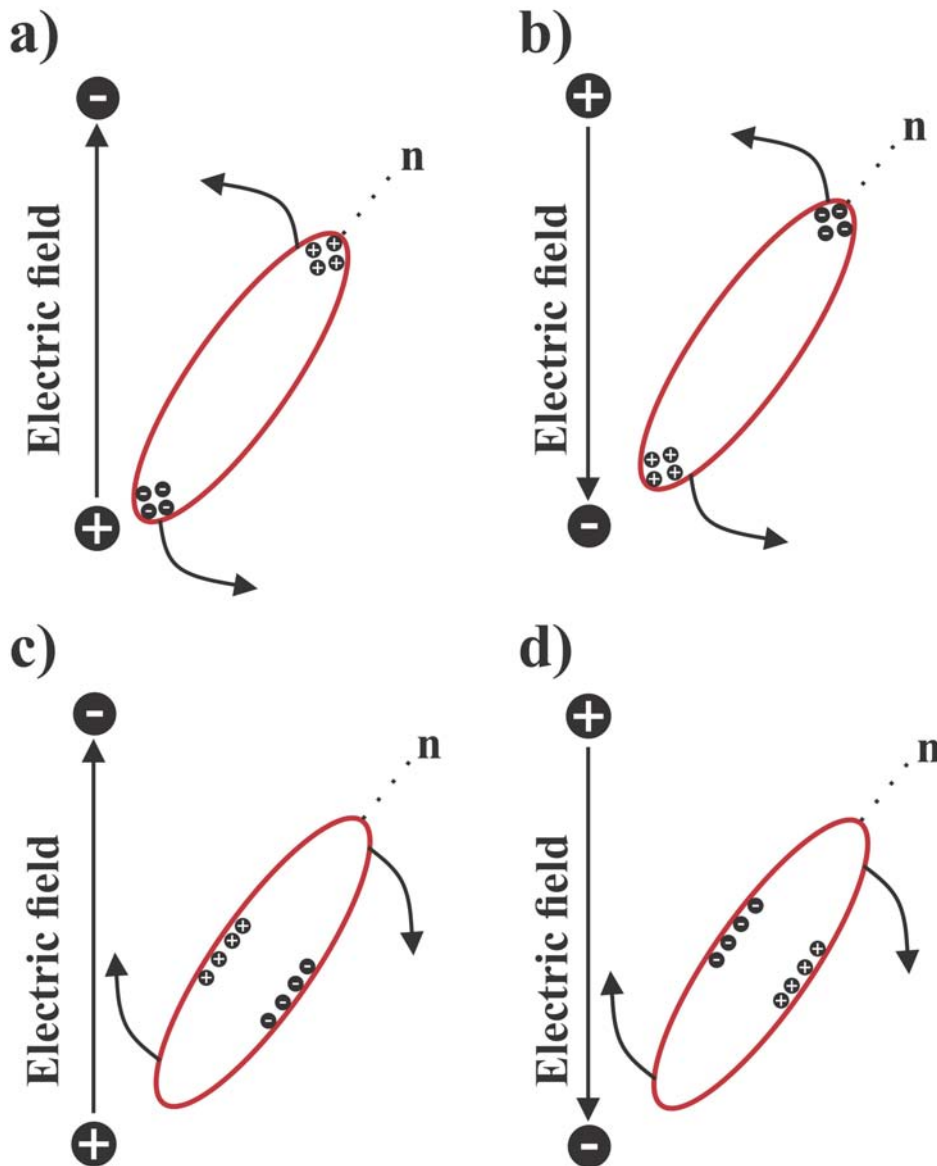
Figure 1.7: Electric field induced orientation of (a,b) positive nematic liquid crystal ($\Delta\varepsilon >$ 0), and (c,d) negative nematic liquid crystal ($\Delta\varepsilon < 0$ unfilled ellipse represents a region of anisotropic nematic material).

1.1.3.3 *Viscosity*

All fluids are viscous in nature except two isotopes of liquid helium (^{3}He and ^{4}He) at certain cryogenic temperatures. Viscosity in general acts as a retarding force to a freely flowing liquid till it comes to an equilibrium state. In isotropic liquids, viscosity is defined as the ratio of shear stress and shear rate. However, in nematic liquid crystals due to the anisotropic shape of molecules, surface induced-ordering, and confinement dimensions, different viscosities can be obtained. Theoretically, six independent viscosities α_1 to α_6 known as Leslie viscosities were first given by Leslie Ericksen theory [9–11] which was later reduced to five by Onsager relation ($\alpha_6 - \alpha_5 = \alpha_2 + \alpha_3$) used by Parodi [12] leading to simplification in the Leslie Ericksen theory. However, the first experimental observation of different liquid crystals viscosities is done by Miesowicz [13]. He parameterized nematic viscosities in sets of Leslie viscosities coefficients, $\eta_1 = (\alpha_3 + \alpha_4 + \alpha_6)/2$, $\eta_2 = (-\alpha_2 + \alpha_4 + \alpha_5)/2$, $\eta_3 = \alpha_4/2$ [14]. Apart from three Miesowicz viscosities, two other viscosities are also defined as a set of Leslie viscosities, $\eta_{12} = \alpha_1$ and rotational viscosity $\gamma_1 = (\alpha_3 - \alpha_2)$ [15, 16]. These viscosities can be measured when the director is held in the following manner:

η_1 when the n-director is parallel to the flow velocity direction (V).

η_2 when the n-director is parallel to the velocity gradient (ΔV).

η_3 when the n-director is orthogonal both to the flow velocity direction (V) and the velocity gradient (ΔV).

η_{12} (Helfrich coefficient) when the n-director is fixed at an angle of 45° with both the flow pattern and the velocity gradient [16].

γ_1 rotation of the n-director around an axis perpendicular to the director.

The rotational viscosity (γ_1) plays a crucial role in determining the switching time (τ) (Eqn. 1.6) in liquid crystals display devices.

$$\tau_{on} = \frac{\gamma_1 d^2}{\varepsilon_o \varepsilon_a (V^2 - V_c^2)} \tag{1.6}$$

However, despite viscosity being an important property, the complete set of viscosities has only be measured for a few liquid crystals as the measurement are complex and difficult due to multiple parametric dependence. Table 1.1 shows five different viscosity coefficient of para-Azoxyanisole (PAA), 4-Pentyl-4-biphenylcarbonitrile (5CB) and N-(4-Methoxybenzylidene)-4-butylaniline (MBBA) nematic type liquid crystals. For someone interested to know different viscosity coffecients of liquid crystals a detailed review by Viktor *et.al* [17] presenting different viscosity of nematic liquid crystals belonging to 320 chemical classes is available in the literature.

Material	$\eta_1(\vec{v} \parallel \vec{\eta})$	$\eta_2(\Delta\vec{v} \parallel \vec{\eta})$	$\eta_3(\vec{v}, \Delta\vec{v} \perp \vec{\eta})$	γ_1	η_{12}	Ref.
PAA@122°C	0.0024	0.0092	0.0034	0.0067	0.0043	[13, 18]
5CB@26°C	0.0204	0.1052	0.0326	0.0777	-0.0060	[18]
MBBA@25°C	0.0240	0.1361	0.0413	0.1093	-0.0181	[18]

Table 1.1: Miesowicz viscosities coefficient (Pa.S) for three nematic liquid crystals.

1.1.4 Surface anchoring

In the absence of any force of interaction, the n-director is solely determined by intramolecular forces (internal order) of the liquid crystals phase. However, introduction of an interface can lead to a preferred alignment direction, dependent on interfacial chemical and steric interactions. Thus, resulting in different molecular alignment of liquid crystals at the interface, propagating over macroscopic distance. There are four main types of molecular alignment (surface anchoring) possible for nematic liquid crystals; random planar, homogenous planar, homeotropic and tilted alignment (fig.1.8).These alignment conditions can be represented in terms of orientation which can be addressed in terms of polar(θ) and azimuth (ϕ)angles (fig.1.9):

a) Homogenous planar: $\theta = 0$, and $\phi = $ fixed at an angle.

b) Homeotropic: $\theta = \pi/2$.

c) Tilted: $\theta = $ fixed at an angle, and $\phi = $ can be fixed at an angle.

d) Random planar: $\theta = 0$, and ϕ fixed at different angles at different regions.
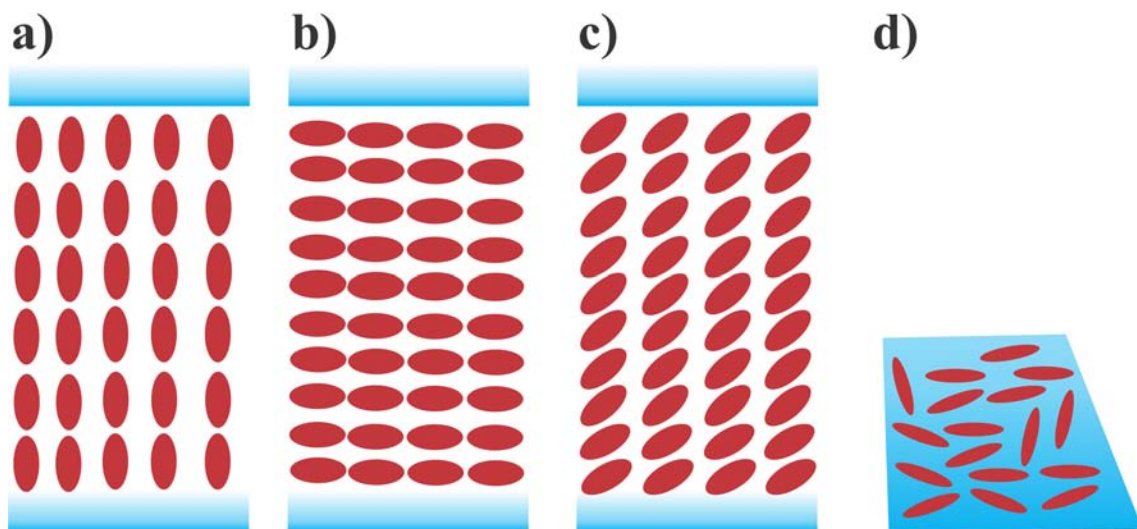
Figure 1.8: Orientation of Liquid crystals at the surface (side view) a) Homeotropic b) Planar c) tilted and d) random planar (top view).
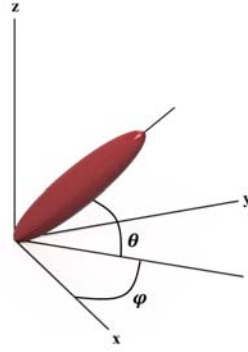
Figure 1.9: Schematic showing polar and azimuth anchoring angle.

1.1.5   Elastic Constants
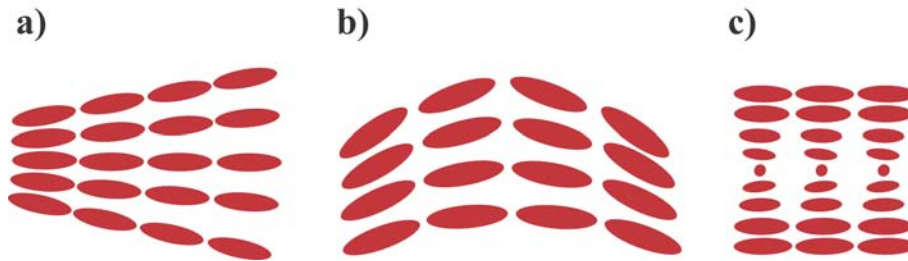
Figure 1.10: Spatial variation in n-director during elastic deformation of nematic liquid crystals a) splay b) bend, and c) twist.

Many solid materials around us exhibit a property of retaining restoring forces when perturbed from equilibrium state by a deforming force. This property is termed as elasticity. Analogous to this behavior liquid crystals have restoring torques that come into play when the n-director is perturbed/deformed from its minimum energy state, and these anisotropic restoring forces are quantified by elastic constants [16]. Based on nematic continuum theory by Frank [19] these arbitrary spatial distortions of nematic n-director can be represented as splay (k_{11}), twist (k_{22}), and bend (k_{33}). Figure 1.10 represents pure splay, twist, and bend distortion in nematic liquid crystals. The bulk elastic part based on continuum theory that provide quantified value of spatial distortion in director is given as (Eqn.1.7):

$$f_d = \frac{1}{2}k_{11}\left[\nabla \cdot \underline{n}\right]^2 + \frac{1}{2}k_{22}\left[\underline{n} \cdot (\nabla \times \underline{n})\right]^2 + \frac{1}{2}k_{33}\left[\nabla \times (\nabla \times \underline{n})\right]^2 \tag{1.7}$$

13

1.1.6 Fréedericksz transition
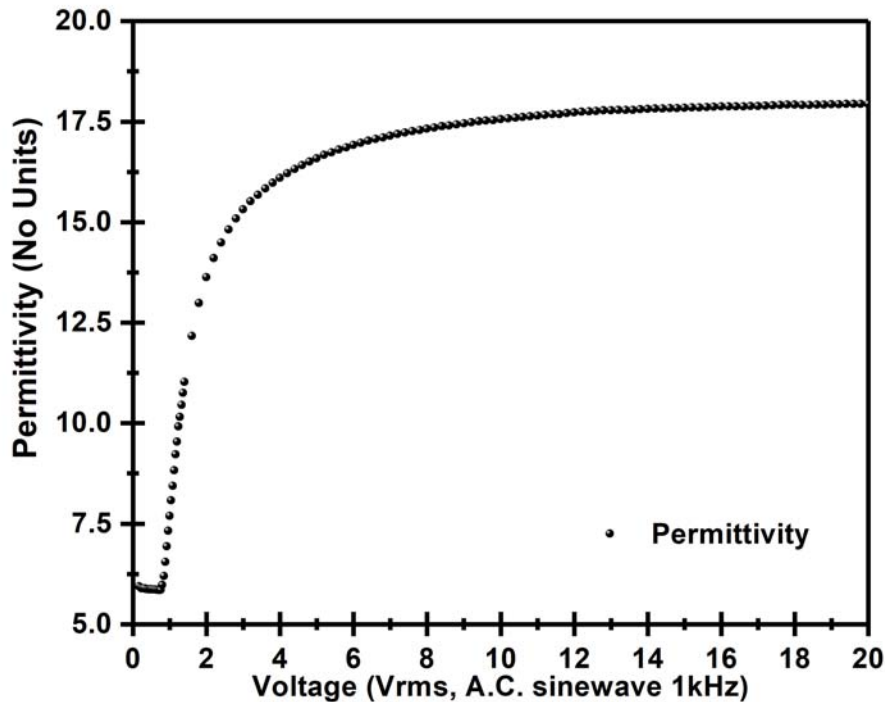
Figure 1.11: Fréedericksz curve for E1 liquid crystal (Planar alignment, nematic layer d=

22 μm) [20]

.

Liquid crystals n-director re-orient in response to external fields (electric, magnetic), due

to the anisotropic nature of liquid crystals molecules. In the absence of any external per-

turbation, the orientation of director is governed by boundary conditions (anchoring and

elastic forces). However, on the introduction of an external field, the **n**-director re-orients

itself in order to minimise the total energy of the system at a given value of external field.

This competition between elastic forces present in the system due to boundary conditions

and external field is termed as *Fréedericksz effect* (fig.1.11) [21]. For a sufficiently, small

voltage, $V_{applied} << V_c$ the director remains in an undistorted state where its orientation

is dictated by anchoring forces. When a voltage above V_c (Fréedericksz threshold) is ap-

plied to the system, the director distorts from its initial state with its orientation depending

14

on the magnitude of the applied E-field. This effect offers a method to measure different elastic constants (k_{11}, k_{22}, and k_{33}) and physical properties of liquid crystals mentioned in section 1.1.3. It should be noted that response of liquid crystals director to external field depends on anisotropy of the molecules, geometry of the system and field direction for example, a material with positive dielectric anisotropy ($\Delta \varepsilon > 0$) in homogenous planar alignment observes distortion in director in response to orthogonal field while a negative dielectric anisotropy material remain undistorted in the same system. The geometry and field direction should be chosen in a way such that it conflicts with the imposed boundary conditions [22]. Fig.1.12 shows two *Fréedericksz* geometries used for determining k_{11}, and k_{33} elastic constant in positive (Fig.1.12 (a)) and negative dielectric (Fig.1.12(b)) anisotropy liquid crystals material.
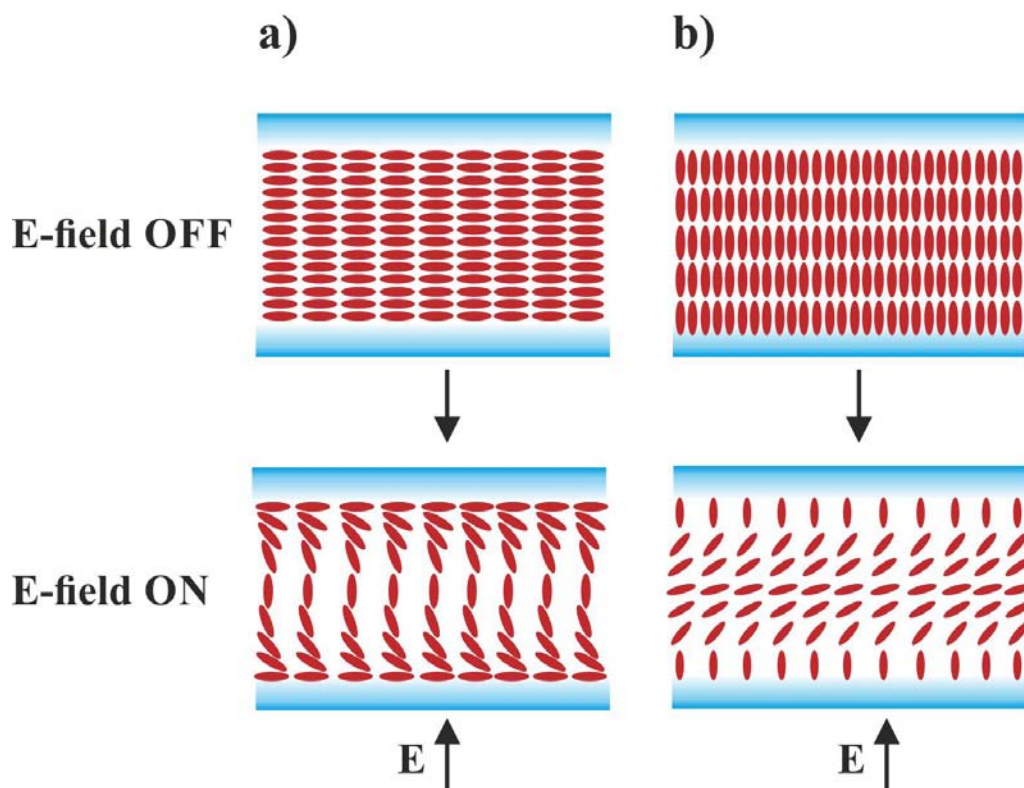
Figure 1.12: Schematic of different Freederickz geometries used for determining elastic constants (k_{11} and k_{33}) in (a) Positive and (b) Negative dielectric anisotrpy liquid crystal.

Figure 1.11 represents the Fréedericksz curve for E1 ($\Delta \varepsilon = 12.7$) in planar homogenous alignment (fig.1.12 a) with an orthogonal electric field. The value of $\varepsilon_{\perp}$ and $\varepsilon_{\parallel}$ can be determined from the region where, $V_{applied} < V_c$, and $V_{applied} >> V_c$ respectively and hence the $\Delta \varepsilon$. The value of V_c (Fréedericksz threshold) can be determined by the curve and elastic constants can be calculated using the Equation 1.8

$$V_c = \pi \sqrt{\frac{k}{\varepsilon_0 \Delta \varepsilon}} \qquad (1.8)$$

Where k can be k_{11}, k_{22} or k_{33} depending on geometry and direction of the applied field. It has been suggested that by judicious selection of geometries coupled with different flow-field conditions, *Fréedericksz curve* measurement can be used for deducing different set of viscosities for liquid crystals [23] mentioned in section 1.1.3. A detailed study on the effect of flow conditions on Fréedericksz curve in different geometries/alignment conditions is studied in Chapter 3.

1.1.7 Topological Defects

Topological defects are inevitable in nature, occurring from cosmology (cosmic strings) to biology (stem cells) [24, 25]. These defects are resultant of broken symmetry and can be described as a "tear" that can't be patched even by continuous variation of order parameter S [26]. In the field of liquid crystals, these defects are often used for phase recognition and understanding the statics and dynamics of the liquid crystals systems for technological applications.

In nematic liquid crystals, considering the 3D spatial sphere of order parameter S three different types of topological defects (Fig. 1.13 a-c) are possible [27, 28]:

1. Disclinations (Point defect in 0-D, Linear defect in 1-D).

2. Hedgehog.

3. Boojums.
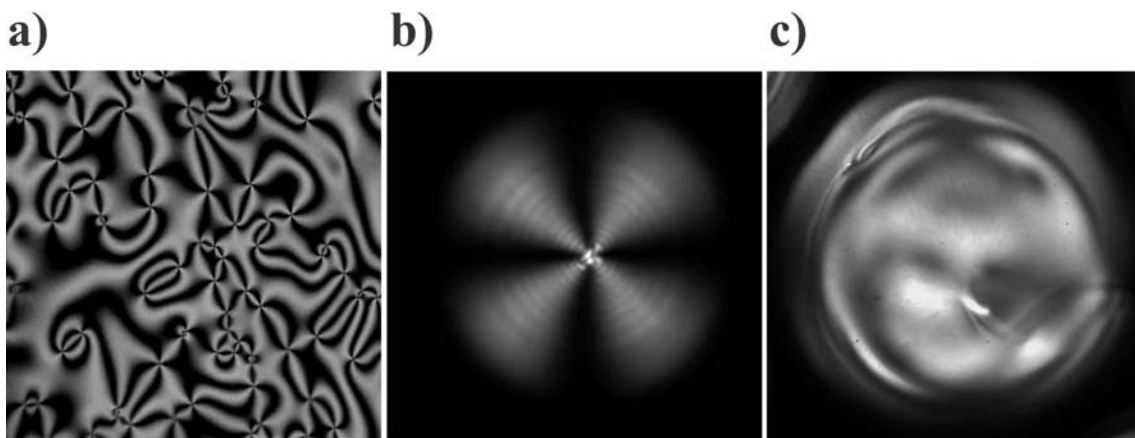
Figure 1.13: Polarising microscope images showing topological defects in nematic liquid crystals a) Schlieren textures formed in a nematic layer, b) Hedgehog, and c) Boojum defects in a nematic droplet

Polarising micrographs showing images of all these topological defects is given in figure 1.13. Among all these disclinations also referred as "*Schlieren texture*" are commonly

observed in 2-D nematic thin films when viewed under cross-polarisers. These appear to be dark brush like textures emanating from a point [22] (fig.1.14 a). Schlieren textures of different winding number (Fig.1.14 b) charge can be formed depending upon the number of even brushes coming out from a point. The winding number (m) is given as $m = \frac{1}{4} \times$ (no of brushes), and defect charge is determined by rotating polarizers for positive charge rotation is same as that polarizers whereas rotation is opposite against polarizers for negative charge [22, 29]. These textures are generally connected with opposite charged Schlieren to provide net neutrality to the system [22].

a)
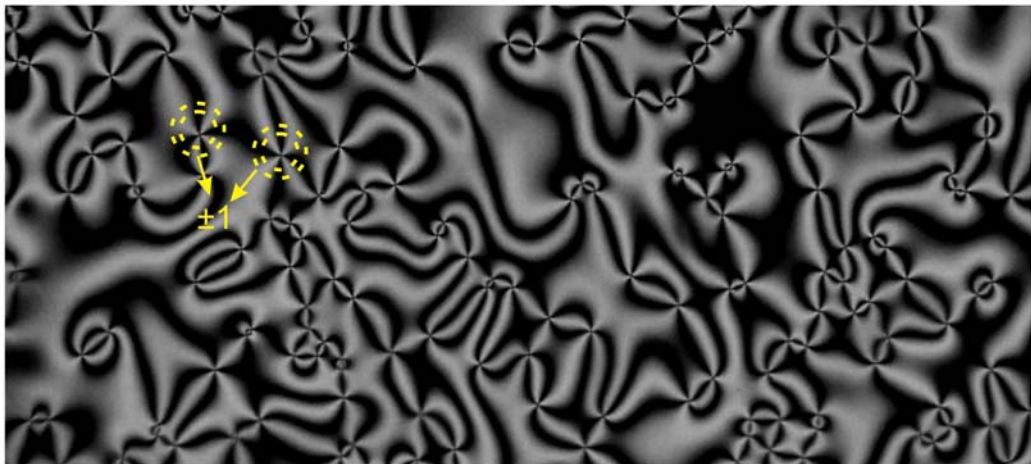
b)
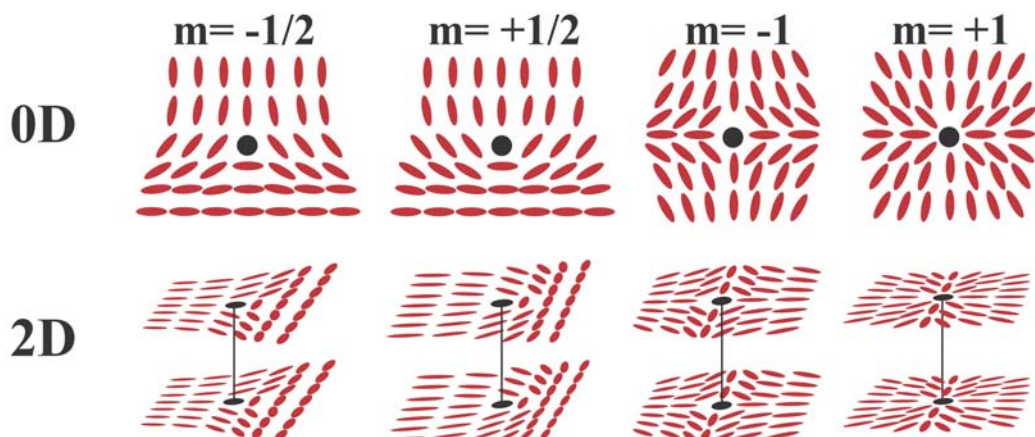
Figure 1.14: (a) Schlieren textures in a nematic layer. (b) Point defects (0-D) and disclination line defects (2-D) in nematic liquid crystals.

18

1.1.8 Flexoelectricity

Flexoelectricity (P_f) is defined as the generation of spontaneous induced polarisation in a material due to curvature distortion. This effect in some ways has a close resemblance to the piezoelectric effect in solids. But unlike piezoelectric effect which occurs due to positional strain, the presence of flexoelectricity in a material is a result of the curvature strain [30]. Moreover, it's a universal effect, unlike piezoelectricity, which is limited to non-centrosymmetric crystals[31] (20 out of 32 point groups). The origin of the flexoelectric effect in liquid crystals relates back to Sir Frederick Charles Frank's research article on the theory of symmetry, elasticity, and defects in liquid Crystals [19, 32]. However, this effect was first discussed in the year 1969, Meyer *et al.* proposed the "dipolar model" which suggests that a minor distortion in liquid crystals due to curvature strain leads to polarization of liquid crystals molecules [33]. Conversely, this can also be done by electric field induced deformation in liquid crystals [33]. Initially, it was thought that the flexoelectric effect is limited to shape asymmetric molecules having wedge and banana shape (Fig. 1.15a-d). However, later research from Prost and Marceau revealed the existence of flexoelectric effect in centrosymmetric molecules (Fig 1.15 e,f) as a consequence of change in quadrupolar density [34]. It should be noted that this effect only arises from splay, bend, or by the merger of both deformations, due to symmetry argument twist deformation doesn't induce flexoelectric effect [35]. The magnitude and direction of this induced polarization (P_f) is described by a splay coefficient (e_1) and bend coefficient (e_3) resulting in flexoelectric polarization given as Equation 1.9.

$$P_f = e_1 \underline{n} (\nabla \cdot \underline{n}) + e_3 (\nabla \times \underline{n}) \times \underline{n} \tag{1.9}$$

In presence of electric field ($\underline{E}$) induced flexoelectric polarisation the free energy density (f_d) equation 1.7 is modified and the resulting equation 1.10 is defined as a combination of elastic and flexoelectric energy:

$$f_d = \frac{1}{2}k_{11}\left[\nabla \cdot \underline{n}\right]^2 + \frac{1}{2}k_{22}\left[\underline{n}\cdot(\nabla \times \underline{n})\right]^2 + \frac{1}{2}k_{33}\left[\underline{n}\times(\nabla \times \underline{n})\right]^2 - e_1\underline{E}\cdot\underline{n}\left(\nabla \cdot \underline{n}\right)$$

$$-e_3\underline{E}\cdot\left[\underline{n}\times(\nabla \times \underline{n})\right] \tag{1.10}$$
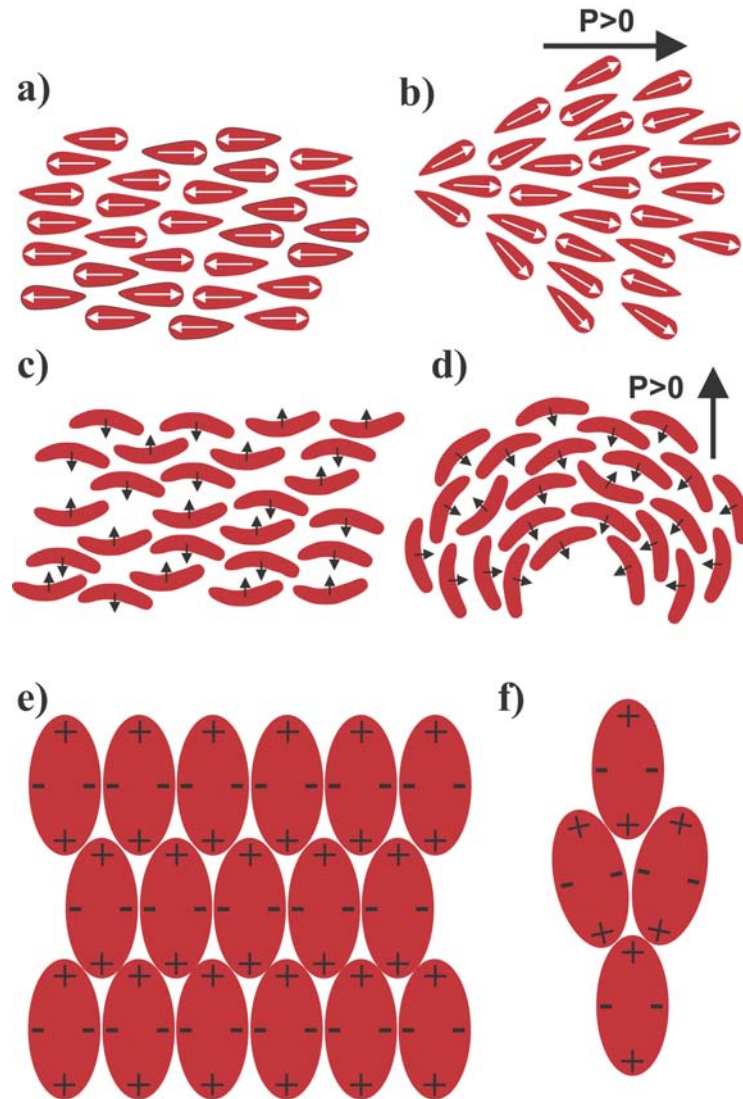
Figure 1.15: Flexoelectricity induced polarization in (a,b) wedge shape and (c,d) banana shape liquid crystals due to curvature distortion. (e,f) Flexoelectricity in an assembly of quadrupole e) undeformed state no bulk polarisation, f) deformed state, dissymmetry gives rise to polarisation.

1.2 Flow and Nematic liquid crystals

In this section we shall focus on flow effects on nematic type liquid crystals with aim to cover the relevant information required for understanding the effect of flow on nematic liquid crystals. A detailed review of flow field effect on liquid crystals is covered in the references [22, 36, 37].

1.2.1 Flow alignment in nematic liquid crystals
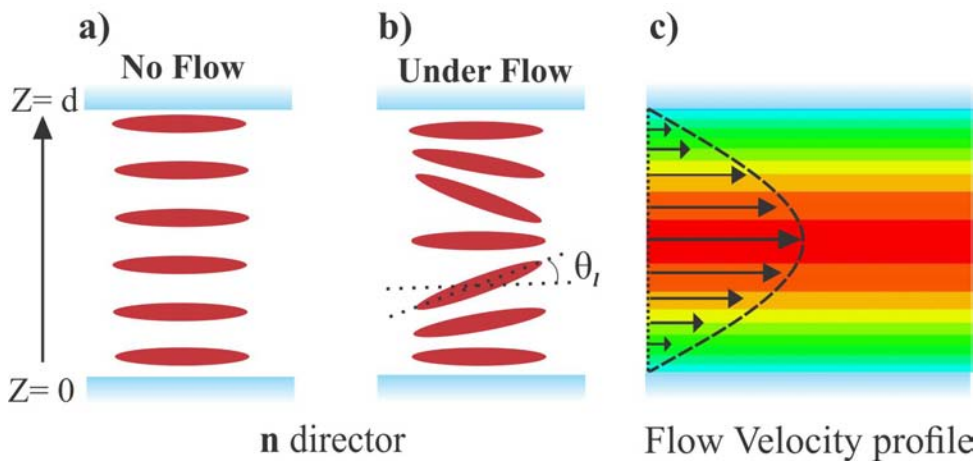
Figure 1.16: Schematic representing flow alignment in homogenous aligned nematic layer. a) Director orientation in absence of flow. b) In presence of flow condition (flow field parallel to n-director). c) Poiseuille flow profile.

On the basis of flow alignment (fig.1.16) nematic liquid crystals can be classified into two type i) flow aligning $(\alpha_2 \alpha_3 > 0)$ with common examples being 5CB liquid crystals [38] ii) non-flow aligning or tumbling nematics $(\alpha_2 \alpha_3 < 0)$ like 8CB liquid crystals [39]. Flow alignment angle or Leslie angle (θ_l) is defined as equation 1.11;

$$\theta_l = \tan^{-1} \sqrt{\frac{\alpha_3}{\alpha_2}} \tag{1.11}$$

Where α_2 and α_3, are second and third Leslie viscosity coefficients.

In case of flow aligning nematic liquid crystals,

21

$$\theta_l = +\tan^{-1}\sqrt{\frac{\alpha_3}{\alpha_2}} \tag{1.12}$$

i.e $\alpha_2\,\alpha_3 > 0$, whereas in case of non-flow aligning liquid crystals (tumbling),

$$\theta_l = -\tan^{-1}\sqrt{\frac{\alpha_3}{\alpha_2}} \tag{1.13}$$

Hence, $\alpha_2\,\alpha_3 < 0$, signify tumbling nematics.

1.2.2   Hydrodynamic stability in nematic liquid crystal flow

Hydrodynamic stability in an isotropic fluid is determined by the ratio of two contributing effects: inertial and viscous effects (Eqn. 1.14), commonly represented in terms of *Reynolds number* (R_e).

$$R_e = \frac{\rho V L}{\mu} = \frac{V L}{v} \tag{1.14}$$

Where ρ is fluid density, V is fluid velocity, L is the length scale, μ is the dynamic viscosity of fluid, and v is kinematic viscosity. $R_e < 2000$ shows laminar regime whereas $R_e > 4000$ shows turbulent regime and $2000 < R_e < 4000$ shows instabilities in transition regime [40]. Hence, it can be inferred that instabilities in isotropic case occur at quite high value of R_e. However, in contrast to isotropic fluids, nematic liquid crystals shows instabilities at quite a low value of $R_e << 1$ (ignoring elastic effect contribution) [28]. Moreover, in the case of liquid crystals in addition to inertial, and viscous effects, there is an additional effect of elasticity which plays a dominant role, in governing the instabilities within the system. Thus, in analogy to R_e, nematic flow stability is represented in terms of *Ericksen number* (E_r) (Eqn. 1.15).

$$E_r = \frac{\mu v L}{K} = \frac{v L}{D} \tag{1.15}$$

Where μ is the viscosity of fluid, V is fluid velocity L is the length scale, K is bulk elasticity of liquid crystals, and $D = \frac{K}{\mu}$ is diffusion constant of director orientation [41]. Thus, the hydrodynamic stability in nematic liquid crystal flow is characterized by *Ericksen number* (E_r)

Chapter 2

Experimental Methods and Techniques

This chapter focuses on experimental methods and techniques used for the studies reported in this thesis. The chapter starts with the fabrication of electrodes for flow cells, followed by microfabrication of co-planar interdigitated electrodes (IDE) that we used for actuating nematic layers using non-uniform electric fields. Further different surface treatments that were used for the formation of the alignment layer is discussed in detail. In the later part of the chapter, different characterization techniques, namely: Polarising optical microscope (POM), Confocal microscopy, Mach Zehnder (MZ-Interferometer), UV-spectroscopy, and Optical coherent tomography (OCT) are also discussed.

2.1 Fabrication of flow cell electrodes

2.1.1 Flow cell electrodes geometry

Two types of flow cells (fig.2.1 a,b) one having lollipop patterned electrode (circular area diameter 10 mm and 12 mm) and other having rectangular pattern electrode *(17.5×20 mm active region surrounded by earth ring)* were used in the studies. In the case of lollipop electrodes (fig.2.1 c), the cell-active circular area has a diameter of 10 and 12 mm and a rectangular connection strip *(3×5 mm)*. In the case of the flow cell having a rectangular electrode, the top surface is a continuous ITO plane *(75×25 mm)*, and the bottom surface

24

(fig.2.1 d) consists of a rectangular ITO electrode active region of *17.5×20 mm* separated from the earth ring by 0.1 mm gap.
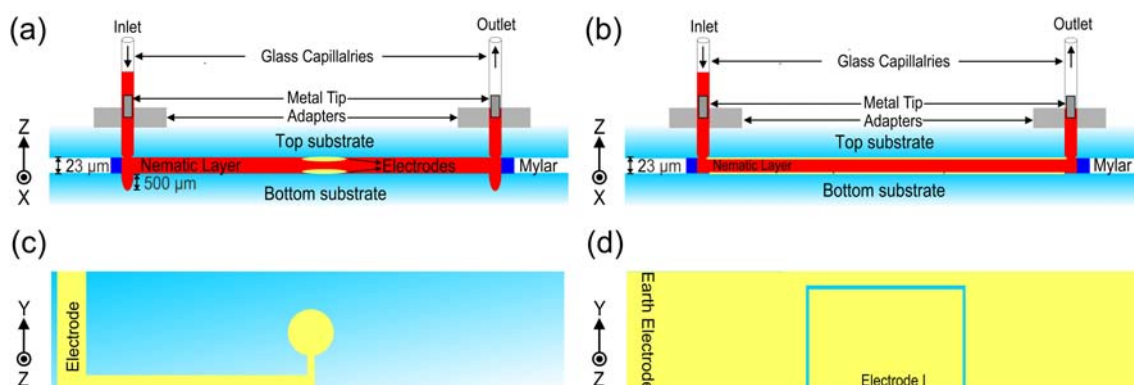
Figure 2.1: Flow cell with (a) lollipop electrodes and, (b) rectangular electrodes. (c, d) shows top view of electrode geometry used in the flow cell. Note the top substrate in rectangular electrode flow cell is a continuous ITO plane.

2.1.2 Flow cell electrodes fabrication

Flow cell electrodes were fabricated using acid-resistant tape (VWR International, UK) as a replacement for patterning photoresist. Initially, Indium tin oxide (ITO) coated borosilicate glass substrates (ITO of 25 nm thickness and 100 Ω/square resistivity, Praezisions Glass and Optick GmbH, Germany) were cleaned following the standard multistage cleaning procedure briefly mentioned in section 2.2 of the chapter. These cleaned substrates were then covered with acid-resistant tape and the desired electrode geometry shown in Section 2.1.1 was drawn on the substrate using a laser cutter (PLS6.150D, Universal Laser Systems, USA). Afterward, the acid-resistant tape was peeled off from the region requiring ITO etching. Substrates were then immersed in the etching solution (1:12.5:12.5, Nitric Acid (HNO_3): Hydrochloric Acid (HCl): DI water (H_2O)) and stirred at 700 rpm for a duration of 10-12 minutes at ambient laboratory condition. After completion of the etching process, the resistance across the etched region was checked using

a multimeter to ensure complete etching of ITO, and substrates were dipped in Deionised (DI) water to stop the etching process. In the last step of the process, the acid-resistant tape was peeled off from the protected/ITO region, and substrates were cleaned again following the multistage cleaning procedure (see section 2.2) before being coated with the alignment layer.

2.2   Microfabrication of Interdigitated electrode (IDE)
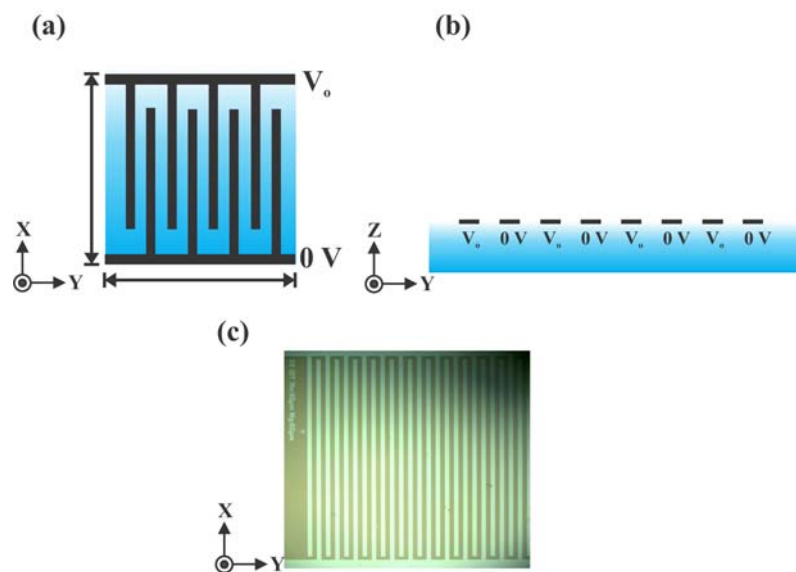
Figure 2.2: Interdigitated electrode (a) Top view (b) Side view.(c) microscope image showing top view of the pattern transferred on the substrate.

Photolithography (UV-lithography) is a widely accepted lithography technique for the creation of reproducible microscopic and nanoscopic patterns on a variety of substrate materials. In this technique a photoactivated polymeric layer (photoresist) is illuminated with UV-light passing through a patterned mask and the desired structure is transferred onto the surface of a substrate. Due to these features of accurate pattern transfer, this lithographic method is widely used in the electronics industry. In this thesis, Interdigitated electrodes (IDE) were made using the mentioned lithography technique. Briefly, the

IDE pattern (fig. 2.2) was transferred from a photomask on ITO coated borosilicate glass slides (ITO of 25 nm thickness and 100 Ω/square resistivity, Praezisions Glass and Optick GmbH, Germany) of size 25×25 mm. The spacing between the electrodes (w_g) and width (w_e) of the electrode was of the same size ($w_e = w_g = 80\mu m$). The electrode pattern was transferred onto the substrate in a series of lithographic steps summarized in Figure.2.3. In the First step (adhesion promotion/cleaning) substrates were cleaned in a multistage process. Initially, substrates were ultrasonicated for 15 mins in 5% Decon90 solution in deionised water (DI) heated at 60°C. These substrates were then transferred to 0.5% Decon90 solution, followed by DI water and treated in a similar manner as above. The cleaned substrate was then submerged in isopropyl alcohol (IPA) and further blow-dried using a Nitrogen (N_2) gun. In the second step (photoresist coating), the clean substrate was kept on the vacuum chuck in the spin coating unit (Laurell WS-6505-6NPP), and positive photoresist (S1813, Dow® Electronic Materials) was spin-coated on the substrate. As the thickness of photoresist film is governed by sample rotation speed and time, the complete spinning cycle (35 secs) was configured in two stages to give a film thickness of 1.5 μm. In first stage excess resist was removed by sample rotation at 500 rpm for 5 seconds in the second stage sample was spun at 3000 rpm for 30 secs to achieve uniform film thickness. Subsequently, in the third step (soft bake), photoresist coated substrates were heated at 105°C for 75 seconds. This step was performed to densify the coating and to drive off the excess solvent in the system [42]. In the next step (mask alignment and exposure), a photomask was placed in holding unit of mask aligner (MicroTec SUSS MJ4B) and the distance between the mask and coated substrate was adjusted to ensure contact mode alignment (substrate kept in contact with mask). After completion of the alignment process, the photoresist layer was exposed to UV light for 1.4 seconds. This

triggered a photochemical reaction and the exposed area became soluble in the developer solution. In the fifth step (development), UV-exposed substrates were immersed in S1813 developer solution for 45 seconds for removal of exposed area and subsequently washed with DI water to remove excess developer solution. In the next step (inspection and hard-bake), the transferred pattern was observed under the microscope (fig. 2.2c) to confirm the development process and then baked at 105°C for 10 minutes to make photoresist resistant to the etching solution. In the seventh step (etching), the ITO coating present between the patterned structure was removed. Substrates were then immersed in an etching solution (1:12:12.: Nitric Acid (HNO_3): Hydrochloric Acid (HCl): DI water (H_2O)), and the solution was stirred at 700 rpm at ambient laboratory condition for the duration of 10-12 minutes. After etching, the resistance across the ITO was checked and the patterned substrates were dipped in DI water. In the last step (resist removal), the resist present over the patterned substrate was removed by rinsing the substrate with acetone and the substrates were then cleaned with isopropanol (IPA) followed by blow-drying. Fabricated electrodes were then cleaned again and coated with alignment before they were used in the experiments.
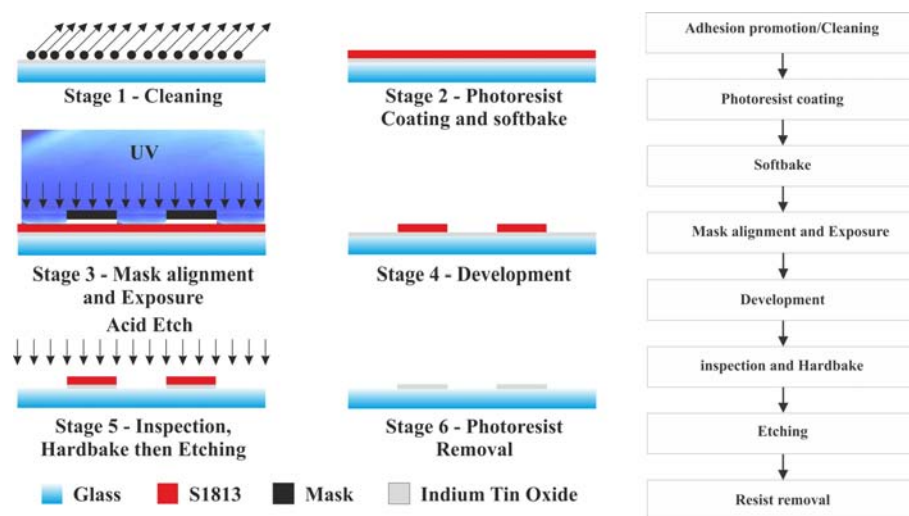
Figure 2.3: Micro-Interdigitated electrode fabrication steps.

2.3 Alignment layers

As discussed in Chapter 1, section 1.1.4, liquid crystals n-director can possess different alignment depending upon interfacial interactions. Several physical, chemical, and physio-chemical methods can be employed for producing the desired alignment conditions. In this section, we will focus on different alignment methods used in this thesis for planar, homeotropic, and hybrid alignment of the n-director.

2.3.1 Planar alignment layer
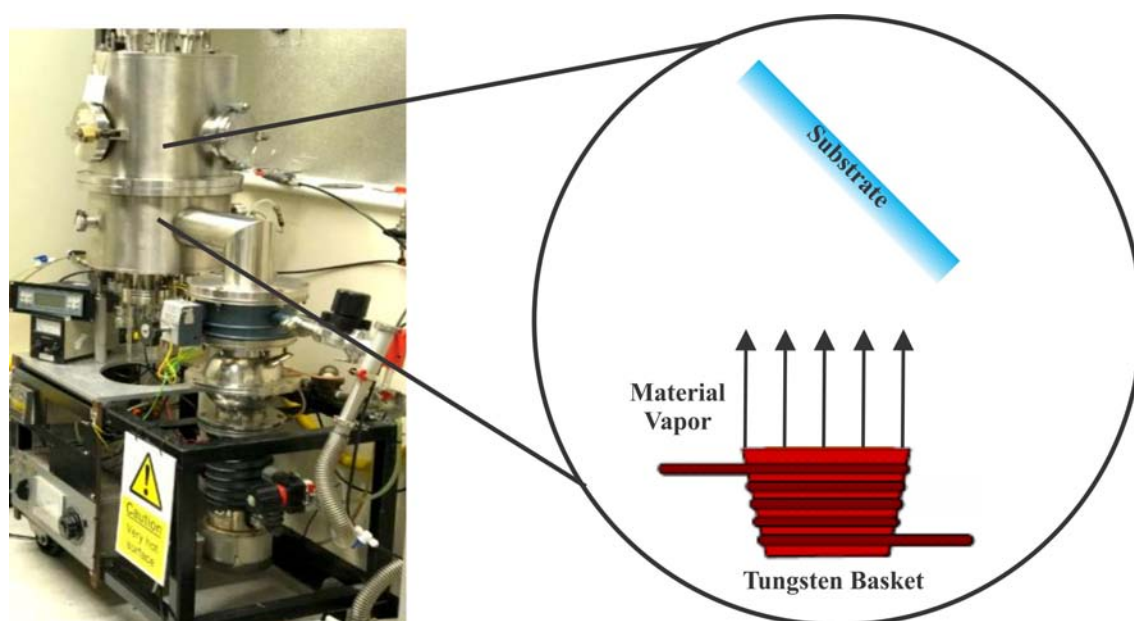
Figure 2.4: Thermal evaporator setup used for deposition of MgF2 and ZnS thin films for planar alignment of n-director on ITO substrate.

Planar alignment of n-director was obtained by oblique deposition of a solid thin film (45°degree to the plane of the substrate) in the direction perpendicular to the desired direction of n-director. Deposition at an angle provides grooves (columnar structure) in the thin film that induces anisotropy, which in turn expected to cause the alignment of the liquid crystals [43]. Resistive heating induced thermal deposition (fig. 2.4) was used for physical vapor deposition (PVD), of thin films. The setup consists of a high vacuum

chamber pumped utilizing a set of diffusion and rotary pumps, substrate material loaded into the chamber and target material placed in a holder heated by means of an external power supply. Briefly, the holder (tungsten basket) containing target material is heated at high vacuum (10^{-6} mbar) and temperature conditions (1400°C) leading to the formation of material vapours. Due to the low-pressure condition in the chamber, the mean free path of material vapours atom is high, so they travel in a straight line towards the substrate where they condense, forming a solid thin film. In this thesis, Magnesium fluoride (MgF_2) and Magnesium fluoride /Zinc sulfide (ZnS) thin films were deposited using this technique to serve as a planar alignment layer for nematic liquid crystals.

2.3.1.1 MgF_2 thin film alignment layer

Magnesium fluoride (MgF_2) thin film ($d \approx 250$ nm) was used for planar alignment of liquid crystals. The magnesium fluoride layer was deposited using the above mentioned PVD technique with the plane of the substrate tilted at 45°to the evaporation direction. This provided mechanical nano-groove planar alignment of the nematic liquid crystal with a negligible pretilt angle [20, 44]. Figure 2.5 a,b shows Scanning electron microscopy (SEM) image of thermally grown MgF_2 onto the ITO substrate. Optical micrographs in figure 2.6 shows planar alignment of 5CB layer between MgF_2 coated substrates.
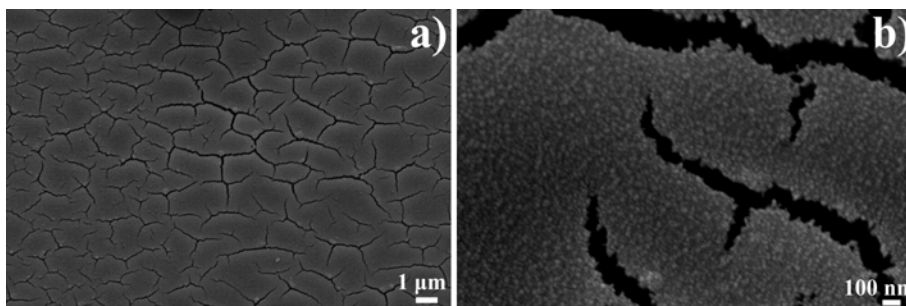
Figure 2.5: Scanning electron microscopy (SEM) image of MgF2 thin film deposited on ITO coated glass slide (a) at 5,500x magnification (b) zoomed-in view at 50,000x.

Figure 2.6: Optical micrograph of MgF$_2$ thin film coated 5CB cell rotated between cross-polarisers. Sample position and polarisers orientation given in the images.

2.3.1.2   MgF$_2$/ZnS thin film alignment layer

MgF$_2$/ZnS thin film (combined thickness, d≈300 nm) was also used for the planar alignment of the n-director. For the formation of MgF$_2$/ZnS thin film initially, the sample was coated with ZnS using the PVD technique mentioned above followed by the deposition of MgF$_2$ on ZnS coated surface. This combination of the thin films was used to provide a robust, long-lasting alignment layer that can sustain high voltages (V_{rms}=300V). In case of MgF$_2$ alignment layer alone, it was observed that nano/micro cracks (Fig. 2.5) present on thin films due to tensile intrinsic stress [45] in MgF$_2$ films grow into micro-cracks on the application of high voltages (fig. 2.7 a,b) leading to the problem of charge leakage and alignment loss after few experimental runs.
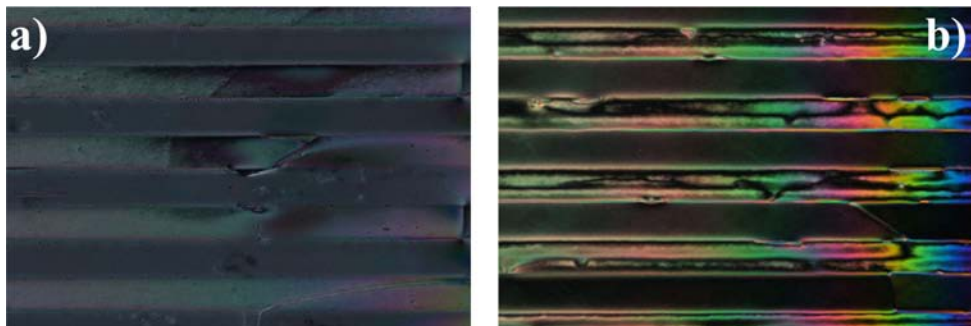
Figure 2.7: MgF$_2$ thin film coated IDE a) During the first run, b) After two runs at high voltages (V_{rms}=300 V).

31
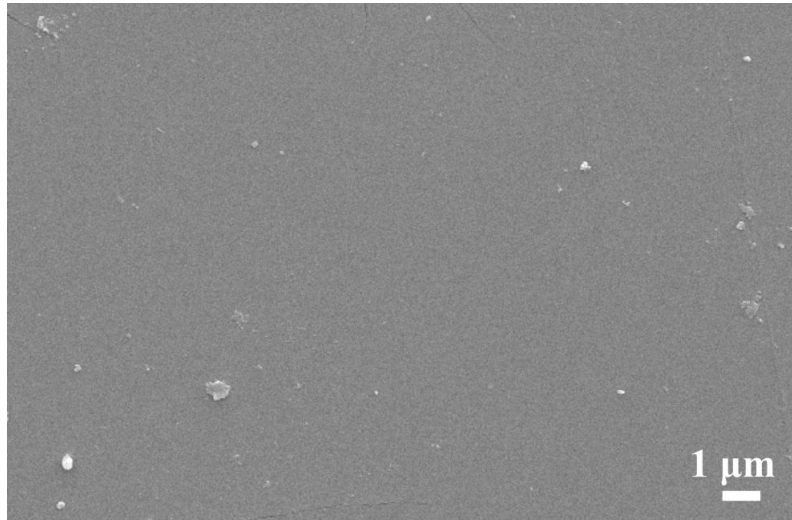
Figure 2.8: Scanning electron microsocpy (SEM) MgF$_2$/ZnS thin film deposited on ITO coated glass slide at 5,500x magnification.

2.3.2 Homeotropic alignment layer

2.3.2.1 Teflon AF coating

For the homeotropic alignment of liquid crystals a solution of Poly[4,5-difluoro-2,2-bis(trifluoromethyl)-1,3-dioxole-co-tetrafluoroethylene], referred as *Teflon AF*, was made in its solvent, Octadecafluorodecahydronaphthalene (CAS numbers 37626-13-4 and 306-94-5, Sigma-Aldrich / Merck KGaA, Darmstadt, Germany), 0.75% by weight. The resulting solution was dip-coated onto the substrates followed by drying at room temperature for 5 min and baking at 60°C for 10 min for removal of residual solvent. This surface treatment provides homeotropic alignment to liquid crystals. Please note the Telfon AF used in this study is an amorphous fluoropolymer this is not similar to standard PTFE which is a crystallite polymer and commonly used as a planar alignment layer. To ensure homeotropic alignment of liquid crystal on Telfon AF coated substrates we have performed different experiments (figure. 2.9) utilising liquid crystal E1 as a standard material.
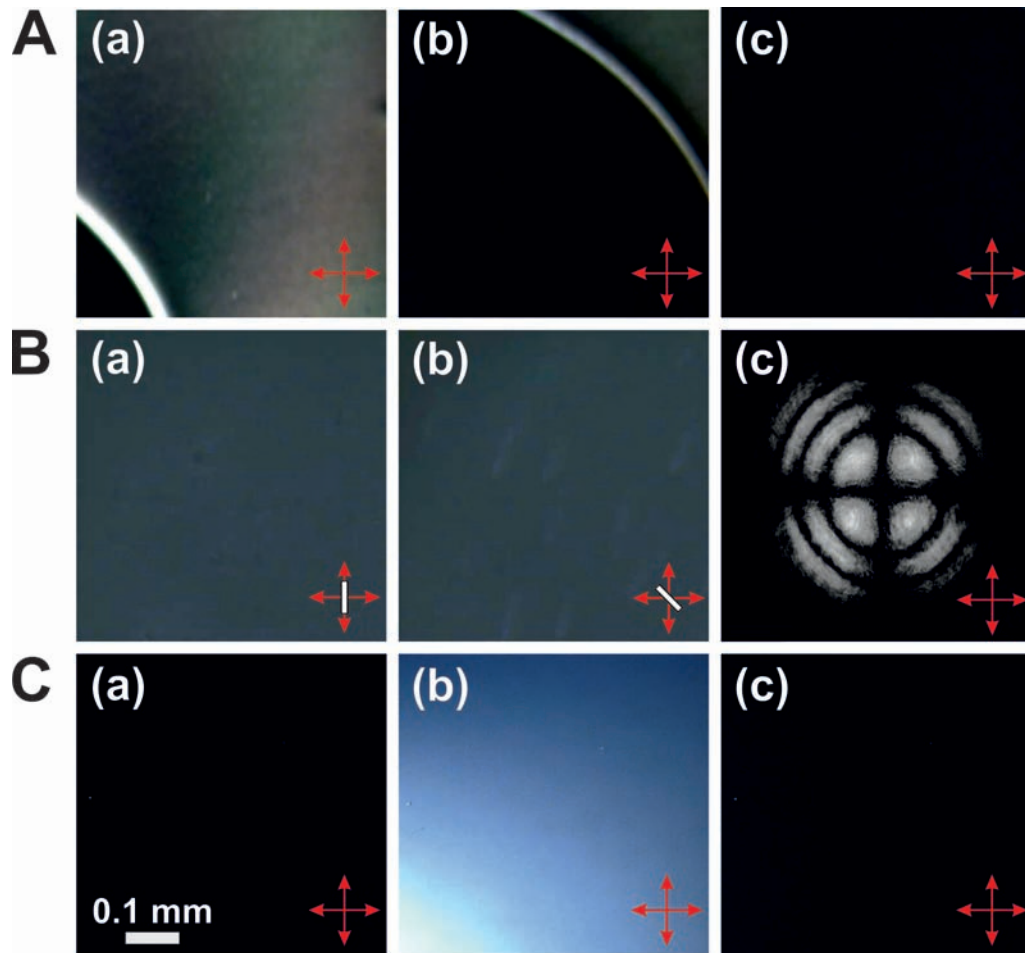
Figure 2.9: Optical micrograph of a test cell containing a layer of the nematic liquid crystal material E1 and with Teflon AF coating on both internal surfaces that imparts homeotropic alignment. The micrograph images were taken using a $10\times$ microscope objective under horizontal plane-polarised light with a crossed vertical analyser. (A) show images of the test cell immediately after capillary filling, in which the transient H-state is observed successively annealing out in the direction towards the top right corner. (B) (a) and (B) (b) show the fully annealed homeotropic state with the cell rotated at different orientations, (a) 0°and (b) 45°. (B) (c) shows a conoscopic image (a thicker cell was used in this image only), at a wavelength of 632.8 nm. (C) shows the optical texture in the cell before (a), during (b) and after (c) mechanical disruption achieved by tapping the cell.

Fig. 2.9 A shows different times immediately after the capillary filling of the nematic material E1 into the test cell. In the top right of Fig. 2.9 A(a) the splay bend state, or "H-state" can be observed that is characteristic of nematic flow in the homeotropic geometry [46]. This domain of the H-state grows out, Fig.2.9 A (b), leaving a uniform homeotropic domain, Fig. 2.9 A(c), that appears dark between crossed polarisers. Fig. 2.9 B shows contrast-enhanced images of the filled test cell at different orientations between crossed polarisers, with the test cell rotated 45°in the clockwise sense for the image in Fig. 2.9 B(b) compared to in Fig. 2.9 B(a). The very similar appearances and uniformity of the 2 images in Fig. 2.9 B (a) and Fig. 2.9 B(b) is consistent with the homeotropic aligned nematic layer exhibiting the expected zero birefringence. The image in Fig. 2.9 B (c) shows a conoscopic figure taken using uniform expanded illumination from a He-Ne laser at a wavelength of 632.8 nm, focused onto the cell with a 20X microscope objective, and with light collected using a 20 microscope objective that was also focused onto the cell. A cell with a larger 40 μm gap was used for Fig. 2.9 B (c) only in order to be able to observe a number of extinction rings. A uniaxial conoscopic figure is obtained, as expected for a cell with homeotropic alignment. Fig. 2.9 C demonstrates the response of the nematic layer in the test cell to the mechanical disruption caused by tapping the cell and monetarily decreasing the cell thickness. Fig. 2.9 C(a) shows the unperturbed layer, Fig. 2.9 C(b) shows the optical texture and expected increase in optical transmission during disruption, and Fig. 2.9 C(c) shows the recovered homeotropic texture immediately after the disruption. Thus, all these experiments ensure the use of Teflon AF as a successful homeotropic alignment layer.

2.3.2.2   Silane coating

In some experiments requiring vapor phase deposition of alignment layer silane (Trichloro (octyl)silane or Trichloro(1H,1H,2H,2H-perfluorooctyl) silane) was used for homeotropic alignment of liquid crystals. The deposition of silane on substrates/microparticles was performed in the vapor phase. Briefly, Substrates were placed in 100 mL media bottle and exposed to 1-2 drops of silane (~5-6 μL) for a time duration of 10-12 mins. This surface treatment provides homeotropic alignment to liquid crystals.

2.3.3   Hybrid alignment layer

Hybrid aligned nematic (HAN) alignment layer was achieved using the combination of planar and homeotropic alignment layer mentioned in the above section 2.3.1 and 2.3.2.

2.4   Characterisation techniques

2.4.1   Electrical Addressing of Devices

The electrical addressing of the device was done using a range of electrical equipment. In the case of Fréedericksz curve measurement, electrical addressing of devices was done using LCR (Agilent 4284A precision LCR meter, Keysight Technologies, UK) controlled using LABVIEW program developed with the help of Dr. Andrew Edwards. For, all other experiments electrical signal was applied to the system using voltage Amplifier (PZD700, Trek Inc., USA) connected with a waveform generator (TGA1244, Thurlby Thander Instruments Limited, UK). The signal from amplifier and waveform generator was monitored using an oscilloscope (TDS2014, Tektronix Inc., UK) and Multimeter (34401A, Keysight Technology, UK).

2.4.2   Polarising Optical Microscope (POM)

Polarisation Optical Microscope (POM) has been a prime tool for studying internal structures and crystal properties of organic and inorganic chemicals. In the field of liquid crystals, Polarisation Optical Microscope provides a unique window to study the director configuration and at the same time is aesthetically pleasing due to vivid colors and defect textures observed in liquid crystals films [47]. In this section, we will look into the experimental aspects of Polarisation Optical Microscope (BX51, Olympus, USA). All experiments were performed in Transmission Mode (light passing through the thickness of the sample was analysed) unless specified. Briefly, unpolarized light from the illumination source of Polarisation Optical Microscope was passed through a polariser leading to the linear polarisation of light dictated by the polariser axis. The linearly polarized light then passes through liquid crystals layer which then splits into ordinary and extraordinary components forming an elliptically polarized light. This elliptically polarised light then passes through another polarizer, referred to as *analyzer*, before reaching the CMOS camera mounted on the microscope.

In our setup, both polarisers and sample placed on a rotating stage are capable of rotating precisely by the precision of 1° degree. When two polarisers axes are mutually perpendicular to each this configuration is termed as *cross-polarised* state, and no light reaches the camera sensors in this situation. However, if sample placed between the crossed polarisers elliptically polarised light passes through the second polarizer (*analyser*) and sample appears to be bright provided liquid crystals director is not parallel to one of the polarisers otherwise this configuration would render dark appearance to the sample. In our experiments, liquid crystals samples were analysed in different configurations of polarisers (specified in the respective polarisation optical micrographs). Depending upon the *region of interest* (ROI), the requirement of optical resolution different dry objective

lens (4x-50x) was used for image or video recording.

2.4.3   Confocal Laser Scanning Microscopy

Confocal laser scanning microscopy (CLSM) is an imaging technique that is commonly employed for obtaining high resolution and high contrast depth images of 3D samples. In the field of liquid crystals, CLSM and polarisation optics modified CLSM is commonly used for imaging fluorescent particles in defects cores and understanding the 3D n-director field [48]. For studies reported in this thesis, CLSM was used for imaging fluorescent polymeric particles trapped in the domain wall formed in the bulk of 2D hybrid nematic layers.
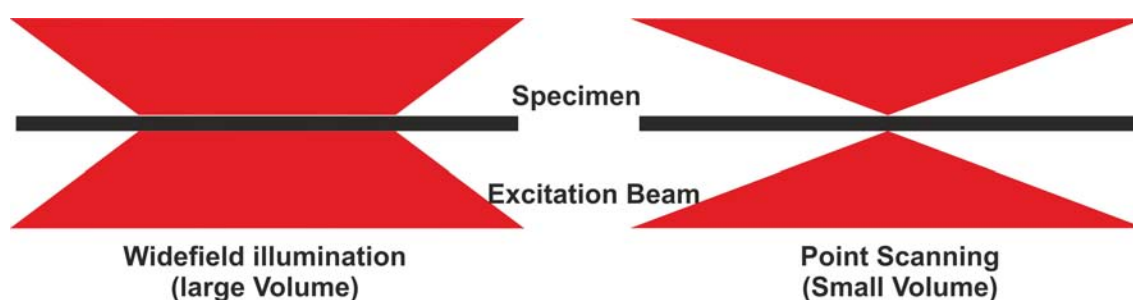
Figure 2.10: Difference in sample illumination in wide-field microscope and confocal microscopy.

The working principle of CLSM is similar to wide-field fluorescent microscope, as both techniques use fluorescence optics for sample imaging. However, unlike wide-field microscope in which the whole sample is illuminated, and the fluorescence emissions are recorded, in confocal microscopy a raster scan is performed over the sample to generate, images of one single optical plane and out of focus signals from the sample were eliminated by use of pin-holes to provide a high-resolution image of the sample. Figure 2.10 shows the difference in sample illumination in the case of wide-field fluorescent microscope and confocal laser scanning microscopy.

2.4.4 Image, Video capturing and Analysis.

Experimental videos were recorded using a CMOS camera (EO-13122C, Edmund optics, UK). Depending upon the region of interest (ROI) and requirement of optical resolution different dry objective lens (4x-50x magnification) was used for image or video capture. Videos are recorded at the desired frame rate (1 fps-2000fps) depending upon the experimental requirement. For a frame rate greater than 200 fps, the high-speed camera (HHC X4, Mega Speed Corporation, US) was used for recording videos. Image analysis was performed using ImageJ [49, 50], and MATLAB in-house image analysis scripts. Specifics about MATLAB codes and ImageJ plugins are mentioned in detail in the individual chapters where they are used.

2.4.5 Cell thickness measurement

2.4.5.1 *UV-Spectroscopy*

Different liquid crystals cells (Hybrid aligned, Planar, Homeotropic) were made respective to the experiment (details given in individual chapters). In general, liquid crystals cells consist of two substrates separated by a polyethylene terephthalate strips (Mylar spacer) of desired thickness. The liquid crystals cell assembly was glued at the endings using Araldite epoxy resin. The thickness of the cell was measured using UV-vis spectroscopy. In particular, an empty liquid crystals cell was placed perpendicular to the light source, and the percent transmission (%T) of light is recorded over a wavelength range (Fig.2.11a) to provide an interference pattern. An integer (m) which was incremented as a function of wavelength (λ) is assigned for each recorded value of maxima, and the optical path difference is calculated using the equation. 2.1

$$2d = m\lambda \tag{2.1}$$
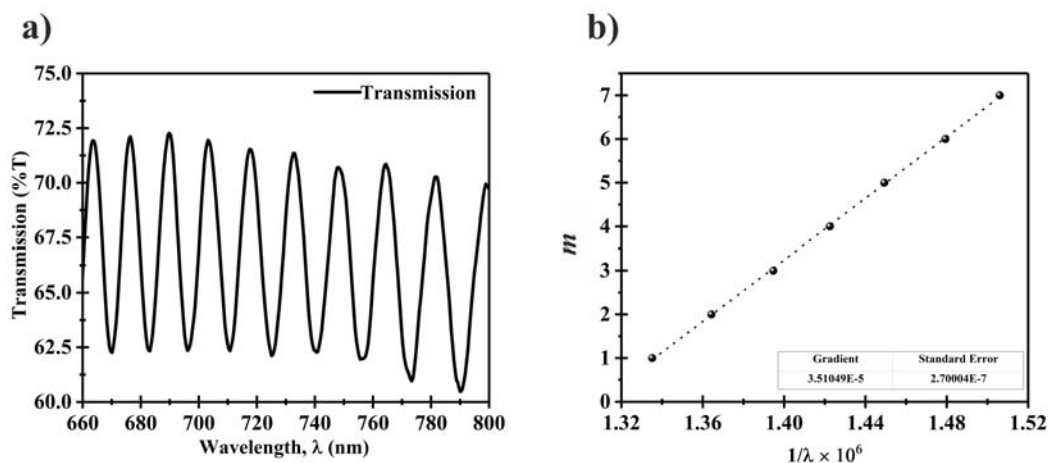
Figure 2.11: a) %Transmittance as a function of wavelength (nm), b) m vs $1/\lambda$ plot for thickness determination.

Where m is an index, d is cell thickness, and λ is the wavelength. The index (m) of the maxima was plotted against the reciprocal of the wavelength($1/\lambda$), and the thickness (d) of the cell is determined by dividing the gradient of figure 2.11b by half. Figure 2.11b reveals a gradient value of (35.10 ± 0.27 μm) which signifies measured liquid crystals cell is of a thickness (17.55 ± 0.135 μm). To verify uniformity in thickness (d) across entire cell dimension, measurement was preformed on different regions of the sample.

2.4.5.2 *Optical Coherent Tomography (OCT)*

Optical Coherent Tomography (OCT) was also used for measuring the thickness of the liquid crystals cells. OCT is a relatively new optical imaging technique that offers a real-time non-invasive and non-contact method for sample analysis. It is based on the Michelson interferometer (MI) and relies on back-reflected light to image cross-section images of subsurface microstructures. In simpler terms, OCT measures the time-of-flight of light echoes from the sample by creating an interference pattern. Briefly, a broadband beam of MI is incident on a beam splitter which then splits into two parts a) The first part travels towards the sample and b) the second part propagates towards the reference

39

mirror. Once both the parts hit their respective targets reflected light from both the arms (reference and sample) is redirected to the detector and recombined to produce an interference pattern [51] (fig.2.12). Broadly OCT is categorized into two types, Time Domain

Light source
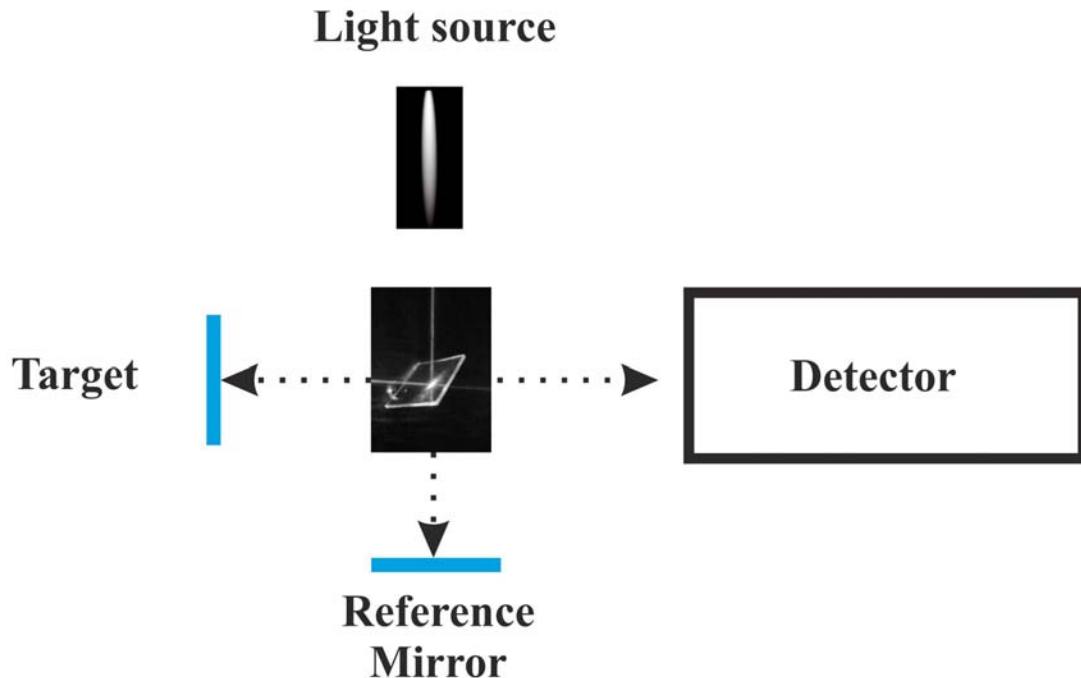
Figure 2.12: Schematic of the operation of Michelson interferometry for OCT scanning.

OCT (TD-OCT) and Fourier domain (FD-OCT). The significant difference between the two OCT is the collection of the signal. In TD-OCT, interference between two beams occurs by movement of reference mirror (i.e., change in reference path). However, in FD-OCT, the reference mirror is fixed at one position and measurement of interference pattern overtime is done as a function of wavelength sweep of laser source. Subsequently, a depth profile is generated by inverse Fourier transformation on the interference spectrum [52]. A major advantage of FD-OCT is the absence of movable parts for depth scans; so if the wavelength sweep of the laser is fast enough FD-OCT provides us an ability to perform scans at much faster rates in comparison to TD-OCT. Figure 2.13 (a, b), shows a cross-sectional scan of the liquid crystals.
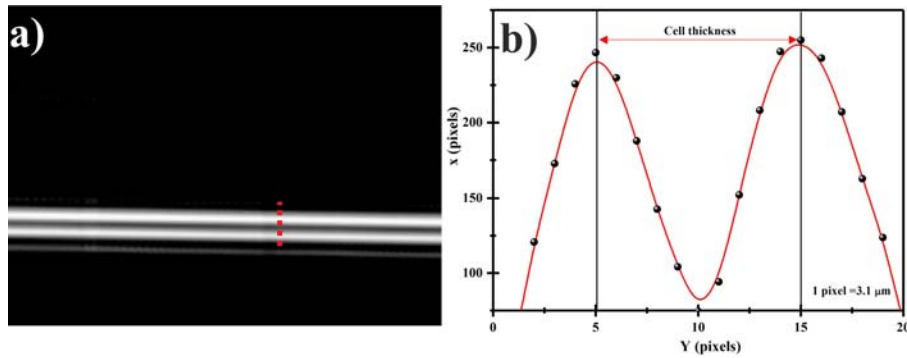
Figure 2.13: a) Depth scan of empty liquid crystals cell (red marked region shows the area across which profile is measured). b) The corresponding thickness profile of scanned liquid crystals cell.

2.4.6 Mach-Zehnder (MZ)-Interferometer
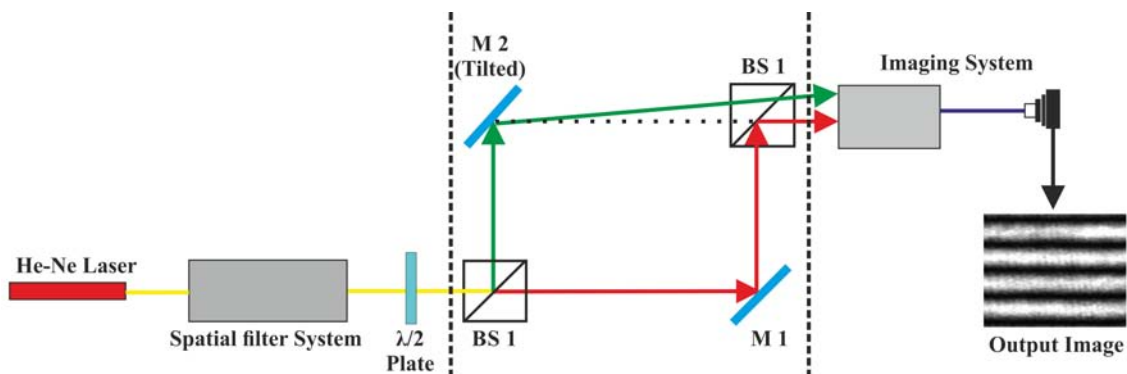
Figure 2.14: Schematic of Mach-Zehnder Interferometer.

The Mach-Zehnder (MZ) Interferometer (fig.2.14) is a versatile diagnostic tool that measures the change in the optical path length introduced by a sample. The instrument works by dividing the amplitude of a beam of light into two separate beams, sending these beams along two different paths (sample and reference), and then recombining the two beams. It is frequently used in different fields of study like aerodynamics, liquid crystals, and optics due to its ability to study transparent materials, gas flows, and the availability of freely accessible working space. For, studies shown in this thesis MZ interferometer is used to

measure the change in the n-director due to an applied electric field in the nematic layer.

2.4.6.1 *Experimental Setup*

The setup used for the experiments (Figure 2.14) consists of three parts a) light source, b) interferometer main body, and c) image capturing system. Initially, in part (a) of the setup coherent, collimated and monochromatic light is produced by 17mW He-Ne laser passing through a spatial filter system. This gives us a filtered beam of light (25 mm diameter) with a gaussian intensity profile. The beam exiting from the filter system was then passed through a $\lambda/2$ a plate which controls the polarisation plane of the beam. In the next step, the polarised light beam enters the main body of the interferometer. Briefly, the incoming polarised beam from part (a) of the setup hits the 50/50 beam splitter (BS1) where the amplitude of the beam is divided into two parts, and created beams are redirected to different arms of the interferometer (sample and reference). The beam in the reference arm travels straight towards the mirror (M1) from where it's redirected to the second beam splitter (BS2), whereas the sample beam interacts with the sample and then hits the mirror (M2) from where it is redirected to BS2 and both the beams recombine at BS2 creating an interference pattern carrying sample information. It should be noted that two beams are set up at a slight angle to each other before they recombine at BS2. This is done to obtain an interference pattern on beam recombination at BS2. In the next part of the setup, the image of the interference pattern is spatially transferred by a system of relay lenses into the microscope objective, which allows it to be recorded using CMOS camera. The images and videos acquired from the setup were then analysed afterward.

2.4.6.2   *Analysis of the interferogram*

It's clear from above that interaction of the light with a medium would lead to the modi-
fication in optical path length, which would reflect itself as a relative change in the fringe
pattern. However, whilst analysing liquid crystals using the above technique one should
be very careful about the polarisation plane of light and sample alignment conditions as
this can severely impact the desired outcome. Figure 2.15a shows a liquid crystal free
surface placed on IDE ($w_e = w_g = 80 \ \mu m$) electrodes under no applied voltage. Since
the alignment of liquid crystals is planar along *y*-axis (perpendicular to electrode length)
and homeotropic on free surface polarisation plane of laser light is set along n_o refractive
index to see the variation only in the surface profile. If polarisation plane if set along n_e in
this case, then the resulting interferogram would see the variation in the refractive index
of the sample due to varying director profile (hybrid alignment) in the sample. Figure
2.15b shows changes in liquid crystals surface profile when a voltage is applied between
IDE creating an undulation in the surface.
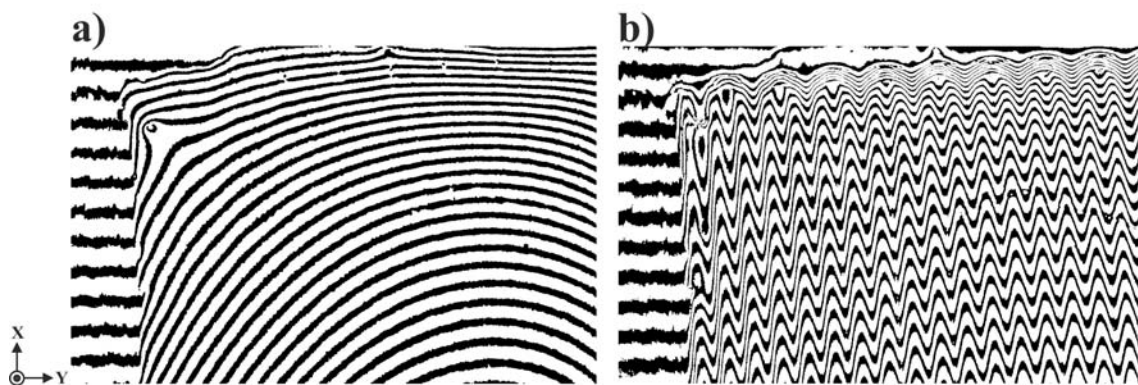
Figure 2.15: a) Processed Interferogram of liquid crystals film ($h = 10.08 \ \mu$m) on IDE
at voltage (V_{rms}, 1 kHz, sinewave), a) 0V, and, b) 22.5V.

2.4.6.3 *Fringe shift measurement*

The relative shift in the interferogram fringes (fig. 2.15a) can be translated to estimate the thickness of the liquid crystals film, by comparing different regions of the sample. For example, the air-glass interface shown in Fig. 2.16.
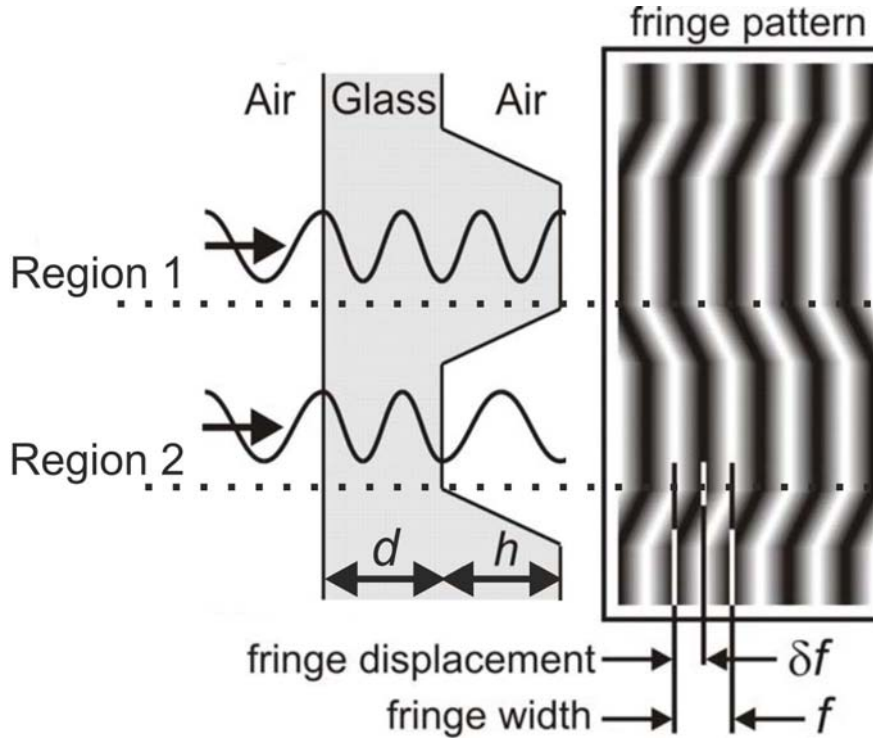
Figure 2.16: Schematic illustration of optical path change within the sample and associated interferogram for surface relief on a layer of glass.

Considering the above case, Optical Path (OP) can be written as,

$$OP = k.r = \frac{2\pi r}{\lambda_{Material}} = \frac{2\pi\, n_{Material}\, r}{\lambda_{air}}\ radians \tag{2.2}$$

where k is the wave vector $\frac{2\pi}{\lambda_{Material}}$, r is the distance traveled in the particular medium and $n_{material}$ is the refractive index of the material.

In Region 1, substituting values in Eqn. (2.2), we get,

$$OP_{Region\ 1} = \frac{2\pi n_{Glass}(d+h)}{\lambda_{Air}} \tag{2.3}$$

Whereas, in Region 2, Eqn. (2.2) becomes,

$$OP_{Region\ 2} = \frac{2\pi}{\lambda_{Air}}(n_{Glass}d + n_{Air}h) \qquad (2.4)$$

Using Eqn. 2.3 and Eqn. 2.4, we get

$$OP_{Region\ 1} - OP_{Region\ 2} = \frac{2\pi h}{\lambda_{Air}}(n_{Glass} - n_{Air}) \qquad (2.5)$$

hence, fringe displacement can be given as,

$$2\pi\frac{\delta f}{f} = OP_{Region\ 1} - OP_{Region\ 2} = \frac{2\pi h}{\lambda_{Air}}(n_{Glass} - n_{Air}) \qquad (2.6)$$

So, by calculating the fringe shift on the interferogram and taking into account the refractive indices of air and the glass we can calculate the thickness (h). Rearranging Eqn. (2.6)

We get,

$$h = \frac{\delta f}{f} \times \frac{\lambda_{Air}}{(n_{Glass} - n_{Air})} \qquad (2.7)$$

2.4.7 Measurement of Physical Parameters of liquid crystals

2.4.7.1 *Clearing Temperature (T_c)*

As discussed in chapter 1, liquid crystals phase exists between solid and isotropic liquids at a certain temperature range ($T_{Melting} < T_{LCphase} < T_c$). At clearing temperature (T_c), liquid crystals convert into isotropic liquids. Determination of T_c can help in estimating the purity of liquid crystals mixtures. In current work, the clearing temperature was determined by placing liquid crystals layer sandwiched between two slides in a temperature controller unit (Linkam LTS 350, UK) capable of precisely controlling temperature by 0.1 ℃. Temperature ($T_{Melting} < T_{Applied} < T_c$) is ramped slowly by 0.1 ℃/min, and photographs were taken using POM equipped with CMOS camera. Fig. 2.17(a-d) shows effect of temperature on 5CB layer.
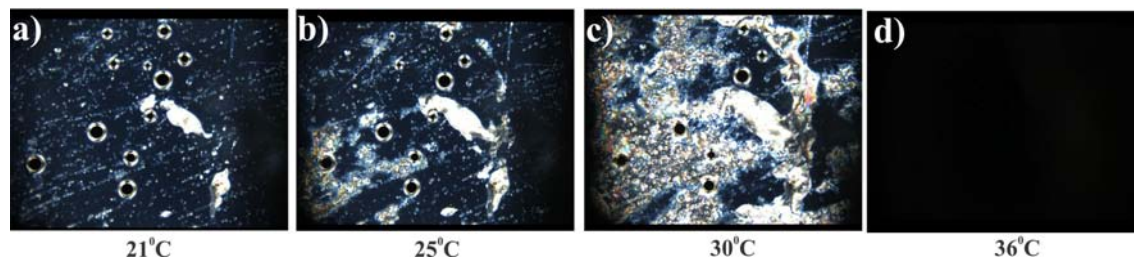
Figure 2.17: POM micrographs of 5CB liquid crystals at different temperatures, a) 21 °C, b) 25 °C, c) 30 °C and d) 36 °C (T_c).

2.4.7.2 *Dielectric anisotropy and Elastic Constants*

Dielectric anisotropy and elastic anisotropy of nematic liquid crystals are determined using the Fréedericksz curve (section 1.1.6). Briefly, liquid crystals are capillary filled in commercial guard ring cells (Merck Ltd, UK) having specific alignment conditions (homeotropic or planar). Then Fréedericksz was recorded by applying V_{rms} (1 kHz, sinewave) using four-terminal probes connected with LCR meter. Test cells were placed in a temperature controller setup during Fréedericksz curve measurement.

In this thesis, the Fréedericksz curve was measured for both positive and negative liquid crystals. For positive liquid crystal planar alignment test cells were used, and negative liquid crystals was filled in homeotropic test cells. Fréedericksz threshold (V_c) for both materials can be readily determined by looking at sharp threshold voltage value above which permittivity increases rapidly (fig. 2.18a). For determining the value of dielectric anisotropy permittivity $\varepsilon_\perp$ and $\varepsilon_\parallel$ was calculated from different regions of the Fréedericksz curve. In planar case $\varepsilon_\perp$ can be determined from the region below V_c (fig. 2.18b). A similar region for homeotropic geometry provides a value of $\varepsilon_\parallel$ in homeotropic alignment. The largest permittivities $\varepsilon_\parallel$ for positive liquid crystals and $\varepsilon_\perp$ for negative liquid crystals) in both alignment conditions can be determined from the region, where $V_{rms} >> V_C$ (fig. 2.18c).

Hence, Dielectric anisotropy ($\Delta\varepsilon$),

$$\Delta\varepsilon = \varepsilon_\parallel - \varepsilon_\perp \quad (+\Delta\varepsilon, \textit{ Positive liquid crystals}) \tag{2.8}$$

$$\Delta\varepsilon = \varepsilon_\perp - \varepsilon_\parallel \quad (-\Delta\varepsilon, \textit{ Negative liquid crystals}) \tag{2.9}$$

can be calculated using the values from the Fréedericksz curve. Elastic constants, k_{11} in planar cell and k_{33} in homeotropic system can be calculated from Equation 1.8 mentioned in chapter 1.
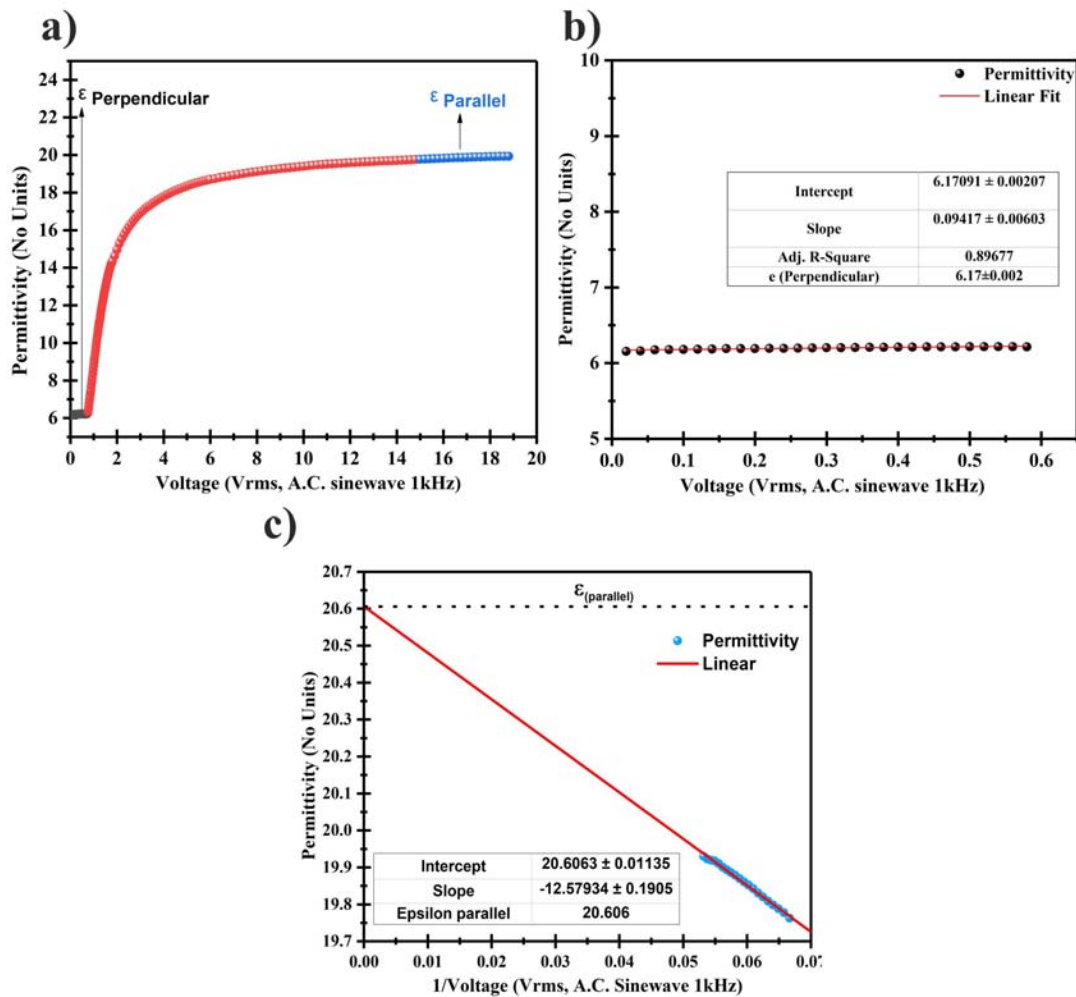
Figure 2.18: a) Fréedericksz curve of 5CB liquid crystals (Coloured region represent the data segment from were $\varepsilon_\perp$ (black region) and $\varepsilon_\parallel$ (blue region) can be deduced). b) Permittivity vs Voltage ($V_{rms} < V_c$) plot. c) Permittivity vs 1/Voltage ($V_{rms} >> V_c$) plot.

Chapter 3

Nematoelectrodynamics in pressure driven Poiseuille flow

The fluidity of liquid crystals combined with their anisotropic properties makes them exclusively distinct from isotropic fluids. When nematic liquid crystals are subjected to flow under application of an electric field they exhibit a gamut of captivating phenomenon, due to the complex interplay of elastic forces, surface anchoring forces, flow, and electric field. In this chapter, Nematoelectrodynamics i.e. the effect of the electric field on the dynamics of n-director is studied in the presence of pressure-driven flow in a thin nematic layer having significant elastic forces. Nematic liquid crystals with two different alignment conditions (planar for $+\Delta\varepsilon$, 5CB and homeotropic for $-\Delta\varepsilon$, LCT 07-1132) in a rectangular micro-confined channel having the flow direction along the length of the channel and electric field applied perpendicular to the direction of the nematic flow was studied. The chapter starts with a brief introduction to the previous work that forms a basis for conducted nematodynamic experiments, followed by experimental setup and results of Poiseuille flow effect on nematic n-director. The finding of this chapter reports how precise tuning of the Poiseuille flow combined with surface-electric field effects can be used

to stabilize and manipulate different unstable modes of the nematic director. In analogy to the $sin(n\pi z/d)$ director distortion modes in a zero flow classic Fréedericksz transition perturbation analysis, we label these modes $n = 0, 1$. The experimental results reported in the chapter were supported by continumm theory based 2D model (developed by Nigel Mottram) that explains the underlying physics of the process.

3.1 Introduction

Electrorheological (ER) fluids like liquid crystals in the cross-disciplinary area of microfluidics have attained considerable research interest in the last few decades. These materials are extensively used in technological applications like Liquid crystals displays [53], smart electro-optical zoom lens [54], and many other innovative products [55]. Due to homogeneity and inexistent complications of suspended particles like particle sedimentation, or agglomeration. liquid crystals are desirable candidates for ER based technology, contrary to other ER fluids [56]. However, the only downside with liquid crystals is their complex behaviour during flow which originates, from the interplay between surface-flow-field induced forces and can severely affect the alignment of n-director [13] and therefore disrupt the quality of the product. To this end, understanding of this complex interplay during pressure driven Poiseuille flow (pressure-induced flow in a long duct) of nematic liquid crystals in micro confinement is of some significance.

Much of the previous experimental work on Poiseuille flow of nematic liquid crystals in microchannels is carried out in absence of the electric field [46, 57–62] or else in a system consisting of thick nematic layer in presence of electric field [23] for which effect of elastic forces on the n-director profile can be neglected during flow. Figure 3.1 reports different experimental studies done on nematic Poiseuille flow. All these reports
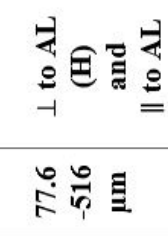
suggested that by judicious selection of alignment, flow conditions, channel aspect ratio, and Liquid crystal alignment, different n-director distortions profiles can be attained in the bulk of the system. Recent reports, from Samble's group [58, 59] shows that the application of Poiseuille flow slightly off-axis to normal on homogenously aligned n-director (θ =low pre-tilt, ϕ=45°) can rotate the azimuth director angle by ±35° causing ±10% variation in Leslie second viscosity (α_2). In another report by the same group (planar alignment, θ=2°, ϕ=87°, flow perpendicular to n-director) the authors revealed the existence of different azimuth distortion due the presence of a small pretilt in static n-director profile. Moreover, a series of early theoretical studies on Poiseuille flow by Ericksen [63], Leslie [9] and, Atkin [64] followed by recent work of Denniston [65], Nasibullayev [66], Carou [67], Jewell [46], Anderson [68], Batista [69], Mandal [70] and Copar [62] show that nematic director can attain distinct profiles in the presence of Poiseuille flow in microchannels depending upon initial parameters (alignment, channel aspect ratio, anchoring conditions, flow direction), flow rates and external fields (electric or magnetic). It's interesting to see that even a minute change in parameters can induce such a pronounced change in the n-director response. The availability of a multitude of parameters and research reported so far generates a need for experimental and theoretical studies in this vast research area of liquid crystals dynamics.
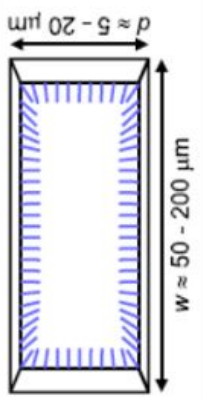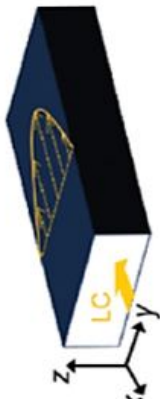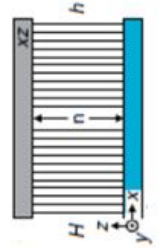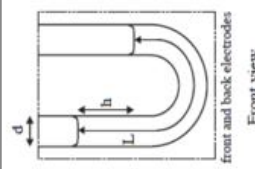
Recently, our group at Nottingham Trent University have reported experimental and theoretical study on effect of Poiseuille flow (applied parallel to alignment of n-director) on director dynamics in planar aligned nematic layer under the influence of electric field (applied perpendicular to flow) in a U-tube geometry using dual-frequency (+$\Delta\varepsilon$@ A.C. 1 kHz sinewave, −$\Delta\varepsilon$@ A.C. 50 kHz sinewave) nematic liquid crystals [23]. Results, from the research, revealed a) At high voltages in a −$\Delta\varepsilon$ liquid crystal, the n-director aligns perpendicular to the electric field; b) For low voltage values, flow dominates the

n-director orientation and director remains parallel to the alignment and flow direction; c) In the case of $+\Delta\varepsilon$, at high voltages director aligns perpendicular to the flow and static alignment director profile (i.e. follows the direction of the field); d) $+\Delta\varepsilon$, low voltage value flow effect dominates as electric field is not strong enough to compete with the flow. e) Moreover, a delay in the Fréedericksz threshold (V_c) was also observed for $+\Delta\varepsilon$ in the presence of flow. This study was further extended for determining the different viscosities parameters of nematic liquid crystals providing a more simplistic approach for determining viscosities coefficient η_1 and η_2 over traditional methods [13, 15]. Whilst the research revealed some interesting results, a number of effects were not investigated in the reported study a) Effect of elastic forces on director response was neglected in the study as the microchannel was thick (170 μm), b) Flow rates used were gravity-driven and experimental runs last for limited duration (approx. 300 secs) which may conceal some dynamic phenomenon occurring in the system. Moreover, an optofluidic study and a detailed study of different director distortion profiles attained during the flow of a nematic layer was missing from the previous report.

The focus of this chapter is to investigate the effect of pressure-driven Poiseuille flow and electric field, on n-director profiles, in a thin nematic layer having significant elastic forces. Two alignment conditions (planar and homeotropic) were studied in the rectangular cell geometry. In the case of a planar nematic layer ($+\Delta\varepsilon$, 5CB), the following important features of flow (parallel to n-director) and electric field (perpendicular to flow) effect on liquid crystals n-director was investigated in the experiments. a) The director-shear stress interaction that tends to orient the n-director towards a preferred 'flow alignment' (Leslie angle) relative to the flow velocity direction; b) a competing electric field effect (Fréedericksz transition) that re-orient the n-director along the electric field and compete with the flow effect; c) Electro-optic study of different director distortion pro-

files attained by liquid crystals under different flow rates was studied. In the case of a homeotropic nematic layer ($-\Delta\varepsilon$, LCT 07-1132), the effect of flow coupled with electric field induced director switching below critical threshold (V_c) of classic Fréedericksz transition was examined.

Nematic liquid crystals	Geometry	Alignment	d	Flow Direction	Electric field Direction	Reference
Para - azoxyani sole (PAA)		Homeotropic, and Planar parallel to page width	77.6 -516 μm	⊥ to AL (H) and ∥ to AL (P)	NP	[54]
5CB (+Δε)		Planar into the page	50 μm	⊥ to AL	NP	[55]
5CB (+Δε)		Homeotropic	30 μm	⊥ to AL	NP	[43]

Material	Setup	Anchoring	Dimension	Orientation 1	Orientation 2	Ref
5CB ($+\Delta\epsilon$)	Rectangular Flow cell (Similar to reference [7])	Planar (splayed) into the page and Planar into the page	70 μm	⊥ to AL	NP	[56]
5CB ($+\Delta\epsilon$)		Homeotropic	5-20 μm	⊥ to AL	NP	[57]
5CB ($+\Delta\epsilon$)		Homeotropic	50 μm	⊥ to AL	NP	[58]
5CB ($+\Delta\epsilon$)		Homeotropic	12 μm	⊥ to AL	NP	[59]
MLC 2048 (DFLC)		Planar parallel to page length	170 μm	∥ to AL	⊥ to AL	[22]

Alignment (AL); Parallel (∥); Perpendicular (⊥); Planar (P); Homeotropic (H); Dual Frequency liquid crystal (DFLC), Not Present (NP).

Figure 3.1: Different experimental studies performed on nematic Poiseuille flow in microchannels.

3.2 Experimental

3.2.1 Device details, construction, and materials

3.2.1.1 Fabrication of flow cell with lollipop electrodes
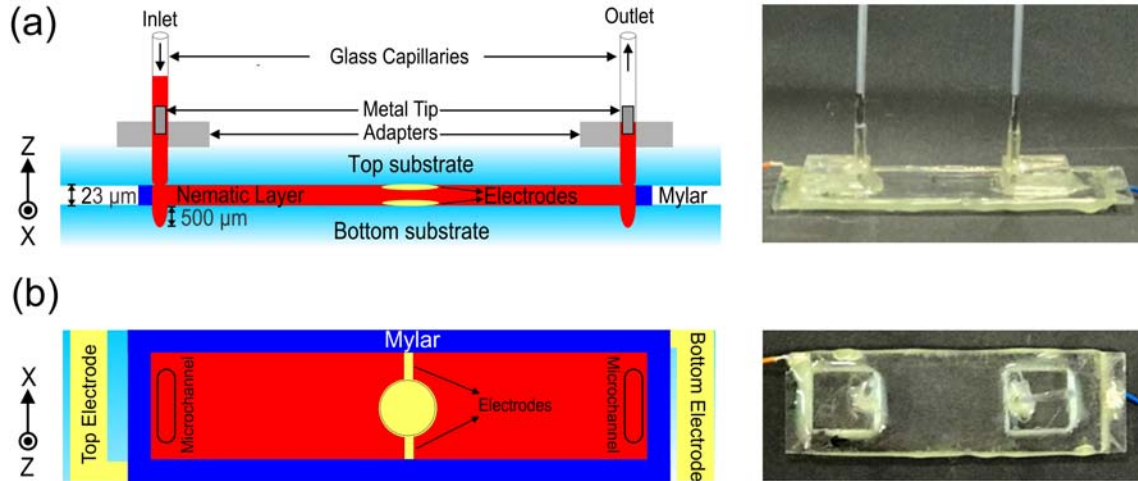
Figure 3.2: Schematic diagram of the lollipop electrodes cell (a) Side profile showing nematic liquid crystals flowing in the y-direction along the length of the rectangular channel, (b) Plane view showing lollipop electrodes between which the electric field is applied orthogonal to the nematic flow direction.

For performing dynamic pressure-driven Poiseuille flow experiments in a rectangular microchannel (40×20 mm, length×width), a cell (fig.3.2 a,b) of thickness $d \simeq 23\mu m$ was constructed using indium tin oxide coated borosilicate substrates (ITO of 25 nm thickness and 100 Ω/square resistivity). Both the substrates of the cell at $z = 0$ and $z = d$ consist of patterned electrodes (lollipop patterned electrode circular area diameter 10 mm and 12 mm for top and bottom electrode respectively) etched into ITO (process details mentioned in Chapter 2 section 2.1.2) layer with a thin solid film alignment layer ($d = 250$ nm) of MgF$_2$ deposited using thermal deposition technique (specific mentioned in Chapter 2 section 2.3) onto the top of each substrate which imparted low-pretilt planar nematic surface alignment with the easy alignment axis in the y-direction, parallel to the length of the

channel. In the case of homeotropic alignment both the substrates were coated with commercial Polyimide alignment layer (Merck KGaA, Darmstadt, Germany). For the introduction of nematic liquid crystal flow in the channel an inlet and outlet hole (diameter$\sim$ 2 mm) was drilled in the top substrate at $z = d$, away from the electrode area. At $z = 0$, lower substrate two microchannel's (d$\sim$ 500 µm) were engraved into the surface, parallel to the inlet and outlet holes of the top substrate. This was precautionary and was done to avoid flow profile convergence and divergence near the inlet and outlet of the cell. The thickness of the channel was maintained using a mylar sheet $(d = 23 \mu m)$ that border the entire channel area. Use of mylar sheet in the cell construction basically serves dual-purposes a) acts as an incompressible thickness layer, b) as a well for liquid crystal flowing in the channel. The entire cell assembly was initially glued using military-grade optical UV-adhesive glue (Norland 61) followed by further gluing using Araldite to prevent leaks. In order, to create connection points for flow microcontroller, an acrylic adapter with hole diameter having internal diameters (ID) of 0.69 mm equal to the diameter of a 19-gauge blunt metal needle was glued on the top substrate. Then a glass capillary tube (ID=1.26 mm) with a 19-gauge hollow metal tip glued to it was inserted into the inlet/outlet points of the cell. These capillary tubes were further sealed with Araldite to prevent any leaks at the junction. Once the device assembly is glued properly, connections were wired using indium soldering. The empty cell capacitance and thickness of cell is measured before performing flow experiments.

For performing dynamic experiments, flow aligning positive liquid crystal 5CB (single component, $+\Delta \varepsilon = 14.2$), and negative liquid crystal LCT-07-1132 (commercial mixture, $-\Delta \varepsilon = 3.44$) was used for planar and homeotropic case studies respectively. To ensure that chemical components of liquid crystals are well dissolved, and liquid crystals mixture are free from contaminants. Both liquid crystals were decanted in 5 mL vials and

heated above respective clearing temperature (T_c) and then cooled down to the nematic phase before being used in the experiments. Liquid crystal flow in the microchannels was introduced using flow microcontroller. The flow rates were varied in the range 10-1000 nL/sec corresponding to average flow velocity 21- 2100 µm/s. Poiseuille flow of a nematic fluid inside microchannel, was strictly laminar with estimated Reynolds number $R_e << 1$ (taking density $\rho \approx 1.024 \ kg/m^3$, and effective dynamic viscosity $\eta \approx 50$ mPas) [62].

3.2.1.2 Fabrication of flow cell with rectangular electrodes
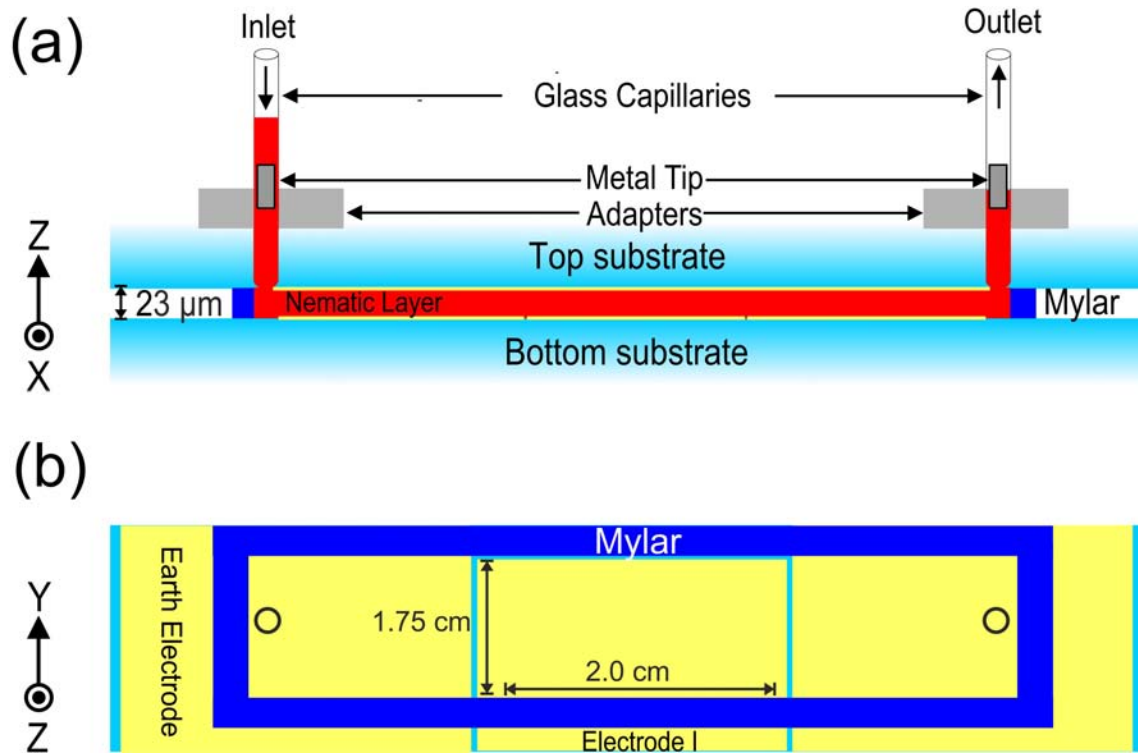
Figure 3.3: Schematic of rectangular electrodes cell (a) Side profile of the cell showing two electrodes on the bottom substrate and continuous ITO on the top substrate (b) Plane view showing rectangular bottom electrodes.

The fabrication process for rectangular electrodes (fig.3.3a) cell is almost identical to the lollipop electrode cell with key differences being a) Unlike lollipop electrodes which have two patterned active circular regions on top and bottom substrates, the rectangular

electrode cell has a continuous ITO plane on the top substrate, and bottom substrate has two electrodes first in the rectangular region (17.5×20 mm) shown in the figure 3.3b and second earth electrode around the channel separated by a gap of 0.1 mm. During experimental studies, both bottom electrodes are held at the same potential. b) Absence of engraved microchannels on the bottom substrate. This was done to investigate the fact that the texture forming in the cell during flow experiments is due to the surface-flow-field interactions occurring in the cell, not because of the ends of engraved microchannels present on the bottom substrates in case of lollipop electrode cell. Please note flow convergence and divergence is not observed in the cell as the distance between active area and the inlet/outlet points is quite large. Our experiments were performed using two different electrodes to ensure that the director dynamics is independent of electrode geometry.

3.2.1.3 Device setup and measurements

Experimental setup (fig.3.4) used for conducted studies consist of a Microfluidics flow controller (CETONI neMESYS low-pressure module 290N, Germany) capable of generating flow rate at a precision of 1 nL/sec, a Polarising Optical Microscope (Olympus BX 51) fitted with a rotating stage and dry objective lens (4x-50x), a homemade flow cell with desired alignment conditions, and a LCR meter (Agilent, 4284A Precision LCR Meter) fitted with four-probe terminal for capacitance measurement. Briefly, fabricated cell was placed on the microscope stage between desired polariser and analyser orientation. The inlet of the cell was connected to the 5 ml glass syringe (Hamilton) placed on the flow controller via polymer tubing and the outlet is connected to a 14 mL glass vial reservoir for the collection of liquid crystals flowing through the channel. The capacitance of the cell was recorded using LCR meter via bespoke LABVIEW program (developed by inputs of Dr. Andrew Edwards). The optical textures of the nematic layer were simultaneously
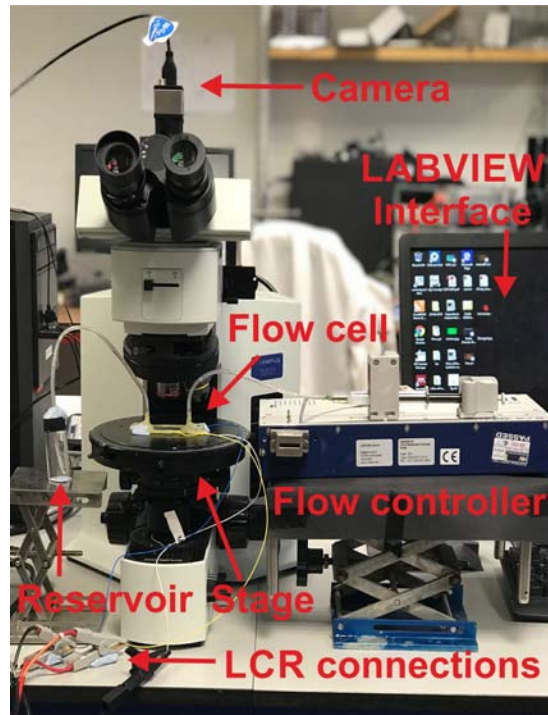
Figure 3.4: Experimental setup used for studying liquid crystals dynamics in a nematic layer subjected to an electric field and pressure driven Poiseuille flow.

recorded with the capacitance measurement using CMOS camera (EO-23121C, Edmund Optics Ltd, Yorkshire, UK) fitted on the Microscope. All experiments are performed at an ambient lab temperature (21±2.5°C) conditions in the cell consisting of lollipop electrodes using V_{rms}, 1 kHz, sinewave unless until specified.

3.3   Results and Discussions

3.3.1   Investigation of Optical textures of a planar nematic layer (5CB) subjected to an electric field in pressure driven Poiseuille flow

3.3.1.1   *Electric field switching of a low-pretilt planar nematic layer in the absence of pressure-driven Poiseuille flow*
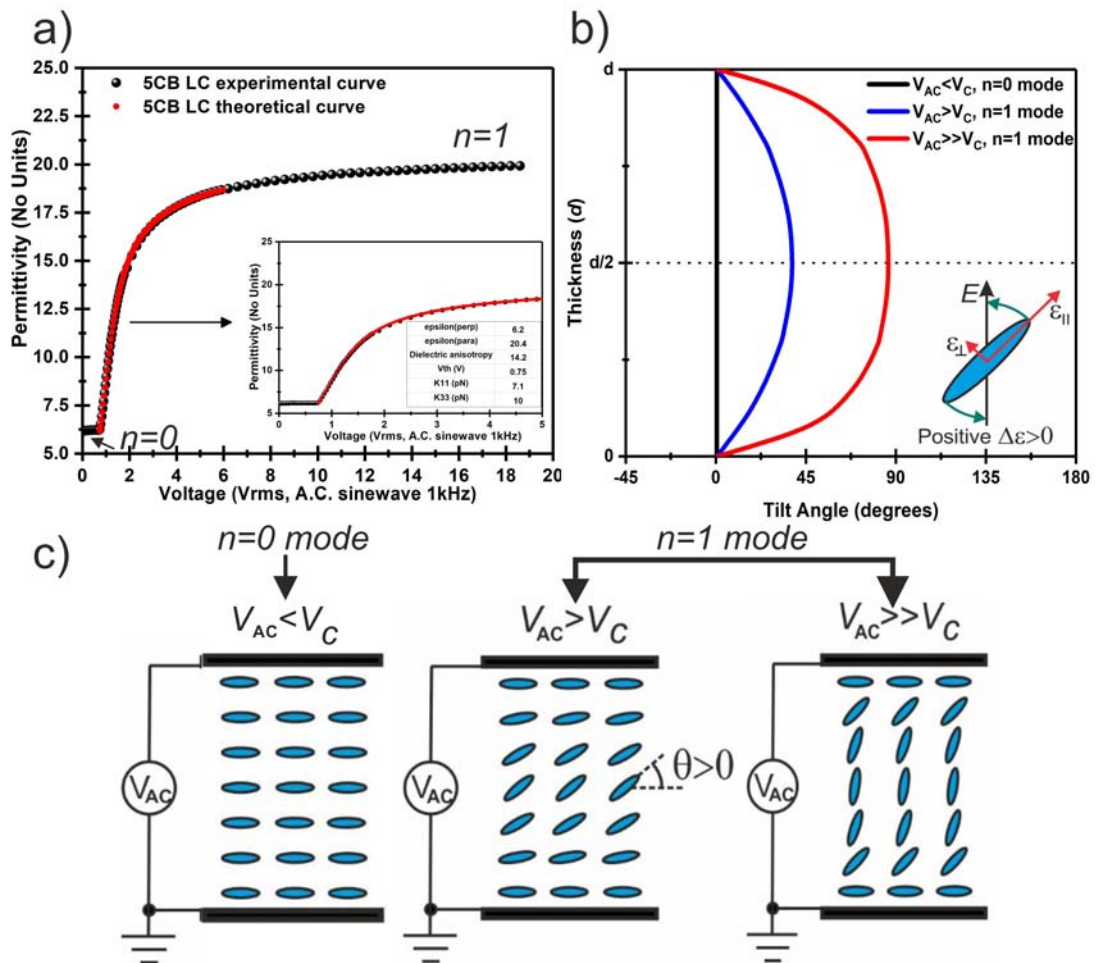
Figure 3.5: (a) Experimental and theoretical Fréedericksz curves for 5CB $(+\Delta\varepsilon)$ liquid crystal measured in planar Merck cell $(d = 22~\mu\text{m})$ with a guard ring. Inset shows a plot with a magnified view near the critical voltage (V_c) and values of physical parameters. (b-c) Shows director profiles in three different region of the classic Fréedericksz curve, representing $n = 0$ and $n = 1$ modes.

In order to establish a control study for the flow experiments and to determine the physical parameters of 5CB liquid crystal, a classic Fréedericksz curve [21] shown in fig.3.5a was measured in Merck commercial cell ($d = 22\ \mu$m) in absence of the flow conditions. For voltage below threshold voltage ($V_c = 0.75V$) director remain stable in its initial unperturbed planar state, $\theta(0) = \theta(d) = 0°$, which is determined by the surface anchoring conditions i.e. classic $n = 0$ mode. As there is no variation in the director profile (see solid black line curve in fig.3.5b), no change in the permittivity value of the cell is observed for $V_{AC} < V_c$. When a voltage $V_{AC} > V_c$ is applied to the system director distort from its unperturbed state, and tends to align along the direction of electric field i.e. towards $\theta = \pi/2$, leading to an increase in the permittivity of the cell with director acquiring classic $n = 1$ mode. This switching is resisted by an elastic forces as a result of which director orientation in the nematic layer varies smoothly in the cell with maximum switching occurring in the centre $\theta_{max} = \theta(d/2)$, and $\theta = 0°$ at the boundaries (see solid blue and red line curve in fig.3.5b). For voltages, $V_{AC} >> V_c$, permittivity increases further with director aligning more in the direction of the electric field i.e. $\theta = \pi/2$ in majority of the cell as shown in the case of solid red line curve in fig.3.5b, and nematic director stays in classsic $n = 1$ mode. The values of the physical parameters deduced from the Fréedericksz curve is given in Inset of figure 3.5a. Figure 3.5b,c shows director profile associated with classic $n = 0$ and $n = 1$ mode observed in different regions of the Fréedericksz curve. To ensure the reliability of physical values measured using home fabricated cell ($d = 22.15 \pm 0.07\ \mu$m, see appendix A, section A.1, fig.A.1), a comparison study of classic Fréedericksz curves measured using commercial cell and fabricated cell was performed (fig.3.6). Both the curves showed a similar trend in response to an increase in the applied voltage with a sharp threshold around $V_c = 0.75V$. However, a variation

in permittivity values ($\Delta\varepsilon = 14.2$ for Merck cell and $\Delta\varepsilon = 11$ for flow cell) is observed, this is mainly attributed to conductance in the electrodes of the flow cell. Also the fabricated flow cell doesn't have a guard ring in the system which might give some error in the measurement.
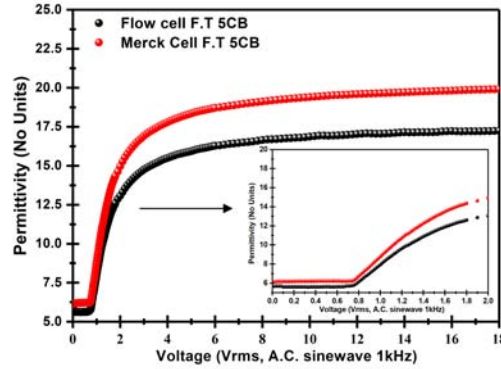
Figure 3.6: Experimental Fréedericksz curves for 5CB liquid crystal measured in Merck cell ($d = 22$ μm) with a guard ring and, fabricated cell ($d = 22.15 \pm 0.07$ μm) in the absence of the flow. Inset shows plots with a magnified view near the critical voltage (V_c) for both the curves.
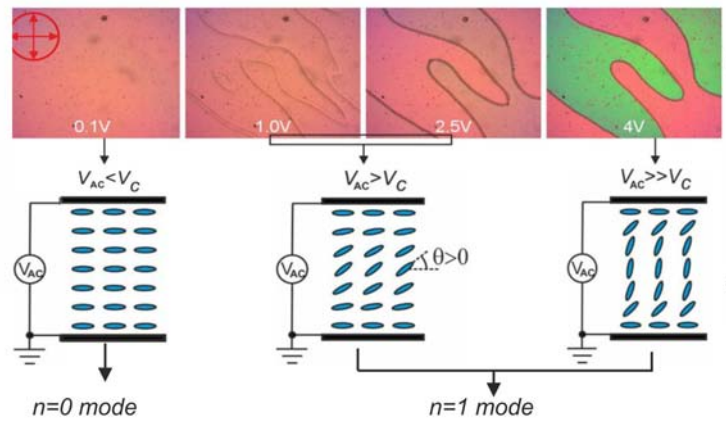
Figure 3.7: (a) Polarising micrographs (x10) of optical textures observed in the cell during measurement of Fréedericksz curves in absence of flow, the sample was placed at 45° to the position of cross-polarisers with a tilt of 5° in direction of the alignment layer. (b) Schematic of the associated director profiles observed at different voltage values.

Figure 3.7 shows micrographs of optical textures observed in the fabricated cell during director switching at different voltage values. For voltages below V_c director stays in unperturbed planar alignment conditions, $\theta(0) = \theta(d) = 0°$, so no change in the birefringence of the nematic layer is observed on the application of the voltage in the system. However, immediately post threshold voltage ($V_{AC} = 1$ V) formation of domain wall was observed in the cell with director switching in two optically distinct domains separated by these domain wall at $V_{AC} = 2.5$ V. A further increase in voltage levels ($V_{AC} = 4.0$ V) the two switched domain becomes more optically distinct. The observed switching degeneracy (fig.3.8a) in the cell is attributed to a negligible pre-tilt angle on MgF_2 solid thin film alignment layer (see chapter 2 section 2.3.1). Due to the absence of surface pre-tilt induced bias on the surface, the director can switch in either direction as shown in figure 3.8b as both switched states are energetically favourable and equivalent. Note here both switched states represents classic $n = 1$ mode.
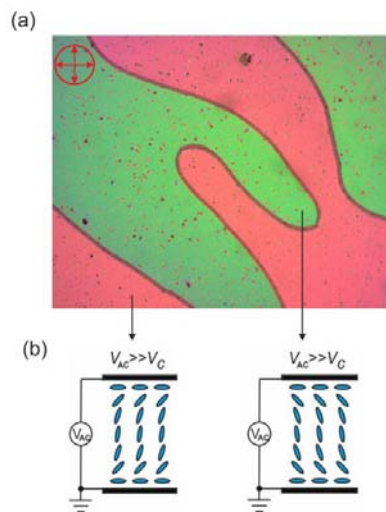
Figure 3.8: ((a) Polarising micrograph (x10) showing the formation of two tilt domains at $V_{rms} \gg V_c$ in cell with MgF_2 solid thin film as a planar alignment (b) Schematic of the director profile in observed domains the sample was placed at 45° to the position of cross-polarisers with a tilt of 5° in direction of the alignment layer.

3.3.1.2 *Defect textures of a low-pretilt nematic layer under pressure driven Poiseuille flow in absence of electric field.*
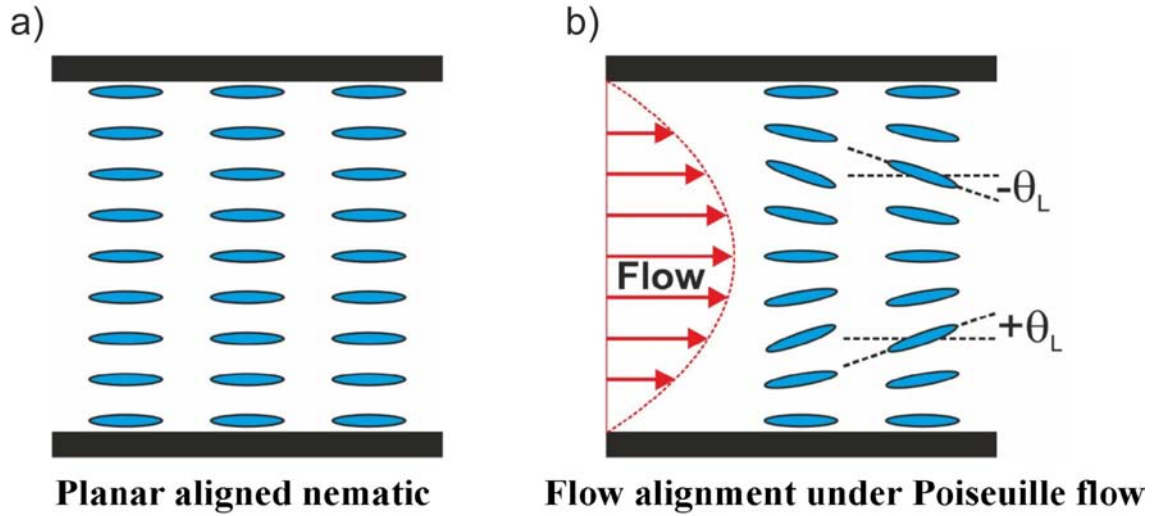
Figure 3.9: Schematic of the planar director profile, (a) in absence of flow, (b) in presence of the flow conditions.

Nematic director is extremely sensitive to imposed conditions, as shown above a small change in the voltage levels leads to a drastic transition in electro-optics of the director profile. In this section we will establish our second control study, exploring the sole effect of pressure driven Poiseuille flow (applied parallel to the direction of initial alignment) on the director profile in the absence of an electric field. To better grasp, the understanding of director response to Poiseuille flow consider a uniform planar nematic layer (fig. 3.9a) between two plates of the cell. In absence of flow in the system, director stays parallel to its surface with $\theta \approx 0°$ i.e. classic $n = 0$ mode (see solid black line curve in fig.3.5b). However, on the introduction of pressure driven Poiseuille flow through the inlet of the cell, the director distorts from its unperturbed state and align itself along the flow direction (fig.3.9b) towards a flow alignment angle called Leslie angle ($\pm\theta_L$). The opposite sign of Leslie angle in two halves of the cell during Poiseuille flow is due to the variation of velocity gradient as a function of cell thickness, which changes at the cell thickness $d/2$.

A key point to note here is even though the presence of Poiseuille flow in the system perturbs the director from its initial from causing it to align at $\pm\theta_L$ with the flow, the magnitude of θ_{avg} in the cell thickness is still zero. we label this (fig.3.9b) as flow aligned $n = 0$ mode, sometimes also referred as flow delayed/extended $n = 0$ mode in the text. An important point to note here is not all the liquid crystals materials are flow aligning in nature (please see chapter 1 section 1.2). Liquid crystals tendency to align with the flow is dependent on second (α_2) and third Leslie viscosity (α_3) For a material to be flow aligning $\alpha_2\alpha_3 > 0$ otherwise the nematic director will tumble in presence of the flow.
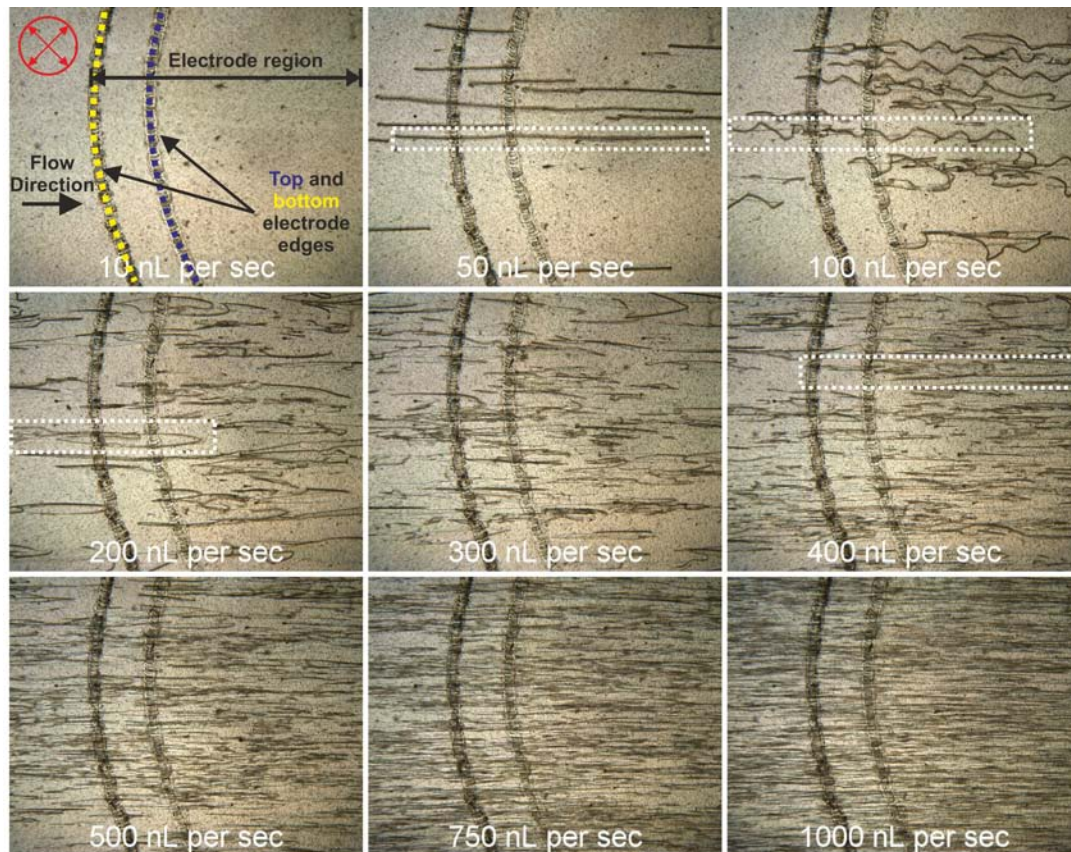
Figure 3.10: Polarising micrographs (x5) of defect structures formed in the cell at different flow rates (nL/sec) in the absence of electric field, different defect textures formed during the flow are highlighted by white dashed boxes, the sample was kept at 45° between cross polarisers.

In the presence of the Poiseuille flow director response evolves from the complex interplay between flow-induced viscous forces and restoring elastic forces. Thus, depending upon flow rates in the system director response can vary significantly and, in some cases, constraints due to the presence of flow conditions can lead to the formation of topological defects in the system. In our cell with planar alignment layer the director aligns well with the surface in the absence of flow, leading to a defect free nematic layer (ignoring the alignment loss due to dust in few instances). However, in the presence of the Poiseuille flow, it was observed that director response varies as a function of flow rates. Figure 3.10 shows polarising micrographs of the cell at different flow rates. In case of flow rate of 10 nL/sec the director response is dictated by the alignment conditions as no formation of defects textures was observed in the cell. For a flow rate of 50 nL/sec thin disclination lines typically with lengths over tens of millimetres were observed in the cell moving in a downstream direction along the flow while simultaneously reducing in length over time. It was found that if the flow rate is kept on for 2-3 hrs then these disclination line self-annihilate leaving behind a defect free system similar to the one shown in case of 10 nL/sec. On increasing the flow rate to 100 nL/sec the thin line disclination undergoes a structural transformation into the second type of defect having a serpentine shape with endpoints attached to a thin disclination line backbone. The observed defects are found to be permanent in nature as no annihilation is observed in the system over a time scale of 2 hours. Moreover, a closer examination by varying the depth of focus of the objective lens it was found that these defects are formed at different depths of the cell with backbone disclination placed closer to the mid-layer of the cell and serpentine shaped disclination existing at a different thickness of the cell. A further increase in the flow rate to 200 nL/sec showed that the these disclinations evolve into larger domains. For flow rate

between 300-400 nL/sec these domains seem to be interacting with each other in some case annihilating or merging to form larger domains. In case of a flow rate greater than 400 nL/sec defect textures enters into a chaotic region with copious defects flowing in the downstream direction at the same time vigorously interacting with each other through intertwining, annihilating, merging and crossing each other. The density of defects in a chaotic regime is found to increase as a function of flow rate [38]. This can be clearly seen in figure.3.10, in case of flow rates ranging from 400-1000 nL/sec. Mainly four different types of defects were observed in the cell highlighted by white boxes in the figure 3.10.

3.3.1.3 *Effect of electric field on defect textures in a low-pretilt nematic layer under pressure-driven Poiseuille flow.*

In the section above we have shown how competing flow-induced forces and elastic forces lead to the formation of different optical textures in the presence of flow. Here we will introduce an additional third parameter i.e. electric field which is applied vertically to the horizontal flow direction. Basically, in this condition, director field emerges from the competition between surface-flow-field induced forces. Figure 3.11 shows different optical textures observed in the cell at varying flow rates and voltage conditions. In the absence of the flow rate (fig. 3.11 a), a similar response to voltage is observed as explained in section3.3.1. Below V_c director stays in unperturbed state, at V_{AC} slightly above V_c domains starts growing in the system which became more distinct at a higher voltage $(V_{AC} >> V_c)$. When a flow rate of 10 nL/sec (fig. 3.11 b) is applied no defect textures were observed to be forming in the cell, unlike 0 nL/sec where domains growth on voltage ramp is observed due to switching degeneracy in the system. An increase in the flow rate to 50 nL/sec introduces disclination lines (fig.3.11 c1,2) at low voltages $(V_{AC}<V_c)$ similar to one formed in absence of voltage signifying the existence of flow dominant region. Above V_c

67

electric field starts annealing the disclination line (fig. 3.11 c3,4) and cell switches into a single domain. A further increase in the flow rate to 100 nL/sec serpentine disclination appears (fig.3.11 d1,2) in the cell maintaining their stability in the system even post V_c for few voltage levels (fig.3.11 d2). However, on voltage increase to $V_{AC} = 2.5$ V and above, these serpentine disclination annihilate and majority region of the cell switches into a single domain with a different domain appears to be growing in the cell (fig.3.11 d3,4) nucleating from the electrode's edges. This edge effect observed at high voltage value is attributed to director re-orientation between switched and unswitched regions. As the two-regions have different viscosities, the flow profile near the starting edge of the electrode converges causing re-orientation of director near electrode edge. Thus, leading to formation of other domain near the edges. For flow rates of 250-400 nL/sec, defects carrying larger domains region (fig.3.11 e1,2) were observed which upon an increase in the voltage ($V_{AC}>V_c$) anneals out in the system. The defect annealing voltage in the system was found to be a dependent on the flow rate as it increases with increase in the flow rate up to 400 nL/sec. Fig.3.11f shows that the defect density decreases in the cell as the voltage is increased from 0.1 V to 4 V. Above 400 nL/sec, defects persists in the system and the director pattern shows a chaotic regime (fig.3.11 g1-4) with different defect textures interacting with each other. These defect textures don't anneal in the system under application of voltage, for levels up to 4.0 V. A zoomed-in view of different defect textures formed at different flow and voltage conditions is shown in figure 3.11 (h-k).
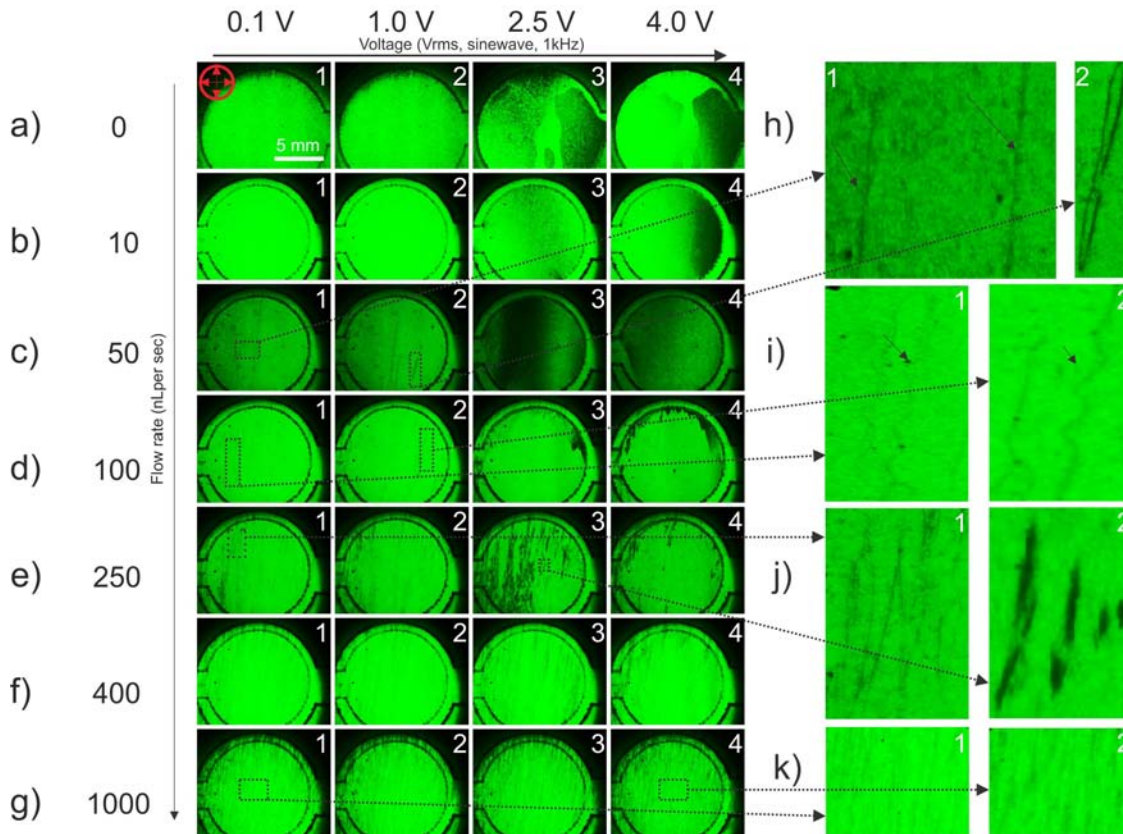
Figure 3.11: (a-g) Polarising micrographs (x4) showing the evolution of defect structures as a function of flow rates and applied electric field. (h-k) Micrograph (10x) showing structural transformation of defects under imposed flow and electric field conditions, (h1) disclination line transforming into (h2) larger domain on voltage increment, (i1) a thin serpentine disclination connected with its endpoints connected with a disclination line transforming into, (i2) its thicker form on voltage increment, (j1) Disclination carrying domains (j2) annihilating at high voltage values, (k1,2) disclinations flowing in chaotic manner at low and high voltages. During the observation, the sample was kept at 45 degrees between cross-polarisers with a green filter ($\lambda = 534$ nm) inserted in the field of view.(Note: All images are visually enhanced for better representation)

3.3.1.4 *Effect of sudden removal and re-application of flow on defect textures in the presence of the electric field.*
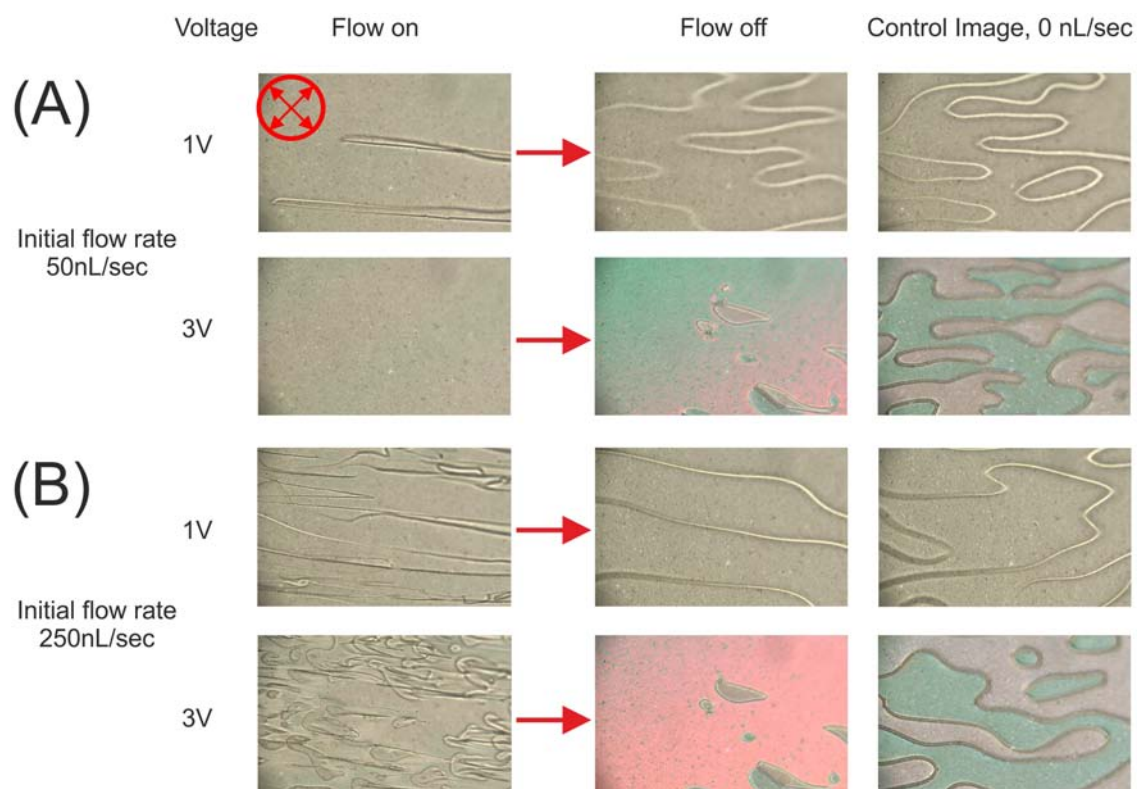
Figure 3.12: Polarising micrographs (x10) showing transformation of defect textures on sudden removal and re-application of flow rates under two different applied voltages (1 V, 3 V) For a) Initial flow rate of 50 nL/sec, b) Initial flow rate of 250 nL/sec, control image (0 nL/sec) shows defect textures in absence of the flow with voltage applied in the cell, sample was kept at 45 degrees between cross-polarisers.

It's evident from the results shown so far that the dynamics associated with nematic director are strongly affected by flow-field interactions. Till now we have focused on optical textures of the director when an electric field is suddenly introduced in the flowing nematic layer. Here we will focus on the opposite situation, where a sudden removal and re-application of flow rate occurs in a nematic layer under voltage. Figure 3.12 shows

optical textures observed in an electrically actuated nematic layer when sudden removal and re-application of flow rate occurs in the system. Micrograph of control (0 nL/sec, no flow switch) was also shown for comparison of the results. Two initial flow rates, 50 nL/sec and 250 nL/sec and voltages $V_{AC} = 1$ V and $V_{AC} = 3$ V were selected for the study. In case I, 50nL/sec, under $V_{AC} = 1$ V disclination lines appear under flow, corroborating the previous experimental observation (section 3.1.3, fig. 3.11c 2) however on sudden removal of the flow domain walls starts forming in the system similar to control image (please also see section 3.1.1, fig. 3.8). In same case nematic layer under high voltage of $V_{AC} = 3$ V forms few optically distinct domains on removal of flow rate in the system. In case II, 250 nL/sec, similar results were found with optical textures showing similarity to control images. All these results reveal that sudden removal of flow conditions forces the director to revert to its classic switched state that consists of two switched domains with opposite tilt orientation co-existing in the system. This is because we need flow to bias switching of the director in one direction, as soon as the flow is removed from the system the degeneracy instantaneously returns as surface forces become more dominant. The time scale of this resetting process is found to vary as a function of flow rate. For a flow rate of 250 nL/sec the resetting time is of order of 10 secs whereas for 50 nL/sec change in the director dynamics is almost instantaneous with system resetting back in less than 1 sec. Furthermore, it was also found that by sudden removal and re-application of flow in the cell one can cycle in between observed optical textures.

3.3.2 Nematic director distortion modes
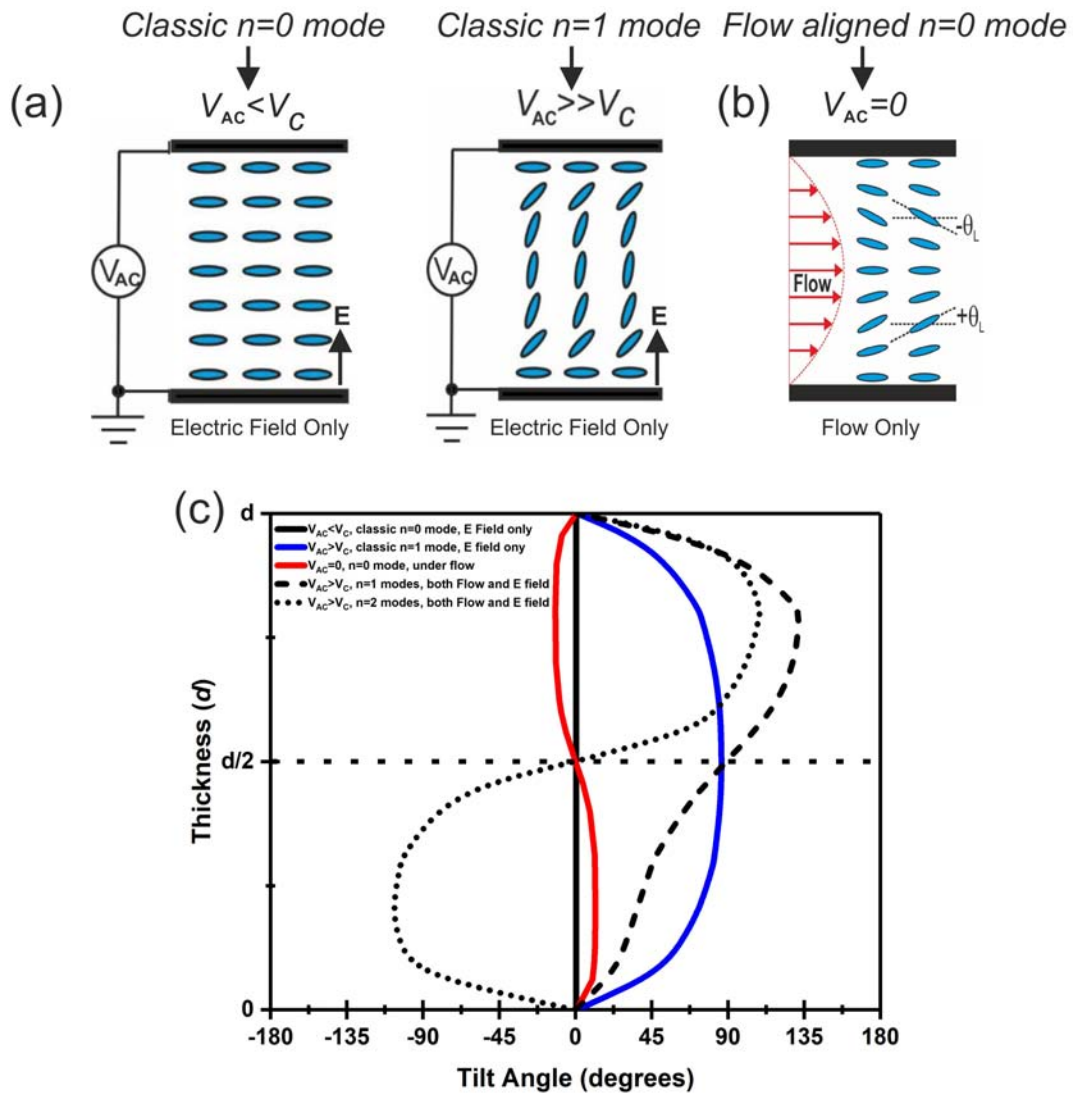
Figure 3.13: (a, b) Schematic of director profiles associated with $n = 0, 1$ distortion mode in a planar aligned $+\Delta\varepsilon$ nematic layer under the influence of different external forces. (c) Director profile plots showing tilt angle (θ) variation as a function of cell thickness (d), solid black and blue line plot represents classic $n = 0$ and $n = 1$ distortion mode observed in presence of external electric field only, the solid red line represents flow aligned $n = 0$ mode, dashed and dot line plots represents higher energy flow distorted $n = 1$ and $n = 2$ mode respectively, these modes are observed under the combine influence of Poiseuille flow and external electric field.

It's clear from the above studies (see section 3.3.1) that the nematic director can acquire different director distortion profiles depending upon initial alignment conditions, magnitude, and direction of the applied external forces (flow or electric field). These distortion profiles can be described in terms of distortion modes (n) associated with the Fréederickz transition bifurcation diagram. In analogy to the $sin(n\pi z)/d$ director distortion modes in a zero-flow classic Fréederickz transition perturbation analysis, we label these modes as $n = 0, 1, 2$. Figure.3.13 (a,b) shows $n = 0$ and $n = 1$ distortion modes, observed in a planar aligned $+\Delta\varepsilon$, nematic layer under the sole influence of electric or flow forces. In presence of electric field only ($V_{AC} < V_c$), the director profile stays at initial alignment conditions ($\theta \approx 0°$, planar alignment) which is defined by surface anchoring forces. We refer to this mode as classic $n = 0$ mode in the text. However, as the voltage is increased $V_{AC} > V_c$, θ tends to align towards $\pi/2$ in the direction of the electric field and acquire classic $n = 1$ mode. In presence of flow only ($V_{AC} = 0$), as discussed in section 3.3.1.2, director aligns itself along the flow direction towards a flow alignment angle ($\pm\theta_l$). We refer to this mode as flow aligned $n = 0$ mode in the text. The solid line plots in figure.3.13 c show tilt angle (θ) variation in director profiles along the thickness (d) of the cell for classic $n = 0$ mode (black solid line), flow aligned $n = 0$ (red solid line), and classic $n = 1$ (blue solid line) mode. All these modes represent different base states that can be acquired by the director under influence of flow or electric field forces. However, under a combination of flow and electric field ($V_{AC} > V_c$) conditions, it is possible to stabilise other higher energy mode which are otherwise unseen in the system. We refer to this mode as flow distorted $n = 1$ mode in the text. The dashed line plot in the figure 3.13 c shows director profile associated with the flow distorted $n = 1$. There is also a possibility of existence of other higher modes like $n = 2$, shown by dotted plot in (figure.3.13 c), however, in our

modelling result it was found that $n = 2$ mode can only exist at particular flow rate (100 nL/sec) with random noise included in the model otherwise the system stabilise itself into flow distorted $n = 1$ mode. The formation and evolution of these states into each other are discussed later in the remainder of the chapter.

It's worth pointing out that the director profiles shown above in figure 3.13, for $n = 0$, $n = 1$, and $n = 2$ mode is for planar aligned $+\Delta\varepsilon$, nematic material. If you have a negative material $(-\Delta\varepsilon)$ with homeotropic alignment $(\theta \approx 90°)$ than in this case director distortion profile associated with $n = 0$, $n = 1$ will be very different from the above case because i) initial alignment $(\theta \approx 90°)$ now is perpendicular to the flow , and ii) nematic director will switch perpendicular to the electric field as $\varepsilon_\perp > \varepsilon_\parallel$. Figure.3.14 shows different $n = 0$ and $n = 1$ distortion modes, observed in a homeotropic aligned $-\Delta\varepsilon$, nematic layer under the sole influence of electric or flow forces.
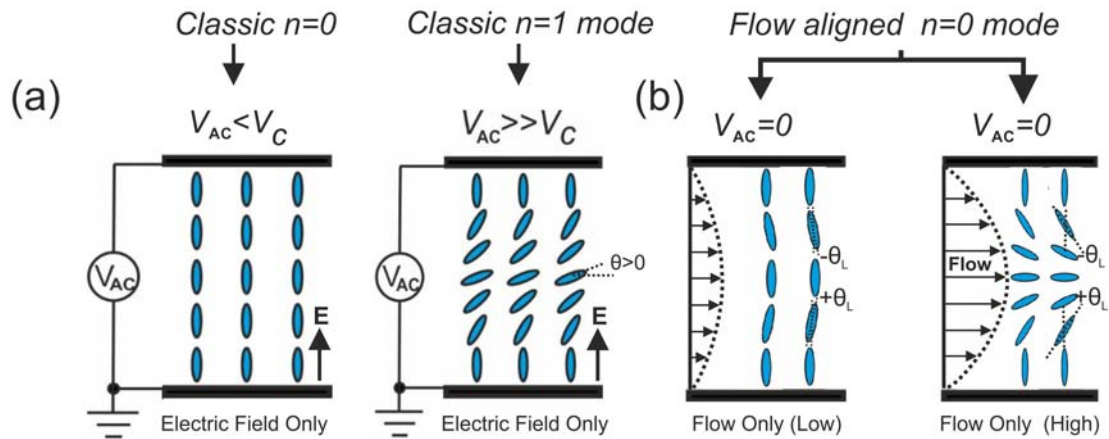
Figure 3.14: Schematic of director profiles associated with $n = 0, 1$ distortion modes in a homeotropic aligned, $-\Delta\varepsilon$ nematic layer in presence of a) external electric field, b) Poiseuille flow in the cell.

3.3.3 Investigation of the permittivity of a planar nematic layer (5CB) subjected to electric field and pressure driven Poiseuille flow
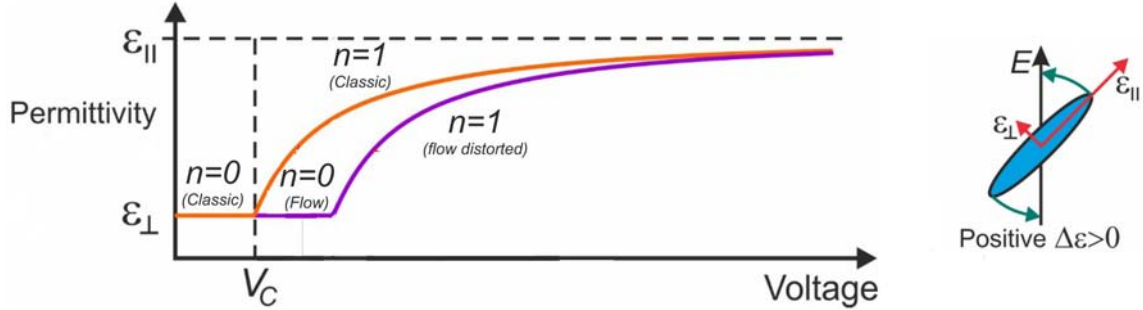
Figure 3.15: Schematic of Fréedericksz curves in presence of electric field only, and in the presence both electric field and the flow conditions.

In section 3.3.1 we investigated the optical response of planar nematic layer under varying flow-electric field conditions. In the current section, we will deduce this response in terms of permittivity of the planar nematic layer under varying flow rates. Figure 3.15 shows classic Fréedericksz transition curve (solid orange line) in the absence of flow in the cell. When there is no flow in the cell, the classic $n = 0$ mode is stable up to V_c, at which point classic $n = 1$ mode becomes stable and permittivity of nematic layer changes from $\varepsilon_\perp$ when $V_{AC} = V_c$, and approaches $\varepsilon_\parallel$ as V_{AC} becomes large. This coincides with increasing tilt angle from $0°$ towards $\pi/2$. An introduction of flow, in this case, will damp the effect of voltage causing deviation in the behaviour of tilt angle (θ), with permittivity response different (solid violet line) from the classic curve (solid orange line). Basically, in this case, the director aligns with the flow at Leslie angle ($\pm\theta_L$) and acquire flow aligned $n = 0$ mode leading to an extension of critical voltage (V_c) mode to a new critical voltage value referred to as $V_{c(delayed)}$ in the text. This extension of flow aligned $n = 0$ mode to $V_{c(delayed)}$ is dependent upon the flow rate applied to the system. For low flow rates, flow

aligned $n = 0$ branch extends slightly over V_c, and with an increase in the voltage post $V_{c(delayed)}$, the equilibria retain their characteristic symmetry, classic $n = 1$ mode with respect to the centre of the cell. In other words, a transition from flow dominant region to voltage dominant region will occur in the cell. In case of high flow rate, flow aligned $n = 0$ mode extends voltage value up to $V_{c(delayed)} = 3V_c$ and cell switches into a new type of mode called flow distorted $n = 1$. This high energy mode is otherwise unstable in absence of the flow and electric field. Experimental data, showing the effect of different flow rates on Fréedericksz curves is shown in figure 3.16a. At low flow rates (10- 25 nL/sec), director response is mainly voltage dominated with flow aligned $n = 0$ mode extending slightly above V_c and system reverts to the classic $n = 1$ mode as the voltage is increased in the cell. In case of Medium flow rate (50-100 nL/sec), flow aligned $n = 0$ region extends nearly 1.2-1.6 times V_c before transition into flow distorted $n = 1$ mode. However, as voltage increase to higher voltages values, of 4 V or higher, the FT curves start shifting towards the classic $n = 1$ mode. Thus, signifying the co-existence of flow distorted $n = 1$ and classic $n = 1$ mode on the same Fréedericksz curve. On comparing these results with optical textures studies annihilation of defects at higher voltages ($V_{AC} \geq 2.5V$) can be related to the transition of the system from flow distorted $n = 1$ mode to defect-free voltage stabilised classic $n = 1$ mode. Note here due to flow induced bias switching degeneracy in absent from the system as discussed before in section3.3.1.4. For, high flow rates (200-1000 nL/sec) conditions, flow aligned $n = 0$ extends up to $3V_c$ and post $V_{c(delayed)}$, flow distorted $n = 1$ mode take over. An increase in $V_{c(delayed)}$ with increases in the flow rate is shown in figure 3.16b. Results show that increases in the $V_{c(delayed)}$ value starts saturating at high flow rates with the transition region smoothed out (due to averaging in measurement performed) with an increase in the flow rate.
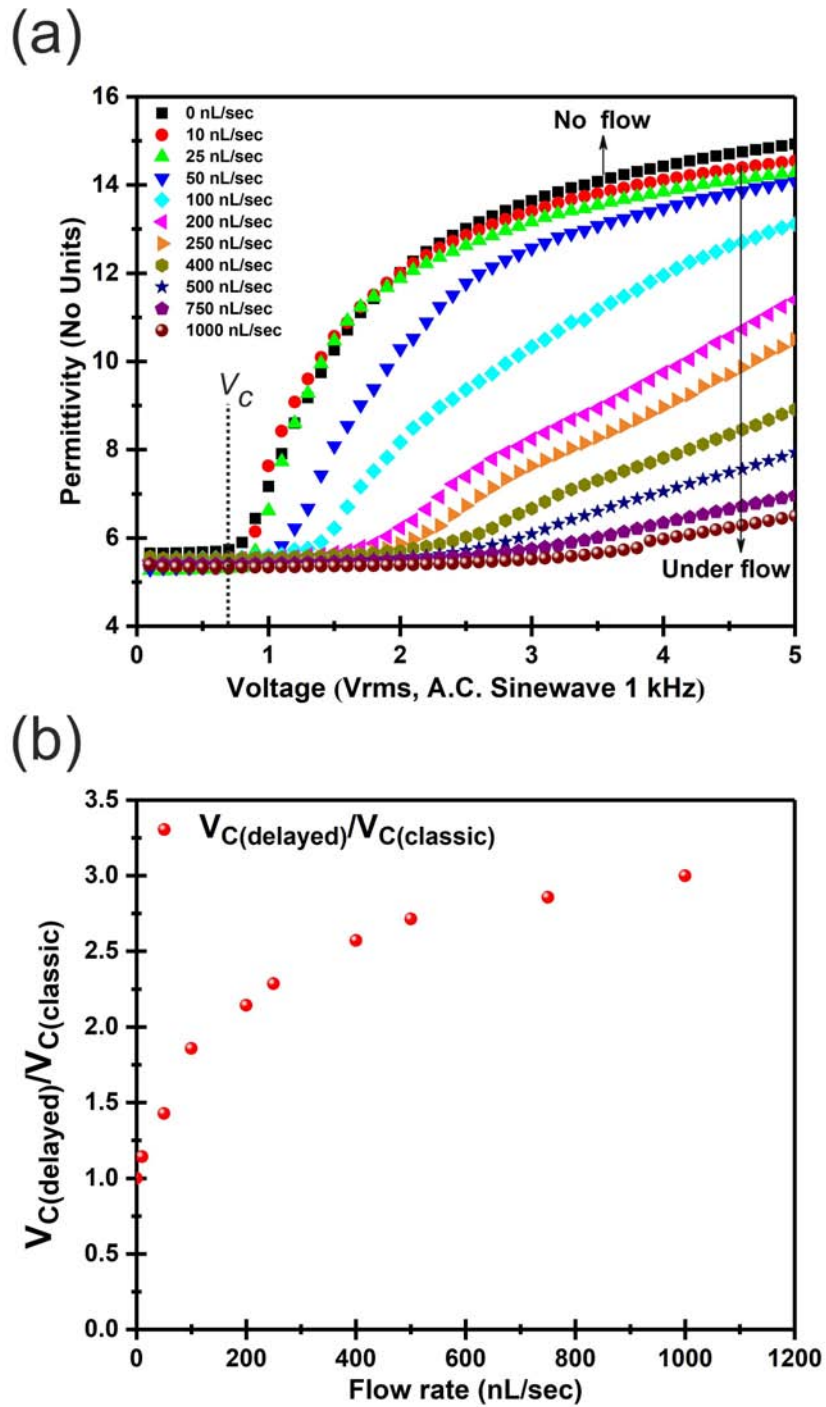
Figure 3.16: a) Experimental Fréedericksz curves measured at different flow rates in the cell ($d = 22.15 \pm 0.07$ μm), Permittivity of the Fréedericksz curve at each voltage value is averaged over 32 readings measured over a duration of 128 seconds. b) Plot showing change in the critical voltage value as a function of the flow rate.

Application of a sudden voltage to static nematic layer induces an electric torque on the n-director making it switch towards an equilibrium state regulated by the applied voltage. The measure of time taken to switch on (τ_{on}) towards a voltage regulated equilibrium is given as:

$$\tau_{on} = \frac{\gamma_1 d^2}{\varepsilon_o \varepsilon_a (V^2 - V_c^2)} \qquad (3.1)$$

Where τ_{on} time is re-orientation time of n-director that varies in the system. Due to this for a slowly increasing and then decreasing voltages a hysteresis behaviour is exhibited in the static Fréedericksz curve particularly at the voltages near-critical threshold hold as τ_{on} based on Equation 3.1 at $V_{AC} = V_c$ becomes infinity causing a hysteretic behaviour in the curve. In the experimental results shown below (fig. 3.17) effect of flow-induced torque on the hysteresis behaviour of Fréedericksz curve is studied. Please note since a 1 kHz, A.C., sinewave is used in our experiments, so hysteresis effect is not caused by residual D.C effects (ions migration) in the system [71].

In presence of low flow rates for which flow aligned $n = 0$ mode transition to classic $n = 1$ mode with a slight delay in V_c hysteresis region is observed in the cell near the threshold values with no change in the hysteresis region compared to static Fréedericksz curve signifying negligible effect of flow on director response. As the flow rate is increased in the system to medium flow rates at which classic $n = 1$ and flow distorted $n = 1$ mode co-exist in the system; hysteresis region is observed near the transition region post V_c delayed for some flow rates which gradually contracts as the flow rate is increased to 100 nL/sec. For high flow rates, no hysteresis is observed in the curve having flow distorted $n = 0$ and $n = 1$ mode. A plausible explanation of the absence of hysteresis from the curve with flow stabilised modes can be attributed to the fact that presence of flow confinement in the cell

decreases the switching region in the cell where hysteresis can be observed and the effect which may exist in the cell average out in measured permittivity value of the Fréederickz curve. Another possibility that can obscure the effect from permittivity curve is increased defect density at a flow rate above 100 nL/sec which decreases permittivity of the cell. A major challenge with the current system is the physical parameter used for studying the flow effect is averaged over time. To get better insights into the system and to elucidate the observations made from the results a detailed study on the electro-optofluidic response needs to be done.
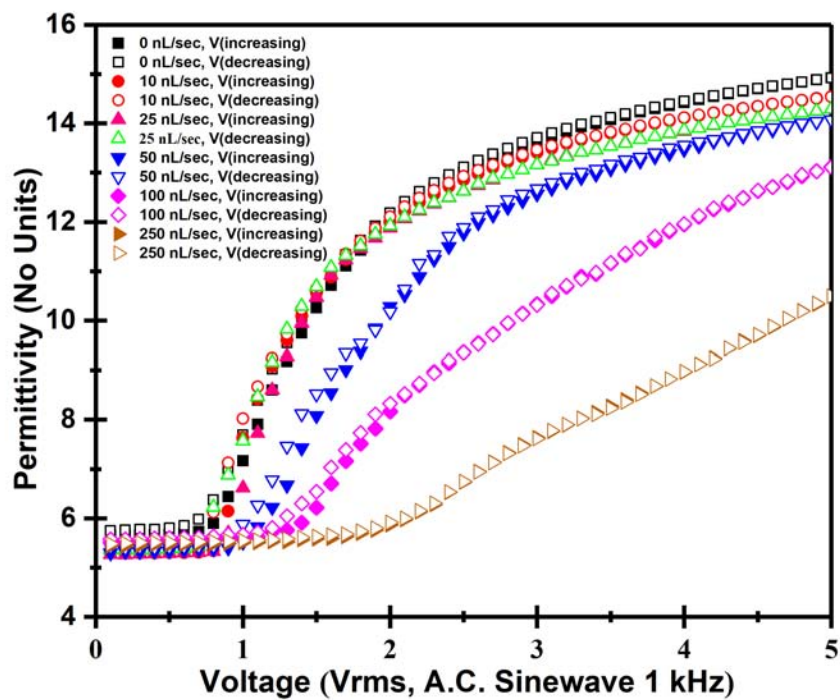
Figure 3.17: Experimental Fréederickz curves measured at different flow rates with first increasing (solid symbols) and then decreasing (open symbols) voltages, measurements at each voltage is averaged over 32 readings taken over a time duration of 128 seconds.

3.3.3.1 *Effect of sudden removal and re-application of flow on the permittivity of a*

nematic layer in the presence of electric field

Sudden removal of flow in the cell is found to have a strong effect on director response

triggering a re-settling process in the cell to a state that is either regulated by the voltage

or surface alignment. Basically, a settlement in director behaviour back to the static case

is observed as shown previously in optical texture study (see section 3.3.1.4). Here we

will study the effect of sudden removal and re-application of flow on permittivity of the

nematic layer. Briefly, at first, a voltage (V1) falling in the region of either of the selected

flow stabilised mode $(n = 0, n = 1)$ is applied to the flowing nematic layer this voltage was

then swapped by an increased voltage (V2) value from the same flow stabilised region.

This was done to ensure that we are tracing the same flow delayed Fréedericksz curve

corresponding to the selected flow rate. Afterward, the flow rate was removed from the

cell and keeping the voltage (V2) on, permittivity of the system is recorded in real-time

until it acquires a stable value. The new applied voltage was then swapped with initial

voltage (V1) and the flow rate is re-introduced in the system with permittivity measured

simultaneously until a stable value is attained. Figure 3.18 a,b shows movement between

flow stabilised $n = 0$ mode to classic $n = 1$ and flow distorted $n = 1$ mode to classic $n = 1$

mode at two different flow rates in the cell. The solid black line represents the static

curve and the red line represents flow delayed Fréedericksz transition. Results from the

studies show that it's possible to cycle in between different director modes by varying the

flow conditions in the cell. Further to this, it was also found that it's possible to move in

between different flow stabilised and voltage stabilised mode in one single cycle. Figure

3.19 a,b shows movement a) from flow stabilised $n = 0$ to distorted $n = 1$ mode on voltage

increase, b) then from flow distorted $n = 1$ to voltage stabilised classic $n = 1$ on sudden

removal of flow and, c) from classic $n = 1$ to flow aligned $n = 0$ mode as flow rate is

re-introduced in the cell.
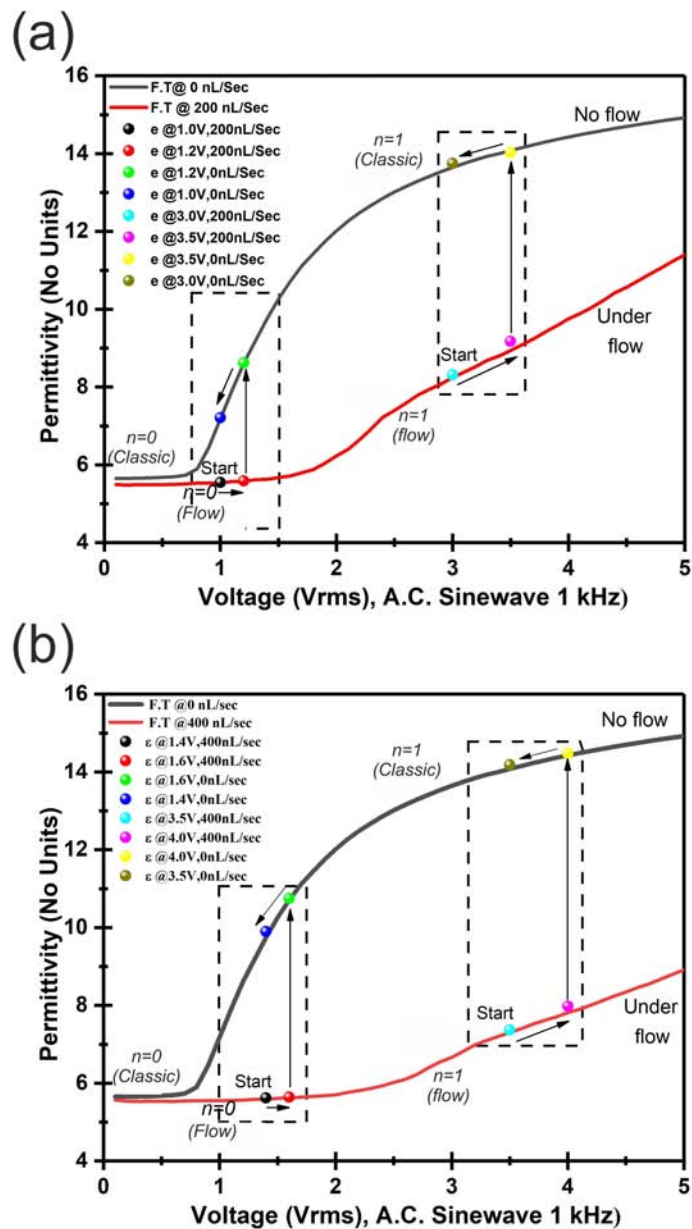
Figure 3.18: Plots showing movement between two different branches of director profile (extended/flow aligned $n = 0$ to classic $n = 1$ and, flow distorted $n = 1$ to classic $n = 1$) on sudden removal and re-application of the flow rates, a) Initial flow rate 200 nL/sec and, b) 400nL/sec, solid black line represent the classic Fréedericksz curves and red line represent the flow delayed Fréedericksz curves.
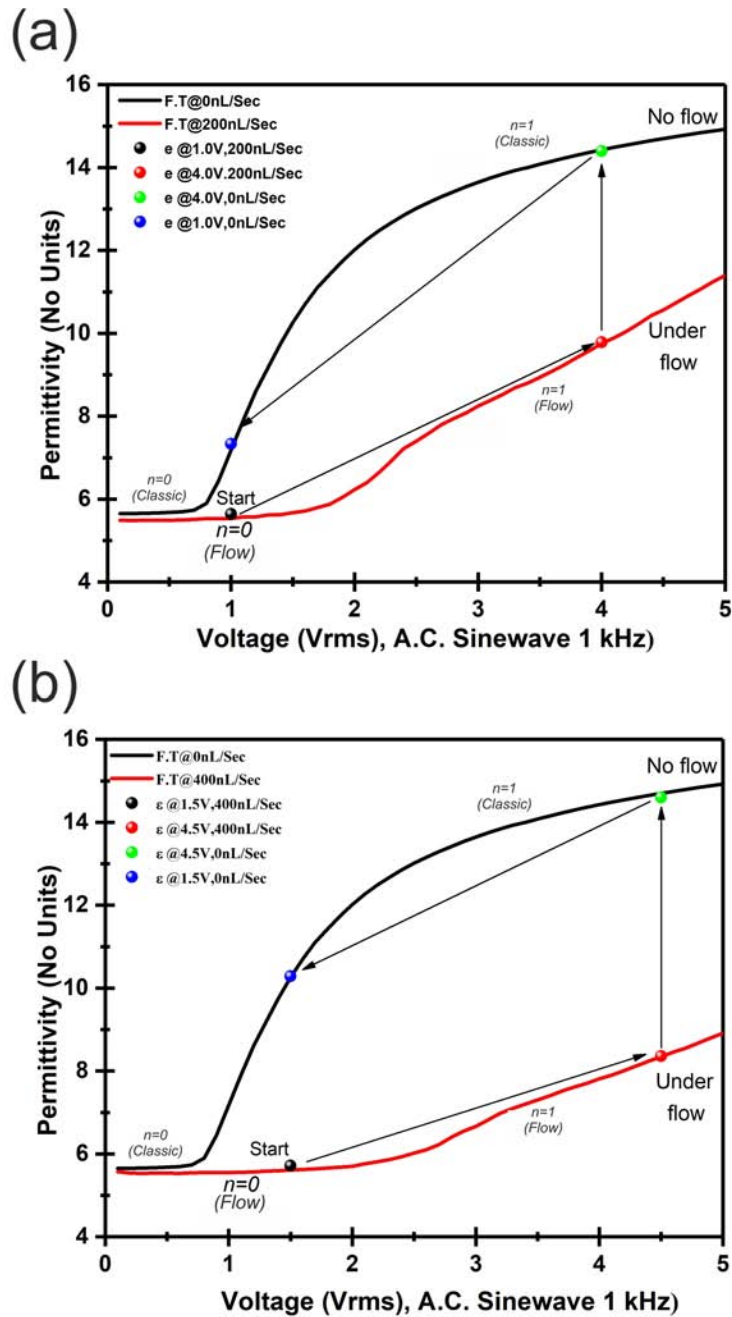
Figure 3.19: Plots showing movement between three different branches of director profile (extended/flow aligned $n = 0$ to flow distorted $n = 1$ to classic $n = 1$ branch) on sudden removal and re-application of the flow rates, a) Initial flow rate 200 nL/sec and, b) 400 nL/sec, solid black line represent the classic Fréedericksz curves and red line represent the flow delayed Fréedericksz curves

3.3.4 Electrode geometry effect on Nematoelectrodynamics of planar nematic layer (5CB)
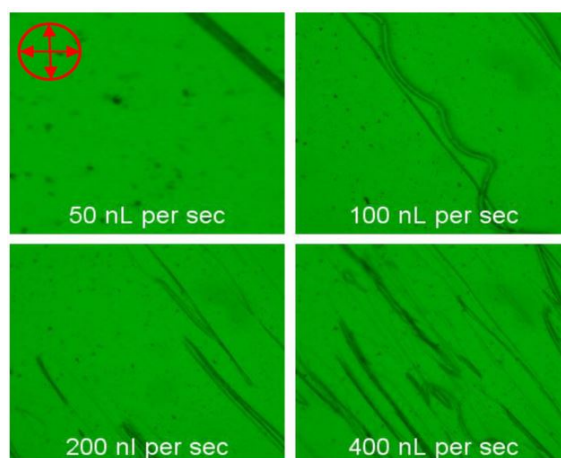
Figure 3.20: Polarising micrographs (x10) of defect structures formed in the rectangular electrode cell at different flow rates in absence of electric field, During the observation sample was kept at 45° between cross-polarisers with a green filter ($\lambda = 534$ *nm*) inserted in the field of view.

For some experiments performed in a cell having lollipop electrode geometry (section 3.3.1.3) a change in the director configuration was observed in near electrodes edges causing a domain region to grow into the active area of the cell for few combinations of voltage and flow rates (fig.3.11d 3,4). This electrode edge effect is thought to be a consequence of viscosity variation in liquid crystal layer in switched and unswitched regions of the cell which modify the flow path near the starting and the trailing edge of the electrodes. To understand the effect of electrode geometry on dynamics of planar nematic layer in pressure driven Poiseuille flow under influence of electric field a series of experiments were performed in the cell ($d = 24.01 \pm 0.9$ μm, please see appendix A, section A.1, fig.A.2), having rectangular electrode geometry. Briefly, cell consists of the top substrate of continuous ITO plate and the bottom substrate has a rectangular active electrode

separated by a guard ring electrode around it. Both the bottom plate electrodes were held at the same potential to avoid director re-orientation near the active region. Results from the study shows that nematic layer flowing in absence of electric field forms the defect textures with similar features to those observed in a cell with lollipop electrodes i.e. at a flow rate of 50 nL/sec thin disclinations line were observed moving in a downstream direction along the flow while simultaneously reducing in length over time. At 100 nL/sec serpentine curve shape disclinations were observed which then grow into bigger domains at 200 nL/sec before entering a chaotic regime with different types of defects interacting with each other while flowing in a downstream direction. In the presence of flow and electric field, no electrode edge induced director re-orientation is observed in the system. However, for Medium flow rates at which both flow distorted $n = 1$ and classic $n = 1$ mode exist in cell for voltages above V_c, a clear transition process from flow distorted $n = 1$ to classic $n = 1$ mode is observed in the cell as voltage is increased in the cell(fig. 3.21).
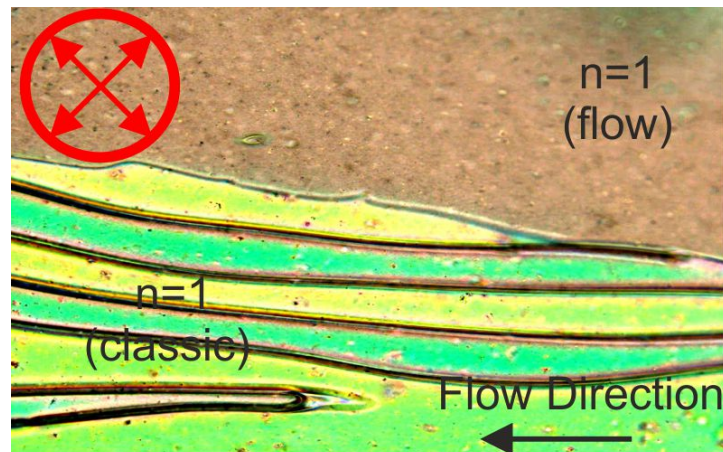
Figure 3.21: Polarising micrographs (x10) showing transition from flow distorted $n = 1$ to voltage stabilised classic $n = 1$ mode as voltage is increased in the cell having nematic layer flowing at 100 nL/sec.
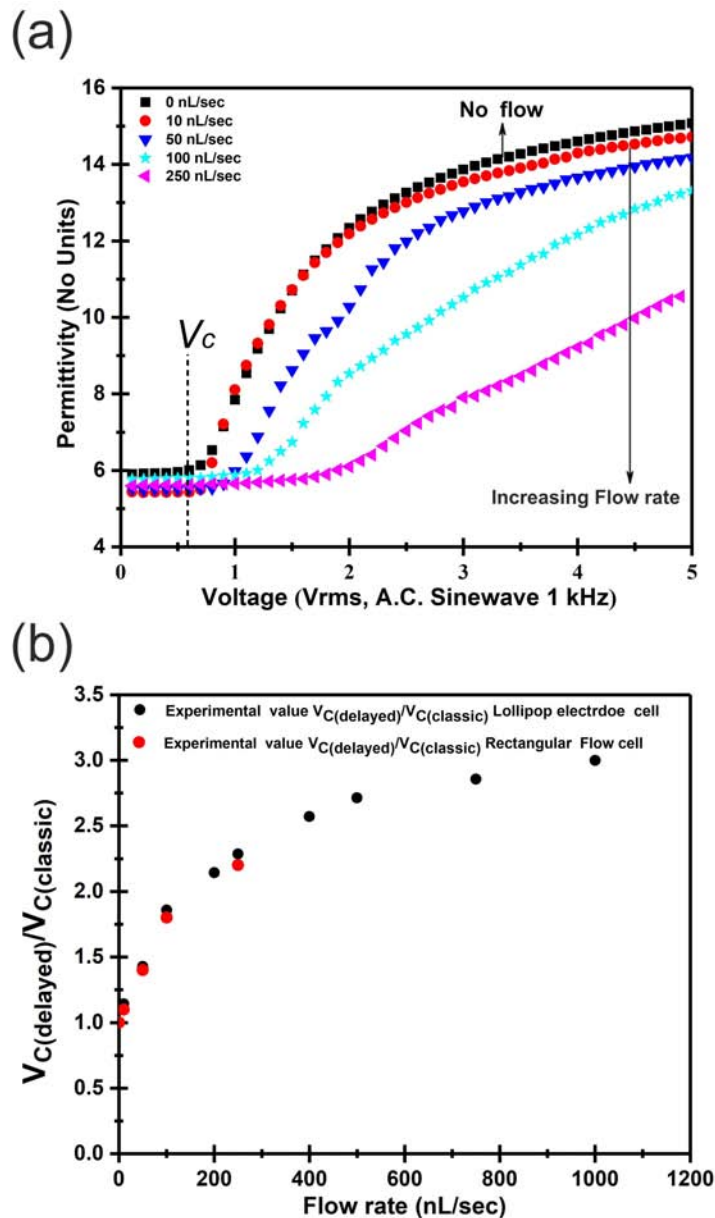
Figure 3.22: Experimental Fréedericksz curves measured at different flow rates in the rectangular electrode cell ($d = 24 \pm 0.9$ μm), Permittivity of the Fréedericksz curve at each voltage value is averaged over 32 readings measured over a duration of 128 seconds. b) Plot showing change in the critical voltage value as a function of the flow rate dashed black line represents the change in the critical voltage value in the cell with lollipop electrode.

Figure 3.22a, shows Fréedericksz transition curve in the presence of different flow rates in the cell. For flow rate of 10 nL/sec, director response is voltage dominated with flow aligned $n = 0$ mode extending slightly above V_c and post $V_{c(delayed)}$ stabilising itself in classic $n = 1$ mode as the voltage is increased in the cell. In case of 50 and 100 nL/sec, flow aligned $n = 0$ region extends nearly 1.2-1.6 times V_c respectively. However, at higher voltage value 4 V curves start shifting towards classic $n = 1$ mode from flow distorted $n = 1$ mode as voltage becomes more dominant. For, a flow rate of 200 nL/sec, flow aligned $n = 0$ extended up to $2V_c$ with smoothening of transition region near V_c, post V_c, flow distorted $n = 1$ mode takes over. All the observed results support the experiments performed in the lollipop electrode cell suggesting no effect of director re-orientation near electrode edges on evolution dynamics of director during flow. The plot in figure 3.22b shows an increase in $V_{c(delayed)}$ with increases in the flow rate. The delayed critical voltage values obtained from experiments performed in rectangular cell presented by red scatter overlaps well with the trend line of $V_{c(delayed)}$ obtained in lollipop electrode cell. In addition to Fréedericksz measurements, experiments investigating hysteresis effect (fig. 3.23) and sudden removal and re-application of flow (fig. 3.24) on nematic layer was also performed in rectangular electrode cell. The experimental results from the studies were found to be similar to those obtained in lollipop electrode cell. In light of experiments performed it reasonable to conclude that the electrode geometry and director re-orientation near edges have negligible effect on director dynamics in presence of flow and electric field. Furthermore, as engraved microchannels in rectangular electrode cell are absent, the defect textures originating in the cell during flow in the absence of electric field can be attributed to surface-flow interactions in the cell.
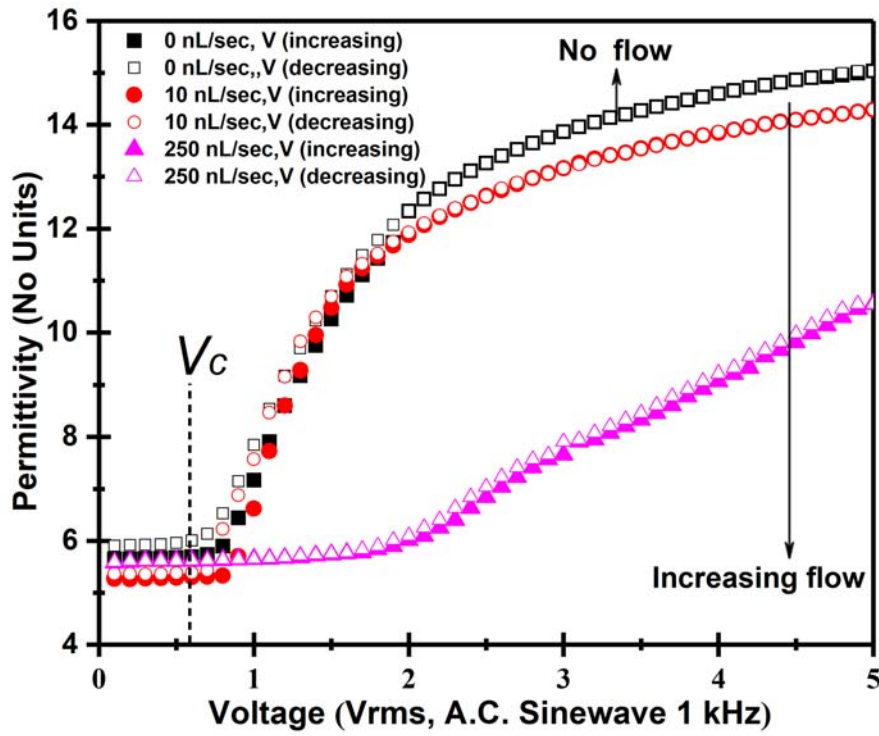
Figure 3.23: Experimental Fréedericksz curves measured in rectangular electrode cell at different flow rates with first increasing and then decreasing voltages, measurements at each voltage is averaged over 32 readings taken over a time duration of 128 seconds
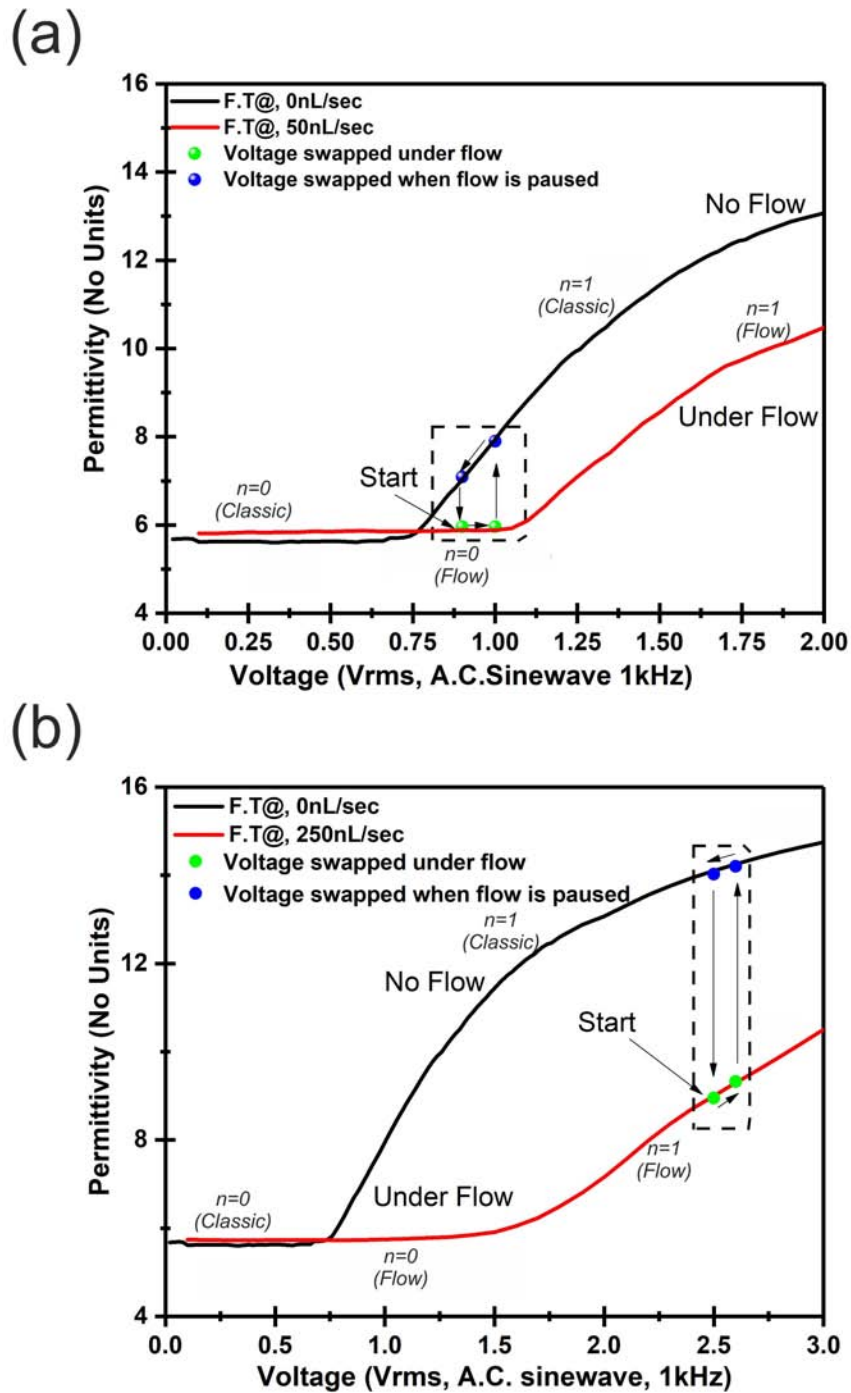
Figure 3.24: Plots showing movement between different branches of director profile on sudden removal and re-application of the flow rates in rectangular electrode cell, a) movement between extended $n = 0$ to classic $n = 1$ initial flow rate 50 nL/sec, b) movement between flow distorted $n = 1$ to classic $n = 1$ initial flow rate 250 nL/sec.

3.3.5 Theoretical model of planar nematic layer under flow and electric field
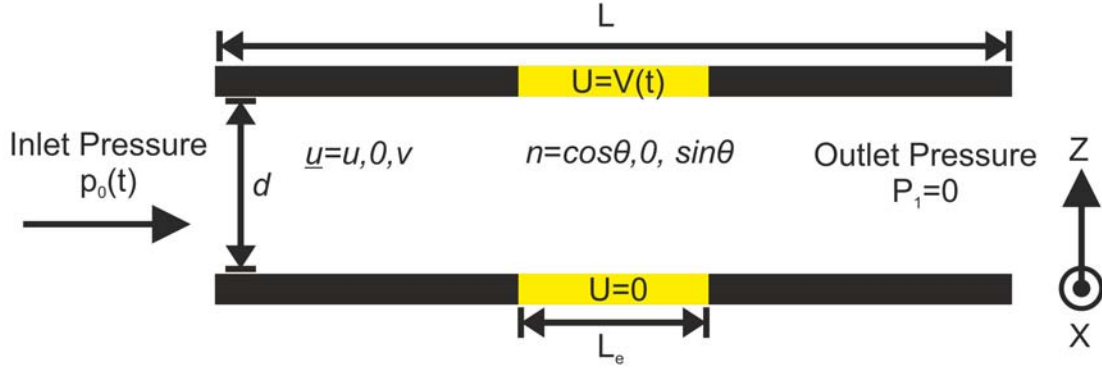
Figure 3.25: Schematic of Model geometry.

This particular section introduces the theoretical model used for modelling liquid crystals dynamics experiment performed above. The full details of the model can be availed from the creator Nigel Mottram. Basically, a two-dimensional Ericksen-Leslie theory [72] based dynamic model was developed to study the flow and electric field effect on a planar nematic layer flowing in a microchannel.

We consider a 2D-dimensional flow of a nematic liquid crystal in a microchannel of length L and thickness d. An electric field applied perpendicular (parallel to z-axis) to flowing nematic (left to right in the figure) between two electrodes patches of length L_e present in the microchannel. Figure 3.25 shows geometry of microchannel used in the model. In the model it is assumed the electrode spans the whole cell, in the y-direction. Note here in the experiment this is not the same, there is a limit to the electrode in the y-direction. Because of the translational invariance in the y-direction in the picture above, we make a modelling assumption that the system is 2D, i.e. that no dependent variable varies with y. We also assume that the director stays in the xz-plane. The system we model is shown in the picture above 3.25.

The dependent variables are the in-plane director angle, the flow speeds in the x and z directions, the pressure and the electric potential. All variables depend on x, z and t. The orientation of the nematic n-director in the model was described by a $\theta(x,z,t)$ relative to the xz-direction. The nematic director orientation in cartesian co-ordinate in terms of θ is given as $n = (\cos\theta, 0, \sin\theta)$.

To realistically model the application of the pressure gradient and the voltage (and to help the numerical code, which has trouble with adaptive time-stepping if variables are changed instantaneously) we assume a (smoothed) ramp functional form for inlet pressure and applied voltage, as shown in the plot below.
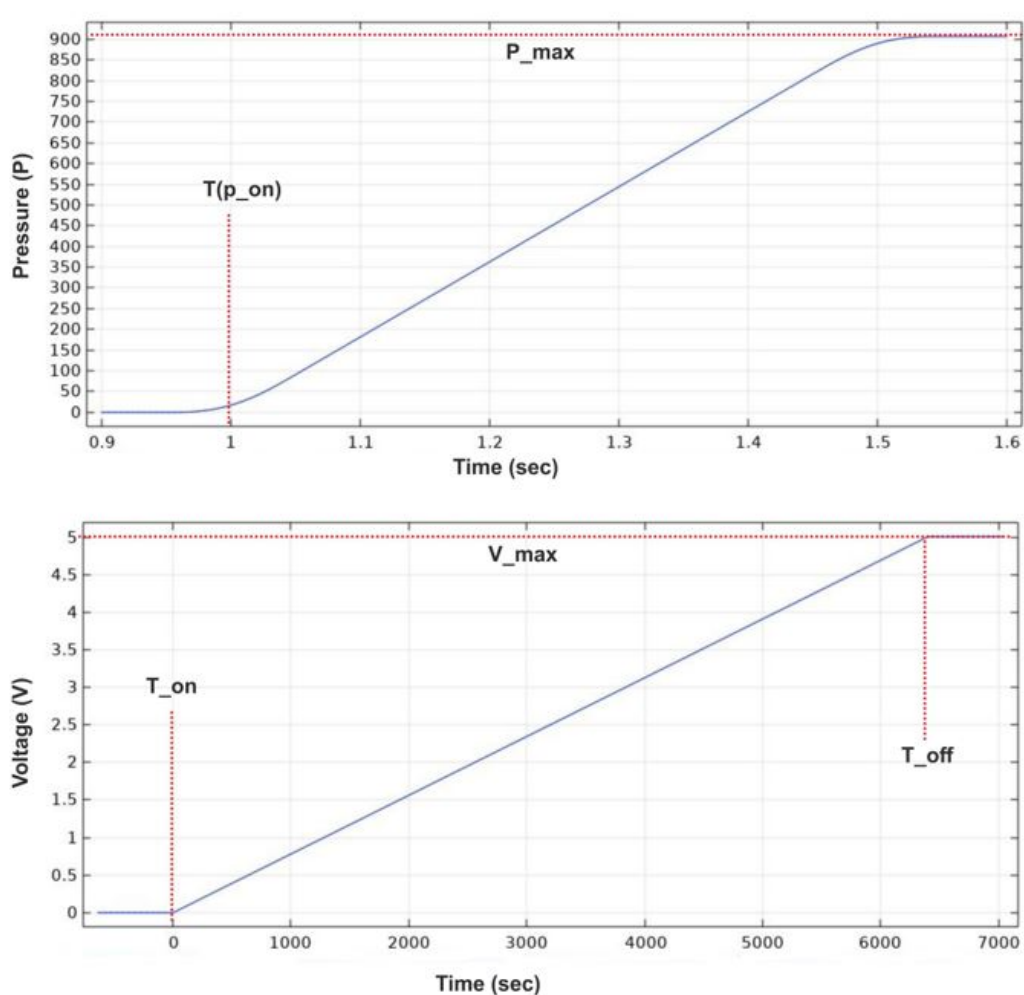
Figure 3.26: Model plot for voltage and pressure variation in the microchannel overtime.

It is therefore possible to model a situation where the voltage is applied before the pressure

gradient, or where the pressure gradient is applied (and the flow allowed to develop) before the voltage is applied. It is also possible to apply stepped voltages, in order to scan a lot of possible voltages, or a slow ramped voltage, which is an approximation of the stepped voltage.

The evolution of director dynamics in the channel and flow speed are governed by the Ericksen-Leslie equations [10, 73] with the electric potential U determined through the coupling of Maxwell's equations [74]. The initial conditions are an initially static system with a director that satisfies the preferred directions at the substrate.

Initial conditions:

$$u = v = 0 \tag{3.2}$$

$$U = 0 \tag{3.3}$$

$$\theta = \theta_1 + \frac{(\theta_2 - \theta_1)}{d}\left(z + \frac{d}{2}\right) \tag{3.4}$$

Here, θ is general form of director angle profile that has different values at each substrate.
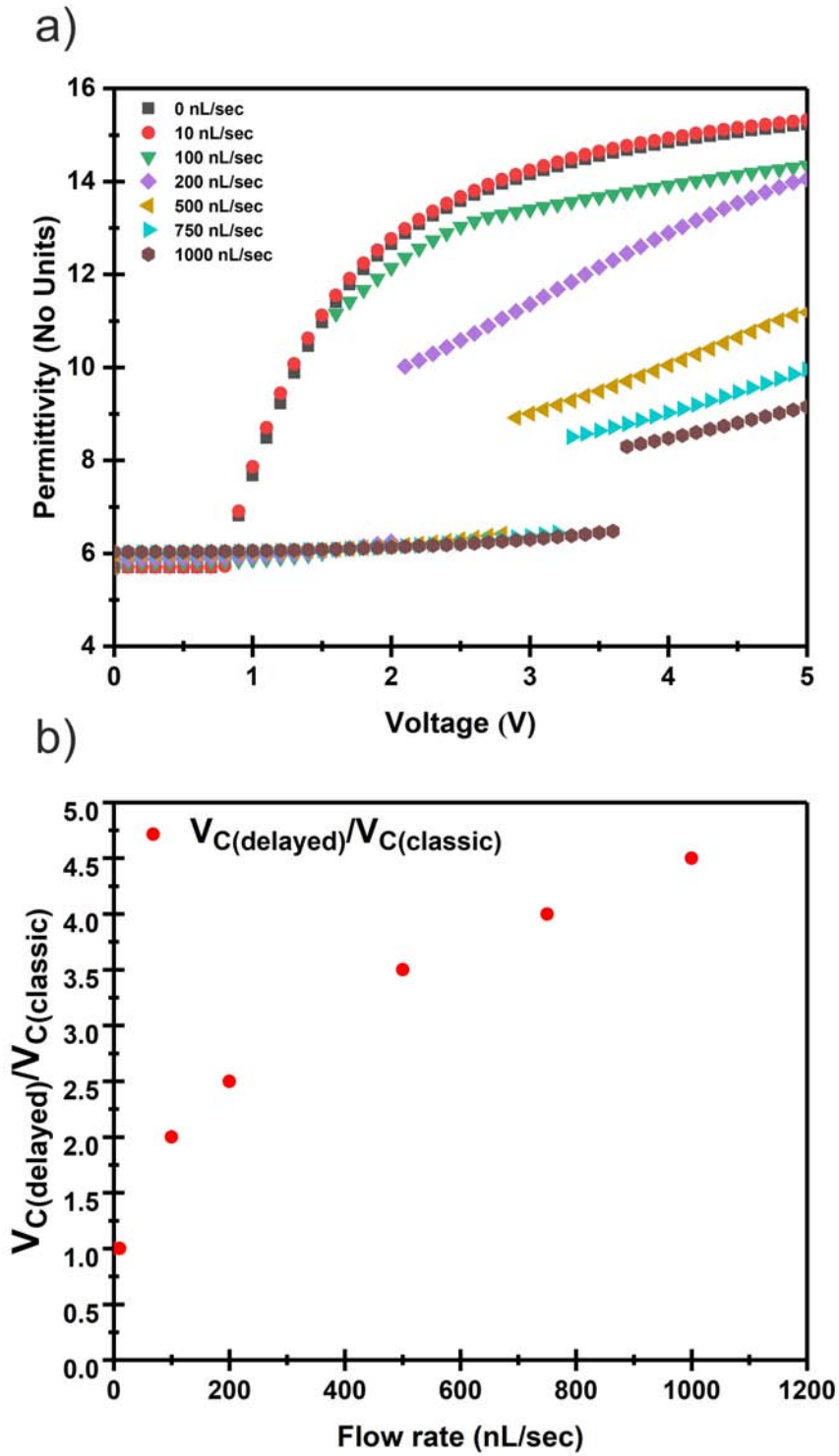
Figure 3.27: Modelling data (a) Fréedericksz curves in presence of different flow rates in the cell (d= 30 μm), b) Plot showing change in the critical voltage value as a function of the flow rate.

Figure 3.27 (a, b) shows theoretical model results of permittivity vs voltage, and a measure of Freedericksz transition ($V_{c(delayed)}$) at different flow rates (nL/sec) in the system. In figure 3.27a we observe a classic Freedericksz curve in absence of the flow (0 nL/sec), and flow delayed Freedericksz curve in the presence of the flow conditions. The low permittivity branch in figure 3.27a excluding black scatter curve corresponds to director angle solutions which are flow aligning i.e. flow aligned $n = 0$ mode. These can be clearly seen in figure 3.28(c) and (d) for voltage range V=0.5V to V=1V and V=0.5V to V=3V respectively. The director aligns (nearly) to the positive flow alignment (Leslie) angle, $+\theta_L$, in the lower half of the cell ($0 - d/2$ μm) and the negative flow alignment angle, $-\theta_L$, in the upper half of the cell ($d/2 - d$ μm). We have referred this branch as flow aligned/extended $n = 0$ mode in previous experimental sections. On this branch the flow dominates any influence of the electric field.

In figure 3.28 for voltages slightly above $V_{c(delayed)}$ in case of low flow rate (10 nL/sec), Medium flow rate (100 nL/sec), and high flow rate (1000 nL/sec) the system abruptly transitions to a different branch, where the permittivity is higher than the flow aligned $n = 0$ mode. This is a branch of solutions where the director can be thought to be distorted by flow. In the experimental sections we have referred this branch as a flow distorted $n = 1$ mode. One can think of this as the influence of the field wanting to make the director angle $\pi/2$ but the flow moving that towards the Leslie angle. Now, it's important to think about which Leslie angle the flow tries to move the director towards. In the lower half of the cell the flow would like the director to be at $+\theta_L$ or $\pi + \theta_L$ or $-\pi + \theta_L$ or any value θ_L plus or minus a multiple of π we will call these angles "positive" Leslie angles. In the top half of the cell the flow would like the director to be at $-\theta_L$ or $\pi - \theta_L$ or $-\pi - \theta_L$ or any value $-\theta_L$ plus or minus a multiple of π we will call these angles "negative" Leslie angles. For a director at $\pi/2$ the closest positive Leslie angle is $+\theta_L$ and the closest negative Leslie

angle is $\pi - \theta_L$ and so, because elasticity doesn't like large transitions between angles in the cell, the system that has both a field and a flow prefers to align the lower part of the cell at a director angle somewhere between $\pi/2$ and $+\theta_L$ and the top half of the cell at a director angle somewhere between $\pi/2$ and $\pi - \theta_L$. We can see this in the high flow rate, situation in figure 3.28 (d), i.e. for 4V and 5V. For lower and Medium flow rate the influence of flow is weaker but we can still see the distorted Freedericksz-like profile in fig 3.28 (b) 1-5V and fig 3.28 (c) 1.5-3V.

The final type of solution in the plots is seen for high voltages and intermediate flows (100 nL/sec), fig 3.28(c) 4-5V. This is a state where flow caused the director to align at $-\pi + \theta_L$ (which is one of the "positive" Leslie angles) in the lower half of the cell and $\pi - \theta_L$ (one of the "negative" Leslie angles) in the top half of the cell. This is a true flow stabilised $n = 2$ mode solution but is likely to be a higher energy than the previous flow distorted $n = 1$ mode director profile solution (although has a similar permittivity). In our modelling results, this state is found to be growing into the system from the edges of the electrode, while we have random noise included in the model. However, system doesn't forms this state in absence of the noise in the model and rather transition into flow distorted $n = 1$ mode.
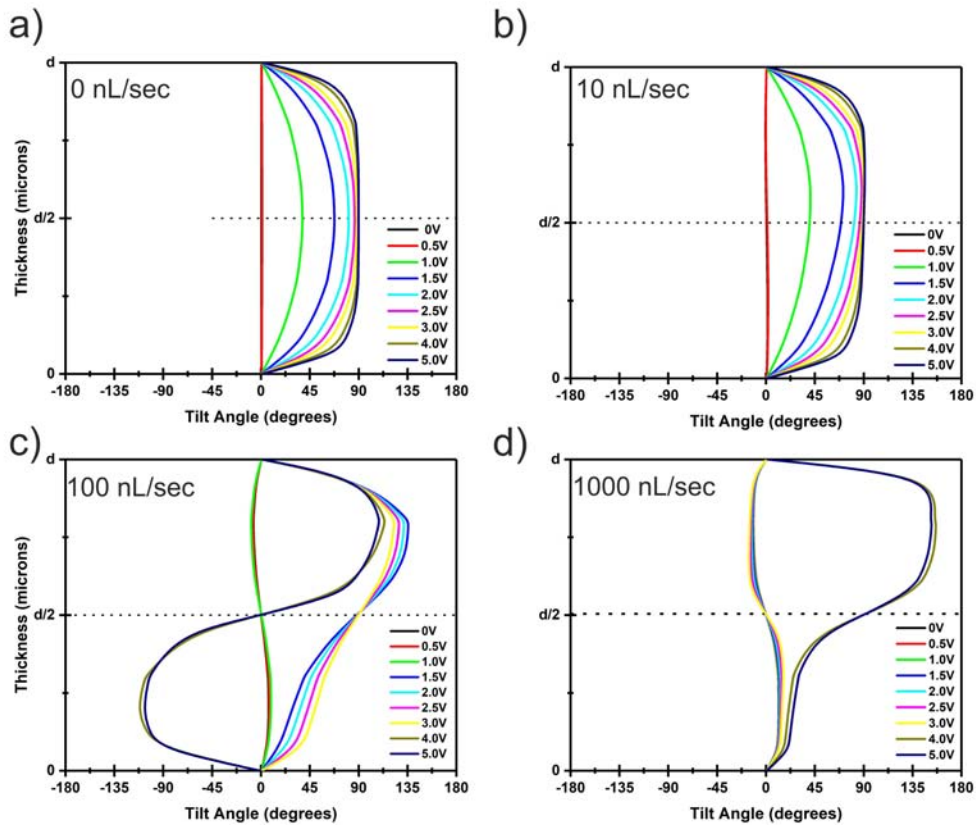
Figure 3.28: Director profile plots in the thickness (d= 30 μm) of the cell at different flow rates (a) 0 nL/sec, b) 10 nL/sec, c) 100 nL/sec , and d) 1000 nL/sec

In addition to results above, in the model we also observed a sudden jump from low permittivity branch to high permittivity branch in presence of the flow. Normally this type of branch switching would cause a structural hysteresis (fig.3.29) rather than a temporal hysteresis is caused by changing the voltage too quickly. In our experimental results shown above we see that there is no sudden transition in the permittivity, although there is a similar flow-induced delay to the Freedericksz transition. The possible reasons for the jump in the model could be due to following:

1. In our model n-director is constrained to the *xz*-plane.

2. The 2-D nature of the model is not enough to model the influence of the 3-D shape of the electrode, fringing fields leading to a director orientation out of the *xz*-plane may be having an effect.
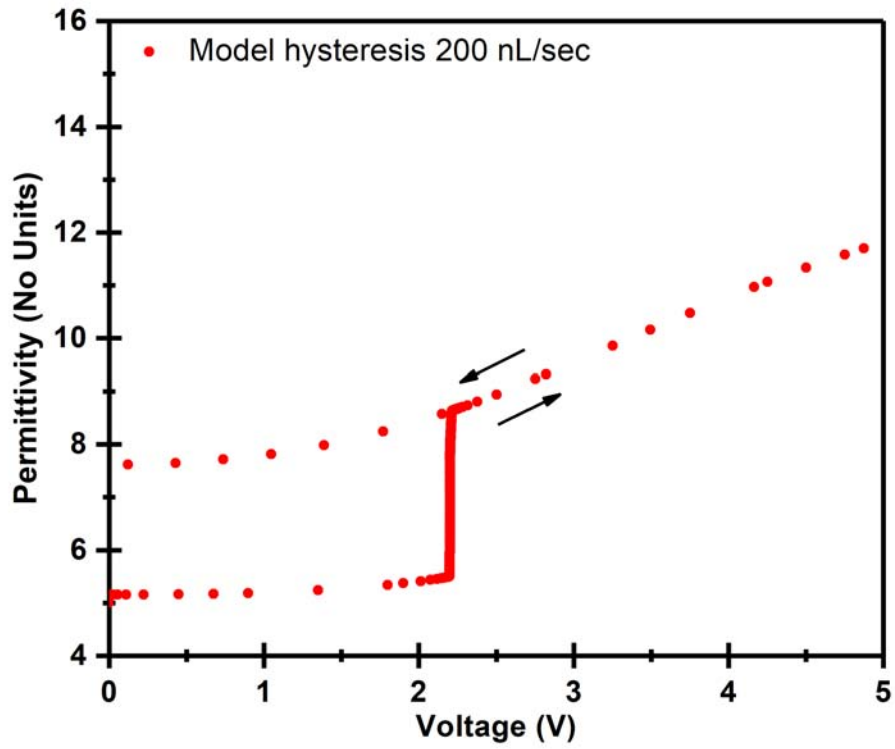
Figure 3.29: Modelling results showing hysteresis in Fréedericksz curve with first increasing and then decreasing voltages.

3.3.6 Investigation of Optical textures in a homeotropic nematic layer (LCT 07-1132) subjected to the electric field in pressure driven Poiseuille flow

3.3.6.1 *Electric field switching of a homeotropic nematic layer in the absence of pressure driven Poiseuille flow*
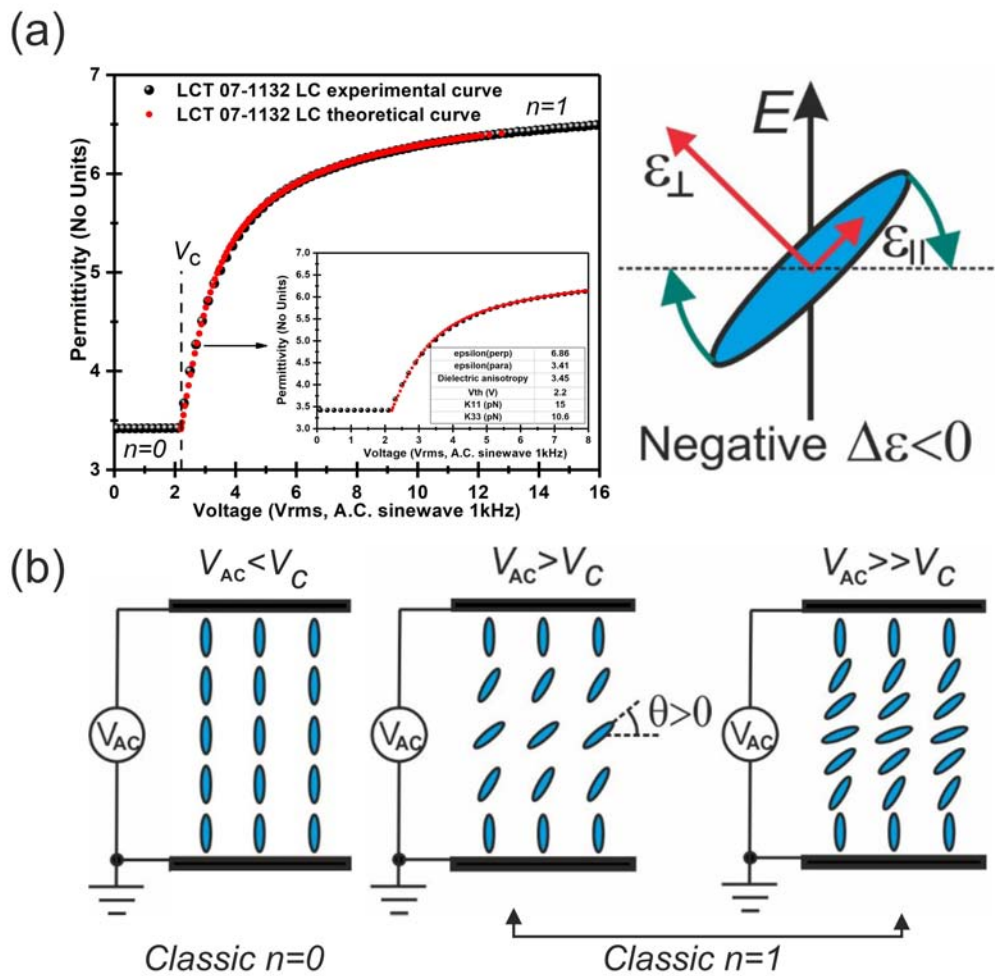
Figure 3.30: (a) Experimental and theoretical Fréedericksz curves for LCT-07-1132 $(-\Delta\varepsilon)$ liquid crystal measured in homeotropic Merck cell ($d = 22$ μm) with guard ring. Inset shows a plot with a magnified view near the critical voltage (V_c) and a table with values of physical parameters deduced from the curves. (b) Schematic of the director profile in three different regions of the curve.

In the first part of the chapter, we investigated the effect of flow and field on a $+\Delta\varepsilon$ planar nematic layer, where flow and field are orthogonal and compete to determine switched director equilibrium state. In this part of the chapter, we will investigate the effect of similar flow-field conditions in a $-\Delta\varepsilon$ homeotropic nematic layer. A key point to note here is nematic liquid crystal material used here has $-\Delta\varepsilon$ so application of flow (parallel to substrate) and electric field (applied along the thickness of the cell) will both cause director to switch parallel to the substrate in other words, in this case, they will work together rather than competing with each other. To determine the physical parameters of LCT-07-1132 liquid crystal a classic Fréedericksz curve (fig. 3.30a) was measured in homeotropic Merck commercial cell ($d = 22\ \mu$m) in absence of the flow conditions. The threshold voltage for liquid crystal is found to be V_c=2.2 V. Hence, the director remains stable below V_c in its unperturbed state, homeotropic alignment condition, i.e. classic $n = 0$ mode, so no change in the permittivity value of the cell is observed. When voltages V_{AC}>V_c is applied to the system director distort from its unperturbed state, leading to an increase in the permittivity of the cell with director acquiring classic $n = 1$ mode. For voltages $V_{AC} \gg V_c$ permittivity increases further, and director profile stays in classic $n = 1$ mode. The values of the physical parameters deduced from the Fréedericksz curve are given in the Inset of Fig. 3.30a. Figure 3.30b shows schematic of director profile for classic $n = 0$ and $n = 1$ mode observed in different regions of the Fréedericksz curve.
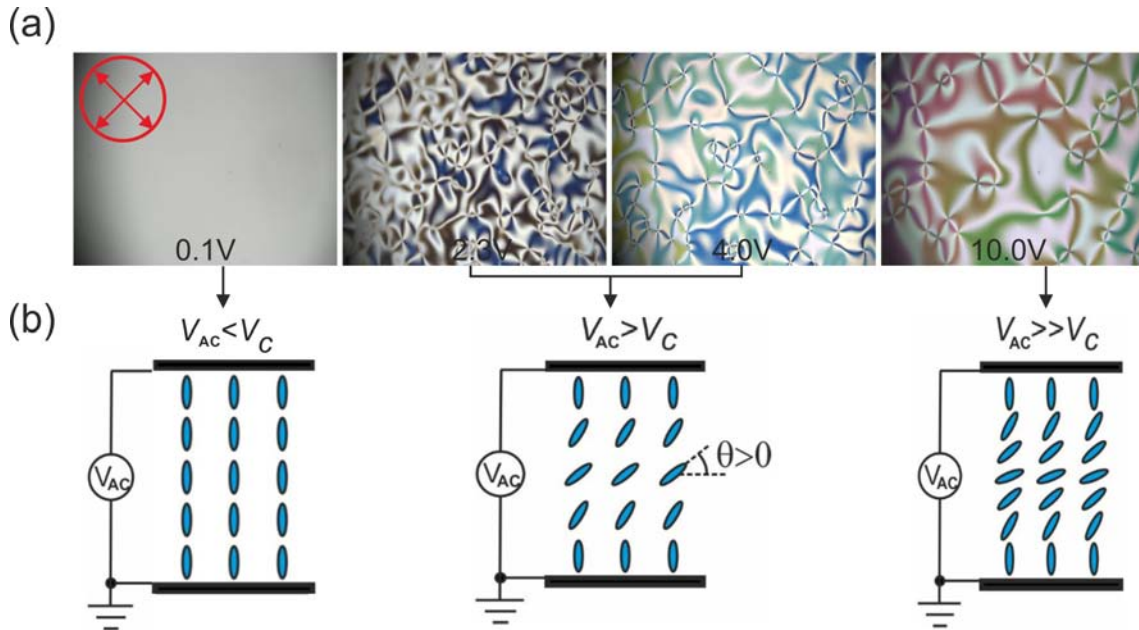
Figure 3.31: Polarising micrographs (x10) of optical textures observed in the cell during the measurement of Fréedericksz curves in absence of flow, the sample was placed at 45 degrees to the position of cross-polarisers. (b) Schematic of the director profiles at three different voltages.

Figure 3.31 shows micrographs of optical textures observed in the fabricated lollipop electrode cell during director switching at different voltage values. For voltages below V_c director stays in unperturbed homeotropic state as no change in birefringence of the cell is observed on the application of voltage to the system. However, immediately post threshold voltage (V_{AC}=2.2 V) formation of topological defect of charge ±1 was observed in the cell. This is due to random out of plane (*xy*-plane) switching of director in the cell. Figure 3.32 shows director orientation in the defect when $V_{AC}>V_c$ is applied to the cell. To understand this better assume director in 3D view, with initial director position in the centre of a conic geometry, on application of voltage director can switch randomly on either side of the cone creating a small point in centre of the geometry where director orientation is ill-defined thus creating a defect of charge ±1. With an increase in the

voltage levels (V_{rms}=10 V) these textures in the cell anneals out over time. A schematic

of side view on switching of cell at different voltage levels is shown in figure 3.32.
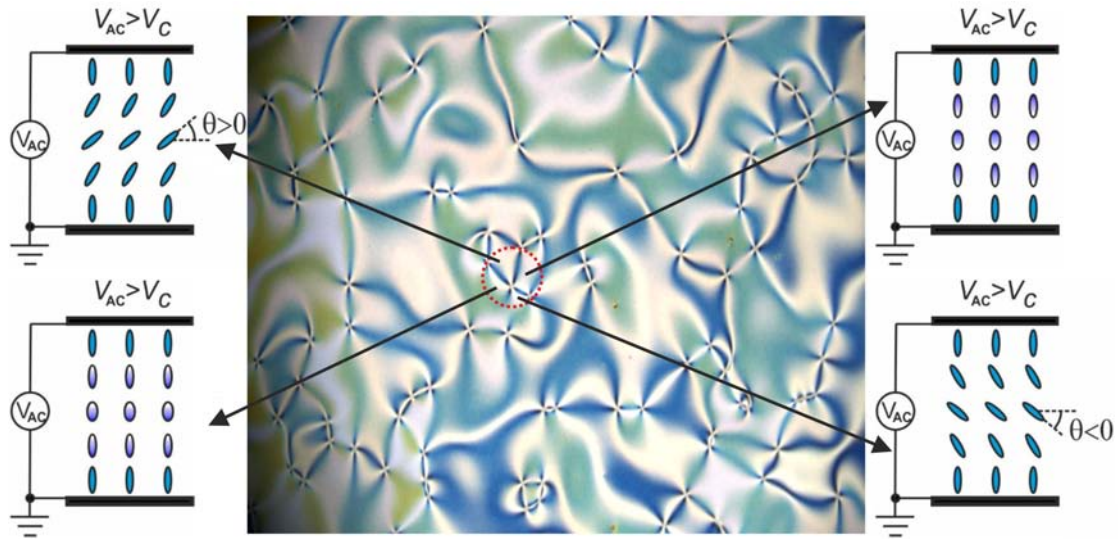
Figure 3.32: Defects observed on switching of homeotropic nematic layer.

3.3.6.2 *Homeotropic nematic layer under pressure driven Poiseuille flow in absence*

of electric field.
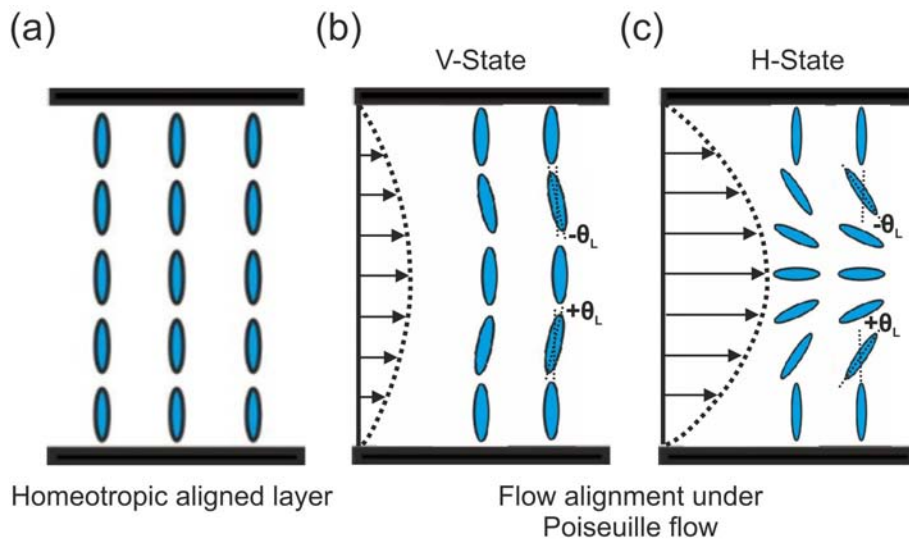
Figure 3.33: Schematic of the homeotropic director profile, (a) in absence of flow conditions, (b) in the presence of weak and, c) strong flow conditions.

Figure 3.33a shows a homeotropic aligned nematic layer in its unperturbed form with director aligned perpendicular to the substrate. When a pressure driven Poiseuille flow is introduced in the cell ($d = 31\pm3\ \mu$m, please see appendix A, section A.1, fig.A.3), director will align along the flow direction at Leslie angle. However, unlike flow alignment in planar case, in homeotropic nematic layer two flow aligned state exist in the cell which can transition into each other depending upon flow rate (u) applied to the cell compared to the value of critical flow rate (u_c). At $u<u_c$, V-state is observed in the cell in which director in the middle stays in the initial homeotropic alignment and rest of the cell tends to orient towards ($\pm\theta_L$). Basically, in V-state (fig. 3.33b) director in the mid-point ($d/2$) of the cell remains in homeotropic aligned state as the flow gradient is zero in the centre. However, in the lower and upper half of the cell, as flow gradient is positive and negative this causes the director to tilt in forward and reverse direction creating a mirror-symmetry in the cell. As the energy of V-state grows rapidly with an increase in the flow rate [46]. For $u>u_c$, director profile transition into H-state where the director in the middle aligns parallel to the flow with a continuous distortion region near cell boundaries aligned at ($\pm\theta_L$). Notice that both states shown in figure 3.33 are mirror-symmetric about the mid-point ($d/2$) of the cell. A similar observation of flow induced transformation of V-state to H-state is observed by Jewell *et.al*[46] when a pressure driven Poiseuille flow is applied to the cell in the absence of an electric field. In our experimental studies, we will examine effect of voltages ($V_{AC}<V_c$) on the flow aligned V-state. Note here, in the absence of the flow rate for voltages $V_{AC}<V_c$, no switching of the director profile is observed for a $-\Delta\varepsilon$ homeotropic nematic layer.
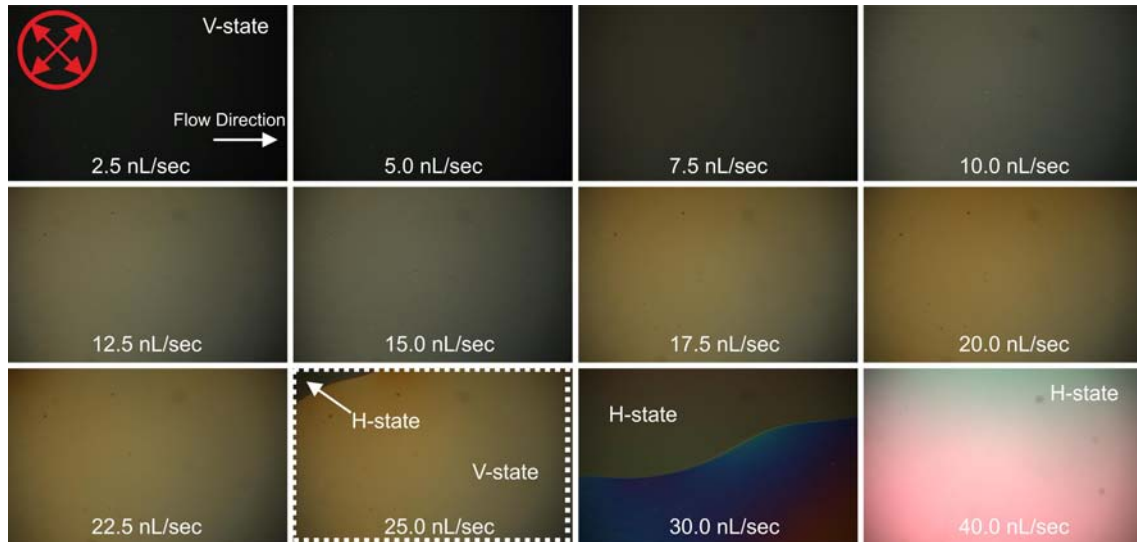
Figure 3.34: (a) Polarising micrographs (x10) showing the evolution of different director states in pressure driven Poiseuille flow with no applied electric field. Image highlighted with white dashed box shows the transition of *V*-state into *H*-state at a critical flow rate (u_c), during the observation sample was placed at 45° to the position of cross-polarisers.

To determine the critical flow rate (u_c) value in system an optofluidic study of nematic layer is performed in absence of electric field. Determination of critical flow rate value is crucial for the experimental studies as the application of voltage to *H*-state would have a very different response in the system. Polarising optical micrograph shown in figure 3.34 shows the existence of two flow aligned states in the presence of pressure driven Poiseuille flow in the cell. For flow rate below u_c=25 nL/sec, cell stays in *V*-state with birefringence of the sample showing variation in shades of grey colour between cross-polarisers with increasing flow rate. At a flow rate of about 25 nL/sec (highlighted by dashed white box), transition from *V* to *H*-state takes place with two state being separated by the domain wall. As the flow rate is increased beyond 25 nL/sec, cell slowly transition into flow aligned *H*-state which can be easily determined by increased birefringence of the cell. Both states are devoid of any topological defects in the system at flow rate below 100 nL/sec. However, for flow rate of more than 100 nL/sec defects were observed in the

system with defect density increasing in with an increase in the flow rate (fig. 3.35).
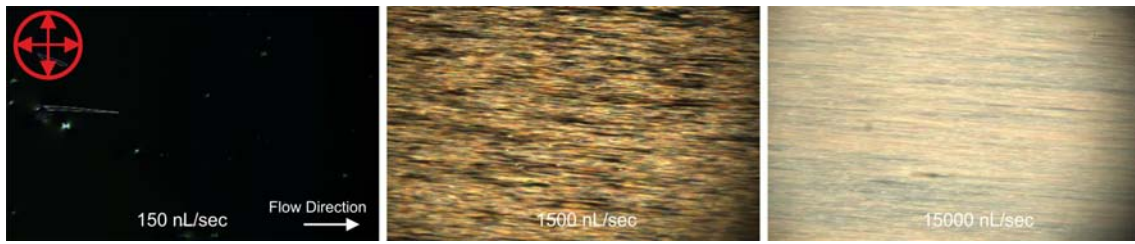
Figure 3.35: Micrograph showing increase in the defect density in homeotropic cell as flow rate is increases in the cell.

3.3.7 Investigation of the Permittivity of a homeotropic nematic layer (LCT 07-1132) subjected to the electric field and pressure driven Poiseuille flow.
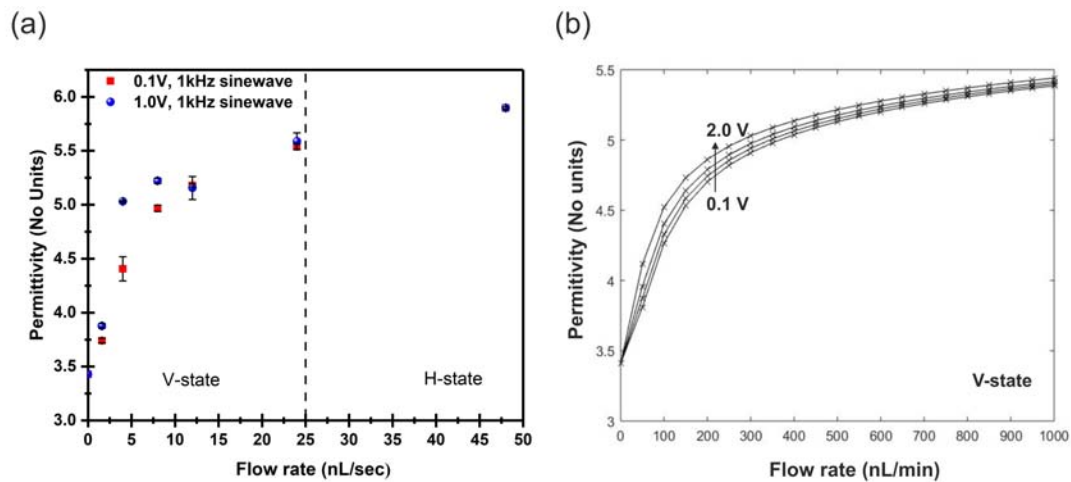
Figure 3.36: a) Preliminary experimental data showing an increase in the permittivity value as a function of flow rate when a voltage, $(V_{rms}<V_c)$ is applied to the cell. Black dashed line represents the critical flow rate (u_c) at which transition from V-state to H-state occurs. b) Preliminary model data showing permittivity response to voltage $(V_rms<V_c)$ as flow rate is increased in the system.

To determine the effect of flow and electric field on V-state different voltages in range of 0-2.0 V and flow rates, 0-25 nL/sec were applied to the system. Briefly a flow rate below u_c was established in the cell that forces the director to transition into flow-aligned V-state from initially unperturbed state. Once the V-state is established in the cell a voltage $V_{rms}<V_c$, is applied and resultant permittivity of the nematic layer is measured using LCR meter. For each measurement shown in figure 3.36a these steps were repeated with sufficient re-settling time (30 mins) back to the unperturbed homeotropic state allowed in between each measurement. Two voltages 0.1 V and 1.0 V are applied to the cell with different flow rates. For both the voltages curve the permittivity of the nematic layer increases with an increase in the flow rate. The result from this study clearly supports the observation from optical micrographs that shows change in optical birefringence of sample in absence of electric field when flow rate is increased in the cell signifying increase in the distortion of the V-state due to the flow alignment effect. In other words, increase in the director distortion of the V-state due to flow, facilitates the electric field to switch director even at $V_{rms}<V_c$. Preliminary experimental data shown in figure 3.36a shows increases in the permittivity of the layer under voltage when flow rate is increased in the system. A similar plot (fig. 3.36b) of increasing permittivity with flow rate is observed in the preliminary model results. Therefore, based on the results so far, it's plausible to observe a promotion in Fréedericksz transition with critical voltage $(V_{c(promoted)})$ preceding initial classic threshold (V_c) with increase in the flow rate. Further to the results shown above it was also observed that the permittivity value of H-state $(u>u_c)$ also increases with the flow, this effect can be seen post u_c in figure 3.36a and figure 3.37. The observed effect is due to the dependence of the average distortion of director in H-state on the magnitude of the flow. However, for a flow rate more than 500 nL/sec a sharp decline

in permittivity (fig. 3.37) occurs due to increases in the defect density in the system.
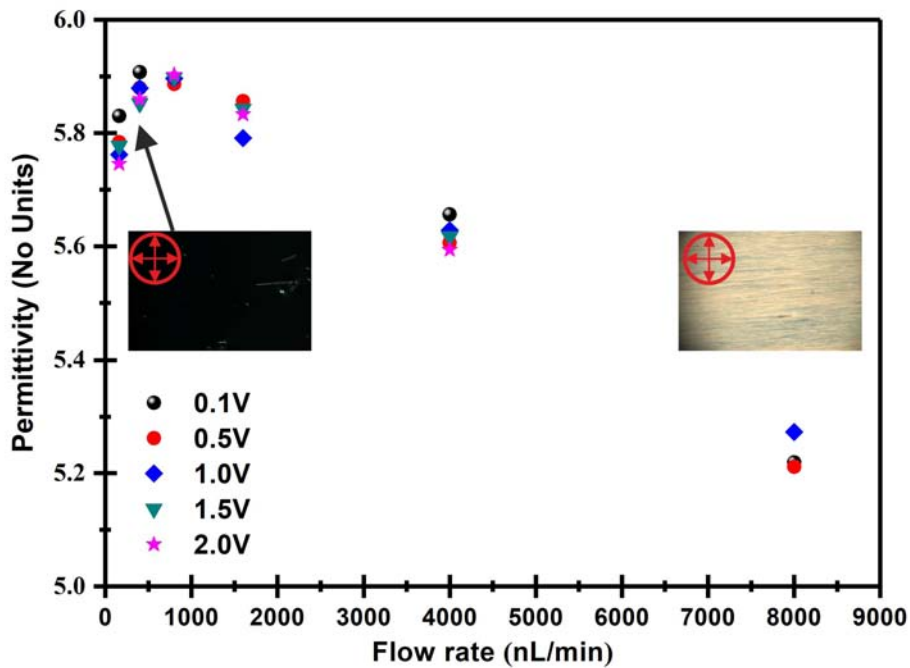
Figure 3.37: Preliminary experimental data showing the effect of defect density on permittivity of the nematic layer as the flow rate is increased in the cell under an applied voltage ($V_{rms}<V_c$).

3.4   Conclusion

In this chapter experimental and theoretical study on the electrodynamics of nematic liquid crystals layer under pressure driven Poiseuille flow is performed in rectangular micro cross-section with uniform planar and homeotropic alignment conditions. The optofluidic and electro-optofluidic response of n-director is monitored under different sets of controlled application of orthogonal flow-electric field conditions. The observation made from the studies can be concluded as: In case of the planar aligned nematic layer ($+\Delta\varepsilon$), flow and electric field competes, and resultant director response is found to vary depend-

ing upon set of chosen conditions. For low flow rate conditions presence of flow seems to have a negligible effect on n-director response as the director switches to $n = 1$ mode of classic Fréedericksz transition for majority of the region post threshold voltage. In case of medium flow rates, both flow dominant and electric field dominant response of n-director is found to exist in the cell. As above threshold value both flow distorted $n = 1$ mode and voltage stabilised classic $n = 1$ is observed. In case of high flow rates, flow distorted $n = 1$ mode is observed, which is otherwise unstable in classic Fréedericksz curve. Moreover. it was also found that presence of flow conditions leads to extension of $n = 0$ mode above classic threshold prompting a flow-delay Fréedericksz transition in the system with critical voltage(V_c) shifting almost $3V_c$ at high flow rates. Dielectric hysteresis measurement performed in presence of flow by cycling voltage up and down on Fréedericksz curve reveals existence of hysteretic behaviour for Medium and low flow rates. However, no hysteresis was observed on Fréedericksz curve with flow distorted $n = 1$ mode at high flow rates. Moreover, it was also found that system can easily transition in between flow distorted and voltage stabilised modes by sudden removal and re-application of the flow rates. For a homeotropic nematic layer $(-\Delta\varepsilon)$, the n-director response to flow and electric field was studied in V-state, where n-director in the middle of the cell is aligned in an initial homeotropic alignment. Both the orthogonal flow and electric field in the system work with each other to align the n-director parallel to the flow direction. Preliminary results from the studies show that it is possible to switch flowing V-state below the critical threshold of classic Fréedericksz curve thus revealing the existence of a flow-promoted Fréedericksz transition.

Chapter 4

Dynamics of topological line defect in a hybrid aligned nematic layer

Understanding the dynamics of topological defects in liquid crystals systems is a challenging task in the soft matter physics community. Many fascinating phenomena like the interaction of topological defects, and their motion under the influence of external and internal forces is both exciting and perplexing for liquid crystals researchers. The studies reported in this chapter is an attempt to generate an understanding of many of these unmet challenges. In this chapter, we investigate the dynamics of topological line defect formed between two distinct Hybrid Aligned Nematic (HAN) domains. Briefly, the dynamic study reported in this chapter is based on electric field-induced reconfiguration and manipulation of -1/2 topological line defect between two distinct hybrid aligned nematic domains having opposing tilt orientation. Application of different applied voltage to the system allows control over the growth of line defect in the system without the need for externally imposed flow conditions. The ability to precisely control the velocity of the line defect was further explored for developing microcargo transportation platform. Deliberately tuning an applied voltage relative to a threshold value (V_c) permits defect trapping

of the colloidal particles and allows subsequent control over particle velocity and bidirectional linear movement over millimetre distances. Experimental findings shown in the chapter were complemented by the theoretical model (developed by Nigel Mottram) that captures the basic physics of the process.

4.1 Introduction

Localised abrupt changes in otherwise continuous structures are ubiquitous in natural systems and often help us to understand system formation and the physical mechanism of these systems. Topological defects are an example of such changes that occurs in many natural and physical systems; from the formation of vortices in Helium (He), Skymiron in particle physics to cosmic strings topological defects play a crucial role in defining properties of the system [75, 76]. A recent report on the formation of topological defects in epithelial cell monolayer found to have a defining role in cell apoptosis [77]. All these examples of growing research make topological defects fundamentally essential to study. In the case of liquid crystals, the distortions in the vicinity of topological defects are formed on a macroscopic scale, which makes them strikingly visible using a microscope. Thus, offering us a unique minilab to conduct bench research on statics and dynamics of topological defects. Understanding of dynamics of these defects on the lab-scale could help in unraveling underlying mechanisms of many analogous natural systems constituting topological defects for example evolution of cosmological defects can be studied in a layer of liquid crystals [78–80]. Beside their fundamental importance, dynamic manipulation of topological defects in liquid crystals suggest their use for advanced technological applications, for example, generation of optical vortices by interaction of light beam with topological defects in liquid crystals could be used for quantum commu-

nication [81–83], optically selective photomask can be designed using topological defects [84, 85], in addition to this, liquid crystal topological defect based colloidal trapping systems can be utilized for making optically healable materials [86], metamaterials [87] and, 3D-microwires [88]. Owing to all inherent advantages over other topological defects containing systems, there has been a burgeoning interest in the development of various liquid crystals-based platforms for micro cargo transportation and positioning systems [89–94]. Although the use of isotropic carrier fluids for microparticles transportation has been extensively researched [95]. The replacement of these isotropic fluids with liquid crystals is more advantageous as they provide a) possibility to transport charged and neutral particles under the application of electric and flow fields [89–91], b) ability to use A.C. field in the system removes the problem of electrochemical reactions arising due to the use of D.C. field in traditional systems [96]. c) complex shapes and structures can be made in the carrier fluid utilizing a range of techniques [88]. However, despite much of the effort, use of liquid crystals topological defects for device applications is often restricted due to limited control over the mobility of microcargo, presence of curved substrates for confinement conditions [90], and complicated setups [91]. So, a reconfigurable microcargo transportation platform based on topological defects in liquid crystals layer, capable of providing precise control on movement and placement of microparticle is desirable. In this work, we use electrical confinement of the domain wall between two opposing hybrid alignment states, without lateral confinement, to significantly distort the shapes of the domains and manipulate the domain wall to evolve a series of parallel intervening walls connected by high curvature tip regions. We have developed a nematic continuum theory model that duplicates the observed time evolution of the tortuous shape of the wall and which quantitatively reproduces the A.C. voltage controlled linear motion of the tip in the low-velocity

range. We have used this high curvature tip feature on the electric field confined domain wall to collect, trap and move a microparticle. This provides straightforward precision A.C. voltage control of the positive and negative linear movement and placement of the particle, without any need for externally imposed flow, nor for lateral confining walls or geometric or alignment texturing.

4.2 Experimental

4.2.1 Device details and preparation
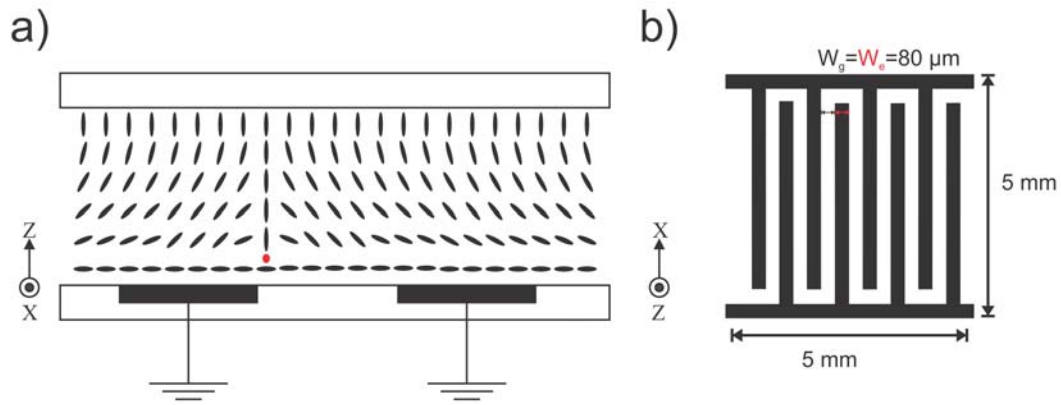
Figure 4.1: Schematic showing, (a) side view of the device with hybrid aligned nematic layer sandwich between the two substrates (b) top view of the interdigitated electrode (IDE) patterned on the lower substrate having $w_e = w_g = 80\,\mu$m.

The device consisted of a nematic liquid crystal layer of thickness $d = 13\,\mu$m sandwiched between two borosilicate glass substrates in the xy plane (fig.4.1a). The lower substrate at $z = 0$ was patterned with an array of transparent co-planar interdigital stripe electrodes running parallel to the x-direction. The lower substrate was coated with a thin solid film which imparted low-pretilt planar nematic surface alignment with the easy alignment axis in the y-direction, orthogonal to the direction of the electrode lines. The opposing up-

110

per substrate at $z = d$ was coated with the amorphous fluorinated copolymer Teflon AF (CAS 37626-13-4, Sigma-Aldrich / Merck KGaA, Darmstadt, Germany) which imparted homeotropic nematic surface alignment (please see also chapter 2 section 2.3.2).

The electrodes on the lower substrate were fabricated on indium tin oxide coated borosilicate glass slides using standard photolithography and etching techniques (detailed process mentioned in chapter 2 section 2.2). The electrode arrangement covered a square area of size 5×5 mm, whilst the electrode linewidth and the gaps between the electrodes were both equal to $w_e = w_g = 80$ μm as shown in fig.4.1b. The entire lower substrate was coated with a magnesium fluoride on zinc sulphide mechanical alignment layer (please see also chapter 2 section 2.3.1) having a combined thickness of 300 nm.

We used nematic liquid crystal material E1, which has a density of 1.01±0.01 g/cm^3 [97, 98] and which is a two-component mixture of 5CB and 7CB (CAS 40817-08-1, and CAS 41122-71-8, Sigma-Aldrich/Merck KGaA, Darmstadt, Germany) in the proportion 60%:40% by weight. This mixture exhibits a stable room temperature nematic phase, and the mixture and its cyano-biphenyl components [99, 100] are established and well characterised materials. We measured the value of the positive dielectric anisotropy, $\Delta\varepsilon$ = 12.3±0.4, and also the values of the splay and bend elastic constants, K_{11} = 7.2±0.5 pN and K_{33} = 10.1±0.8 pN respectively, for the E1 mixture that we used in our experiments using the A.C. voltage Fréedericksz effect [21, 101] (fig.4.2). The layer spacing in the device was maintained with polyethylene terephthalate strips (PET, 13 μm, Goodfellow, Cambridge, UK). The colloidal micro particles used in the micro cargo experiments were polymer microspheres of diameter 5.0±0.1 μm (density 1.05 g/cm^3, Duke scientific Corp., USA) that were sparsely dispersed in the liquid crystal mixture before filling into the device. The particles were coated with trichloro(octyl)silane to impart homeotropic surface alignment, sonicated, and dispersed in the nematic E1 at 0.05% by weight.
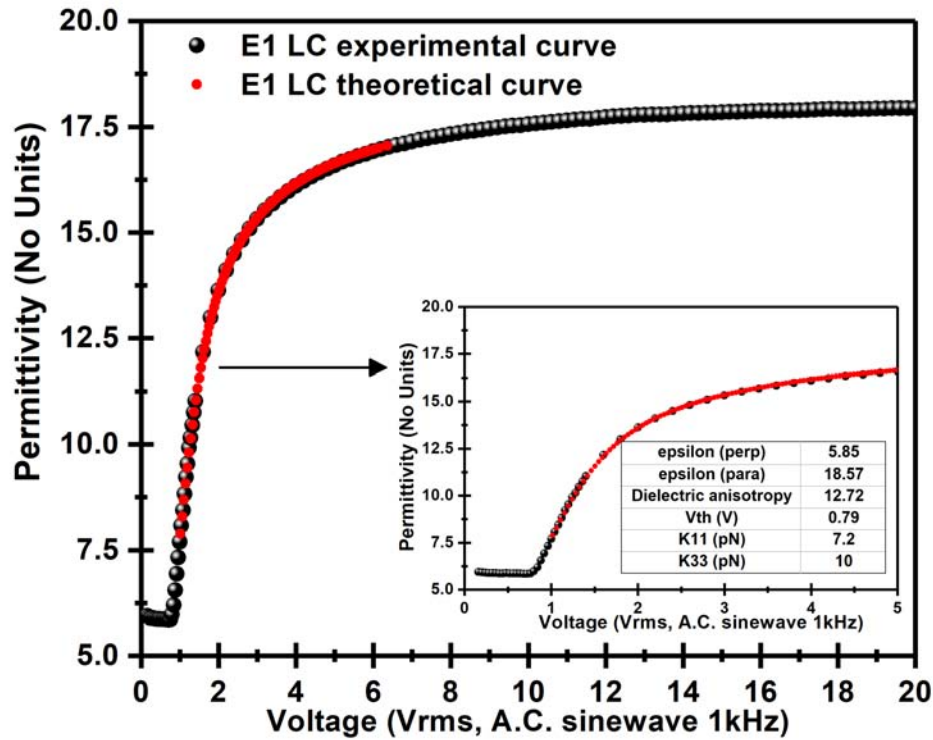
Figure 4.2: A.C. voltage Fréedericksz transition curve for the nematic liquid crystal material, E1, which is a two-component mixture of 5CB and 7CB in proportion 60% to 40% by weight. The material was contained within a commercial cell (Merck Chemicals Ltd.) with a cell gap of 22 μm. One surface of the cell had a continuous electrode whilst the other surface had a circular electrode with guard ring. The aligning agent on the cell surfaces was a rubbed polyimide (PI) polymer that gave a surface pretilt below 0.5° with a parallel configuration of the easy alignment axes on opposite surfaces. The solid black circles show the permittivity measured at 21°C as a function of an A.C. sinewave voltage (1 kHz) using an Impedance Analyser (Agilent 4284A). The solid red circles shows a fit to the experimental data using nematic continuum theory [10].

4.2.2 Device addressing and polarising optical microscopy (POM) measurements

The nematic liquid crystal layer could be subjected to a spatially periodic electric field, **E**, by applying an A.C. voltage to alternate electrodes in the array whilst the interposed electrodes were held at earth potential. All experiments were performed on the open bench in a temperature-controlled laboratory (21±1°C). The A.C. sinewave voltage (1 kHz, R.M.S. voltage values given in the text) was provided by a waveform generator (TGA1244, Thurlby Thander Instruments Limited, Cambridge, UK) combined with a voltage Amplifier (PZD700, Trek Inc., Medina, New York, USA). Videos and still images of the device under operation at different voltage values were recorded using a polarising microscope (BX51, Olympus, Essex, UK) fitted with a CMOS camera (EO-23121C, Edmund Optics Ltd, Yorkshire, UK). Analysis of the video images, including feature and particle tracking, was performed using homemade MATLAB programmes (see appendix section A.3.2) and the Image J plugin MTrackJ [49, 50].

4.3 Results and Discussions

4.3.1 Creation and electrical distortion of a topological defect line.

The nematic layer was subject to low-pretilt planar alignment at the lower substrate and to homeotropic alignment at the opposing upper substrate. This hybrid alignment arrangement leads to symmetry breaking and to two distinct, and equally energetically probable nematic n-director distortion profiles. These degenerate Hybrid Aligned Nematic HAN(/) and HAN(\) alignment states are shown in Fig. 4.3 (a) by the open ellipses in the left and right-hand side highlighted boxes respectively. This schematic diagram represents a *yz* cross-section through the nematic layer, where the orientation of each ellipse indicates

the out of plane tilt angle θ of the nematic n-director at that position. Consider the spatial variation in the n-director tilt orientation only in one dimension, the vertical z-direction. In the HAN($/$) state the nematic n-director orientation changes smoothly and monotonically across the layer from horizontal planar at the lower surface ($z = 0$) to vertical homeotropic at the upper surface ($z = d$), with the tilt increasing by rotation in the anticlockwise sense as a function of the distance z from the lower surface. In the HAN($\backslash$) state, the orientation change is in the opposite, clockwise, sense as a function of z. Hence, towards the middle of the layer, $z \approx d/2$, the n-director tilt orientations in the HAN($/$) and HAN($\backslash$) states will be orthogonal.

Uniform domains containing only HAN($/$) or HAN($\backslash$) alignment states can co-exist within a hybrid aligned nematic layer, separated by domain walls. In Fig. 4.3 (a) a simplified representation of a such a domain wall is shown, with HAN($/$) on the left and HAN($\backslash$) on the right. The wall depicted runs along the x-direction, into the page, and is centred on a topological line defect of strength $\frac{-1}{2}$, shown by the red filled circle. Away from the wall, the one-dimensional z-variation of the tilt angle within each HAN state is undisturbed. In the vicinity of the wall, there is a smooth and continuous distortion in the nematic tilt angle in both the y- and z-directions, of extent governed by the nematic elastic forces and the surface alignment. There is highly localised and abrupt spatial variation in the nematic n-director orientation close to the defect, associated with alignment induced frustration and symmetry breaking [75, 102].

Zero voltage
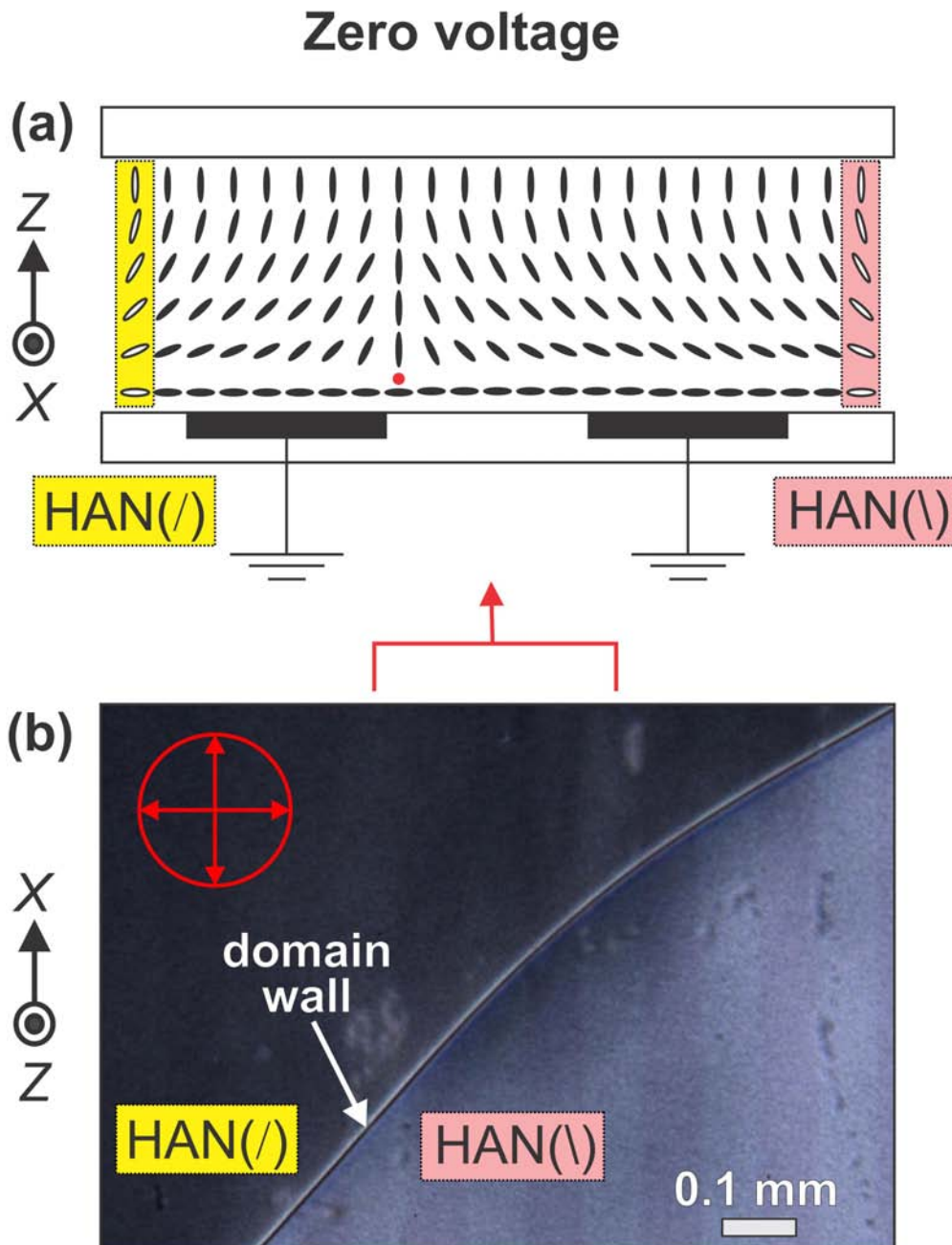
Figure 4.3: The nematic layer with no applied voltage: (a) Illustration of the orientation of the nematic n-director in cross-section showing the coexisting HAN(/) and HAN(\) alignment states separated by a domain wall containing a topological line defect of strength $\frac{-1}{2}$ (note that the location of the line defect, the red dot, is arbitrary in the zero-voltage state), (b) Optical micrograph of the actual device under plane-polarised light with a crossed analyser showing two coexisting HAN regions separated by a domain wall running diagonal to electrodes.
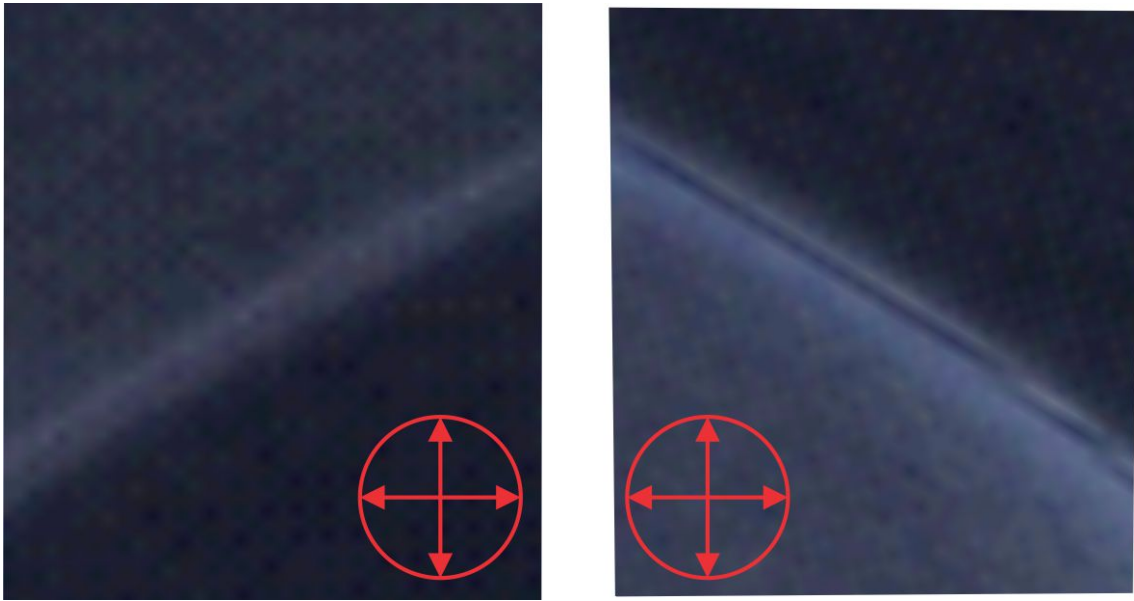
Figure 4.4: Variation in optical contrast of HAN layer on the sample rotation between cross-polarisers.

Fig. 4.3 (b) shows an optical micrograph of the nematic liquid crystal device under plane-polarised light. We have introduced a slight tilt to the device to provide optical contrast so that the two HAN domains are distinct in the micrograph. The HAN(/) domain covers the area in the top left half of the image, and the HAN(\) domain covers the area in the bottom right half of the image. Tilting the device further and rotating the device between crossed polarisers enabled the identification of these states (fig.4.4). The HAN(/) and HAN(\) opposing tilt domains were separated by a domain wall, visible as the light coloured diagonal line in the micrograph. The electrodes, visible as dark vertical bands in Fig. 4.3 (b) and depicted by the filled rectangles in Fig. 4.3 (a), were all held at earth potential and so they did not exert any influence over the position and orientation of the domain wall. Therefore, the actual position of the domain wall only depends on the x position of the zy cross-section taken through the layer in Fig. 4.3 (b). Our stable two-domain structure and diagonal domain wall geometry was intentionally achieved by careful placement of the

homeotropic (Teflon AF) treated PET spacers, exploiting the fact that defects naturally occur at the corners of a laterally confined nematic layer and can provide defect line pinning points [103].

Once desired HAN domains are formed in the cell, we then applied an A.C. voltage of 12.0 V to alternate electrodes. This started a dynamic evolution process, in which the domain wall was distorting in shape and continuously extending in length as a function of time. The wall shape became increasingly crenulated, due to the dominant growth direction along the edges of the electrodes, forming an array of roughly parallel fingers of each domain encroaching into the region previously occupied by the other domain. After 40 s the applied voltage was abruptly reduced to V_C= 5.7 V. The step down to this critical stabilising voltage V_C arrests any dynamic changes of the domain structures, halting significant domain wall movement. The resulting stationary optical texture of the nematic layer is shown in the micrograph in Fig. 4.5 (b), in which the inter-penetrating HAN(\) and HAN(/) regions have become intercalated, separated by a tortuous domain wall.
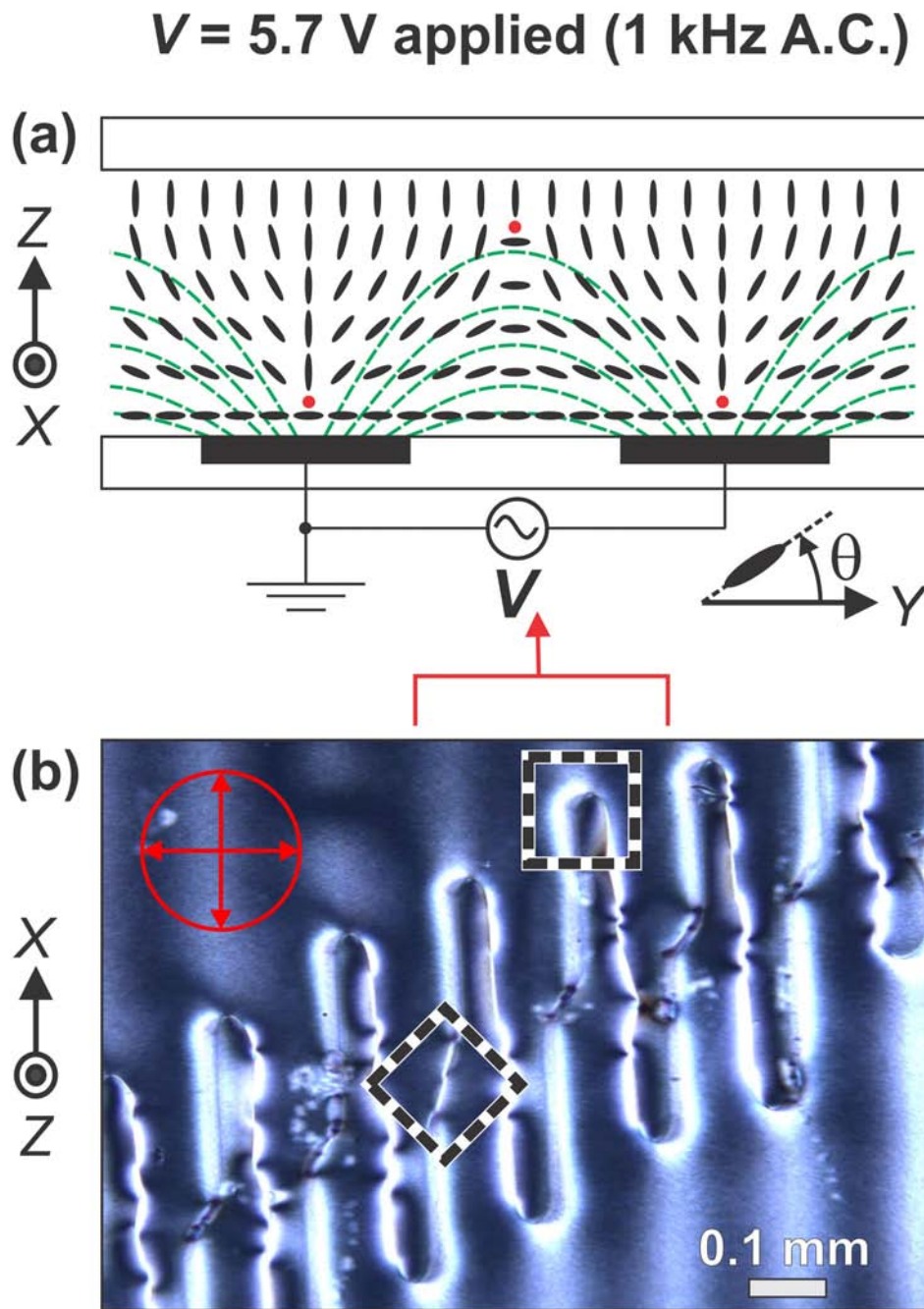
Figure 4.5: The nematic layer under an applied voltage V, producing electrical confinement: (a) Illustrating the nematic n-director configuration with the domain wall moved into the gap region between the electrodes, (b) The optical micrograph shows that electrical confinement has produced a tortuous domain wall shape with intercalated electric field distorted HAN(/) and HAN(\) regions. The crossed polariser and analyser orientations are shown by the arrows in the circle on the micrographs

Fig. 4.5 (a) illustrates how electrical confinement of the nematic n-director can give rise to this alternating arrangement of opposite tilt domains in the intercalation region. The dashed green lines show the electric fields when a voltage is applied to the electrodes. The nematic material, E1, has a positive dielectric anisotropy and so electrostatic forces act to align the n-director orientation parallel to the local electric field direction. The tilt orientation of the HAN(/) state is commensurate with the direction of the electric field on the right-hand edge of the electrode so this grows along that side at the expense of the HAN(\) state which is commensurate with the direction of the electric field on the left-hand electrode edge. The walls between the resultant electric field distorted HAN domains are shown in the centre of the electrode (HAN(\)-HAN(/)) and in the centre of the gap (HAN(/)-HAN(\)) in Fig. 4.5 (a). In the micrograph of the actual device in Fig. 4.5 (b) the walls are observed to run along the sides of the electrode, just inside the cell gap, with a *"kink"* in the wall connecting across the centre of the electrode gap, highlighted in the figure by the dashed diamond. The domain wall crosses each electrode with a high curvature cusp at the tip of each inter-penetrating finger-shaped domain, highlighted in the dashed square in Fig. 4.5 (b). The orientation of the diagonal domain wall before the voltage was applied drives an asymmetry in shape about x at the tip of each finger. This zero voltage diagonal domain wall between the HAN(/) and HAN(\) alignment states is labelled in Fig. 4.3 (b).

When the applied voltage was removed from the device, and all electrodes were held at the same earth potential, the optical texture was found to revert back to the state shown in Fig. 4.3 (b). With no electric field, the inter-penetrating finger-shaped domain, highlighted in the dashed square in Fig. 4.5 (b) retracted, and the domain wall distortion relaxed. After a period of time (of order 80 s) the domain structure returned back to the zero voltage equilibrium arrangement of Fig. 4.3 (b), in which opposite tilt domains were separated by

an undistorted diagonal wall. This undistorted diagonal wall can be seen as a bright line

in Fig.4.3 (b) trapped between two optically distinct domains. The domain wall contains

elastic energy due to the spatial distortion of the n-director as well as energy associated

with a reduction in nematic order at the core of the topological defect. Hence in the

absence of an applied voltage, the system returns to the state where the length of the

domain wall is minimised by being substantially straight.

4.3.2 Frequency dependant response of hybrid nematic layer.
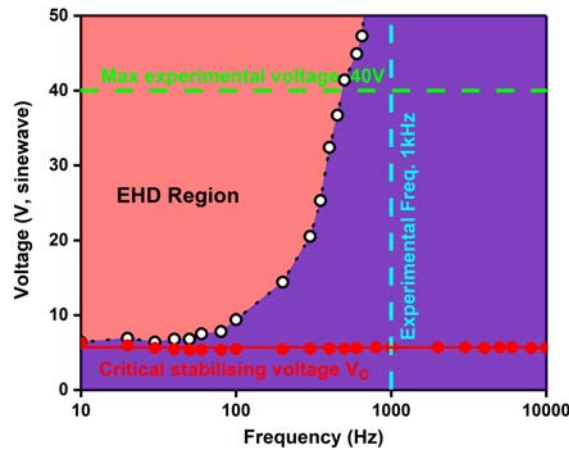
Figure 4.6: An A.C. sinewave voltage V was applied between adjacent interdigital electrodes on the lower bounding substrate of the nematic layer. At a critical stabilising voltage, $V = V_C$, the domain wall movement was halted, and the prevailing domain structure was held static. The filled red circles show the variation of the value of V_C with the sinewave voltage frequency. On the same plot, the open black circles show the frequency variation of the minimum voltage at which the onset of electrohydrodynamic convection occurs. The red region shows the frequency-voltage regime within which electrohydrodynamic (EHD) convection is observed in the layer. The solid line and the dotted line are guides for the eye and dashed blue and green line represents frequency and maximum voltage used in defect line movement experiments.

As discussed in Section 4.3.1, applying an A.C. sinewave (1 kHz) voltage V that is equal to the critical stabilising voltage V_C arrests the motion of the dynamically changing domain structures and halts any further significant domain wall movement whilst the voltage is being applied. However, for certain combinations of voltage and frequency values electrohydrodynamic effect (EHD) might occur in the system leading to deviation of the system from the above behaviour. To separate out EHD effect from those reported in our studies frequency dependant response of hydrid nematic layer was studied. The frequency-dependent value of the critical stabilising voltage is shown by the solid red circles in Fig. 4.6. To within experimental scatter of ±0.2 V, the value of V_C remains constant over the frequency range f = 40 Hz to 10,000 Hz. However, for frequencies below 40 Hz the value of V_C increases, and this rise becomes more prominent as the frequency is further lowered to 10 Hz. This increase can be attributed to ionic migration and shielding effects that have been previously observed in nematic devices with interdigital electrodes [104]. At low frequencies, we also observe another effect related to the finite resistivity of the nematic liquid crystal, electrohydrodynamic convection [22, 105]. In our device, electrohydrodynamic convection produces periodic circulating flow motion of the nematic liquid crystal in the *y*-direction, perpendicular to the electrode stripes. The frequency-voltage regime in which electrohydrodynamic convection occurs is indicated by red region in Fig. 4.6. The open circles indicate the minimum A.C. voltage for onset of the instability at different frequencies, which exhibits a sharp increase as a function of the frequency which is a characteristic of the phenomenon [22, 105]. Figure 4.7 demonstrates the effect that this flow produces on the periodic motion of a single polymer microsphere of diameter 5.0 ± 0.1 μm. This micro particle is contained within the nematic carrier fluid in a region of the device that is well away from any domain walls. In figure 4.7 be-

low time sequence from 20 second videos of the device under plane-polarised light with a crossed analyser are shown for an applied A.C. sinewave voltage of 15 V, for each of three different frequencies. At 10 Hz (fig. 4.7 a) the micro particle executes periodic harmonic motion in a direction perpendicular to the electrodes, since 15 V and 10 Hz is well into the electrohydrodynamic convection regime indicated in Fig. 4.6. At 200 Hz (fig. 4.7 b) the micro particle executes slow periodic harmonic motion perpendicular to the electrodes, where 15 V and 200 Hz is just into the electrohydrodynamic convection regime indicated in Fig. 4.6. At 1 kHz (fig. 4.7 c) the particle remains stationary since there is no electrohydrodynamic convection. Please note we do not observe any electrohydrodynamic convection at the frequency of 1 kHz and the voltages up to 40 V (A.C. sinewave) that we use in all of our domain wall evolution and micro cargo transport experiments reported in the remainder of this chapter.
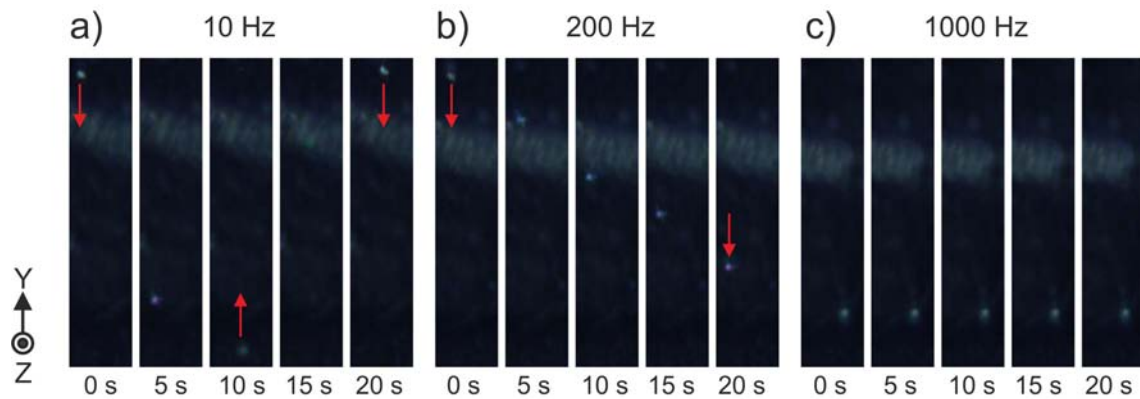
Figure 4.7: Electrohydrodynamic (EHD) convection effect on the motion of single colloidal particle contained in nematic bulk when an A.C. sinewave voltage 15 V is applied to the device at different frequencies a) 10 Hz, b) 200 Hz and, c) 1000 Hz (1kHz). Please note the motion of the particle is perpendicular to the length of electrodes.

4.3.3 Dynamical properties of the topological defect line

In this section, we will describe the results of the study of the voltage dependence of the linear motion of the tip of a finger-shaped HAN domain that was produced by electrical confinement. The domain texture shown in Fig. 4.5 (b) was used as the starting point for each different applied voltage used in the study. This texture was reproducibly re-established after each voltage measurement using the steps described in Section 4.3.1, i.e. first allowing the domain wall to relax back to its zero voltage equilibrium arrangement, then applying 12 V for 40 s, and then abruptly changing the voltage to $V_C = 5.7$ V to stabilise and immobilise the texture. This resetting procedure created the required high curvature cusp, as highlighted in the dashed square in Fig. 4.5 (b), enabling the investigation of both retraction and growth of the intercalated domain structure, and allowing quantitative comparison between the tip translation recorded at different voltages.

The time-dependent position of the domain tip (dashed box in Fig. 4.5 (b)) was measured from videos of the nematic layer between cross polarisers under a polarising optical microscope. The voltage-controlled domain tip movement was in the *x*-direction, orthogonal to the direction of the electric fields produced by the interdigital electrodes. The time when the applied voltage was abruptly changed from the critical stabilising voltage $V_C = 5.7$ V to a new voltage V was taken as t = 0 s. The distance moved by the tip in the *x*-direction from its position at t = 0 s is plotted in Fig. 4.8a, with data shown for a range of applied voltages, between $V = 0$ and $V = 40$ V (R.M.S., 1 kHz, A.C. sinewave). Fig. 4.8c shows orthogonal view of the tip of a finger shaped domain wall moving at different speeds at three different applied voltages, in the negative *x* direction at 0 V, held static at $V = V_C$, and, at a higher velocity in the positive *x* direction at 15 V.
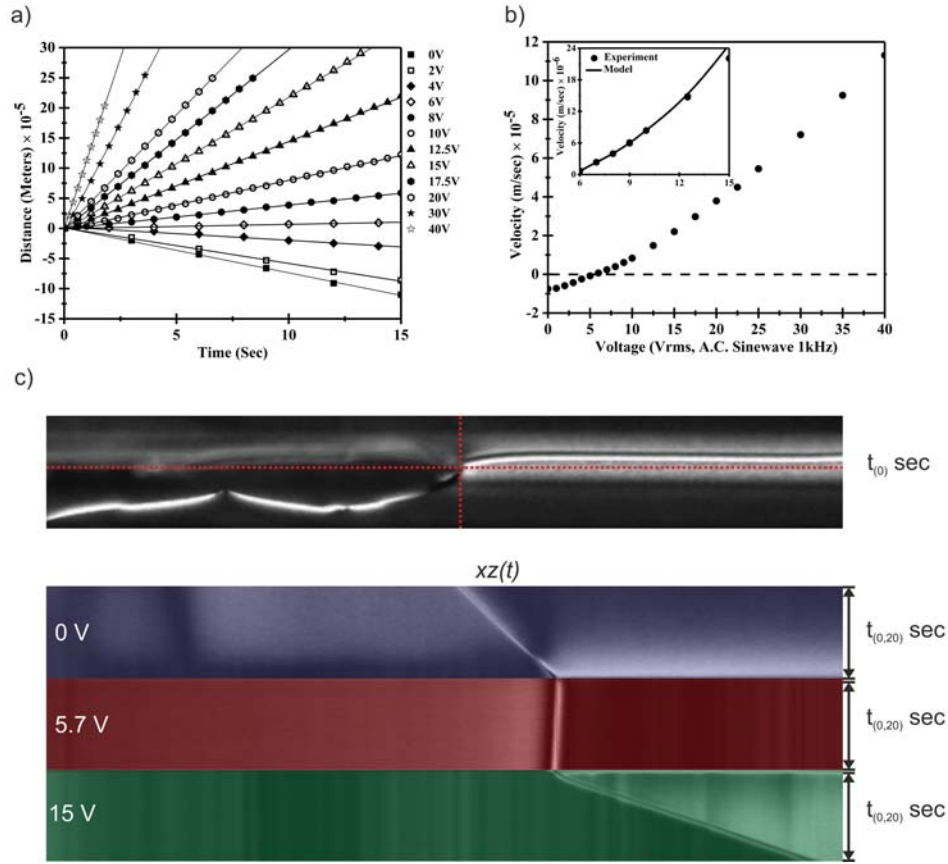
Figure 4.8: (a) The distance moved versus time by the tip of a finger-shaped electrically confined domain in the *x*-direction for a range of applied different voltages. Linear fits to the data, shown by the solid lines, show that the tip moves at a constant velocity. (b) The velocity versus voltage for the movement of the tip obtained from linear fits to the distance versus time data. The inset shows a theoretical model (please see section 4.3.4) fit to the data for low tip movement velocities.(c) Orthogonal view montage of time sequence image of defect line showing distance moved by the tip of a finger-shaped electrically confined domain (tracked tip region is highlighted by intersection region of the dashed red line) in the $\pm x$-direction over a time duration of 20 s for different voltages. Highlighted Blue (Note: vertically flipped image in representation), red and green colour in the figure represent the different voltages $\Delta V = V - V_C < 0$, $\Delta V = V - V_C = 0$ and, $\Delta V = V - V_C > 0$ respectively.

The data taken at all of the different voltages exhibit a linear dependence of the distance on the time, demonstrated by the solid straight-line regression fits through each set of data points in Fig. 4.8a. A negative gradient is found for applied voltages below V_C, with the data for $V = 0$ V showing the most negative gradient and the highest negative velocity. As described in Section 4.3.1, the energy of elastic distortion around the domain wall and the energy cost of the defect line within the wall leads to a torque that acts to straighten the wall and retract the intercalated domains, pulling the tip in the negative direction when the electric field confinement is removed. The gradient increases monotonically as the voltage is increased, changing from negative to just positive when $V = 6.0$ V. This increase results from the torque on the nematic n-director due to electrical confinement becoming increasingly dominant at higher voltages over the torque that acts to straighten the domain wall, creating in a more tortuous domain wall shape at higher voltages with a faster positive movement of the tip of the penetrating electrically confined domain. Fig. 4.8b shows the velocity versus voltage dependences for the movement of the tip obtained from linear fits to the distance versus time data. The velocity increases monotonically in the voltage range from $V = 0$ V to $V = 40$ V and exhibits a super linear dependence on voltage. The inset shows a theoretical fit to the data for low tip movement velocities, which will be discussed in Section 4.3.4. Hence the key observations are that the electric field constrained domain tip is held stationary at a critical stabilising voltage $V_C = 5.7$ V, it moves with a constant velocity along a line in the negative x-direction under a lower applied voltage $\Delta V = V - V_C < 0$, and it moves with a constant velocity in the positive x-direction under a higher voltage when $\Delta V = V - V_C > 0$, where $|\Delta V|$ determines the velocity in the range -7.5×10^{-6} ms^{-1} to 113×10^{6} ms^{-1}. The tip can, therefore, be moved and positioned on demand, controlled by the magnitude of the applied voltage.

Further to the observation mentioned above we also note that the quality of fit between the experimental results and theoretical model (please see section 4.3.4) in the inset velocity versus voltage graph in Fig. 4.8b deteriorates at higher voltages. This is because above 12 V the highly distorted regions localised around the defects embedded in the domain wall move closer to the substrates and our model that neglects the z-direction cannot describe this process. To demonstrate the movement of defect line in bulk of the nematic layer optical micrographs of the high curvature tip of the electrically confined finger shaped domain at different voltages was captured at two different points of focus of a $50\times$ microscope objective shown in fig.4.9. In Fig. 4.9a the point of focus was close to the upper substrate near to the top of the layer, i.e. $z = d$, whilst in Fig. 4.9b the position of focus was close to the lower substrate, i.e. $z = 0$. The domain wall containing the disclination line can be seen in the images as the "C-shaped" cusp in the centre of the images with the cusp point towards the left-hand side of the images. The images of the defect lines with applied voltages of 10 V, 12 V and 15 V (R.M.S. amplitude of A.C. sinewave voltage at 1 kHz) are sharper when the point focus towards the top of the nematic layer (Fig. 4.9a) compared to when the point of focus is towards the bottom of the nematic layer (Fig. 4.9b). The images of the disclination line are in sharpest focus with an applied voltage of 15 V with the focus towards the top of the layer (Fig. 4.9a), demonstrating that the disclination line moves towards the upper surface as the voltage is increased in the system.
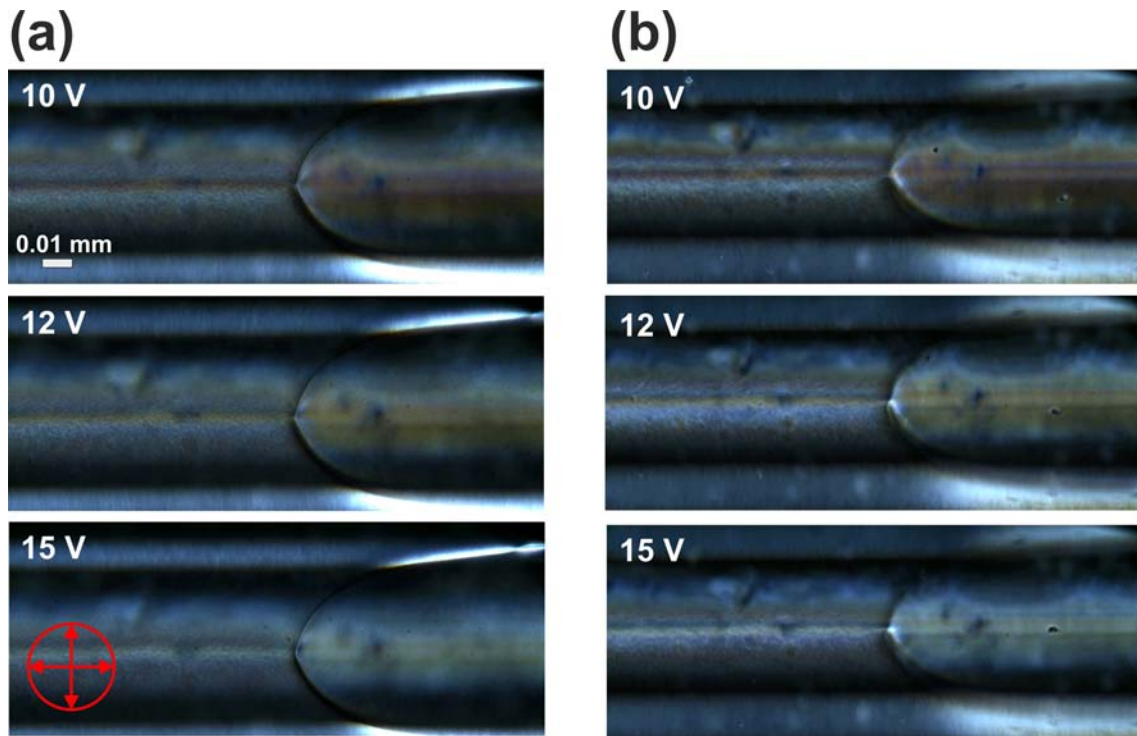
Figure 4.9: The Polarising optical micrographs of the high curvature tip of the electrically confined finger shaped domain at different applied voltages with two different points of focus of a 50x microscope objective. The device was orientated with the electrodes (along the x-direction) running horizontally. The nematic layer (thickness $d = 13$ μm) was examined in transmission under white light illumination between crossed polarisers with the polariser orientated horizontally and the analyser vertically. The images in (a) were taken with point of focus close to the upper substrate at the top of the layer, i.e. $z = d$, whilst in (b) the vertical position of the device was moved closer to the objective to image through the layer with the position of focus close to the lower substrate, i.e. $z = 0$. The x, y and z coordinates with respect to the layer are defined in Fig. 4.1 of the chapter.

4.3.4 Theoretical Model for topological defect line growth

A nematic continuum theory-based dynamic model was developed by our collaborator Professor Nigel Mottram (Nigel.Mottram@glasgow.ac.uk) which reproduces all of the key features of electrically confined domain evolution that have been observed in the experiments. The orientation of the nematic n-director was described by a tilt angle $\theta(x,y,z,t)$ relative to the y direction, and a nematic director of the form $n = (0, \cos\theta, \sin\theta)$. The HAN alignment states were then described by a linear variation of the tilt angle in the z-direction,

$$\theta(x,y,z,t) = \left(\theta_o(x,y,t) + \left(\frac{\pi}{2} - \theta_o(x,y,t)\right)\frac{z}{d}\right) \tag{4.1}$$

which corresponds to the situation with strong elastic effects in the single elastic constant approximation, $K = K_{11} = K_{22} = K_{33}$. This method of prescribing a z-dependence of the tilt angle enables a two-dimensional model to be created. The key physical contributions to the energy of the system will originate from elasticity (E_f), the electric polarisation of the nematic n director (E_e), and the surface alignment anchoring (E_a), and will now be considered in turn. The Frank elastic energy E_f is given by,

$$E_f = \int_0^L \int_0^{2\pi n/\lambda} \int_0^d \frac{K}{d}\left(\left(\frac{\partial\theta}{\partial x}\right)^2 + \left(\frac{\partial\theta}{\partial y}\right)^2 + \left(\frac{\partial\theta}{\partial z}\right)^2\right) dz\,dy\,dx \tag{4.2}$$

The integration from $z = 0$ to $z = d$ in Eq. 4.2 can be performed after substitution of Eq. 4.1. The x-extent of the cell is taken to be $0 \leq x \leq L$, and the y-integration is over an integer n number of periods of the electrode pitch $\lambda = w_e + w_g$ The periodic electric field produced by the interdigital electrodes is modelled by the function

$$\mathbf{E} = E(y,z)\left(0, \cos\left(\frac{\pi}{2} - \frac{\pi}{\lambda}y\right), \sin\left(\frac{\pi}{2} - \frac{\pi}{\lambda}y\right)\right) \tag{4.3}$$

which describes an electric field direction that is a function of y only, and a field strength that $E(y,z)$ decays into the cell in the z-direction with the y-periodicity imposed by the electrodes. The electrostatic energy E_e is then simplified through integration in the z-direction to give

$$E_e = -\int_0^L \int_0^{\frac{2\pi n}{\lambda}} \int_0^d \frac{\varepsilon_o \Delta\varepsilon}{2}(\mathbf{E}\cdot\mathbf{n})^2 \, dz dy dx = -\int_0^L \int_0^{\frac{2\pi n}{\lambda}} \frac{\varepsilon_o \Delta\varepsilon d}{2} E(y)^2 \sin^2\left(\theta_m + \frac{\pi}{\lambda}y\right) dy dx, \tag{4.4}$$

where $\theta_m(x,y,t)$ is the tilt angle of the director in the middle of the cell, at $z = d/2$, so that $\theta_m = ((\pi/4) + (\theta_o/2))$ rad

Assuming that the electric field reorientation is stronger closest to the electrodes, we include a surface energy effect only at the lower surface, so that the surface energy is

$$E_a = \int_0^L \int_0^{2\pi n/\lambda} \frac{W_0}{2}\sin^2(\theta_o) dy dx, \tag{4.5}$$

where the lower surface anchoring strength, W_0, expresses the amount of energy required to break the lower surface planar anchoring to transform from a HAN(\\) to a HAN(/) state.

The rate of dissipation due to n-director rotation, parameterised by a phenomenological viscosity γ that is related to the nematic rotational viscosity, γ_1, is

$$D = -\int_0^L \int_0^{2\pi n/\lambda} \int_0^d \gamma\left(\frac{\partial\theta}{\partial x}\right)^2 dz dy dx = -\int_0^L \int_0^{2\pi n/\lambda} \frac{\gamma d}{3}\left(\frac{\partial\theta_o}{\partial x}\right)^2 dy dx. \tag{4.6}$$

The Rayleigh dissipation principle and the above equations and definitions are then used to derive the governing equation for the tilt angle of the director in the middle of the cell, namely

$$\frac{2\gamma d}{3}\frac{\partial \theta_m}{\partial t} = K\left(\frac{2d}{3}\left(\frac{\partial^2 \theta_m}{\partial x^2} + \frac{\partial^2 \theta_m}{\partial y^2}\right) + \frac{(\pi - 2\theta_m)}{d}\right) + \frac{W_0}{2}\sin(4\theta_m) - \frac{\varepsilon_0 \Delta \varepsilon}{2}E(y)^2 \sin$$

$$\left(2\left(\theta_m + \frac{\pi}{\lambda}y\right)\right).(4.7)$$

We have then used Equation 4.7 to model spatial variations of the mid-layer tilt angle $\theta_m(x,y,t)$ in the xy plane, as a function of time, to provide a description of the dynamic evolution of the domain wall shape. The electric field $E(y)$ was prescribed using numerical finite element simulations [106]. With no applied voltage, and well away from the distortion associated with a domain wall, hybrid alignment leads to two stable orthogonal mid-layer tilt directions at equilibrium, $\theta_{me} = (\pi/4)$ rad for the HAN(/) alignment state and $\theta_{me} = (3\pi/4)$ rad for the HAN(\) alignment state.
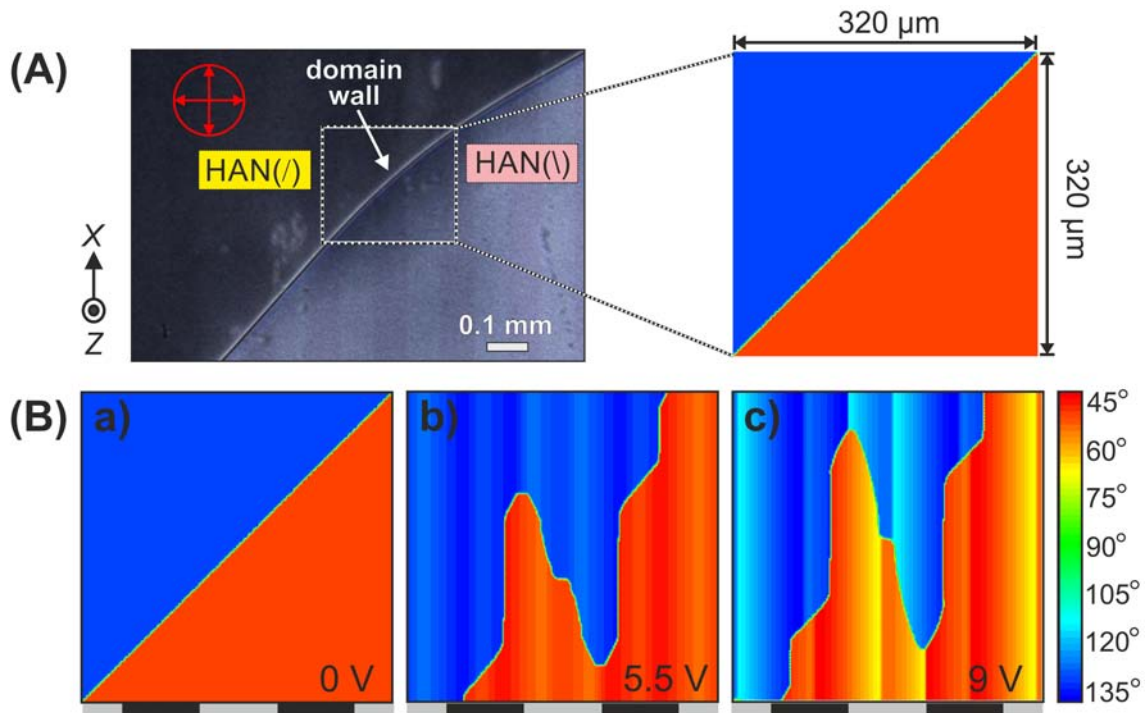
Figure 4.10: (A) Optical micrograph showing area of the device modelled in the theoretical model (highlighted in figure by dashed box). (B) Numerical simulations of the time evolution of the domain wall (solid line) between two opposing HAN domains under the application of different voltages. The colours indicate the value of the tilt angle of the director in the middle of the cell, where $\theta_m(x,y,t)$, according to the legend given to the right of the figure. Black and grey colour bands shown below each image represents electrodes (black) and electrode gap (grey) regions. (a) Zero volt equilibrium state. (b) The static distorted static domain wall shape obtained after a period of dynamic deformation with 9 V applied, followed by abruptly changing the voltage to 5.5 V which arrested the dynamic domain evolution. This shows a close resemblance to the experimental domain wall texture in Fig. 4.5 (b). (c) A snapshot of the domain wall during dynamic extension after voltage had been again increased to 9 V.

Dynamic simulations result produced by solving Equation 4.7 are shown in Fig. 4.10. Time-dependent solutions for $\theta_m(x, y, t)$ were produced with the aid of a commercial finite element partial differential equation solver [106] using the following parameters: $\gamma = 2.49$ Nsm^2; $W_0 = 55 \times 10^{-5}$ Jm^{-2}; $d = 13 \times 10^{-6}$ m; $K = 7.5 \times 10^{-12}$ N; $\Delta\varepsilon = 12.3$; and $\lambda = 160 \times 10^{-6}$ m. The colours indicate in figure 4.10 indicate the value of the tilt angle of the director in the middle of the cell, $\theta_m(x, y, t)$, as a function of position.

The boundary conditions ($\theta_m = (\pi/4)$ rad for HAN(/), and $\theta_m = (3\pi/4)$ rad for HAN(\)) were selected to produce a diagonal domain wall separating two opposing HAN states as the initial zero voltage equilibrium state in the simulation, shown in Fig. 4.10 (B)a. This emulated the experimental situation previously shown in the optical micrograph in Fig. 4.3(b). Voltages were then applied in the simulation as in a similar sequence to that described at the beginning of Section 4.3.3, i.e. 9 V for 16.8 s, followed by changing the voltage to $V_c = 5.5$ V for 16.8 s. The value of the energy barrier W_0 was adjusted to ensure that the value of the critical stabilising voltage (V_C) in the model 5.5 V was close to the value of V_C found in the experiments. This procedure resulted in the static domain wall structure shown in Fig. 4.10 (B)b, which reproduces all the key features observed experimentally in the optical micrograph in Figure 4.5b, including the kink (highlighted by dashed diamond box in 4.5b) across the region between electrodes, and the tips of the finger shaped domains where the domain wall crosses above the electrodes. The voltage in the simulation was increased back to 9 V which caused the tip regions to move again in the x-direction. This was accompanied by further domain wall deformation and encroachment of the electrically confined finger shaped domains into the regions initially occupied by the oppositely tilted HAN domain. Fig. 4.10 (B)c shows a snapshot of the domain wall during this dynamic extension process.

The inset velocity versus voltage graph in Fig. 4.8b demonstrates an excellent fit between the theoretical model and the experiment results at low voltages when $V \geq V_C$, using only the values of γ and W in equation.4.7. as the adjustable fitting parameters. The quality of fit deteriorates at higher voltages, above 12 V, where the highly distorted regions localised around the defects embedded in the domain wall move closer to the substrates (see also section 3.3 fig.4.9). This cannot be described in our model that neglects the z-direction. Hence, it's reasonable to say that the model reproduces a critical stabilising voltage, it also quantitatively describes the observed linear distance versus time behaviour and super-linear voltage dependence of the velocity for applied voltages immediately above this value, and also accurately reproduces the observed domain structures and domain wall shapes.

4.3.5 Effect of disclination line tension on dynamical properties of the topological defect line

So far in this chapter, we have only discussed the dynamical properties of defect line growth for a single length of disclination line which is re-established for each voltage measurement using the steps described in section 4.3.1 and section 4.3.3. In this section, we will investigate the effect of defect line tension on dynamical properties. As explained before domain wall contains elastic energy due to the spatial distortion of the n-director as well as energy associated with a reduction in nematic order at the core of the topological defect. Hence increasing or decreasing the length of the domain wall will lead to different tension in the defect line which can significantly affect the dynamics of the system. To investigate this effect, we studied dynamical properties of three different textures of domains walls formed between two distinct hybrid aligned nematic domains: (a) partially stretched domain wall which is attained by following the same steps mentioned above in section 4.3.1. (b) stretched out domain wall which is attained by increasing the time duration of the voltage applied in case of (a), (c) closed loop domain wall which was attained by stabilising the defect loops annealing in the device. Please note closed loop domain wall was not usually observed in the system, however, at some instances defect line get stuck to the dust in the sample during growth studies leading to the formation of closed loop domains wall which anneals out in the system without application of any critical voltage in the system.
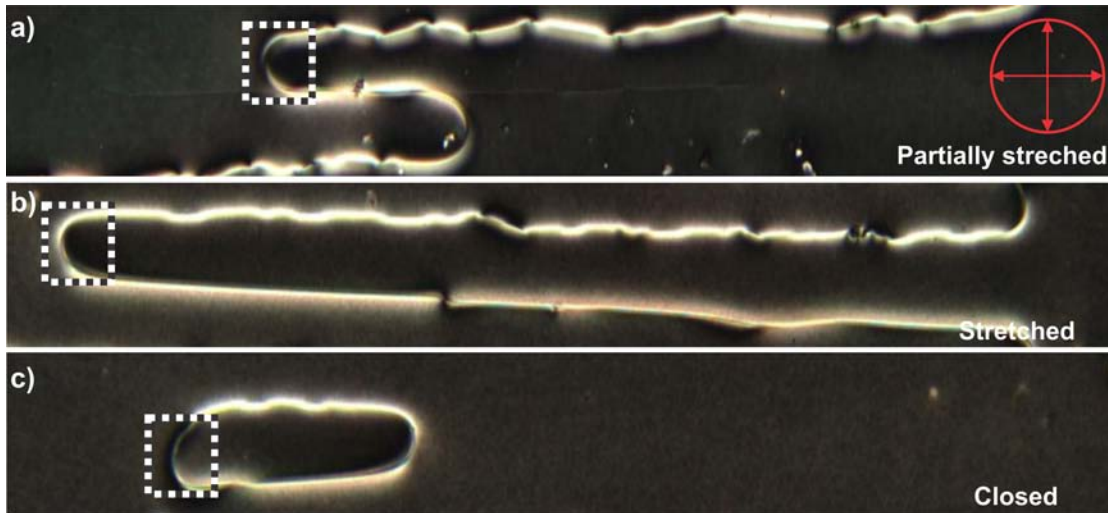
Figure 4.11: Optical micrograph of the actual device under plane-polarised light with a crossed analyser showing two coexisting HAN regions separated by different domain wall textures. Please note sample was not tilted in the above image.

The domain textures shown in Fig. 4.11 was used as the starting point for each different applied voltage used in the study. These textures were reproducibly re-established after each voltage measurement. The time-dependent position of the domain tips (dashed boxes in Fig.4.11) for each domain textures was measured from videos of the nematic layer between cross polarisers under an optical microscope. The voltage-controlled domain tip movement was tracked in the x-direction, orthogonal to the direction of the electric fields produced by the interdigital electrodes. The critical stabilising voltage V_C is found to be the same for these domains textures and time when the applied voltage was abruptly changed from the critical stabilising voltage $V_C = 5.7$ V to a new voltage V was taken as t = 0 s. The distance moved by the tip in the x-direction for three different domain wall textures from its position at t = 0 s is plotted in Fig. 4.12 a-c, with data shown for a range of applied voltages, between $V = 0$ and $V = 40$ V (R.M.S., 1 kHz, A.C. sinewave).
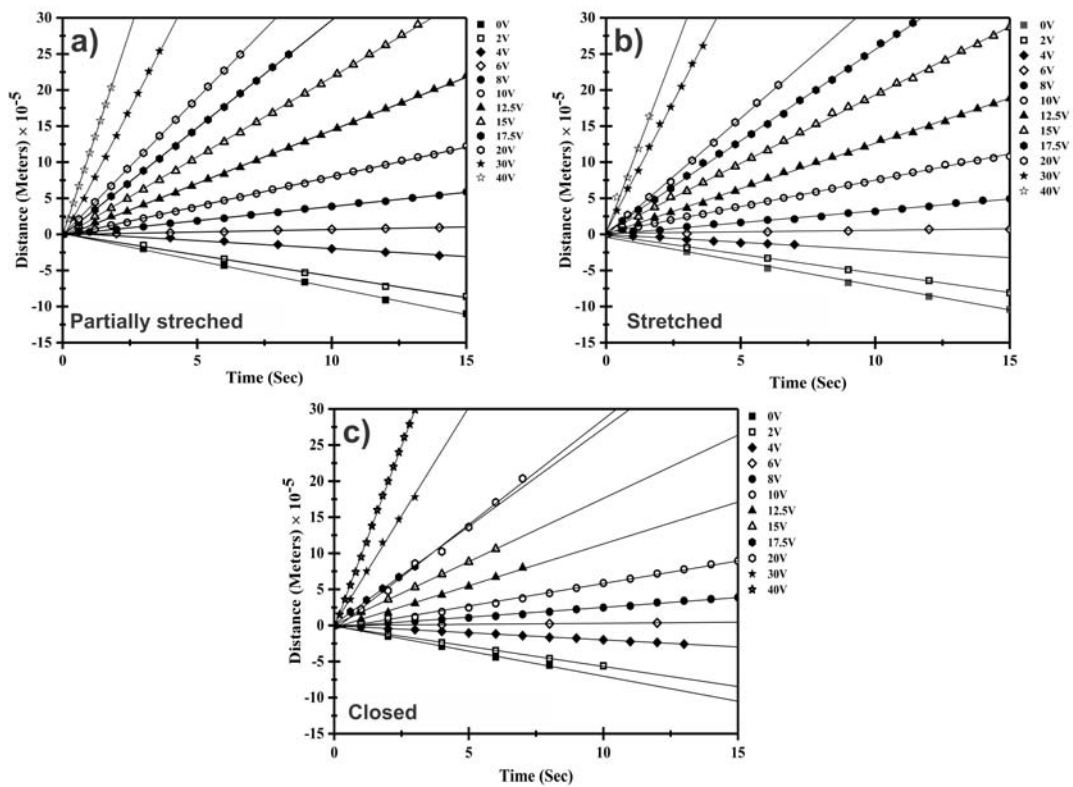
Figure 4.12: The Distance versus time plot showing movement of kink (dashed boxes in Fig.4.11) of different electrically confined domains textures in the *x*-direction for a range of applied different voltages. Linear fits to the data, shown by the solid lines, show that the tip moves at a constant velocity.

The data taken at all of the different voltages for three different domain wall textures exhibit a linear dependence of the distance on the time, demonstrated by the solid straight line regression fits through each set of data points in Fig. 4.12a-c. Fig. 4.13 shows the velocity versus voltage dependences for the movement of the tip. In all the three cases velocity increases monotonically in the voltage range from $V = 0$ V to $V = 40$ V, and exhibits a super linear dependence on voltage. The figure4.13b shows a theoretical fit to the data for low tip movement velocities. Please note our model cannot reproduce closed domain wall textures due to defined boundary conditions so data for the closed

domain wall textures is omitted from the graph. Fig.4.14 shows results from numerical simulations showing different static distorted static domain wall textures obtained after a period of dynamic deformation.
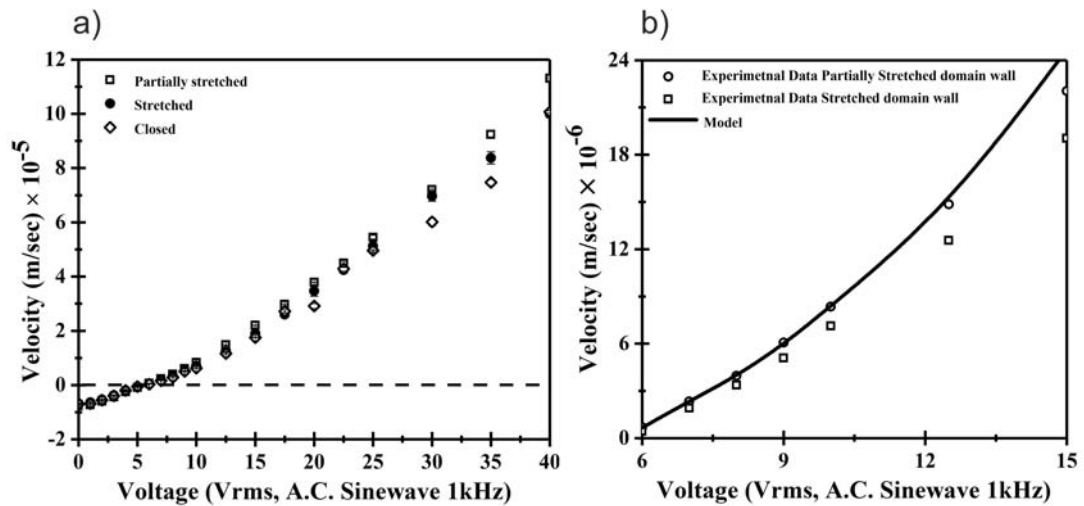
Figure 4.13: (a) The velocity versus voltage plot for the movement of the kink of different domain textures obtained from linear fits to the distance versus time data. (b) Theoretical fit (solid black line) to the data for low tip movement velocities.
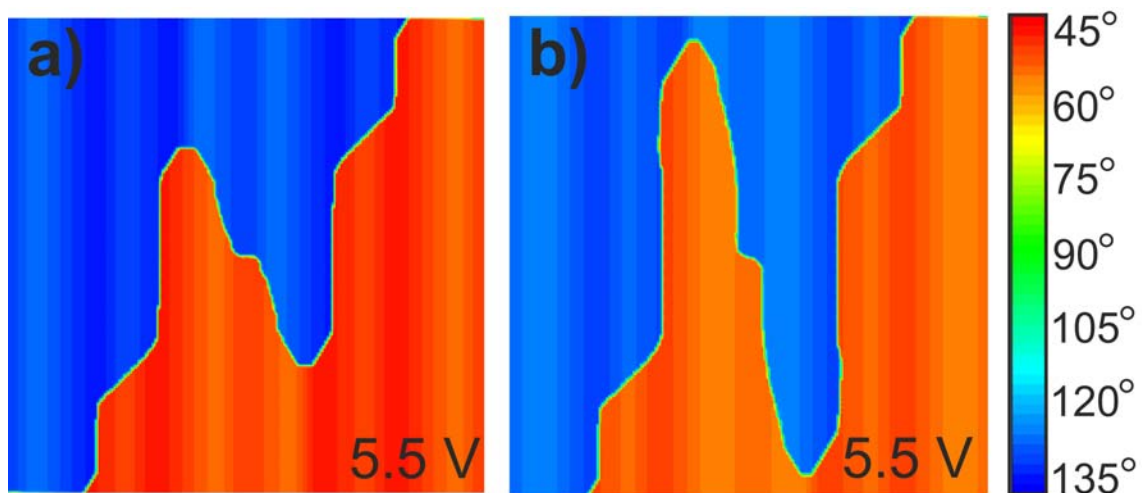
Figure 4.14: Numerical simulations showing different domain wall textures between two opposing HAN domains a) Partially stretched (PS) and, b) Stretched (S) domain wall.

137

The observations from line tension study are that the electric field constrained domain tip of all the domain textures is held stationary at a critical stabilising voltage V_C = 5.7 V, it moves with a constant velocity along a line in the negative x-direction under a lower applied voltage $\Delta V = V - V_C < 0$, and it moves with a constant velocity in the positive x-direction under a higher voltage when $\Delta V = V - V_C > 0$, where $|\Delta V|$ determines the velocity in the range. Therefore, irrespective of domain texture, the tip can be moved and positioned on-demand, controlled by the magnitude of the applied voltage. Please note for all the studies shown in the chapter partially stretched domain wall is used unless specified.

4.3.6 Electrically controlled topological micro-cargo transportation

4.3.6.1 *Levitation and trapping of colloidal particle dispersed in the nematic layer.*
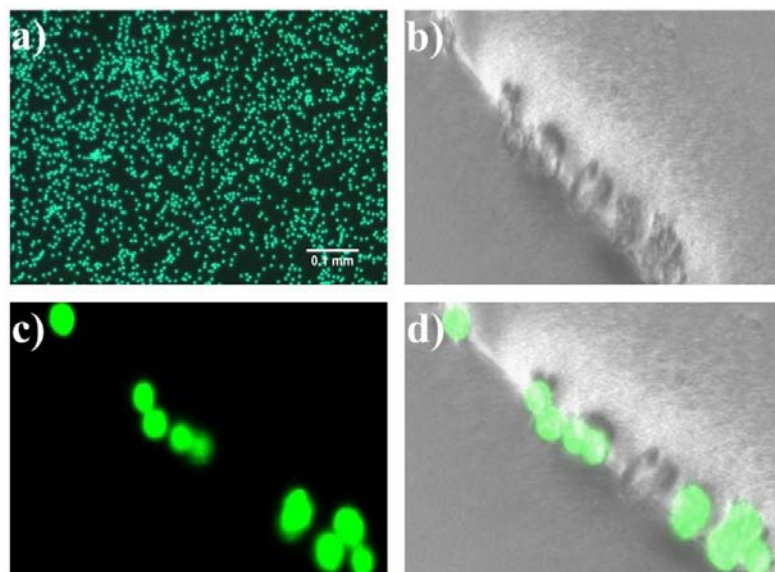
Figure 4.15: Polarising Optical Microscope image of fluorescent particles (5±0.1 μm) under UV illumination (b-d) Confocal images of fluorescent particles trapped in the domain wall in absence of the voltage, b) light field showing trapped particles (grey colour) in domain wall, c) darkfield image showing only trapped particle (green colour) and, d) Superimposed image of particle observed in dark field over light field image.

In the above sections, we have demonstrated how the tip of the defect line can be controlled on demand by simply tuning the voltage in the device. In this section, we will extend this study to develop a lab on a chip-based device capable of transporting microcargo. For this fluorescent polymeric microsphere (fig. 4.15a) of density 1.05 g/cm^3 and diameter 5.0±0.1 μm dispersed within the nematic carrier fluid were used as microcargo in the experiments. These dispersed particles in the vicinity of defect line trap inside the domain wall (Fig.4.15b-d) as a consequence of the systems attempt to minimize the total elastic energy of the nematic layer by removing disclination core [107, 108]. Thus, enabling us to develop a voltage regulated topological defect line based microcargo system. However, for efficient transportation of the cargo its essential to avoid sedimentation of the particle in the bulk. To avoid this problem, prior to the dispersion, particles had been functionalised with trichloro(octyl)silane in the vapor phase to impart homeotropic alignment of E1 at the surface of the particle. The heterogenous alignment on particle and lower substrate was intentionally used in the study to avoid particle sedimentation. Since the particles have homeotropic surface treatment, whilst the lower substrate of our device has a planar nematic alignment, the uniform director field near the wall is incompatible with the director distortions around the sphere. This will lead to an elastic repulsion preventing the particle to settle down in the device. This balance between elastic repulsion from the lower surface and the gravity forces driving sedimentation can be estimated using Equation 4.8 [109].

$$z_{elastic} = \left(\frac{3}{2}A\right)^{1/2} \left(\frac{KR}{g\Delta\rho}\right)^{1/4} \tag{4.8}$$

Where $Z_{elastic}$ represents the equilibrium height of an elastically levitating particle. For parameters of our system (K = 7.5 pN, R = 2.5 μm, $\Delta\rho$ = 40 kg m^{-3}) $z_{elastic}$ is found to be

17 μm. Hence based on the calculation done above elastic forces are more than sufficient

to prevent sedimentation of the particle in our device which has a layer thickness of $d =$

13 μm and so micro particles are located within the layer and away from surfaces.
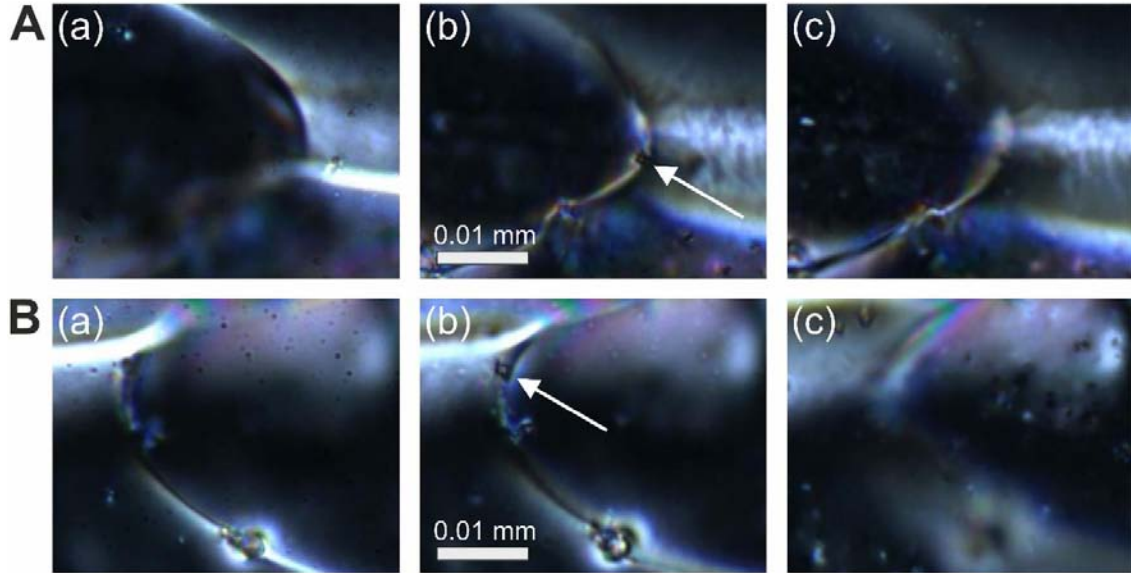
Figure 4.16: Polarising optical micrographs of colloidal particles trapped at the domain

wall between two opposing HAN domains. The wall was held static by applying a voltage

equal to the critical stabilising voltage, $V_C = 5.7$ V. The nematic layer (thickness $d = 13$

μm) was imaged using a 50x microscope objective in transmission under white light

illumination between crossed polarisers with the polariser orientated horizontally and the

analyser vertically. Images were taken at two different positions of the device at different

ends of a finger shaped domain wall. The images (A)(a) and (B)(a) were taken with

the point of focus close to the upper substrate at the top of the layer, i.e. $z = d$. The

vertical position of the device was moved closer to the objective to image through the

layer, bringing the particle within the layer at intermediate focus in (A)(b) and (B)(b), and

with the position of foci close to the lower substrate, i.e. $z = 0$, in (A)(c) and (B)(c).

To ensure this claim we performed an experimental study in which the positions of two different trapped particles was estimated near the high curvature tip of an electrically confined domains which were held stationary with an applied voltage equal to the critical stabilising voltage, V_C = 5.7 V. Fig.4.16 shows micrographs with three different points of focus of the 50x microscope objective. The images in Fig. 4.16A and the images in Fig. 4.16B are of different positions within the experimental device, with the positions of two different in-focus particles are indicated by the white arrows. In Fig. 4.16 A(a) and Fig. 4.16 B(a) the point of focus was close to the upper substrate near to the top of the layer, i.e. $z = d$, whilst in Fig. 4.16 A(c) and Fig. 4.16 B(c) the vertical position of the device was moved closer to the objective to image through the layer so that the position of focus was close to the lower substrate, i.e. $z = 0$. In Fig. 4.16 A(b) and Fig. 4.16 B(b) the vertical position of the device was moved to different points of focus that gave the sharpest images of the particles and that were intermediate between the upper and lower substrate focus points. From the positions of the microscope specimen stages at the different points of focus, we estimate that the centre line of the 5 μm diameter particles were between 4 μm and 5 μm above the lower substrate for the particle in Fig. 4.16.A, and between 9 μm and 10 μm above the lower substrate for the particle in Fig. 4.16B. Thus, the study supports our claim that particle levitates in the nematic bulk, rather than being adhered at any of the bounding surfaces.

4.3.6.2   Microcargo collection and bi-directional transportation in the nematic layer.

So far in the reported studies, we have shown that particle with homeotropic surface treatment levitate in the nematic bulk and get trapped into the domain wall. Now, we will use all these features to demonstrate efficient control over microcargo collection and movement in the nematic layer. Fig.4.17 shows a series of snapshots of the device under a polarising microscope that follows the dynamic process of a moving domain wall interacting with one of the particles, including collection, trapping, and transporting the particle. In Fig. 4.17a, a voltage of 7 V is applied to the device, which is above the critical stabilising voltage, V_C = 5.7 V. This causes the domain wall to elongate, moving in the positive x-direction and also towards the nearest electrode edge in the negative y-direction where it connects with an initially separate micro particle. The microparticle is static under an applied voltage for 12 seconds, up until the point at which the wall and the particle connect, indicating an absence of significant thermally or electrically driven flow in the sample. The applied voltage is then abruptly reduced to 1 V at 14 s, below V_C, which causes the domain wall to retract and move in the negative x direction. Fig. 4.17b. shows how the particle has adhered to the domain wall and moves with the retracting wall, remaining at the high curvature tip as it moves in the negative x-direction. Hence the microsphere has been attracted to and trapped at the region of strong elastic deformation at the domain wall [107, 110]. A Montage time sequence image showing the dynamic process of a moving domain wall interacting with one of the particles, collecting, trapping, and transporting the particle is shown in fig. 4.17.
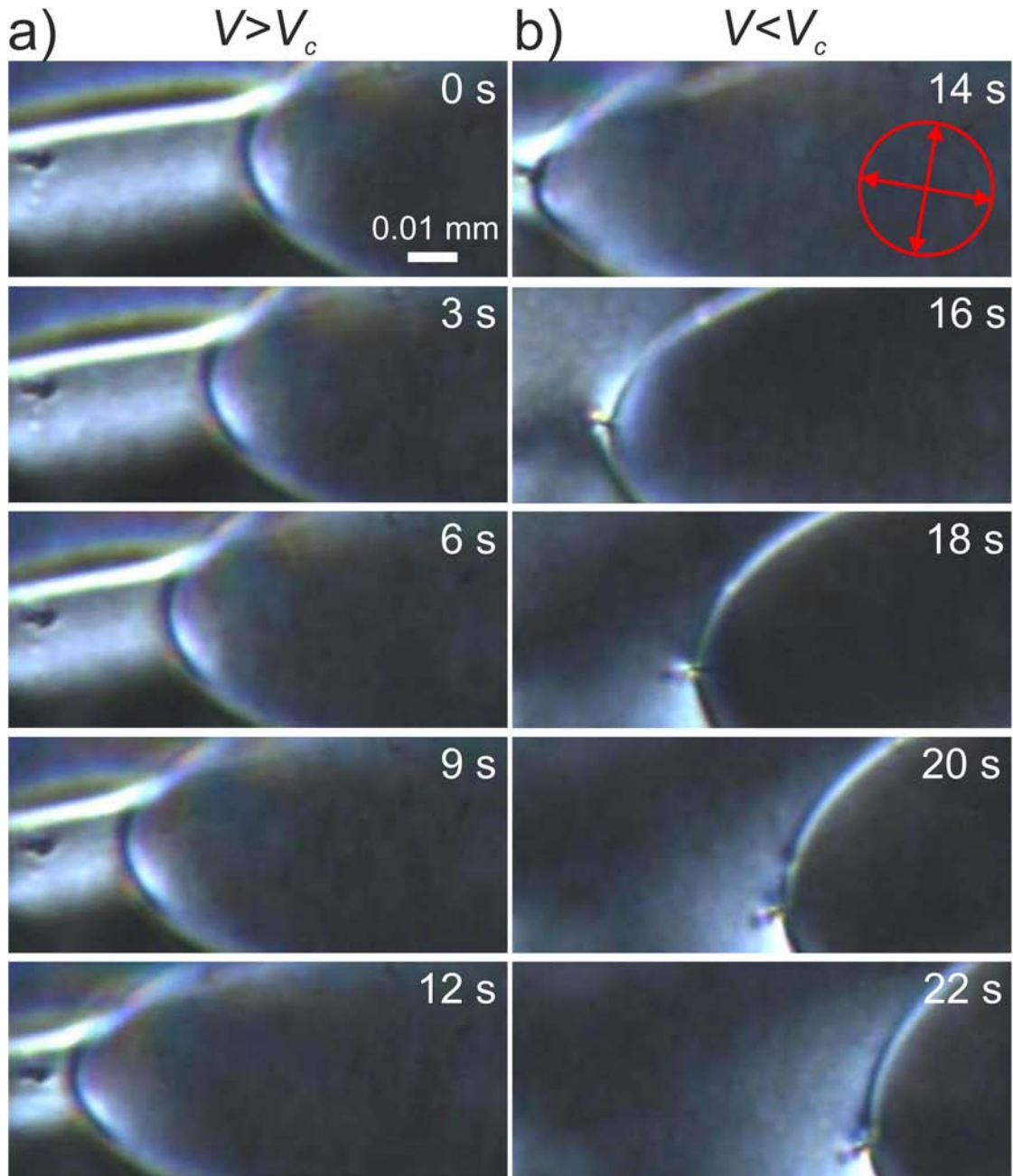
Figure 4.17: Optical micrograph of the nematic layer under plane-polarised light with a spherical micro particle towards the left-hand side of the images. A domain wall is shown trapping and collecting the particle: (a) The wall dynamically extends and moves to the left under applied voltage 7 V, above V_C (where $V_C = 5.7$ V), overlapping the position of the particle. (b) At time 14 s the voltage is abruptly reduced to 1 V, below V_C, and the domain wall retracts whilst transporting the adhered particle at its tip. The crossed polariser and analyser orientations are shown by the arrows in the circle on the micrograph.
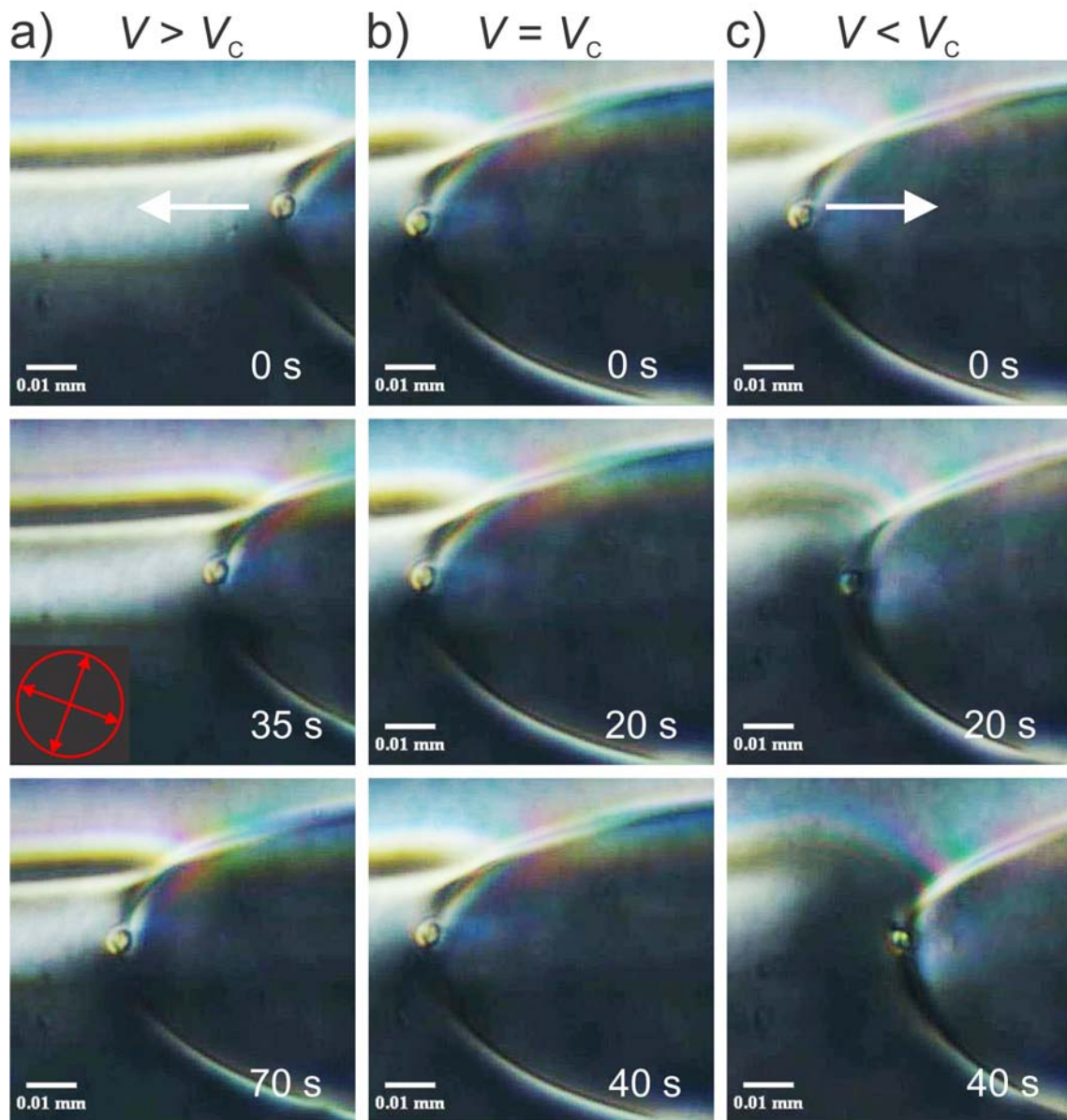
Figure 4.18: Optical micrographs showing transportation of a colloidal micro particle by the high curvature tip of the electrically confined finger shaped domain: (a) The particle was moved in the negative *x*-direction when the applied voltage was 6.5 V, above the critical stabilising voltage $(V > V_C)$, (b) The particle is held stationary when $V = V_C = 5.7$ V, (c) The particle is moved in the positive *x*-direction when the applied voltage was 4 V, below the critical stabilising voltage $(V < V_C)$. The crossed polariser and analyser orientations are shown by the arrows in the circle on the micrograph.

Fig.4.18 shows a series of snapshots of the device under a polarising microscope that follows the dynamic process of a moving domain wall transporting and positioning a micro particle. In Fig. 4.18a the particle was moving in the negative x direction when the applied voltage is 6.5 V, above the critical stabilising voltage V_C, in Fig. 4.18b the particle stopped when the applied voltage was set exactly to $V_C = 5.7$, and in Fig. 4.18c the particle was moving in the positive x direction when the applied voltage was decreased to 4 V. In each case the images show that the particle remained located to the region of the high curvature tip of a finger-shaped electrically confined domain. Hence, voltage control of the distortion and extent of the domain wall using the magnitude of voltage relative to the critical stabilising voltage, $\Delta V = V - V_C$ provides both positive and negative precision bidirectional movement of the micro particle along a line. At any point, setting the voltage abruptly to V_C stops the particle movement and holds the particle at the position that it has reached, providing the capability to reversibly place the trapped micro particle on demand.

4.3.7 Effect of nematic layer thickness on dynamical properties of the topological defect line
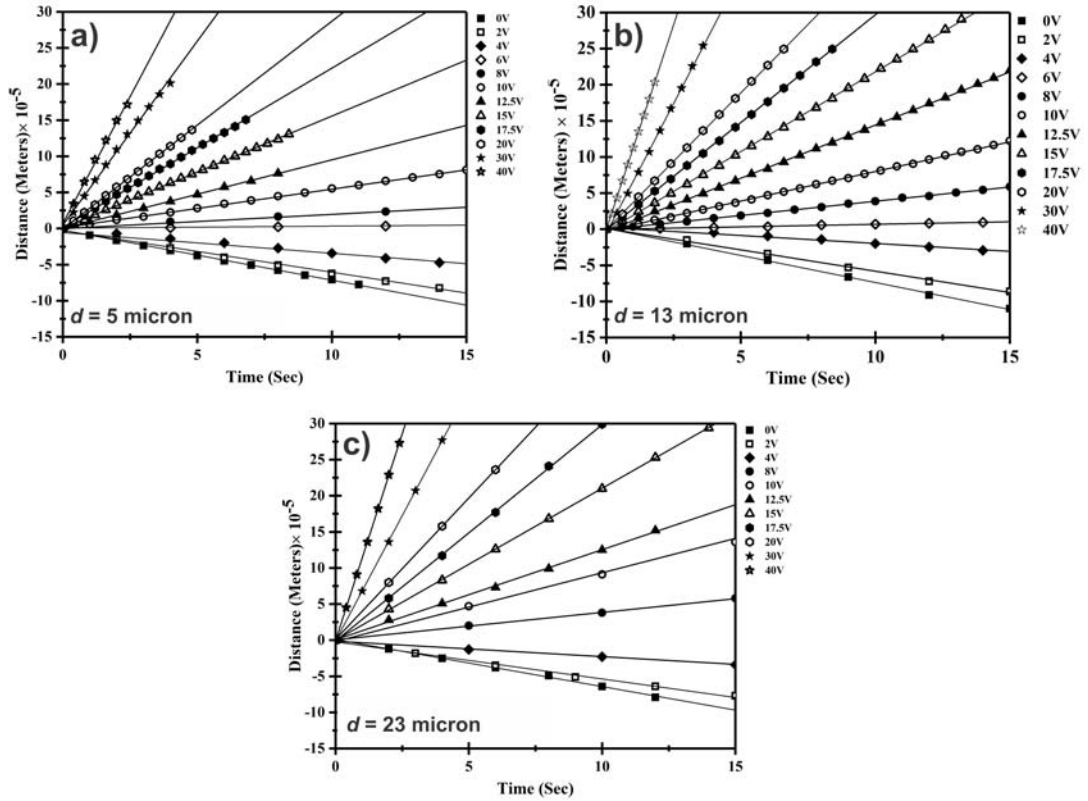
Figure 4.19: The distance moved versus time by the kink of the electrically confined domain wall at different applied voltages for a range of nematic layer thickness a) 5, b) 13 and, c) 23 μm. Linear fits to the data, shown by the solid black line, show that the tip moves at a constant velocity at different voltages.

To investigate the effect of nematic layer thickness (d) on the voltage-dependent linear motion of the tip of the domains wall. A thickness dependent study ($d = 5, 13, and 23$ μm) was performed in the device. The different spacing of nematic layer in the device was attained by using polyethylene terephthalate (PET) strips of varying thicknesses. In all the experiments domain texture shown in Fig. 4.5(b) was used as the starting point of the measurement, like previous experiments this texture was reproducibly re-established

146

after each voltage using the steps described in Section 4.3.1. This helps in the investigation of both retraction and growth of the intercalated domain structure and allows quantitative comparison between the tip translation recorded at different voltages for the selected range of nematic layer thickness. The time-dependent position of the domain tip was measured from videos of the nematic layers ($d = 5, 13, and 23 \ \mu$m) at different voltage values. The distance moved by the tip in the x-direction from its position at $t = 0s$ is plotted in Fig. 4.19, with data shown for a range of applied voltages, between $V = 0$ and $V = 40$ V (R.M.S., 1 kHz, A.C. sinewave) in three different thickness of the device. Experimental results taken at all the different voltages for the selected range of thickness show a linear dependence of the distance on the time, corroborating the observations made in the previous study (section 4.3.3). This linear dependence of domain tip movement is demonstrated by the solid straight-line regression fits through each set of data points in Fig. 4.19a-c. The velocity versus voltage dependence of the movement of the tip of the domain wall for different thickness ($d = 5, 13$ and, $23 \ \mu$m) is shown in Fig. 4.20. Overall, the velocity trend of the domain wall tip in all the three sets ($d = 5, 13,$ and $23 \ \mu$m) exhibits a super linear dependence on voltage in the range from $V = 0$ V to $V = 40$ V, with velocity increasing monotonically with an increase in the voltage values. Whilst the overall trend remained the same, each set of velocity measurements is quite distinct from each other with V_C value shifting slightly towards higher voltages with a decrease in the thickness. Table 4.1 shows different values of V_C in varying nematic layer thickness. More interestingly it was also found that reducing the system thickness by 18 μm (comparing 5 and 23 μm data set) lead to an almost 2 fold increase in the velocity of the domain wall tip in the voltage range ($V > V_C$), However, below V_C, velocity of the tip is almost identical in all three sets. Thus, these results suggest an alternative route of

attaining higher tip velocities in the same system which previously lies outside the range

of the experiments shown in the above sections.
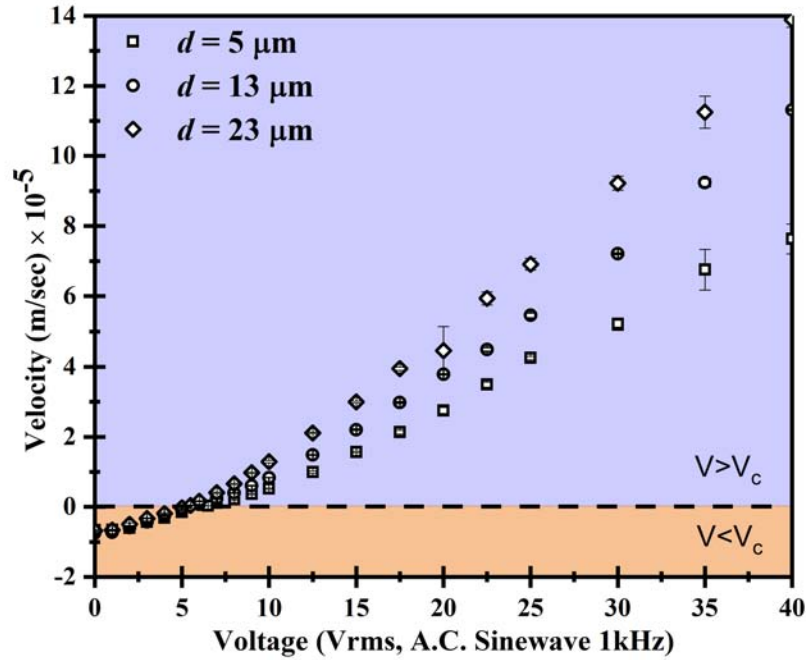
Figure 4.20: The velocity versus voltage for the movement of the kink in varying thick-

ness of nematic layer, obtained from linear fits to the distance versus time data

System Thickness (d μm)	Critical Voltage (V_C) @ 21±1°C.
5	6.1±0.1 V
13	5.7±0.1 V
23	5.4±0.1 V

Table 4.1: Critical voltage (V_c) value in different thickness of the nematic layer.

4.3.8 Effect of voltage post dynamical growth of the defect line.

4.3.8.1 *Formation of an array of alternating HAN domains in the cell.*
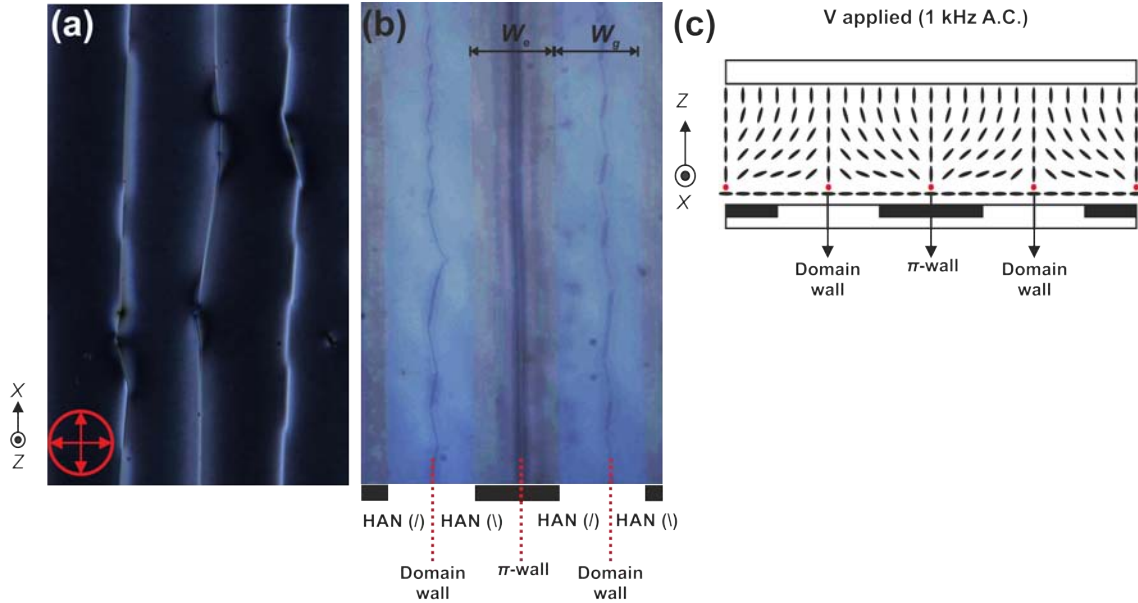
Figure 4.21: Hybrid aligned nematic layer with two co-existing HAN(/), HAN(\) domains, separated by zig-zag domain walls under applied voltage V (1kHz, sinewave), (a) sample image under vertically crossed-polarisers (b) sample image in reflection mode showing domain walls (highlighted by red dashed lines) located in the centre of electrode and electrode gaps, (c) Schematic illustration of the orientation of the nematic n-director in cross-section showing alternating HAN domains formed in the cell under an applied voltage.

In the above sections, we discussed the dynamics properties of topological domain wall growing with different velocities in the system at varying voltages. In this section, we will investigate the post-growth effect. To be specific, we will investigate the system once the growing domain wall reaches the extremum of the electrodes. On closer examination of the system, we found that application of the voltage $(V > V_C)$ for a sufficient duration of time, domain wall extends both in the electrode's gaps and also above the electrode's

149

region. On completing electrode edge to edge movement, keeping the voltage on, we observed the formation of an array of alternating HAN tilt domains (Fig.4.21 a,b) in the system. One domain for which the tilt angle through the layer varies from $\theta(0) = 0$ to $\theta(d) = +\pi/2$ (HAN (/)), and another for which the tilt angle through the layer varies from $\theta(0) = 0$ to $\theta(d) = -\pi/2$ (HAN (\)). These two HAN domains with opposite n-director tilt directions we found to be are separated by domain walls, illustrated by red circles in Figure 4.21c. Briefly a π-wall forms on the electrode centre and a defect line forms in the electrodes gaps as the nematic director couples with in-plane A.C. electric fields. These degenerate hybrid aligned nematic HAN(/) and HAN(\) domains creating alternating HANs in the cell are shown in Figure 4.22a. Tilting the device further in clockwise and anti-clockwise sense along *y*-direction between crossed polarisers enabled the identification of two HAN states. Figure 4.22 shows an optical micrograph of two HAN domains visible in pink and green colour under plane-polarised light. The difference in the birefringence of opposing HAN domains in the two images shown below is due to the change in the tilt direction of the device. Changing the tilt direction leads to shift in the birefringence of the observed states. To understand the formation of alternating HAN domains in the system, a much more sophisticated 2D Q-tensor model was developed by our collaborator Nigel Mottram. Results (fig. 4.22b) from the tensor model also revealed the existence of alternating HAN domains separated by domain walls in the cell.

Cautionary Note:

Note here existence of disclination wall, shown above in figure 4.3 is not necessary for the formation of alternating HAN domains (fig. 4.21c) in the system. Application of in-plane A.C. electric fields to the device utilising same IDE electrode geometry given above in figure 4.1b and hybrid alignment conditions will lead to the formation of alternating HAN domains in the system due to director coupling with in-plane A.C. electric fields.

a)

b)
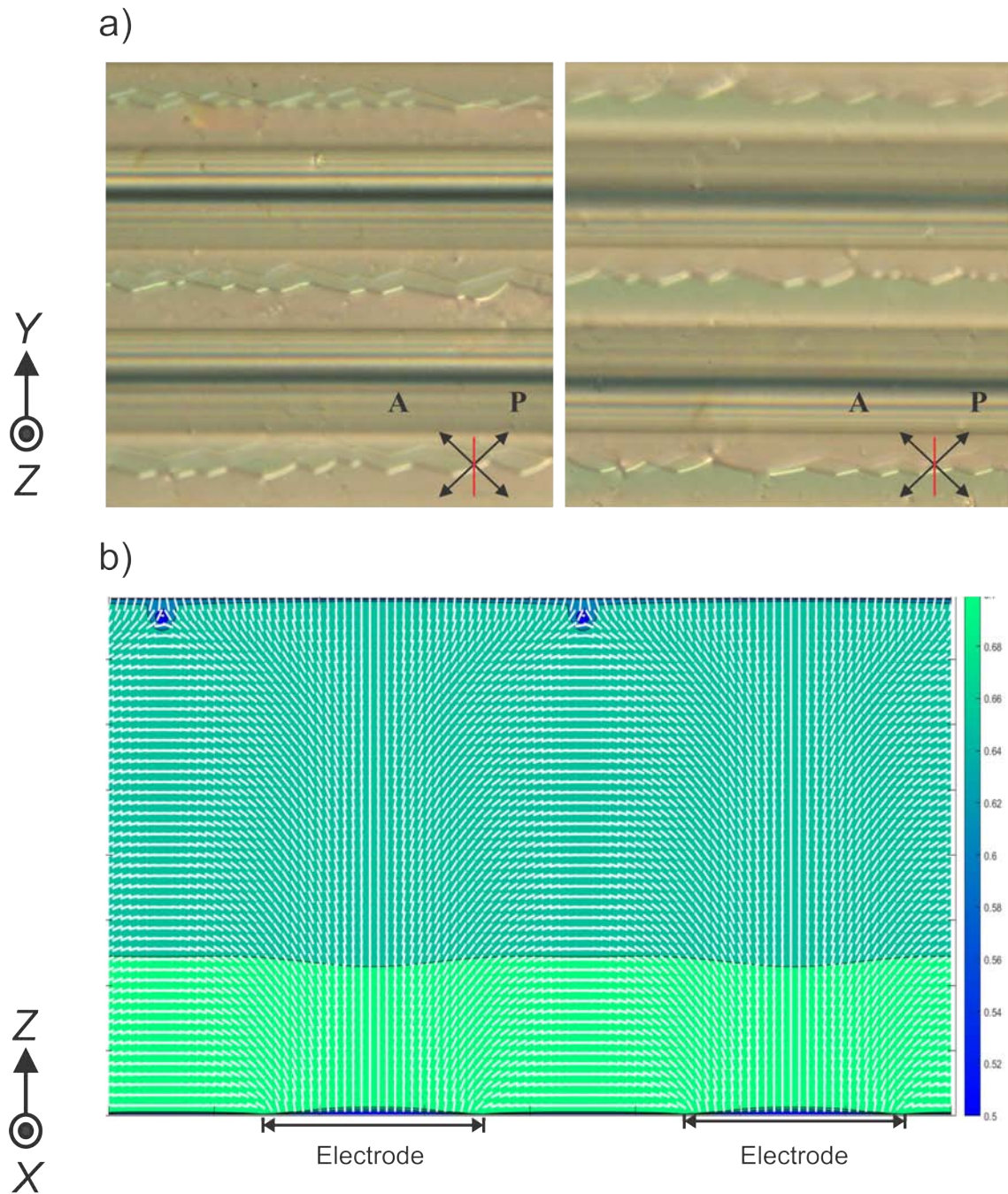
Figure 4.22: (a) Alternating HAN states formed in a hybrid layer under the action of applied voltage, the sample was placed between cross-polarisers with tilt in clockwise and anti-clockwise sense along *y*-direction in the first and second image (moving from left to right) respectively. (b) Q-tensor modeling results showing the formation of alternating HAN domains in the device.

4.3.8.2 *A.C voltage induced structural transformation of disclination line into zig-zag defect line.*
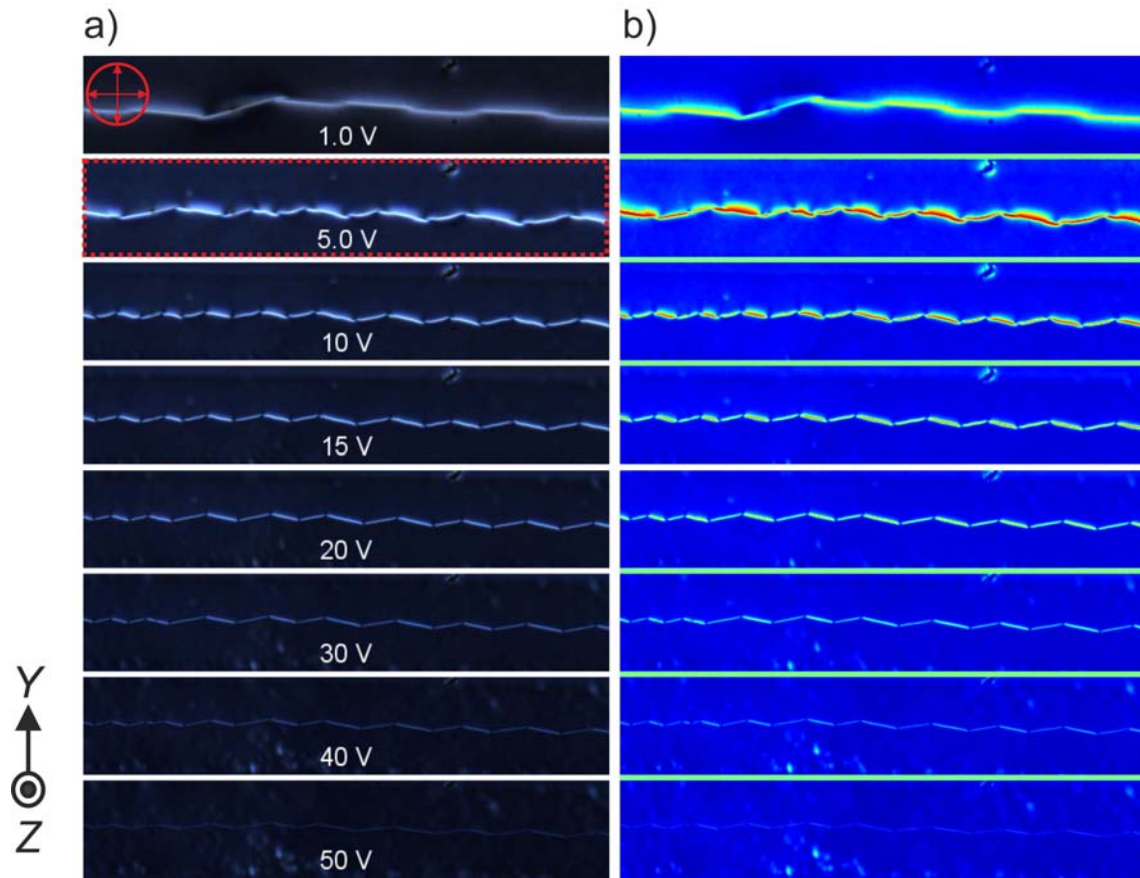
Figure 4.23: Structural transformation of the defect line formed in the electrode gap into zig-zag defect line on increase of electric confinement (V_{rms}, 1 kHz, A.C. sinewave) in the device. (a) composite of actual images of defect line at different voltages, (b) corresponding pseudocolour images.

So far, in the above section, we discussed the formation of alternating HAN domains in the system. Now, we will investigate the effect of voltage on the structure of the defect line formed between the electrode gaps. The defect line shown in the case of $V = 5$ V (highlighted by the red dashed box) in the above figure 4.23 was used as the starting point for each applied voltage in the study. This defect line is reproducibly re-established after each voltage measurement by switching the system on and off i.e. first creating the

defect line at 5 V and then applying desired voltage, then abruptly switching the voltage off in the device, and then repeating the first step again for the next measurement. This resetting procedure created the required defect line in the electrode gap region, enabling us to investigate the effect of electrical confinement on defect line structure as voltage is varied in the device. Figure 4.23 shows the structural transformation of defect line as voltage is varied in the system. In case of voltage diminution defect line relaxes in the system, as shown in figure 4.23 1 V image. However, as voltage is increased in the device from $V = 5$ V to $V = 50$V increase in the electrical confinement occurs in the system leading to the structural transformation of $-1/2$ defect line into periodic zig-zag defect line with different twist handedness. This structural transformation of defect line into zig-zag is a resultant of intrinsic anisotropy of elastic coefficient $(K_{11} \neq K_{22} \neq K_{33})$ of nematic liquid crystal as smaller K_{22} lead to a twist deformation on voltage increment in system [90]. Briefly, at low-voltage $(V < 5V)$ defect line maintain its curvilinear shape without the formation of any zig-zag pattern as the electric field is not strong enough to induce twist deformation in the system. As the voltage is increased defect line shifts its position in the electrode gap region due to dielectric coupling to in-plane A.C. electric fields and at same time twist the director near the core region of defect line to minimize the total energy of the system, forming a zig-zag pattern. Plot showing shift in the position of defect line in xy-plane on voltage increases is given in figure 4.24. In addition to structural transformation to zig-zags, the defect line also moves in the depth of the sample, moving in upwards direction towards the top substrate as voltage is ramped in the system. Thus, making it harder to resolve at higher voltages (please see 50 V image in figure 4.23).
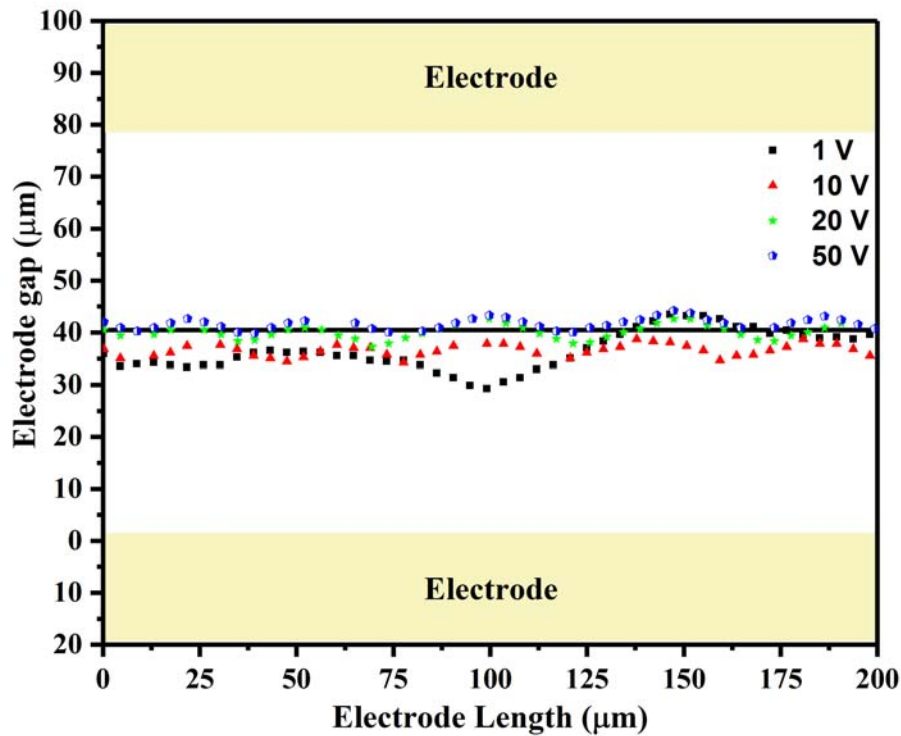
Figure 4.24: Plot showing change in the position of defect line in the electrode gap as the voltage is increased in the system.

4.4 Conclusion

In conclusion, we have presented an experimental and theoretical study on the time-dependent electric field reconfiguration and manipulation of a topological line defect between two opposing hybrid aligned nematic liquid crystal domains. Our system shows an interesting example of dynamics study on electrical constrained-induced topological defect growth. Results from the studies show a high curvature tip region of the topological defect line can be moved with constant velocity on-demand in both positive or negative directions, or held stationary at any position during its travel, simply by tuning the value of a low applied voltage. Furthermore, it was also found that the defect line tension doesn't

affect the dynamics of the domain wall growth. However, variation in the thickness (d) of the nematic layer significantly affects the growth velocity of the wall, particularly at higher voltages. The capability to move domain wall on demand was further exploited for micro cargo transport application, providing electrically controlled linear translation and precision positioning of a colloidal particle in a soft matter device. This approach avoids the requirement for externally imposed and controlled flow and also avoids the requirement for alignment patterning or lateral confinement walls and structures within the liquid layer. At the same time, this study also offers the opportunity to transport either neutral or charged particles, whilst the use of an A.C. voltage avoids electrochemical degradation effects that can be associated with D.C. electric fields. The study reported in this chapter has potential relevance to the design of the next generation of micromachines and lab-on-chip devices. In addition to above mentioned applications formation of alternating hybrid aligned domains on complete edge to edge growth of topological defect line in the device offers a unique system to study the flexoelectric response of the nematic material in response to the D.C. voltage. As the presence of hybrid alignment impart a splay-bend n-director spatial distortion across the nematic layer which produces an effective flexoelectric internal bias even in the absence of any externally applied voltage. In the next Chapter 5 we will investigate this effect in detail in both closed and open (free top surface) systems.

Chapter 5

Influence of flexoelectricity on alternating HAN structures and free surface wrinkles

The present chapter reports an experimental investigation on the polarity-dependent movement of zig-zag defect walls and surface wrinkles formed in a hybrid aligned nematic (HAN) layer (d=13 μm) under the application of in-plane electric fields. Application of electric field (A.C. 1 kHz) to a hybrid nematic layer leads to the formation of alternating hybrid domains of opposing tilt orientation (HAN(/) and HAN(\)) separated by zig-zag defect walls in the middle of the electrodes gaps and π-wall over the electrodes. The resultant nematic director configuration presents flexoelectric polarisation in the device due to splay-bend deformation. Application of D.C. voltage (low-frequency square-wave (0.1 Hz and 0.05 Hz)) to the device, leads to polarity-dependent movement of the zig-zag defect wall in the system. Two positive nematic materials, low permittivity E1 ($\Delta\varepsilon = 12.3 \pm 0.4$), and high permittivity MDA 13-2167 ($\Delta\varepsilon = 400.12$) were investigated, both in closed and open device geometry. The key finding from the chapters reports a

strong polarity-dependent movement of zig-zag defect walls in the high permittivity nematic material which in the case of open device geometry is accompanied by the voltage sign dependent lateral shift of the surface wrinkle.

5.1 Introduction

The origin of flexoelectricity in liquid crystals is associated with shape anisotropy of the liquid crystal's molecules and their polarisation at the microscopic scale as discussed in Chapter 1 section 1.1.8. Taking this into account, in case of nematic liquid crystals one might get deluded due to the simple rod shape of the nematic molecule. However, it should be noted that on a molecular scale the anatomy of a simple nematic molecule is far more complex than being a simple ellipsoid due to the presence of several angled bonding, dipoles in the molecule structures. In an unperturbed state molecules in nematic liquid crystals having permanent dipoles, are expected to align parallel to the average molecular orientation, the n-director, as they are to align antiparallel and so there is no net bulk polarization [104]. However, the presence of an electric field in the system can induce a spatial distortion in the director as a result of this flexoelectric polarisation (P_f) occurs in the nematic system. This effect in nematic liquid crystals is commonly used in displays like Zenithal Bistable Display (ZBD) [111–113]. Due to the commercial importance of the flexoelectric effect, understanding and experimental determination of flexoelectricity coefficients in liquid crystals is of some significance for the development of new applications and optimisation of existing display systems.

Whilst the flexoelectric effect being a universal property [32, 114] offers potential benefits over piezoelectric effect (limited to 20 non-centrosymmetric groups, having unique crystallographic axes)[115]. The measurement techniques and quantitative knowledge of

the materials required for possible engineering applications are still limited due to the number of challenges. a) It's difficult to separate flexoelectric effect from other electrical effects (surface alignment induce bias, ionic shielding) in the system as they may contribute or damp the net flexoelectric effect., b) only certain set of geometries can be used for studying the flexoelectric effect as in some geometries dielectric anisotropy $(\Delta\varepsilon)$ of the material, which dictate the director re-orientation along the electric field, may suppress the flexoelectric effect., c) to study, flexoelectric effect one require inhomogeneity in the device which is sensitive to anchoring conditions, e.g. presence of weak anchoring on one of the substrate eases curvature induce distortion or formation/movement of topological defect contained by strong anchoring conditions can change the interior topology resulting into flexoelectric polarisation. Moreover, because flexoelectric polarisation is dependent on the gradient in the director, this effect could not be studied in thicker nematic layers. All these complications make studying flexoelectric effect an extremely challenging task.

To this date, much of the work on the measurement of flexoelectricity [116–127]. is performed on Hybrid Aligned Nematic (HAN) geometry [128]. The presence of heterogenous alignment conditions (planar and homeotropic) impart a strong splay-bend spatial distortion in n-director across the hybrid nematic layer which produces an effective flexoelectric polarisation [124, 128] in the device. Madhusudana *et.al* used HAN geometry for measurement of flexoelectric coefficient of MBBA [122], purely making use of the fact that application of different polarities of D.C. voltage would lead to different director responses along the thickness of the cell as shown in fig.5.1. Another method for measurement of flexoelectric coefficient $(e_1 + e_3)$ of MBBA was suggested by Prost and Pershan [129], where the author used symmetric interdigital electrode in a homeotropic geometry (fig.5.2a). Application of low and high-frequency electric field to the device leads to

different light scattering behaviour due to flexoelectric (fig.5.2b) and dielectric response (fig.5.2c) of the nematic layer. Figure 5.2d shows the difference in light scattering from the flexoelectric effect (±1) and dielectric alignment effect (±2).
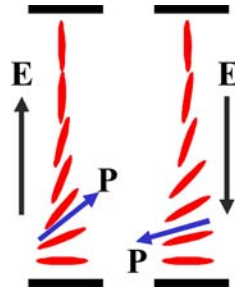
Figure 5.1: Schematic illustration of different director distortion observed in hybrid aligned layer during different polarity of D.C. voltage.
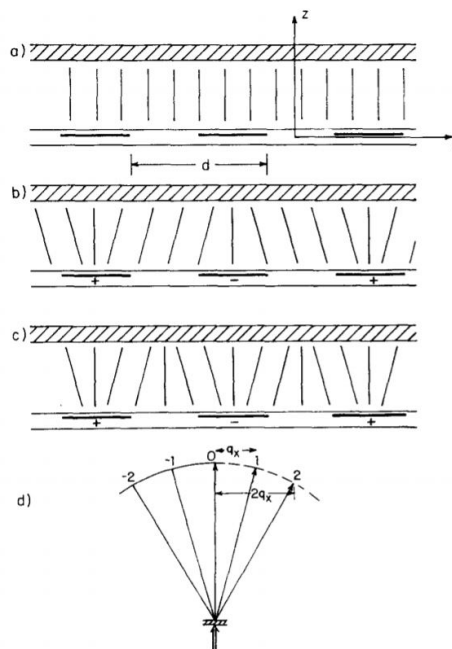
Figure 5.2: Schematic illustration of Prost and Pershan experiment: (a) homeotropic geometry used in the study in absence of the voltage, (b) nematic director distortion due to flexoelectric effect, (c) nematic director distortion due dielectric coupling, and (d) direction: 0-incident beam, $\pm$ 1-light scattered from flexoelectric effect, $\pm$ 2-light scattered from the dielectric alignment effect.

The study reported in this chapter is reminiscent of earlier flexoelectric work by Prost and Pershan [20] shown above in fig.5.2. However, contrary to their experiments we used hybrid aligned geometry $(\theta(0) = 0°, \theta(d) = \pi/2)$ and utilise the movement of topological defect (zig-zag defect line) in the nematic layer as a feature to determine the flexoelectric response of the system. In the previous chapter, we have shown that application of in-plane A.C. electric fields to hybrid aligned nematic layer of positive nematic material (E1), leads to the alternating arrangement of hybrid domains with opposite n-director tilt directions (HAN (/) and HAN (\)) separated by π-walls over the electrodes and zig-zag defect in the middle of the electrodes. In this chapter, the magnitude of movement of the defect line (perpendicular to electrode length) was studied for two positive dielectric anisotropy nematic materials, low permittivity, high ionic content nematic E1 $(+\Delta\varepsilon = 12.3)$, and high permittivity nematic MDA 13-2167 $(+\Delta\varepsilon = 400)$. Both the materials were studied in open (free top surface) and closed systems to determine the influence of anchoring strength and dielectric anisotropy on flexoelectric polarisation. The first half of the chapter investigates the effect of D.C. voltages on the movement of zig-zag defect in two different systems (open and closed) using both the nematic materials. In the second half, we will investigate the open system to further look into the effect of D.C voltages on the surface wrinkle of high permittivity material.

5.2 Experimental

5.2.1 Device details and preparation
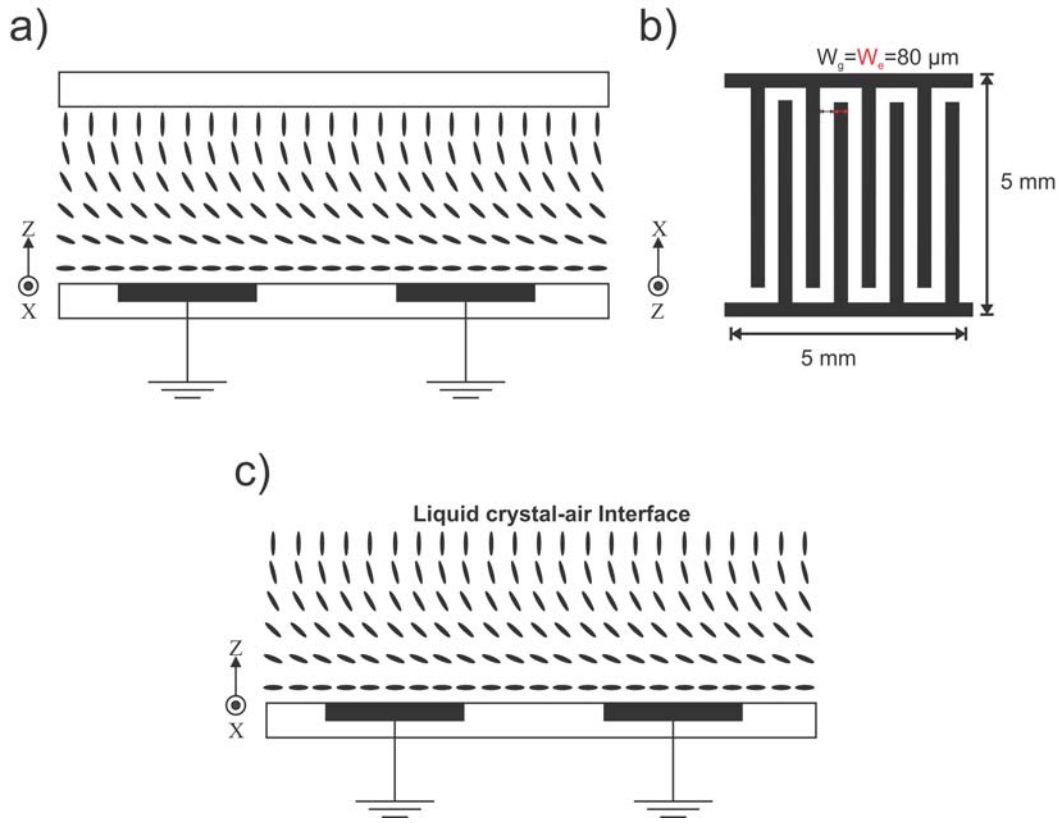
Figure 5.3: Schematic showing, (a) closed system with side view of the device with hybrid aligned nematic layer sandwich between the two substrates (b) top view of the interdigitated electrode (IDE) patterned on the lower substrate having $w_e = w_g = 80 \,\mu$m, and (c) open system (free top surface) with side view of the device with hybrid aligned nematic layer sandwich between the two substrates

5.2.1.1 *Fabrication of closed system.*

The device consisted of a nematic liquid crystal layer of thickness $d = 13 \,\mu$m sandwiched between two borosilicate glass substrates in the *xy*-plane (fig.5.3a). The bottom substrate at $z = 0$ was patterned with interdigital stripe electrodes (IDE) running parallel to the *x*-direction. The bottom substrate was coated with a thin solid film (MgF$_2$ on

ZnS, combined thickness 300 nm) which imparted low-pretilt [44] planar nematic surface alignment with the alignment axis in the *y*-direction, perpendicular to the direction of the electrode length. The opposing top substrate at $z = d$ was coated with homeotropic Teflon AF (CAS 37626-13-4, Sigma-Aldrich/Merck KGaA, Darmstadt, Germany) surface treatment (please see also chapter 2 section 2.3.2). The thickness of the device was maintained with polyethylene terephthalate strips (PET, 13 μm, Goodfellow, Cambridge, UK). The electrodes (IDE) on the bottom substrate were fabricated on indium tin oxide coated borosilicate glass slides using standard photolithography and etching techniques (detailed process mentioned in chapter 2 section 2.2). The electrode arrangement covered a square area of size 5×5 mm, whilst the electrode linewidth and the gaps between the electrodes were both equal to $w_e = w_g = 80 \ \mu$m as shown in fig.5.3b.

Cautionary Note: Please note polyethylene terephthalate strips (PET, 13 μm) used in the fabrication of the above-mentioned device was not coated with homeotropic coating (Teflon AF) due to which we don't observe the formation of diagonal domain wall in the device as shown previously in chapter 4 section 4.3.1.

5.2.1.2 *Fabrication of Open system.*

For the open system (fig.5.3c), device fabrication is almost similar to the closed system with the major difference being the removal of the top substrate at $z = d$ and the spacers (polyethylene terephthalate strips, 13 μm) from the device. Basically, in this system, we have an air-nematic liquid crystal interface on the top which provides homeotropic alignment of liquid crystals at $z = d$. To verify, homeotropic alignment of MDA-13-2167 on the air-liquid interface, we perfomed a quick experiment in which a small pin-hole was made in mylar sheet (PET, 5 μm) using a laser cutter and a thin layer of the liquid crystal is coated on it using a razor blade. This allows the formation of liquid crystal film over

the pin-hole having a liquid-air interface on the top and bottom. Observation of the system under cross-polarisers shows homeotropic alignment of liquid crystals film. Fig.4a-c shows the alignment of liquid crystal film between cross-polarisers before, during and after air-induced disruption respectively.
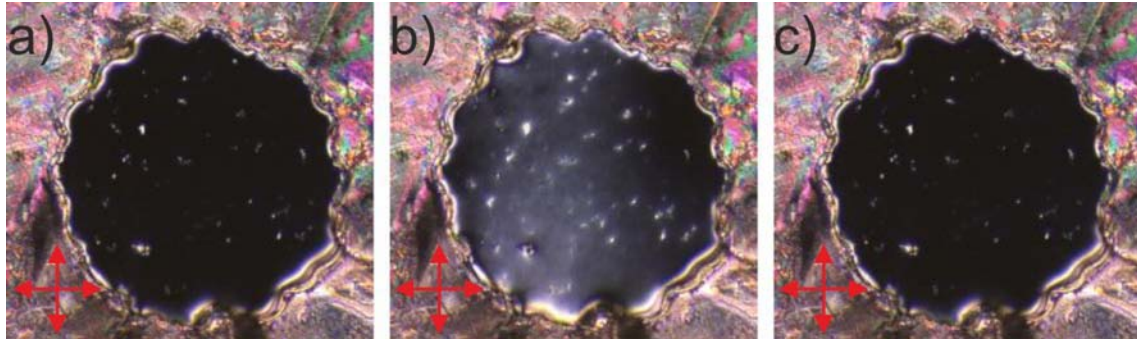
Figure 5.4: Polarising optical micrograph shows the optical texture in the free-standing liquid crystals film, (a) before, (b) during, and (c) after disruption of the film is achieved by blowing the air around the film.

The thickness of the liquid crystal (MDA 13-2167) layer used in the open system was measured using MZ-interferometer. Briefly, sample orientation and polarisation plane of laser source were set up in such a way that nematic director lies orthogonal to polarisation plane of light. This was done to observe a single refractive index (n_o) of liquid crystals along which there is a minimal change due to hybrid alignment conditions in the device. The thickness of the film at a particle region of interest was then determined from interferogram using following parameters $\lambda_{laser} = 632.8\ nm$, δf=0.001408 m, f=0.000184 m, n_{LC}=1.48 (n_o refractive index), $n_{air} = 1$ in equation 2.7. the thickness of the liquid crystal layer in our system was found to be $10.08 \pm 1\ \mu$m.

We used low permittivity, high ionic content material E1 ($+\Delta\varepsilon = 12.3 \pm 0.4$), and high permittivity MDA 13-2167 ($+\Delta\varepsilon = 400$) (Merck KGaA, Darmstadt, Germany) nematic liquid crystal materials, in our experimental studies. Detailed composition and physical parameters measured using Freederickz curve of E1 liquid crystal are mentioned in chapter 4 fig.4.2. High permittivity liquid crystal MDA 13-2167 is a commercial mixture procured through collaborating industrial partners Merck Ltd, UK. The values of positive dielectric anisotropy, $+\Delta\varepsilon = 400.12$, and the values of the splay elastic constant, $k_{11}=$ 8.07 pN, for the MDA 13-2167 (fig. 5.5a) was measured using the A.C. (1 kHz, sine wave) voltage Fréedericksz effect [21, 101]. The frequency-dependent response of the high permittivity material, MDA 13-2167 (fig. 5.5b) was determined by measuring the permittivity of the liquid crystals in homeotropic and planar commercial cells.
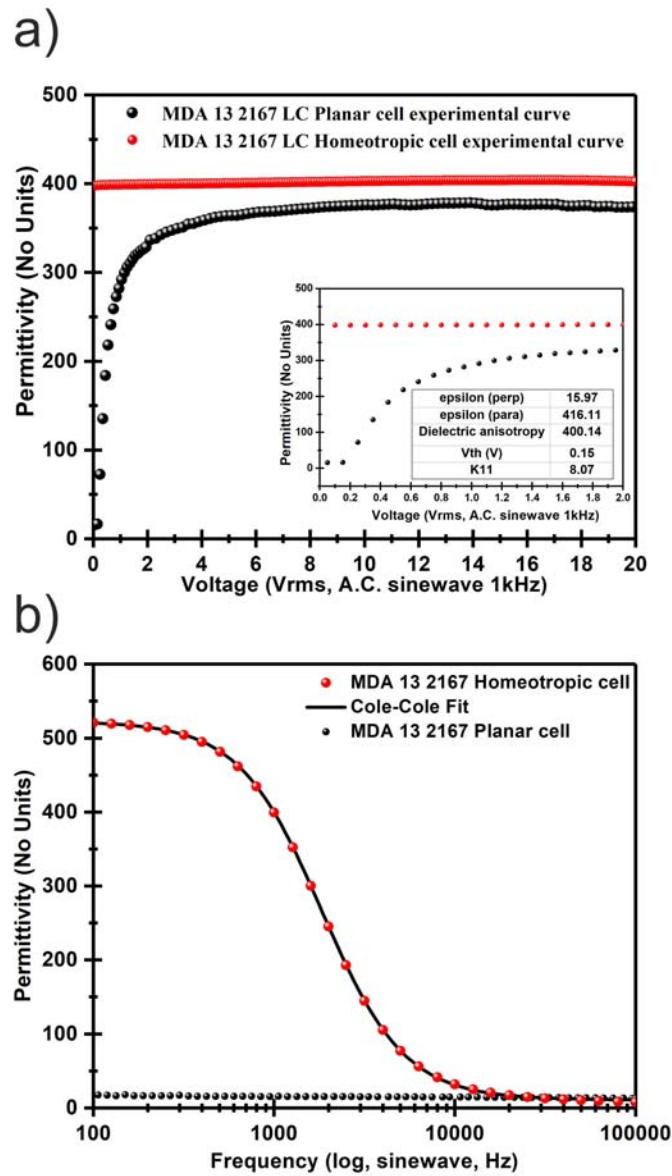
Figure 5.5: a) Experimental Fréedericksz curve of MDA-13-2167 ($+\Delta\varepsilon$=400), measured in planar (solid black dots) and homeotropic (solid red dots) commercial cells ($d = 22$ μm), at $f = 1$ kHz. Permittivity value shown in the curve at each voltage value is averaged over 32 readings measured over a duration of 240 seconds. b) Frequency-dependent permittivity response of MDA-13-2167 layer in planar (solid black dots) and homeotropic (solid red dots) system at a voltage of 0.1 V and 1.0 V respectively. The black solid line represents best theoretical fit of the Cole-Cole equation [130].

5.2.2 Device addressing, Polarising microscope and Interferometry.

Electrical addressing of hybrid nematic layer to a spatially periodic electric field, **E**, is done by applying a voltage to alternate electrodes in the array whilst the interposed electrodes were held at earth potential. All experiments were performed on the open bench in a temperature-controlled laboratory (21±1°C). The voltage was provided by a waveform generator (TGA1244, Thurlby Thander Instruments Limited, Cambridge, UK) combined with a voltage Amplifier (PZD700, Trek Inc., Medina, New York, USA). Videos and still images of the defects observed in the devices (open and closed system) under operation at different voltage values were recorded using a polarising microscope (BX51, Olympus, Essex, UK) fitted with a CMOS camera (EO-23121C, Edmund Optics Ltd, Yorkshire, UK).

In case of the open system, the formation of the sinusoidal surface wrinkle at nematic-air interface and their dynamic response under an applied A.C./D.C. voltages was studied by placing the device (open system) in a Mach–Zehnder interferometer setup. The interferometer was illuminated with He–Ne laser radiation at a wavelength of 632.8 nm with sample orientation and polarisation plane of laser source set up in such a way that nematic director lies orthogonal to polarisation plane of light. This setup was done to ensure that we only observe the surface wrinkle profile and not the variation in director due to hybrid alignment conditions. Electrical addressing of the device was done using the same setup mentioned above. Analysis of the video and images, of all the experimental studies, was performed using MATLAB programme (see appendix A.3.1) and ImageJ[50].

5.3   Results and Discussions

5.3.1   Understanding the flexoelectric influence on hybrid aligned nematic layer consisting of alternating HAN domains.
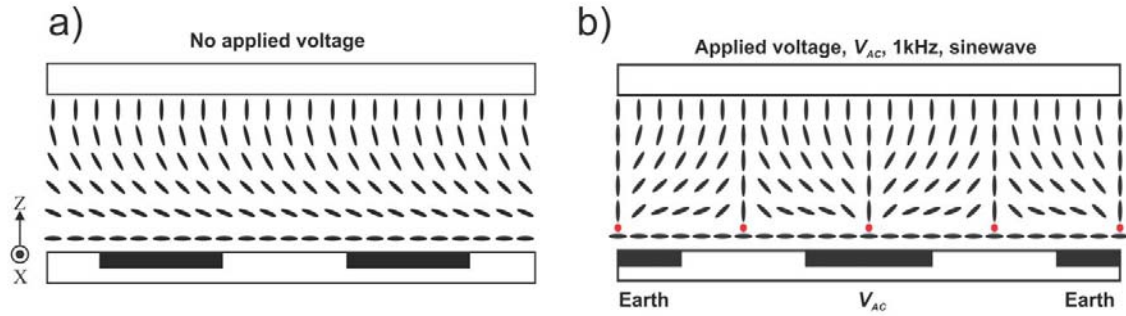
Figure 5.6: The nematic hybrid aligned layer (a) Illustration of the orientation of the nematic n-director with no applied voltage in the cell: (b) Illustration of the orientation of the nematic n-director under applied voltage (A.C. 1 kHz, sine wave) showing the co-existing alternating HAN domains (/\) separated by defect walls in the cell (note that the zig-zag defect forms in the electrode gap region and π-wall forms over the electrode region, position of both the defects are shown by the red dot in the schematic).

The nematic layer was subject to low-pretilt planar alignment [44] with the easy alignment axis in the $y-$direction, orthogonal to the direction of the electrode lines at the lower substrate $(z = 0)$ and to homeotropic alignment at the top $(z = d)$ in both open and closed device. Presence of hybrid alignment conditions in the device can lead to orientation of director tilt angle $\theta(0) = 0$ to $\theta(d) = \pm\pi/2$ through the nematic layer as shown in fig.5.6a (top substrate removed in case of open system), When an A.C. voltage (1kHz, sine wave) is applied to the alternate electrodes to create in plane electric field, dielectric reorientation torques acts on nematic director and system leads to the formation of alternating hybrid domains $((\theta(0) = 0$ to $\theta(d) = +\pi/2$ (HAN (\)), and $\theta(0) = 0$ to $\theta(d) = -\pi/2$ (HAN

(/))), separated by π-walls and zig-zag defect line over the electrodes and gaps regions respectively as illustrated by red circles in fig.5.6b. This switching behaviour commensurate with the direction of the electric field lines in the device as, nematic materials used got positive dielectric anisotropy and electric field tries to align director parallel to field direction [20].

The resultant system consisting of alternating HAN domains have flexoelectric polarisation associated with it in both the tilt domains (HAN (/\)) due to electric field stabilised splay-bend director distortion, shown by blue arrows in Fig.5.7a. Thus, application of D.C. voltage (fig.5.7b) in such a scenario will leads to a competition between electric field and flexoelectric polarisation direction. Basically, the fringing fields penetrating the nematic layer realise two different director distortions (fig.5.7c), one in which flexoelectric polarisation and electric field are in similar direction so a minimal director re-orientation takes place, whereas in other HAN domain electric field is in opposite direction to flexoelectric polarisation due to which re-orientation torque acts on the nematic director leading to a shift in the zig-zag defect wall in the direction determined by the polarity of the electric field applied across the wall present between two opposite HAN tilt domains. Figure 5.7d shows movement of the defect line from initial positive electrode to new positive electrode when the polarity is swapped in the system. This effect is thought to be a consequence of the different flexoelectric polarisation directions associated with HAN (/) and HAN (\) tilt domains.
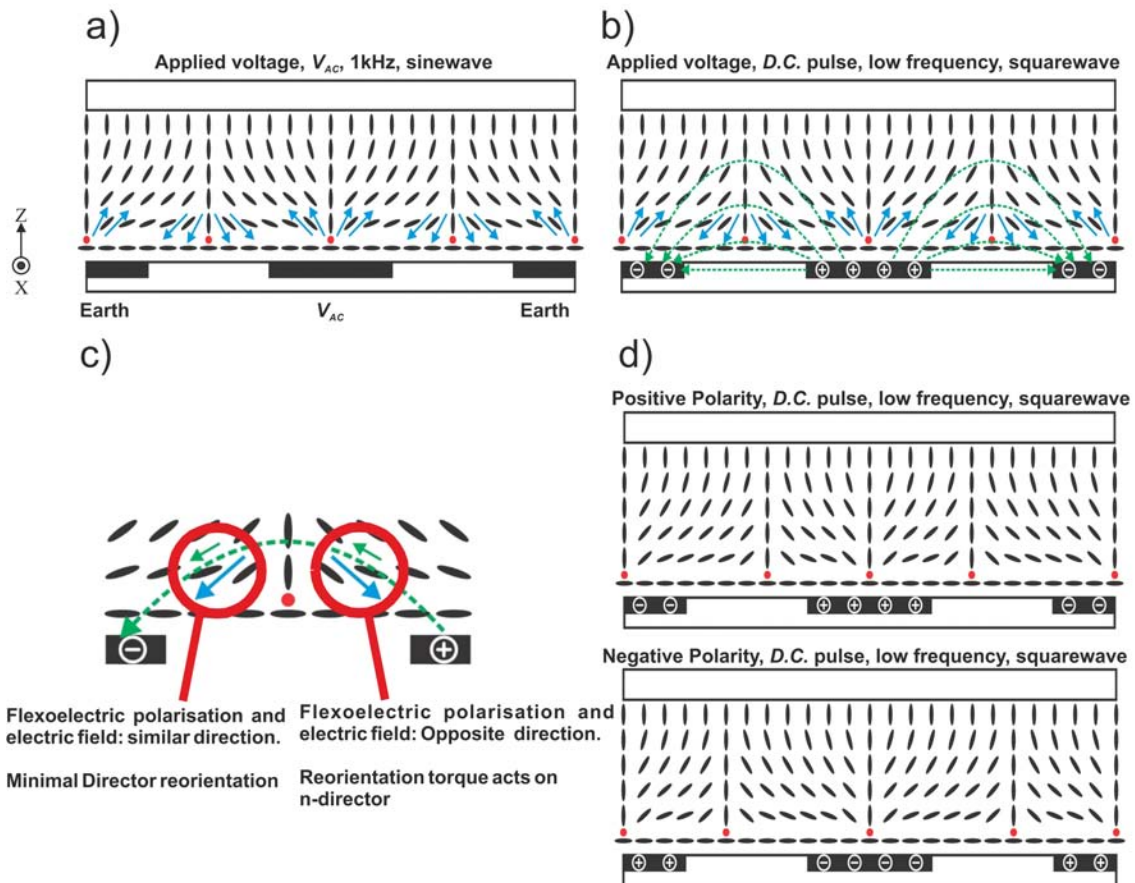
Figure 5.7: The nematic hybrid aligned layer under an applied voltage, (a) Schematic showing flexoelectric polarisation direction (blue arrows) due to splay distortion in the alternating HAN domains whilst system is held static by applying $V_{A.C.}$. (b) Application of D.C. voltage (low frequency, squarewave) to alternate electrodes showing in-plane fringing field (green dashed arrow) penetrating the nematic layer. (c) schematic showing electric field (green dashed arrow) and flexoelectric polarisation (blue arrow) directions in two HAN domains separated by defect line in electrode gap. (d) D.C. voltage polarity dependent movement of defect wall (red dot) in the electrode gap region.

5.3.2 Effect of D.C. voltages on defects formed in a hybrid aligned nematic layer.

To investigate the magnitude of the shift of the zig-zag defect wall as a function of the magnitudes of applied D.C. voltages, and magnitudes of dielectric anisotropy ($\Delta\varepsilon$). We used E1 and MDA 13-2167 positive nematic materials in both open and closed system studies. The D.C. voltages used in our experiments was basically a square wave, having low enough frequency to be considered as D.C. We used two different square wave frequency (0.1 Hz (10s) and 0.05 Hz (20s)) in our experiments. The minimum voltage is 0 V_{rms} and maximum voltage is V_{rms} changing the polarity between positive and negative. Note here each period of the low frequency square wave consist a pair of $\pm$D.C. polarity each having a of length T/2 (i.e. for f=0.1Hz, T=10s, a single D.C. polarity length= 5s). Average of the D.C. voltage in the system is always zero. Selection of two different frequency of the square wave allow us to observe saturation in defect wall movement on polarity swap and at the same time provide us an ability to detect effect of ions in the system.

A total of six experimental studies were performed having different sets of experimental conditions mentioned in Table 5.1. In all these studies, initially an A.C. voltage (V, 1 kHz, square wave) was applied to the device for a duration of 10 secs, this allows the formation of alternating HAN structures in the device with zig-zag defect lines in the electrode gaps regions and π-walls over the electrodes. At the time of application of A.C. voltage no movement was observed in the defects. However, depending upon the magnitude of the A.C. voltage initial defects position varies, this is due to dielectric coupling to in-plane electric fields. As voltage increases, electrical confinement increases, and more director aligns along the field lines due to which a slight shift in initial position can be observed.

Study	Nematic material	System	D.C. Voltage	Square wave Frequency
1	E1	closed	varied	0.1Hz
2	E1	closed	varied	0.05Hz
3	MDA 13-2167	closed	varied	0.1Hz
4	MDA 13-2167	closed	varied	0.05Hz
5	MDA 13-2167	open	varied	0.1Hz
6	MDA 13-2167	open	varied	0.05Hz

Table 5.1: Experimental conditions used for studying effect of D.C. voltage on defects formed in hybrid aligned layer.

Once defects are positioned in the system, at $t = 10s$ the A.C voltage is swapped with D.C. voltage of the same amplitude. Application of D.C. voltage trigger polarity dependent response of the system with zig-zag defect moving in y-direction, orthogonal to length of the electrodes (as discussed in section 5.3.1). The polarity varying D.C. voltage was left on for next 50s and at $t = 60s$ voltage is turned off for 5 mins to allow the device to resettle, ready for next voltage measurement.

In the following subsections we will show results of the conducted studies and explain the scientific motivation behind them. A detailed comparison of all the results from six studies was discussed in the next section 5.3.3.

5.3.2.1 *Defect movement study in E1 closed system*
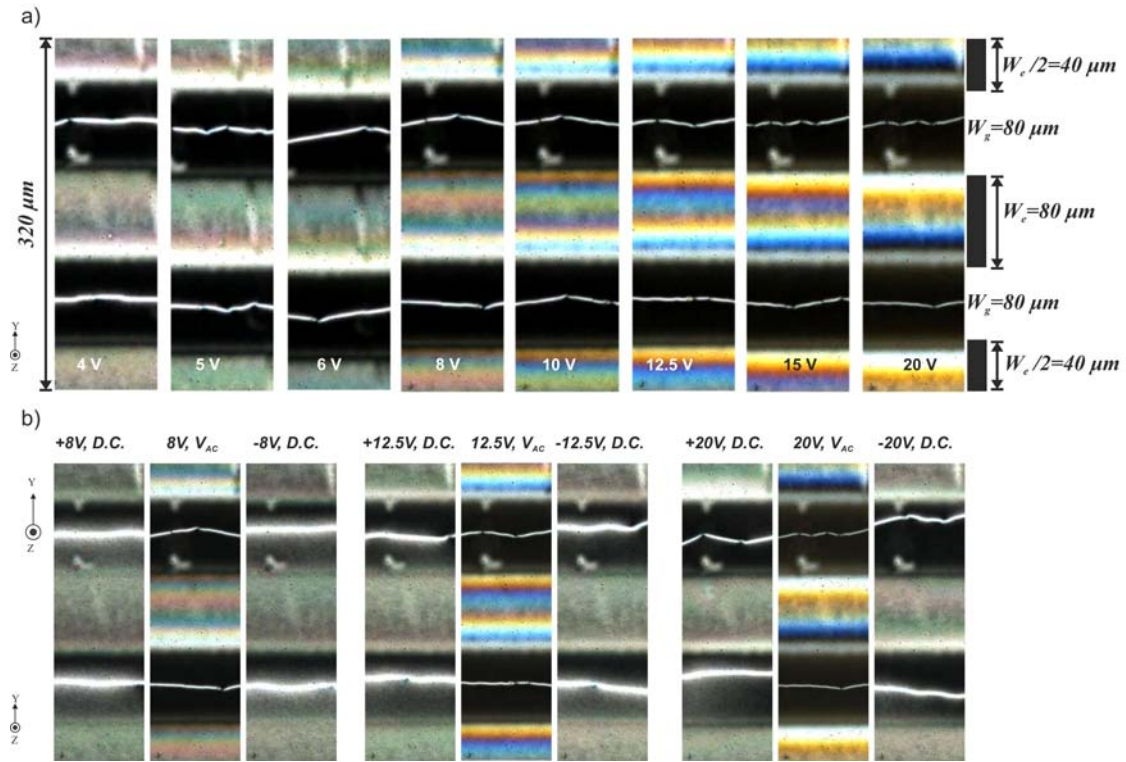
Figure 5.8: (a) Optical micrograph of the actual cell consisting of E1 liquid crystals layers under plane-polarised light with a crossed analyser, showing defect wall separating alternating HAN domains at different A.C. voltages (please note device is not tilted in the picture above due to which a difference in birefringence of two domains is not observed). (b) Polarity dependent movement of defect wall in E1 liquid crystals layer under different applied D.C. voltages (0.05 Hz, square wave). The central image in each voltage set shown above displays initial defects position in the electrode gap under $V_{A.C.}$ (1 kHz, square wave).

Figure 5.8a shows actual snapshot of the device taken at $t=$ 5s, showing formation of alternating HAN domains in E1 nematic layer (d=13 μm) in a closed system. Different magnitude of A.C voltage was applied to the device, $V = 4V$ to $V = 20V$. For $V < 4V$ alternating HAN arrangement is not observed in the above system as electric field is not

strong enough to penetrate the thickness of the nematic layer. For $V > 4V$ alternating HAN arrangement was observed in the system with zig-zag defect line waning as electrical confinement is increased in the device. This defocusing of zig-zag defect line is due to the movement of the zig-zag defect line in depth of the device, as magnitude of the voltage increases, spatial variation in n-director due to electric field due to which the defect line moves towards the top surface. Figure 5.8b shows micrograph of the device showing position of zig-zag defect in electrode gap (w_g) during different polarity of D.C. voltages (square wave, 0.05 Hz, $V = 8V$, $12.5V$ and $20V$). Plots showing effect of different magnitude of D.C. voltages on movement of the zig-zag defects for two different frequency of square wave, 0.1 Hz and 0.05Hz is shown in Figure 5.9 and 5.10 respectively.
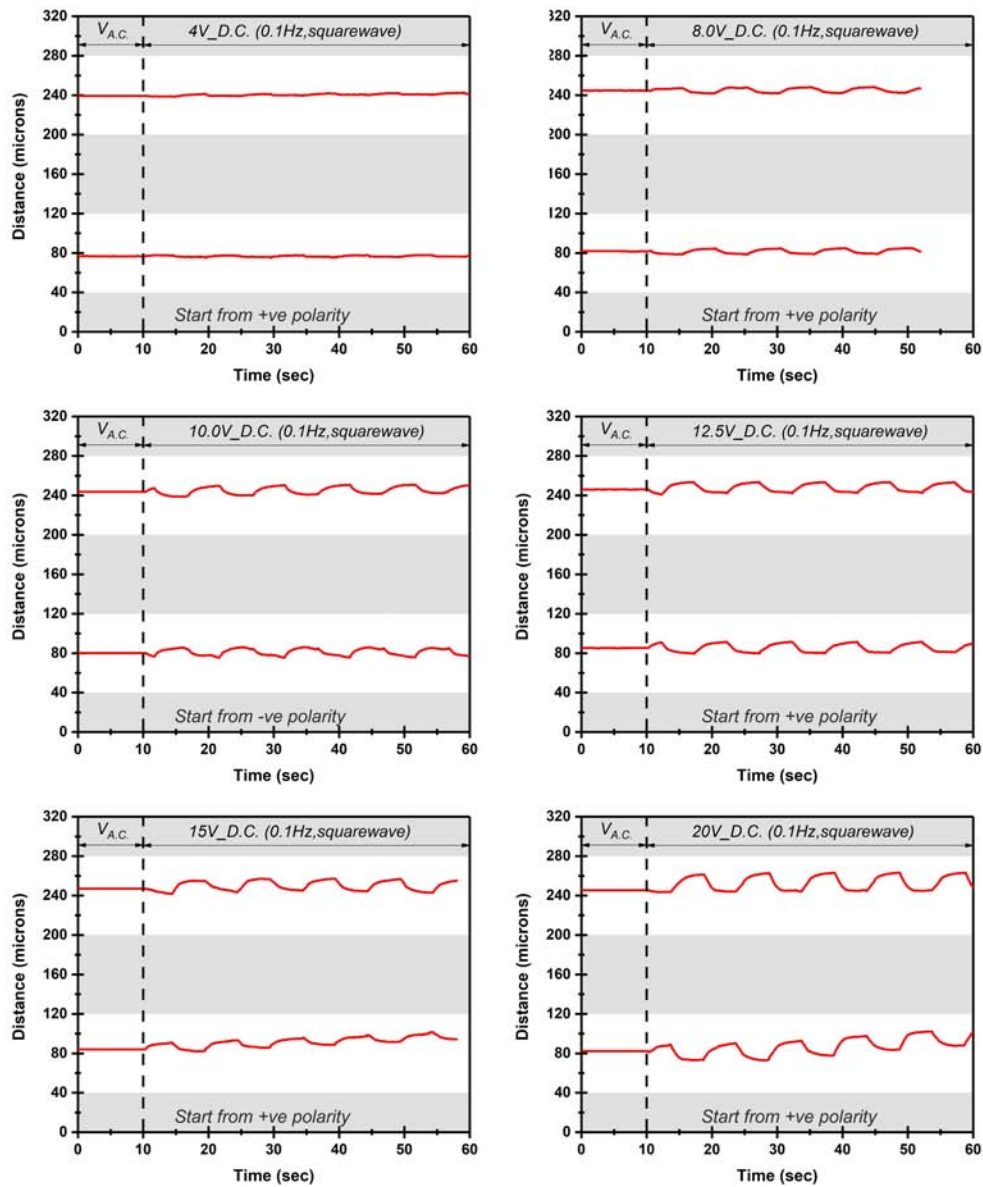
Figure 5.9: E1 (closed system) plots showing polarity dependent movement of zig-zag defect wall (solid red line) overtime in the electrode gap (white regions in the plot) under different D.C. voltages (D.C., 0.1 Hz, square wave). Start polarity sign of each D.C. voltage after the swap is mentioned on respective plots (please note the length of first ($\pm$) polarity cycle immediately after voltage swap from A.C. to D. C. is arbitrary and in most of the cases it's not equivalent to (T/2) of the set square wave frequency. Gray colour area represents the region of the electrode in the plots
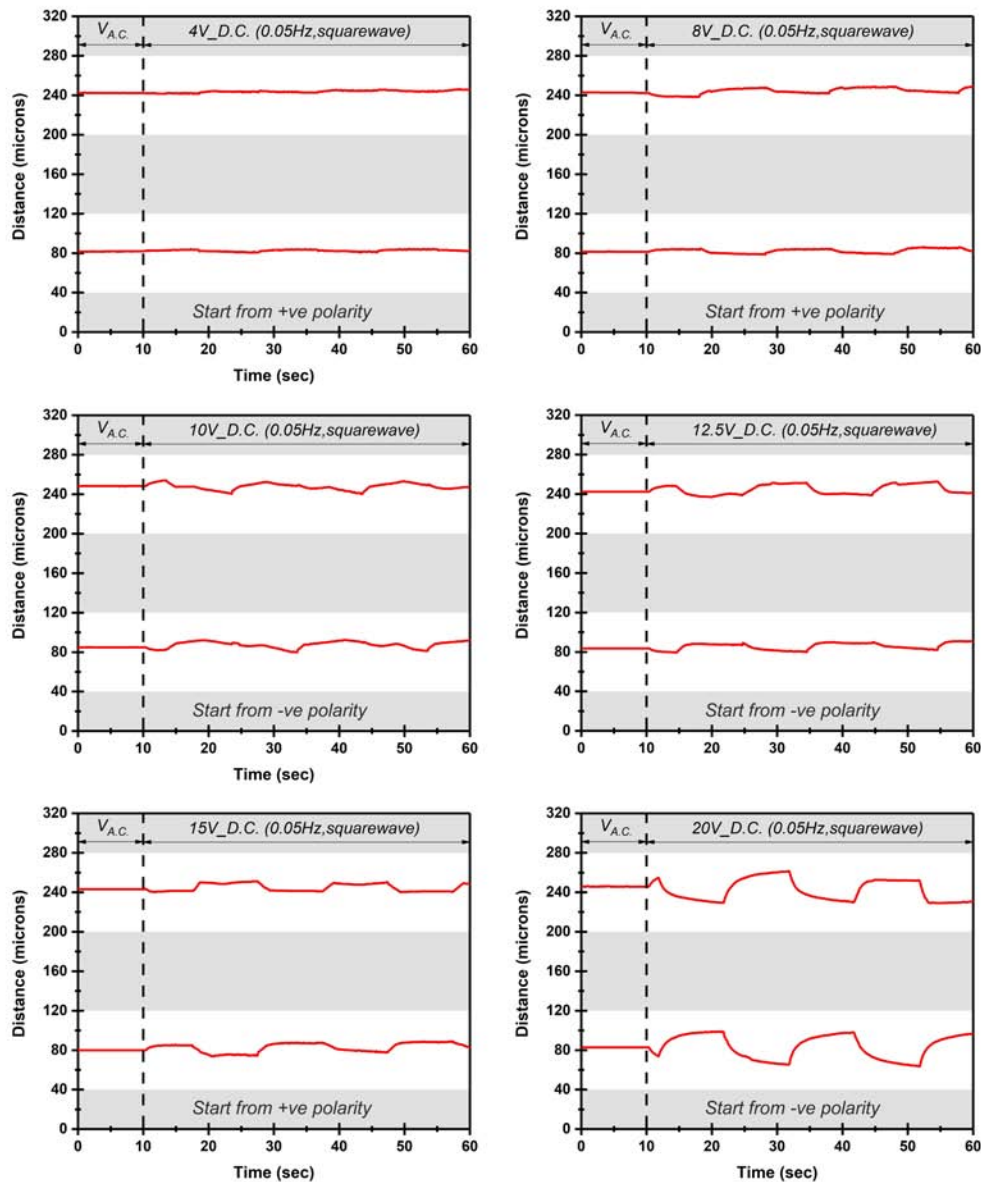
Figure 5.10: E1 (closed system) plots showing polarity dependent movement of zig-zag defect wall (solid red line) overtime in the electrode gap (white regions in the plot) under different D.C. voltages (D.C., 0.05 Hz, squarewave). Start polarity sign of each D.C. voltage after the swap is mentioned on respective plots (please note the length of first (±) polarity cycle immediately after voltage swap from A.C. to D. C. is arbitrary and in most of the cases it's not equivalent to (T/2) of the set squarewave frequency. Gray colour area represents the region of the electrode in the plots.

5.3.2.2 *Defect movement study in MDA 13-2167 closed system*

In the previous subsection, we investigated the effect of D.C. voltage on low permittivity, nematic material E1 in a closed device. This subsection reports the similar study in presence of high permittivity nematic material MDA 13-2167 ($+\Delta\varepsilon = 400$).The motivation behind this study is based on simple understanding of the fact that electric field induced distortion in case of high permittivity material would be higher and therefore the flexo-electric effect which is a resultant of curvature strain, would be much more pronounced in comparison to low permittivity material (E1) used in previous study. Fig.5.11 shows formation of alternating HAN domains in a closed system consisting of nematic layer of MDA 13-2167 under different applied A.C. (1 kHz, squarewave) voltages. For $V > 4$ V, nematic layer switches to alternating HAN structures, forming the defects in the system. However, for $V < 4$ V electric field is not able to switch the nematic layer. For a range of A.C. voltage, $V = 4V$ to $V = 15V$, similar to E1 case mentioned above, a slight shift in initial zig-zag defect position with increase in the magnitude of the A.C. voltage was also observed in high permittivity material.

As expected, on introduction of D.C. voltages (low frequency, square wave), system reveals a good polarity-dependent response for two different square wave frequency (f=0.1 Hz and f=0.05Hz) as shown, in composite figure 5.12 and 5.13. In case of squarewave, f=0.1 Hz (fig.5.14), it was found that movement of defect doesn't saturate well overtime on polarity swap in the system. However, for f=0.05 Hz (fig.5.15), a saturation in defect movement was observed. Furthermore, as it's almost inevitable to avoid contamination in liquid crystals due to sample ageing issue, ions-leaching an ionic-shielding effect was observed at few voltage levels (V= 8V, 9V and 10V) in data set of square wave, having f=0.05 Hz. Presence of ionic contamination in the systems alters the magnitude of the movement of the defect, forcing it to move further away from electrode edge overtime

after each swap of voltage polarity. In addition to results above, interestingly, it was also found that application of D.C. voltages ($f = 0.05$ Hz), $V > 10$ V in the device leads to the destruction of alternating HAN structures (fig.5.16). As for $V > 10$ V, the movement of the zig-zag defects present in two different sets of alternating HANs is so much that they even cross over some of the electrode region and end up merging with adjacent zig-zag defect leading to the destruction of alternating HAN structures in the device.
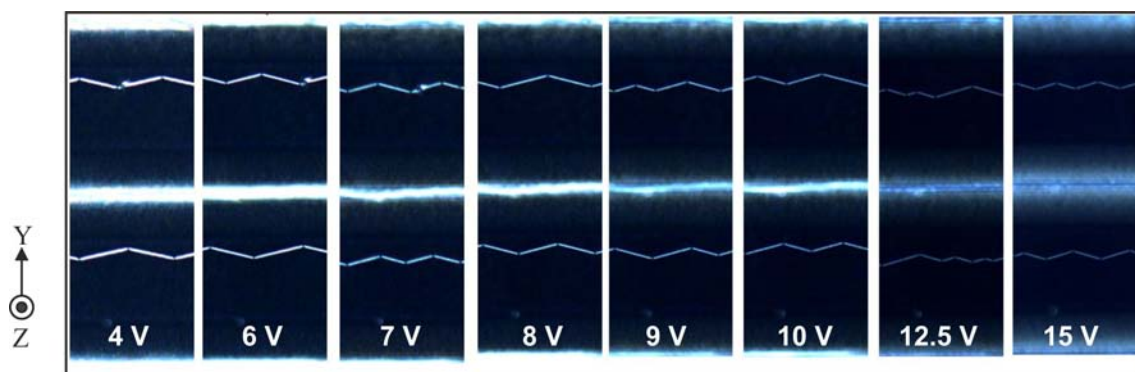
Figure 5.11: Optical micrograph of the actual device (closed system) consisting of MDA 13-2167 liquid crystal layer under plane-polarised light with a crossed analyser, showing sets of alternating HAN domains with defect walls separating two-hybrid domains at different A.C. voltages (please note device is not tilted in the picture above).
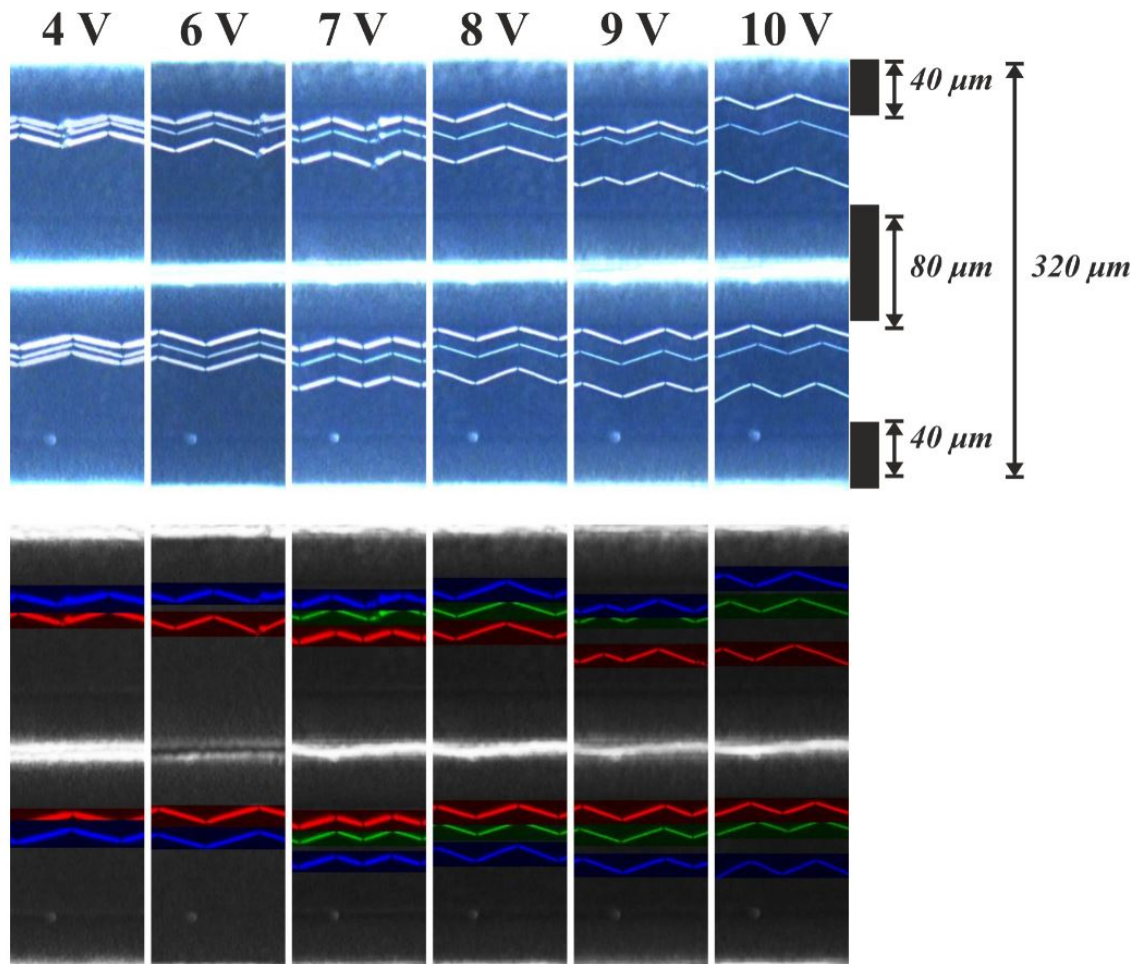
Figure 5.12: MDA 13-2167 (closed system), composite image showing polarity dependent zig-zag defect wall movement in electrode gaps at different applied D.C. voltages (D.C., 0.1 Hz, square wave). The pseudo colour image is shown below the picture where, green, red, and blue colour represent zig-zag defect position in the sample during A.C, +D.C. and -D.C. voltages respectively.
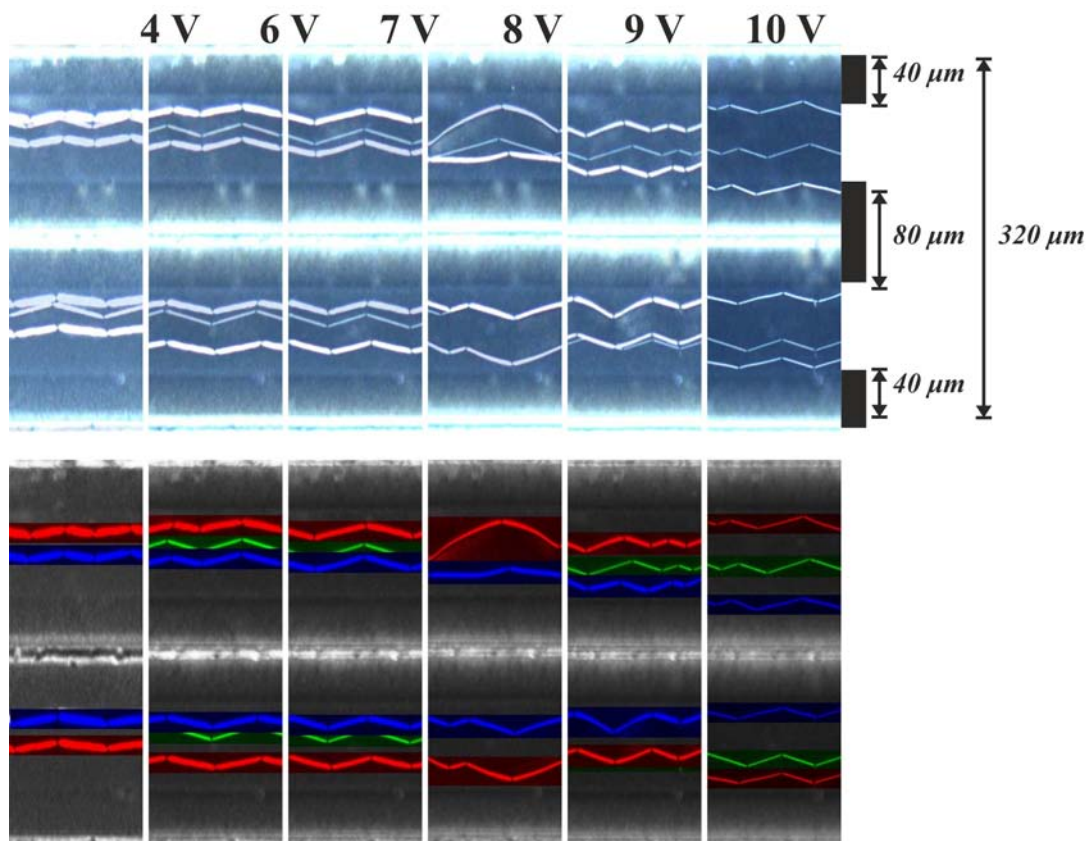
Figure 5.13: MDA 13-2167 (closed system), composite image showing polarity dependent zig-zag defect wall movement in electrode gaps at different applied D.C. voltages (D.C., 0.05 Hz, square wave). The pseudo colour image is shown below the picture where, green, red, and blue colour represent zig-zag defect position in the sample during A.C, +D.C. and -D.C. voltages respectively. .
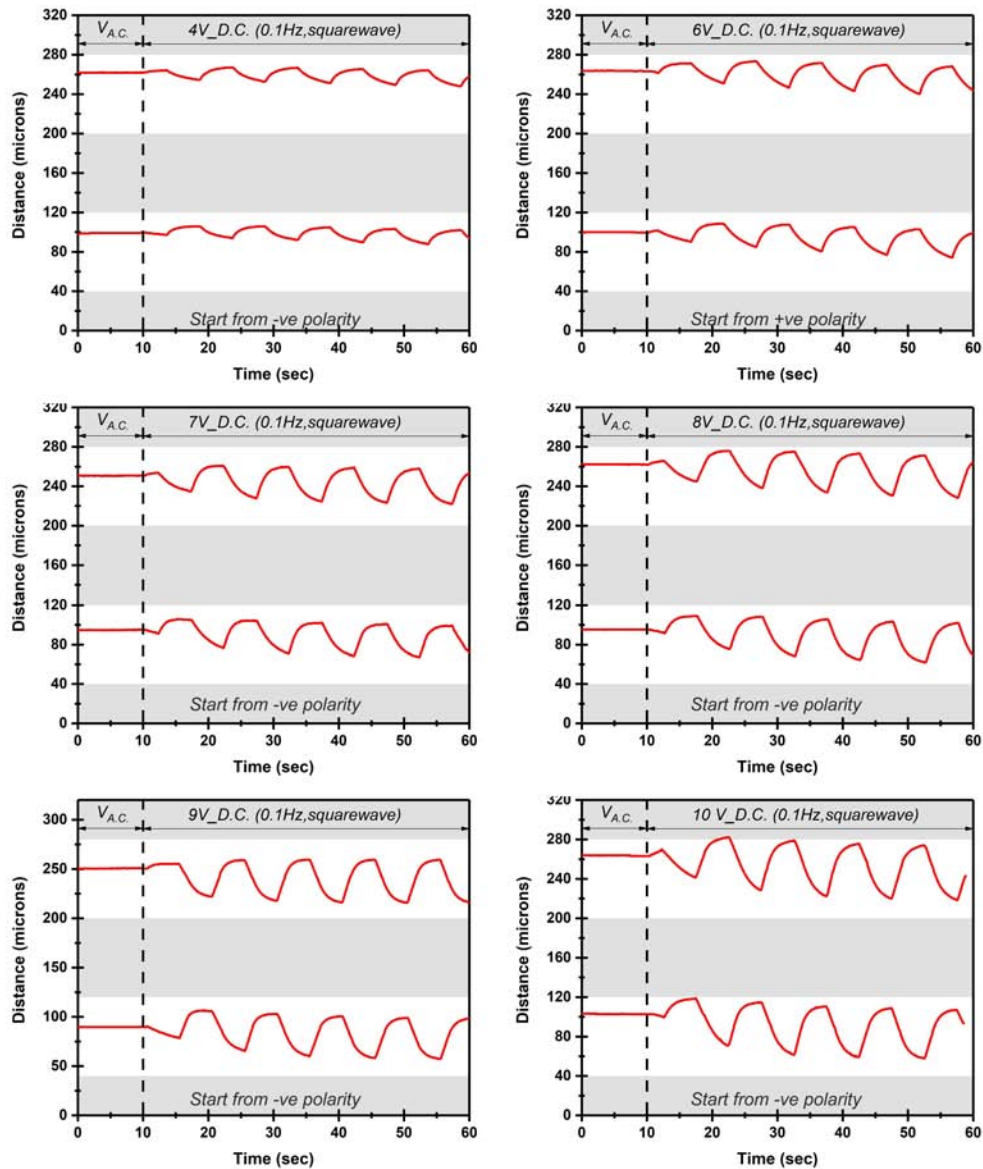
Figure 5.14: MDA 13-2167 (closed system) plots showing polarity dependent movement of zig-zag defect wall (solid red line) overtime in the electrode gap (white regions in the plot) under different D.C. voltages (D.C., 0.1 Hz, square wave). Start polarity sign of each D.C. voltage after the swap is mentioned on respective plots (please note the length of first (±) polarity cycle immediately after voltage swap from A.C. to D. C. is arbitrary and in most of the cases it's not equivalent to (T/2) of the set square wave frequency. Gray colour area represents the region of the electrode in the plots.
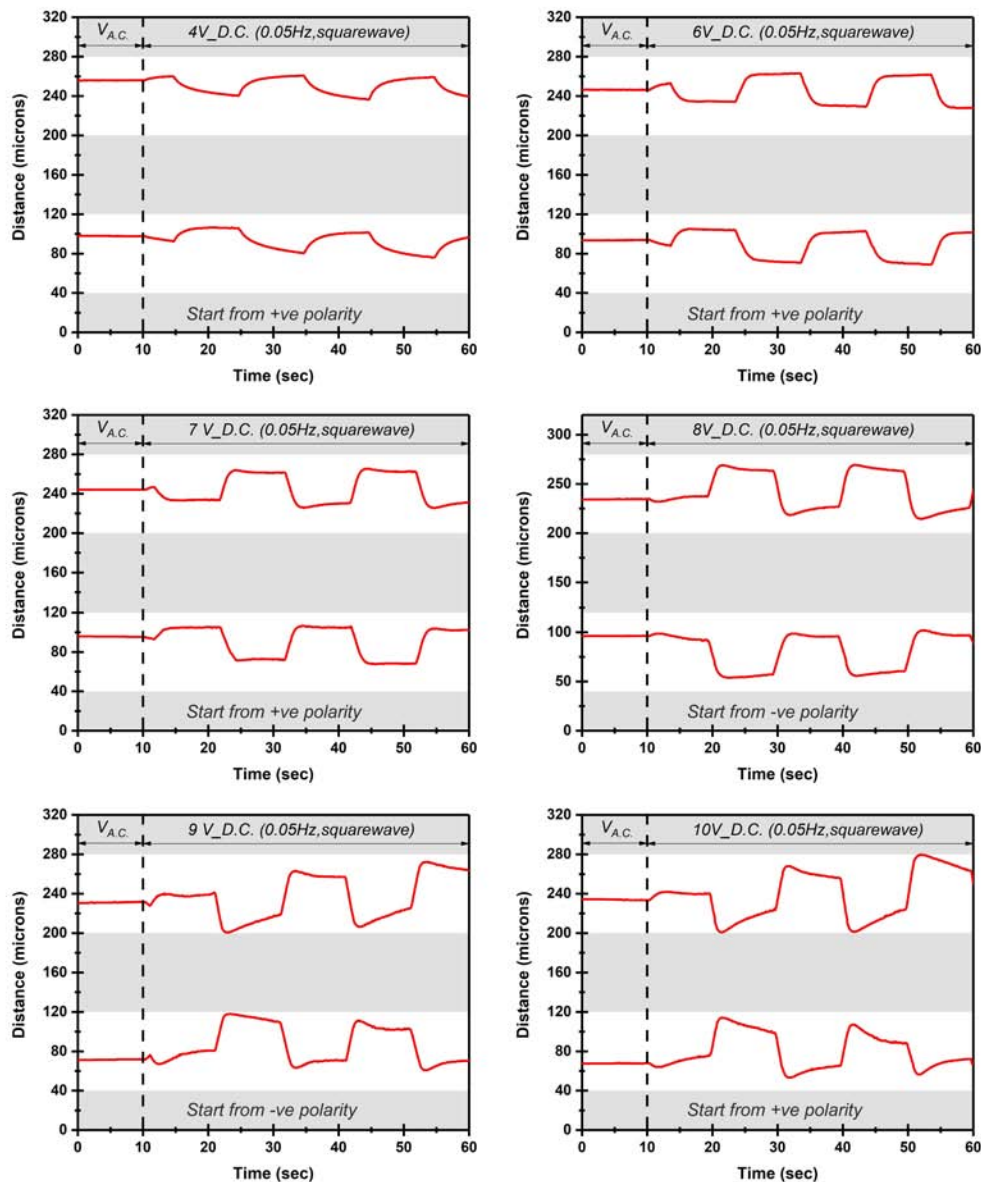
Figure 5.15: MDA 13-2167 (closed system) plots showing polarity dependent movement of zig-zag defect wall (solid red line) overtime in the electrode gap (white regions in the plot) under different D.C. voltages (D.C., 0.05 Hz, square wave). Start polarity sign of each D.C. voltage after the swap is mentioned on respective plots (please note the length of first (±) polarity cycle immediately after voltage swap from A.C. to D. C. is arbitrary and in most of the cases it's not equivalent to (T/2) of the set square wave frequency. Gray colour area represents the region of the electrode in the plots.
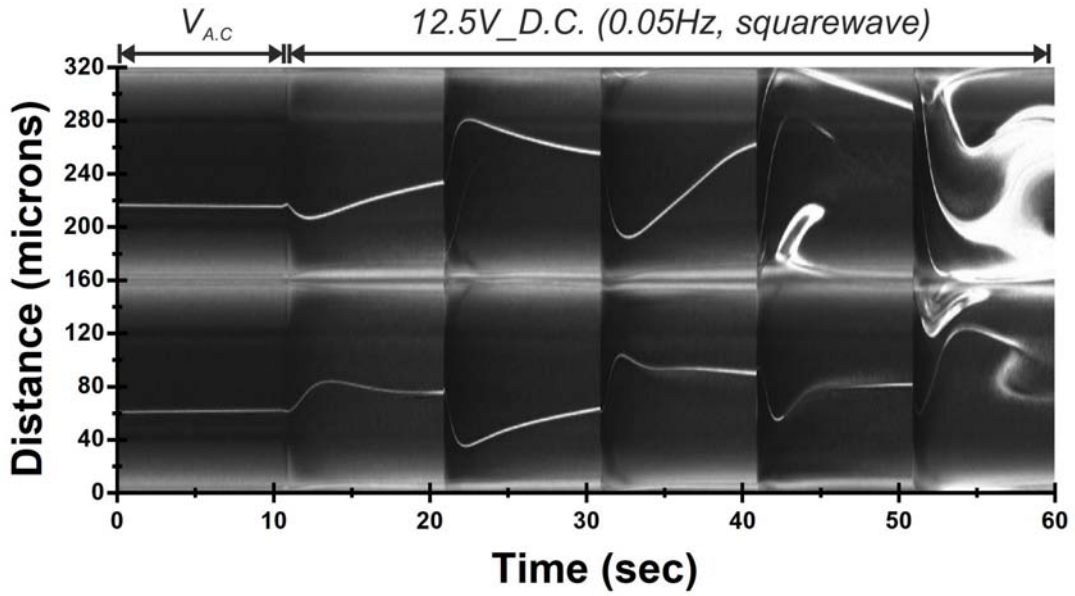
Figure 5.16: Image plot showing merging of the two HAN domains in MDA 13-2167 (closed system), at an applied D.C. voltage of 12.5 V (0.05 Hz, square wave).

5.3.2.3 *Defect movement study in MDA Open system*

So far in the above sections, we have only focused on closed system, where we got a Teflon coated top at $z = d$, imposing strong homeotropic anchoring conditions. In this section we will look into the system with the top substrate removed i.e. we now got air-nematic interface on the top. Previously, in experimental section 5.2.1.2 we have shown that for nematic MDA 13-2167, air-nematic interface provide homeotropic alignment. So, the hybrid alignment conditions still prevail, however the anchoring energy on top $(z = d)$ will be significantly less. This is particularly interesting for understanding the existence and origin of flexoelectric effect as flexoelectricity inducing director distortion relies on the anchoring conditions. Basically, weaker the anchoring energy on the top, easier it is for the electric field to tilt the director adjacent to homeotropic alignment. In simpler terms keeping above understanding in mind one will expect enhanced flexoelectric response in

the system with weak anchoring on one substrate. Note here we will still need a strong anchoring condtion on one of the substrate to dictate the director re-orientation along the field lines. A number of theoretical and experimental reports[128, 131], corroborates the above assumption. Helfrich *et.al* reported polarity dependent flexoelectric-optical effect in a homeotropic geometry having strong anchoring on one substrate and weak on other [128].

In our system, an increase in flexoelectric response translates to increase in the magnitude of the defect movement. To investigate this, we followed the same steps mentioned above in section.5.3.2. Similar to previous observation, introduction of A.C. voltage $(V > 4V)$ in the system forms alternating HAN structures (fig.5.17) in the nematic layer. For, $V < 4V$ device stays in its initial unperturbed state on account of inefficacy of electric field to switch the nematic layer. On application of D.C. voltage system reveals similar polarity dependent response for both the frequency of the square wave (f=0.1Hz, and f=0.05 Hz). Figure 5.18 and Figure 5.19 represents defects position during different D.C. polarity having magnitude of applied voltages ($V = 4V$ to $V = 12.5V$). Polarity plots for the same, showing movement of the defects overtime under two different square wave frequency in the system are given in fig.5.20 and fig.5.21. As shown in the section above, for voltages $V > 10V$ in the system, a destruction of alternating HAN structures was observed for both the square wave having frequency f=0.1 Hz, and f=0.05 Hz, with zig-zag defects merging into one another (fig.5.22 and fig. 5.23) on voltage increase.
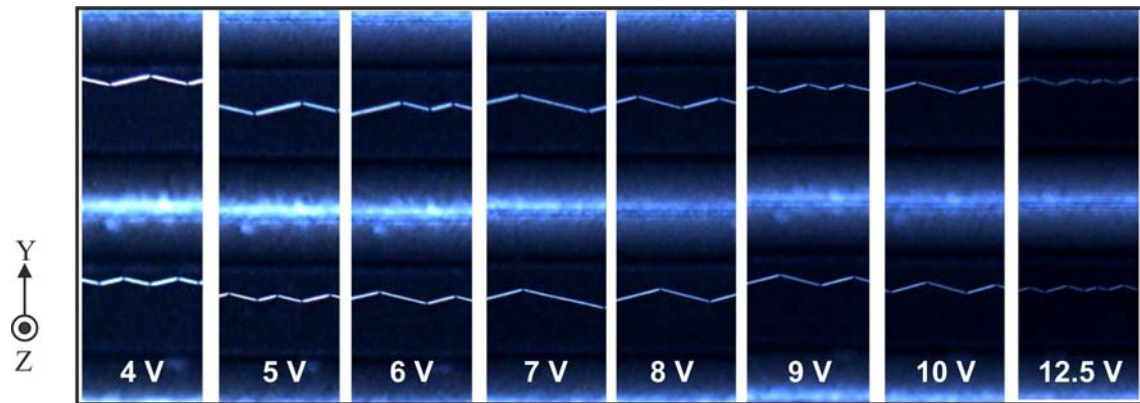
Figure 5.17: Optical micrograph of the actual device (open system/no top) consisting of MDA 13-2167 liquid crystal layer under plane-polarised light with a crossed analyser, showing defect walls separating alternating HAN domains at different A.C. voltages (please note device is not tilted in the picture above).
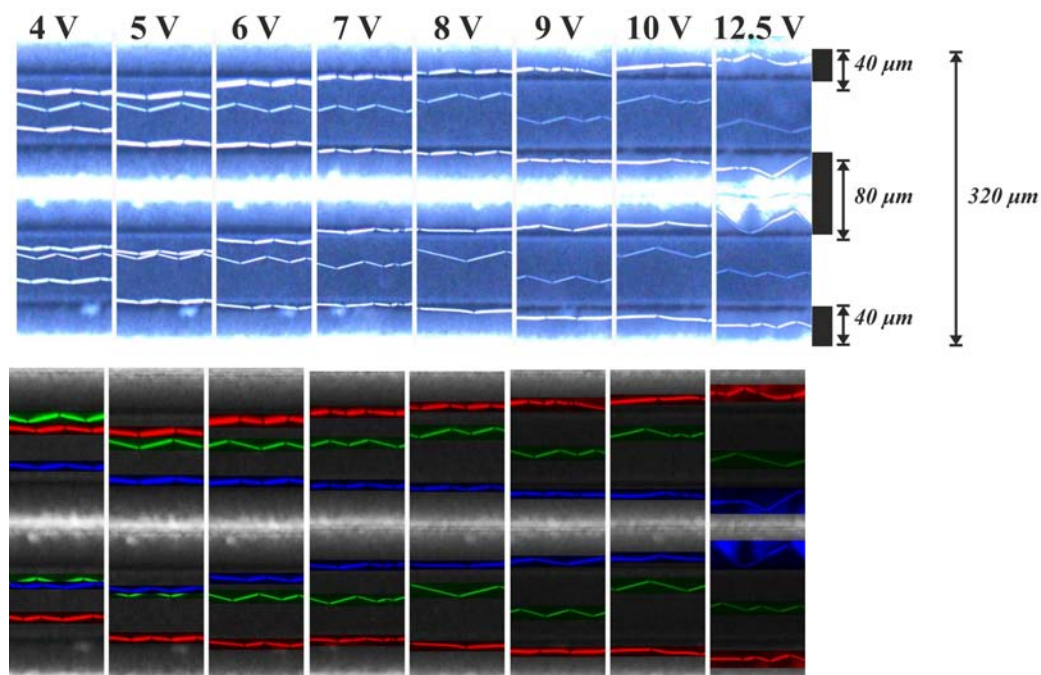
Figure 5.18: MDA 13-2167 (open system), composite image showing polarity dependent zig-zag defect wall movement in electrode gaps at different applied D.C. voltages (D.C., 0.1 Hz, square wave). The pseudo colour image is shown below the picture where, green, red, and blue colour represent zig-zag defect position in the sample during A.C, +D.C. and -D.C. voltages respectively.
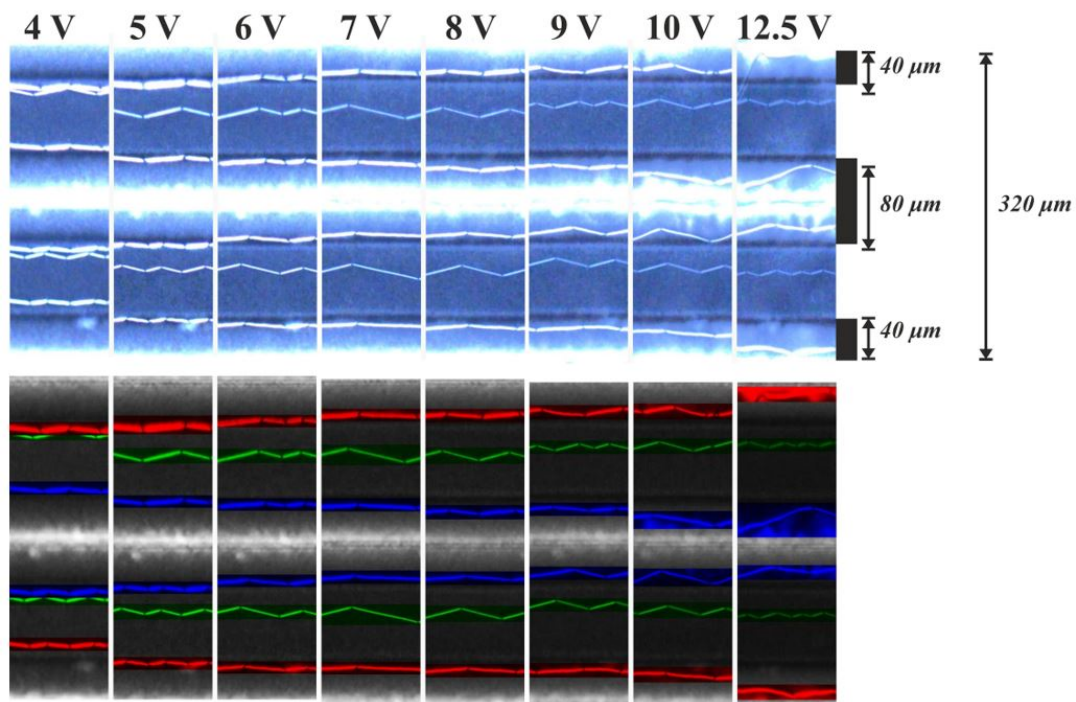
Figure 5.19: MDA 13-2167 (open system), composite image showing polarity dependent zig-zag defect wall movement in electrode gaps at different applied D.C. voltages (D.C., 0.05 Hz, square wave). The pseudo colour image is shown below the picture where, green, red, and blue colour represent zig-zag defect position in the sample during A.C, +D.C. and -D.C. voltages respectively.
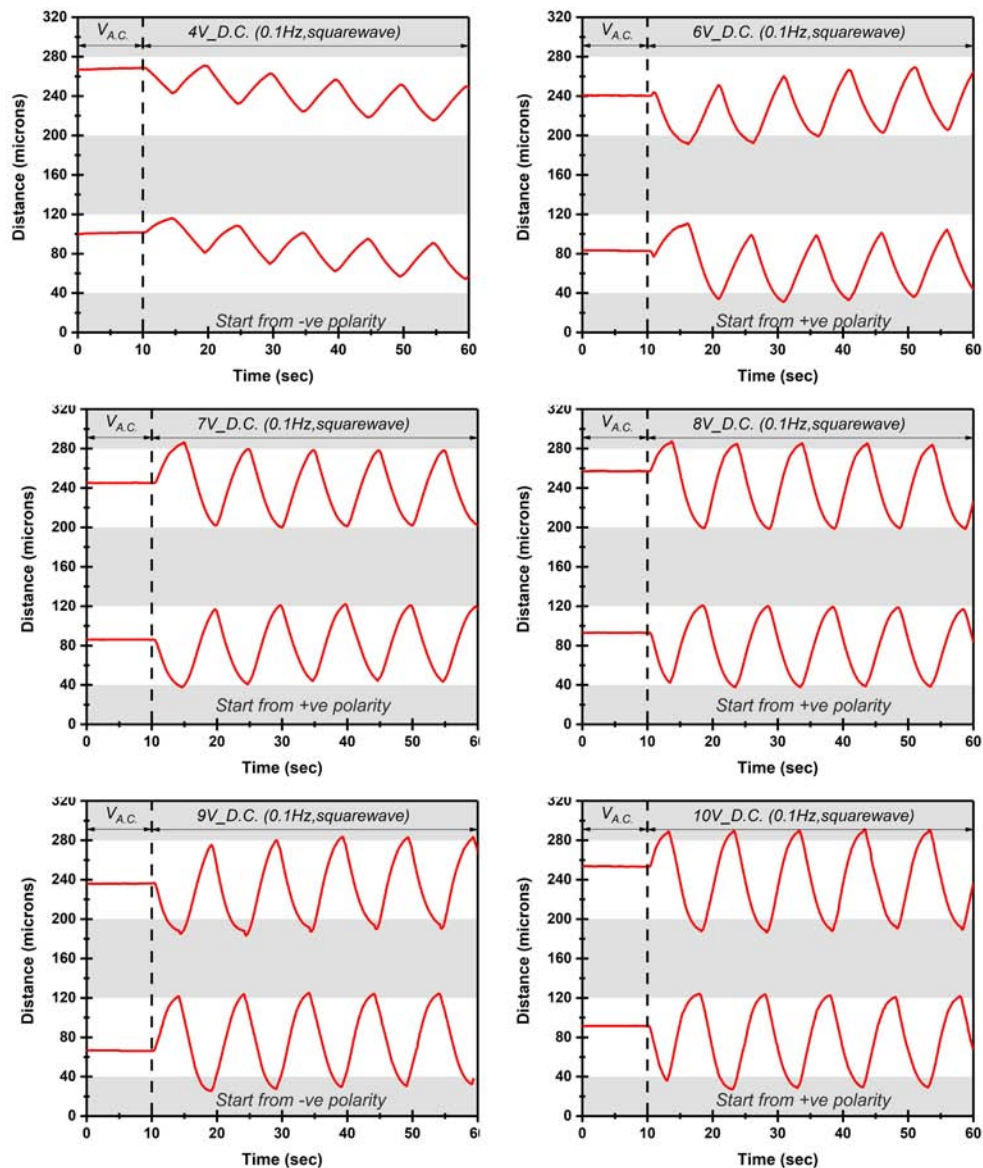
Figure 5.20: MDA 13-2167 (open system) plots showing polarity dependent movement of zig-zag defect wall (solid red line) overtime in the electrode gap (white regions in the plot) under different D.C. voltages (D.C., 0.1 Hz, squarewave). Start polarity sign of each D.C. voltage after the swap is mentioned on respective plots (please note the length of first (±) polarity cycle immediately after voltage swap from A.C. to D. C. is arbitrary and in most of the cases it's not equivalent to (T/2) of the set square wave frequency. Gray colour area represents the region of the electrode in the plots.
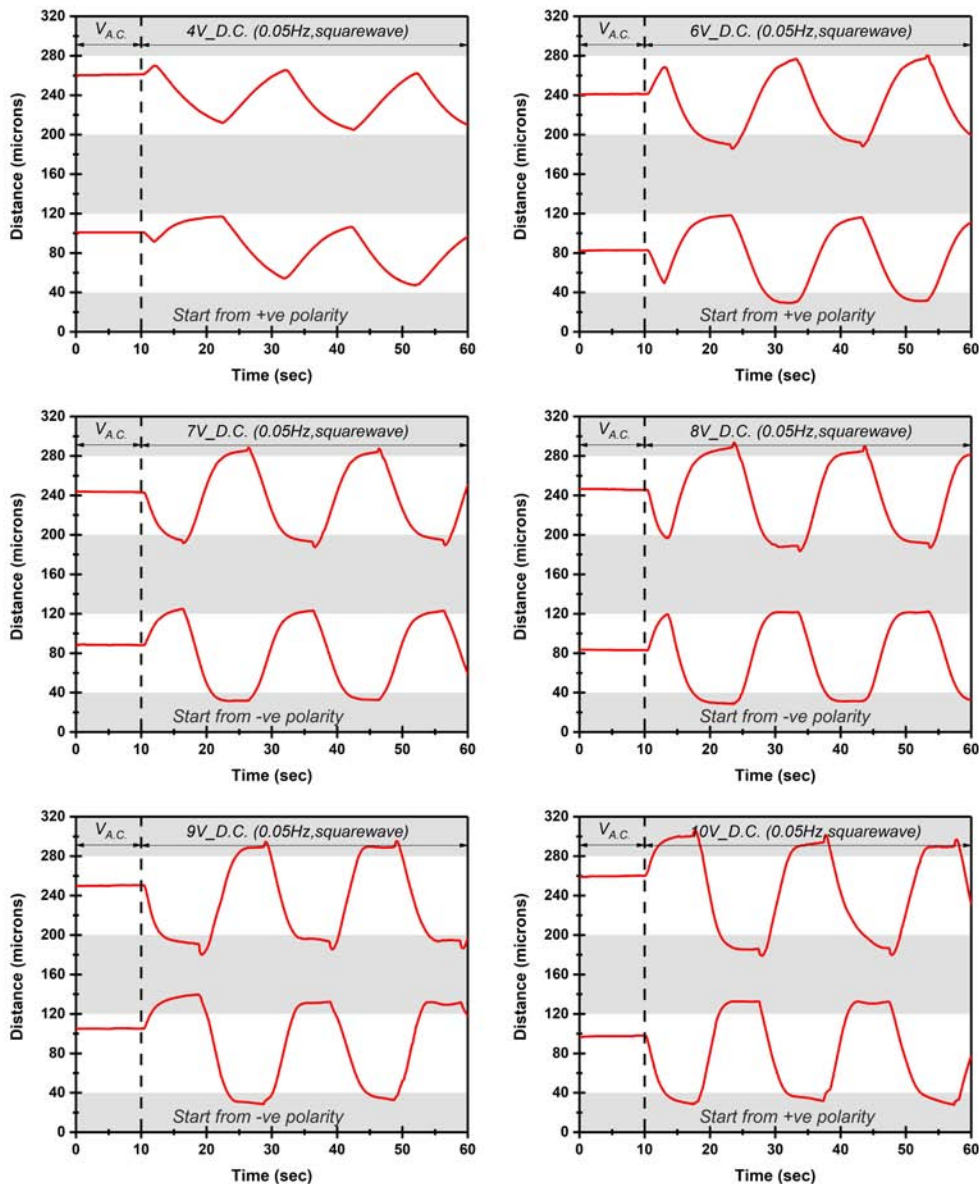
Figure 5.21: MDA 13-2167 (open system) plots showing polarity dependent movement of zig-zag defect wall (solid red line) overtime in the electrode gap (white regions in the plot) under different D.C. voltages (D.C., 0.05 Hz, square wave). Start polarity sign of each D.C. voltage after the swap is mentioned on respective plots (please note the length of first (±) polarity cycle immediately after voltage swap from A.C. to D. C. is arbitrary and in most of the cases it's not equivalent to (T/2) of the set square wave frequency. Gray colour area represents the region of the electrode in the plots.
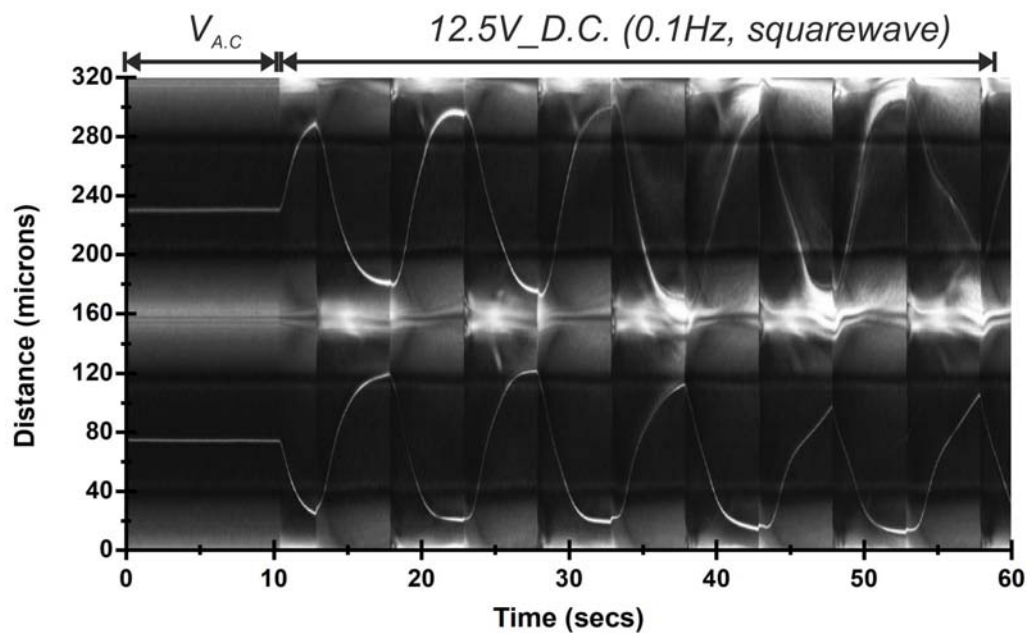
Figure 5.22: Image plot shows merging of the two HAN domains in MDA 13-2167 (open system), at an applied voltage of 12.5 V (0.1 Hz, square wave).
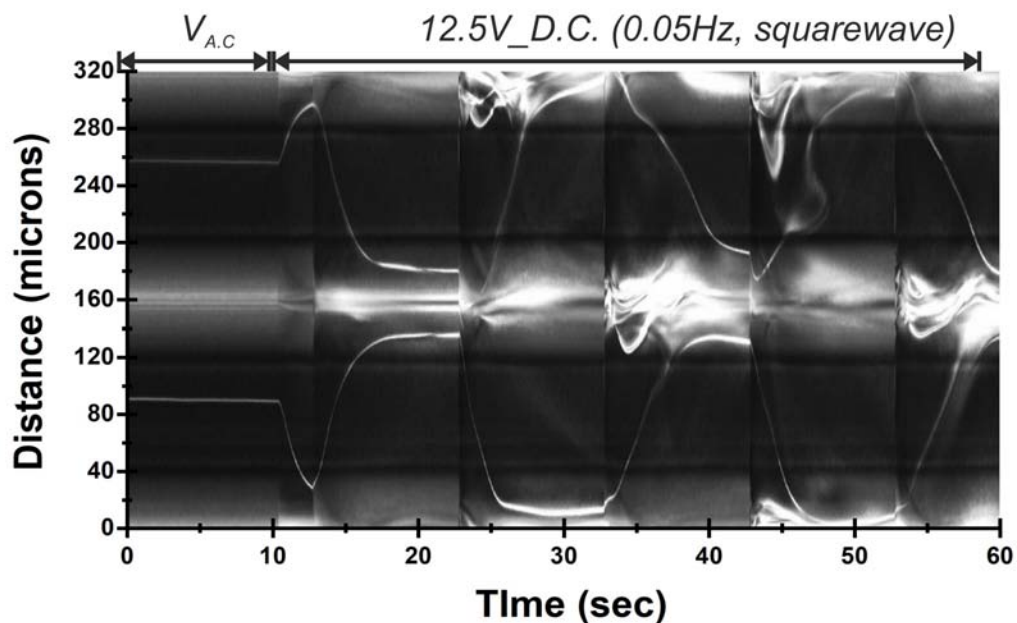
Figure 5.23: Image plot shows merging of the two HAN domains in MDA 13-2167 (open system), at an applied D.C. voltage of 12.5 V (0.05 Hz, square wave).

5.3.3   Comparison of defect movement studies

It's evident from all the motives mentioned above that to determine the extent of flexoelectric polarisation in a system one requires an in-depth understanding of relation of flexoelectricity with other physical parameters. The results from all the six studies are used to investigate the effect of dielectric anisotropy, anchoring energy on the flexoelectricity. The selection of these system is sensible because:

a) Study 1 and 2 (E1 closed system): Provides control measurement for comparison of the defect movement. As E1 contain high ionic content, it will help us to understand how our system responds to ions.

b) Study 3 and 4 (MDA closed system): Being high dielectric anisotropy nematic material it will help us to understand the effect of dielectric anisotropy on flexoelectric polarisation (i.e extent of defect movement) in the system.

c) Study 5 and 6 (MDA open system): Explores the effect of surface-anchoring energy on flexoelectric polarisation.
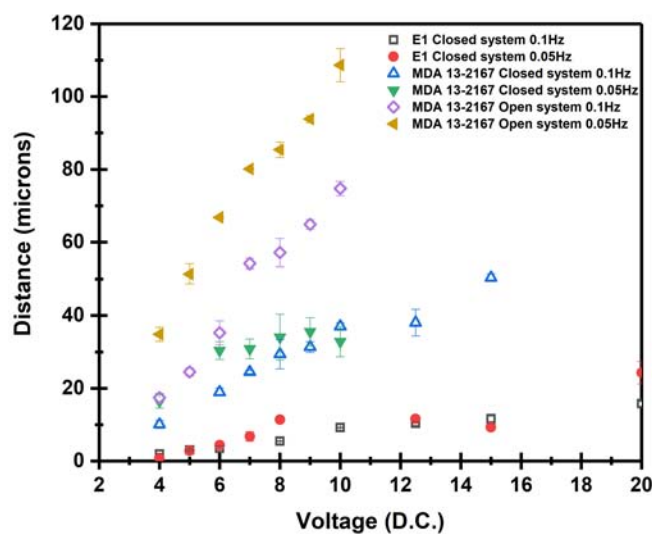
Figure 5.24: Plot showing magnitude of defect movement as a function of different D.C. voltages (square wave, f=0.1 Hz and f=0.05Hz) in six conducted studies.

Figure 5.24 shows magnitude of defect movement as function of applied D.C. (square wave, f=0.1 Hz and f=0.05Hz) voltages, in all the studies. In the six conducted studies we found that magnitude of defect movement increases linearly with an increases in the applied D.C. voltage in the system. The key observation from all the studies are:

a) In case of E1 closed system (study 1 and 2), two different frequency (0.1Hz, and 0.05Hz) of square wave seems to have negligible effect on the defect movement in majority of the voltage measurements. In both the studies, negligible shift in the defect position was observed for low voltages $V \leq 6V$, for voltage range $V = 7V$ to $V = 15V$ a slight shift of 10±1.5 μm was observed in the system. However, as the magnitude of the voltage is increased to $V = 20\ V$, a significant shift (18±2 μm) was observed in the system. This study concluded that in case of low permittivity material (E1), for $V \leq 10\ V$, defect movement due to flexoelectric polarisation in the system is small.

b) In case of MDA 13-2167 closed system (study 3 and 4), two different frequency (0.1Hz, and 0.05Hz) of square wave seems to have similar effect on the defect movement for applied voltage range $(V = 4V$ to $V = 15V)$. However, unlike E1, a sharp increase in movement of defect was observed with voltage increment for both the frequency of the square wave. A maximum movement of 34±3 μm and a minimum movement of 12.5±2 μm was observed at 10 V (0.05Hz) and 4V (0.05Hz) respectively. Results from the study supports the fact that high dielectric anisotropy materials show high flexoelectric polarisation in the system.

c) In case of MDA 13-2167 open system (study 5 and 6), maximum movement in defect was observed compared to previous four studies. However, contrary to the above observation, two different pulse length of D.C. voltage seems to have quite distinct effect on the system. Defect movement in case of longer pulse length is significantly higher than then

the shorter pulse length. This is because a time period of 5s is not sufficient for the defect to attain a steady state. Results from the data sets having pulse length of 10s shows defect remain in transient state for a time period of 6 secs. Furthermore, in this two studies a maximum movement of about 108 μm and 75 μm and a minimum movement 35 and 17 μm was observed in case of D.C. pulse length 10s and 5 s respectively. It clear from the results that presence of weak anchoring on the top and high dielectric permittivity increases the flexoelectric effect in the system.

In summary, we can conclude that in our system flexoelectricity in nematic is dependent upon dielectric anisotropy and anchoring strength of the homeotropic substrate. Larger the dielectric anisotropy, greater will be the flexoelectric effect and therefore the movement of the defect. In case of anchoring conditions presence of weak homeotropic anchoring, enhances the flexoelectric effect in the system.

5.3.4 Understanding the flexoelectric influence on nematic- air interface of hybrid aligned nematic layer.

So far, we have discussed the effect of D.C. voltage on internal ordering of the liquid crystals i.e. the formation of defects in the hybrid nematic layers and their polarity dependent movement. In this section we will study the surface effect on nematic air interface, that occur in the system whilst defect shows polarity dependent movement in the device. Before, discussing the D.C. voltage effects let us understand the effect of A.C. voltage on nematic-air interface.

5.3.5 Effect of A.C. voltage on nematic air interface
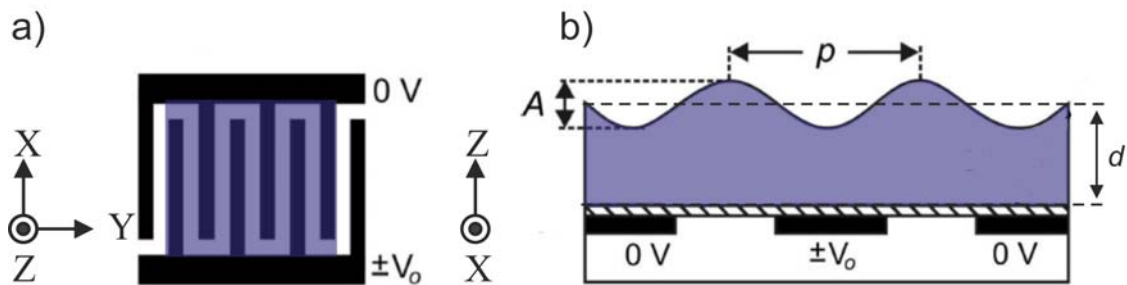
Figure 5.25: Schematic of the open system, a) liquid crystal film (purple colour region) spread on the interdigitated electrodes at an applied voltage (top plane view), b) side view of the film at an applied voltage, showing the formation of wrinkle profile on the liquid-air interface.

Application of the voltage to the interdigitated electrodes (IDE) in the device, creates a non-uniform spatially varying electric field which has the same period as the electrodes. Due to the presence of the non-uniform electric field, liquid crystals experience a dielec-

tric force in the direction of the increase in magnitude of the electric field gradient. At a certain threshold value, when the magnitude of the dielectric force is greater than the surface tension of the liquid crystal droplet. The droplet resting on IDE substrate spreads across the electrode patch creating a uniform film as shown in Fig.5.25a. As the voltage is increased further than the intial spreading voltage, dielectric force forms a wrinkle on the surface of the spread film. This is due to preferential collection of liquid crystals in the region of high electric field gradient, which exist near the electrode edges [132, 133]. Fig.5.25b shows a schematic of wrinkle formed in the system when a voltage was applied to the device. The period of the wrinkle is equal to the electrode pitch and the crests and troughs are parallel to the length of the electrodes along x-direction.

To study, the evolution of wrinkle profle at nematic-air interface as a function of applied A.C. voltage, the device was imaged using MZ interferometer. As described above in section 5.2.1.2, liquid crystal director orientation (along y-axis) and polarisation plane of interferometer light (along x-axis) is setup orthogonal to each other allowing us to observe the change in the surface profile of the nematic layer under different applied voltage.

In our experiment, a droplet of MDA 13-2167 liquid crystals (0.3± 0.05 µl) was initially dispensed on the center of the electrode patch (5×5 mm, $w_e = w_g = 80$ $µ$m) coated with solid thin film planar alignment layer (easy alignment axis in the y-direction) of MgF$_2$/ZnS. We then apply a A.C. voltage (100 V, 1kHz , sine wave) to the device high enough to spread the droplet into a thin layer covering the entire electrode patch. The spread film was then allowed to relax and voltage is removed from the system. With the knowledge of the refractive index of the liquid crystals, the thickness of the spread film layer is determined using interferometer as discussed previously in section.5.2.1.2. Note here because the solid thin film alignment layer is a wetting surface we don't observe retraction in the spread film on voltage removal. A range of A.C. voltage ($V = 0$ to

$V = 20V)$ was then applied to the spread film, with a relaxation period of 5 mins in between each voltage measurement. There was some redistribution of liquid across the film as the magnitude of the voltage is increased. The images (interferograms) of resulting wrinkle profile was captured at each voltage level and analysed further.
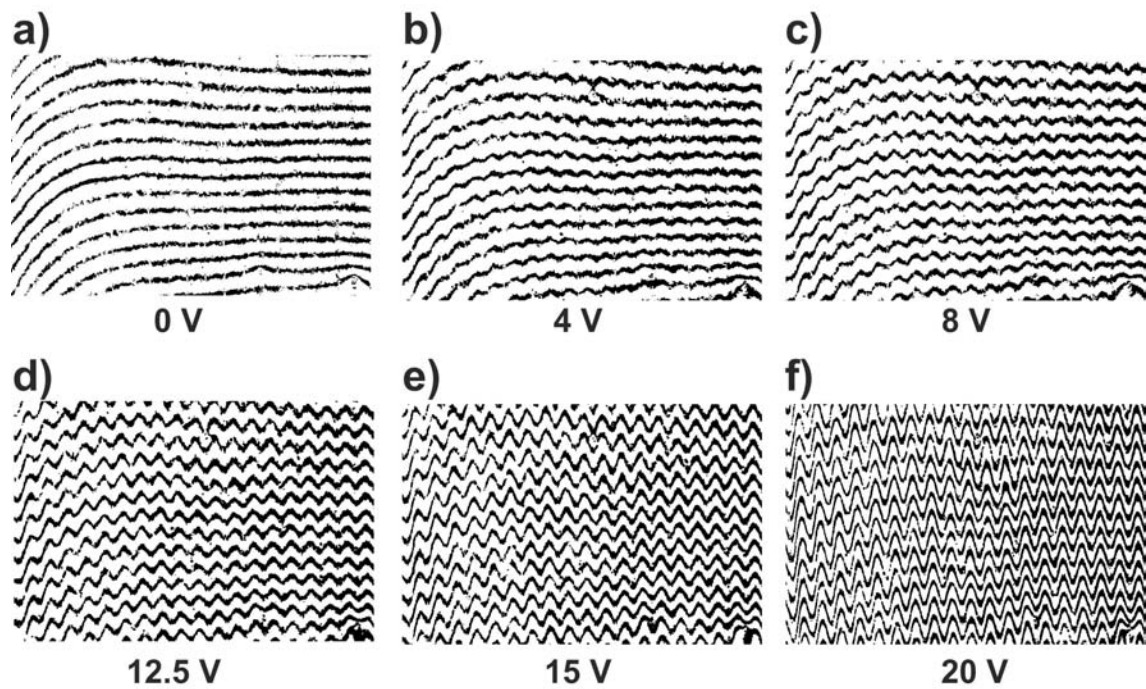
Figure 5.26: Digitised interferogram images, MDA 13-2167 film (d=10.08±1 μm) showing variation in the wrinkle amplitude as a function of applied A.C. voltages (1 kHz, sinewave).

Figure 5.26 represents digitised interferograms of the nematic layer ($d = 10.08 \pm 1\ \mu$m) showing wrinkles formation at nematic-air interface under different applied voltages, $V = 4 - 20$ V. In the absence of the voltage, no change in the surface profile of the initial spread film was observed. However, as the voltage is increased in the system from $V = 4$ V to $V = 20$ V, surface profile evolves it's pattern into a sinusoidal wrinkle with amplitude of the wrinkle increasing on voltage ramp. Plots showing growth of the wrinkle amplitude as a function of different applied A.C. voltage is given in figure 5.27. The peak-to-peak (p-p) amplitude of the wrinkle ranges from 0.17-3.14 μm under an applied voltage range, $V =$

$4 - 25$ V. The formed wrinkles on the nematic-air interface are found to be reproducible and static for fixed A.C. voltages.
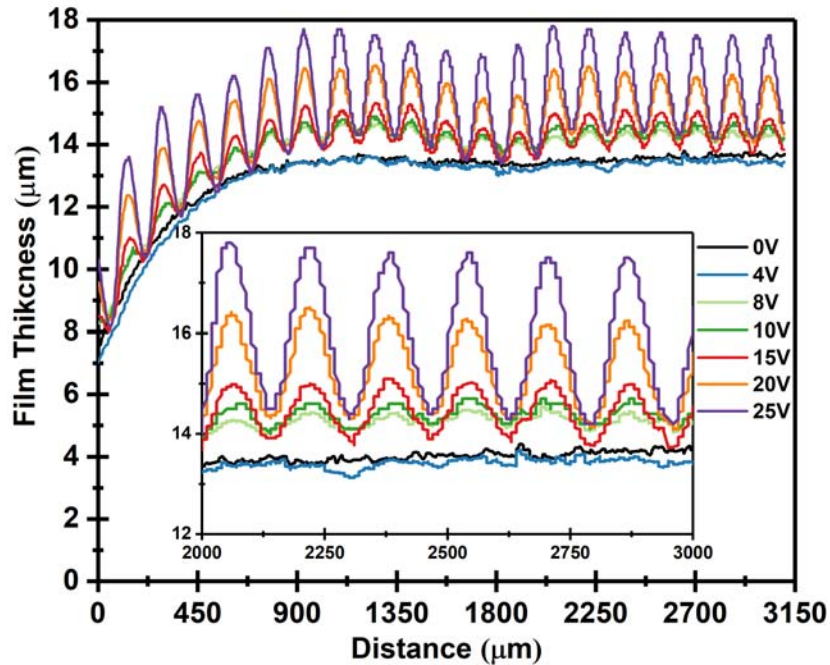
Figure 5.27: MDA 13-2167 film ($d = 10.08 \pm 1$ μm), wrinkle profiles obtained from interferogram images showing variation in wrinkle amplitude at different applied A.C. voltages (1 kHz, sine wave).

5.3.6   Effect of D.C. voltage on free surface wrinkles formed at nematic-air interface

It evident from the studies reported in the section5.3.2 and section 5.3.5, that the application of A.C.voltages in an open device geometry creates an alternating HAN domains in the nematic layer and surface wrinkles on the nematic-air interface. In the previous studies we have also established that application of D.C. voltage to a nematic layer having free top surface lead to polarity dependent movement of the defect. Now, to understand the effect of D.C. voltage on surface wrinkle together with the defect movement. We se-

lected two different voltages, 4V and 10V from our previous data sets for further studies. The selection of the voltages is based on three facts a) at both the voltages alternating HAN domains exist in the device, b) application of selected D.C. voltage doesn't lead to destruction of the HAN domains, c) surface wrinkle at nematic-air interface was observed for both the voltages.

We now describe the results of the study of the D.C. voltage effect on the surface wrinkle. The surface wrinkle formed on application of A.C. voltage was used as a starting point for the applied D.C. voltage of the same amplitude. Briefly, we followed the same steps as described above in section 5.3.2 i.e , initially an A.C. voltage (V, 1 kHz, square wave) was applied to the device for a duration of 10 secs, allowing formation of surface wrinkle in the device, after 10 sec A.C. voltage is swapped with D.C. voltage of the same amplitude. The polarity varying D.C. voltage (i.e square wave having f=0.1Hz and f=0.05Hz) was left on for next 50s and at t=60s voltage is turned off for 5 mins to allow the device to resettle. These steps are repeated for each voltage measurement reported in the studies.

Figure 5.28 and 5.30 shows series of snapshopts of device under interferometer that follows the dynamics process of surface wrinkle lateral shift as the polarity of the applied D.C. voltages (4V, 10V) was swapped at two different square wave frequency (0.1Hz and 0.05Hz) in the system. The first image in each set of time series, shows the wrinkle profile in presence of A.C. voltage, then afterawards a positive (+) D.C. voltage was applied followed by a (-) D.C. voltage. Plots shown in figure 5.29 and figure 5.31 have been extracted from the images taken on the interferometer corresponding to Figure 5.28 and 5.30. The green solid line in the plots shows A.C. wrinkle profile, and the solid red and blue line represents time-evolution of wrinkle profile in presence of positive and negative D.C. cycle respectively. The final wrinkle profile at respective polarity of D.C. voltage is

shown by dashed line in the plots. Experimental results from the interferometry shows that upon application of A.C. voltage (1kHz, square wave), the nematic-air interface corrugates along y-direction creating a sinusoidal surface wrinkle having period (P_w) equal to electrode pitch (P_e) and amplitude depending upon magnitude of applied voltage (V). The observed wrinkle having a period of 160 μm similar to to electrode pitch arise from dielectric reponse of the nematic layer subjected to non-uniform electric field. However, as, the A.C. voltage is swapped with the D.C. voltage (square wave, 0.1Hz and 0.05Hz) system reveals a flexoelectric reponses, with evolution of a surface wrinkle having periodicity of $2P_e$ (320 μm). The formed surface wrinkle got higher amplitude compared to A.C. wrinkle at the same voltage level. This is due to frequency dependent dielectric anisotropy of the nematic material, as shown in fig.5.5 the dielectric anisotropy $(+\Delta\varepsilon)$ of MDA 13-2167 is 400.12 at 1 kHz and 523 for, $f < 300Hz$. Interestingly, we found that similar to behaviour described above in section 5.3.1, and illustrated in Figures 5.7(c) and 5.7(d), in which a D.C. voltage shifts the defects between opposite HAN domains in a direction determined by the polarity of the electric field applied across the wall, is accompanied for the case of a nematic film with an upper free surface by a polarity dependent asymmetry which is superimposed onto the periodic surface wrinkle. The wrinkle formed at air-nematic interface for two different polarities($\pm$) of D.C. voltage was found 180 degree out of phase from each other. This effect can be can be clearly observed in dashed wrinkle profile shown in figure 5.29b and figure 5.31b. To ensure the observed effect, we also imaged the side profile of wrinkle, outside the interferometer setup. Figure. 5.32 shows actual image of side profile of wrinkle formed at interface during different D.C. Polarity.
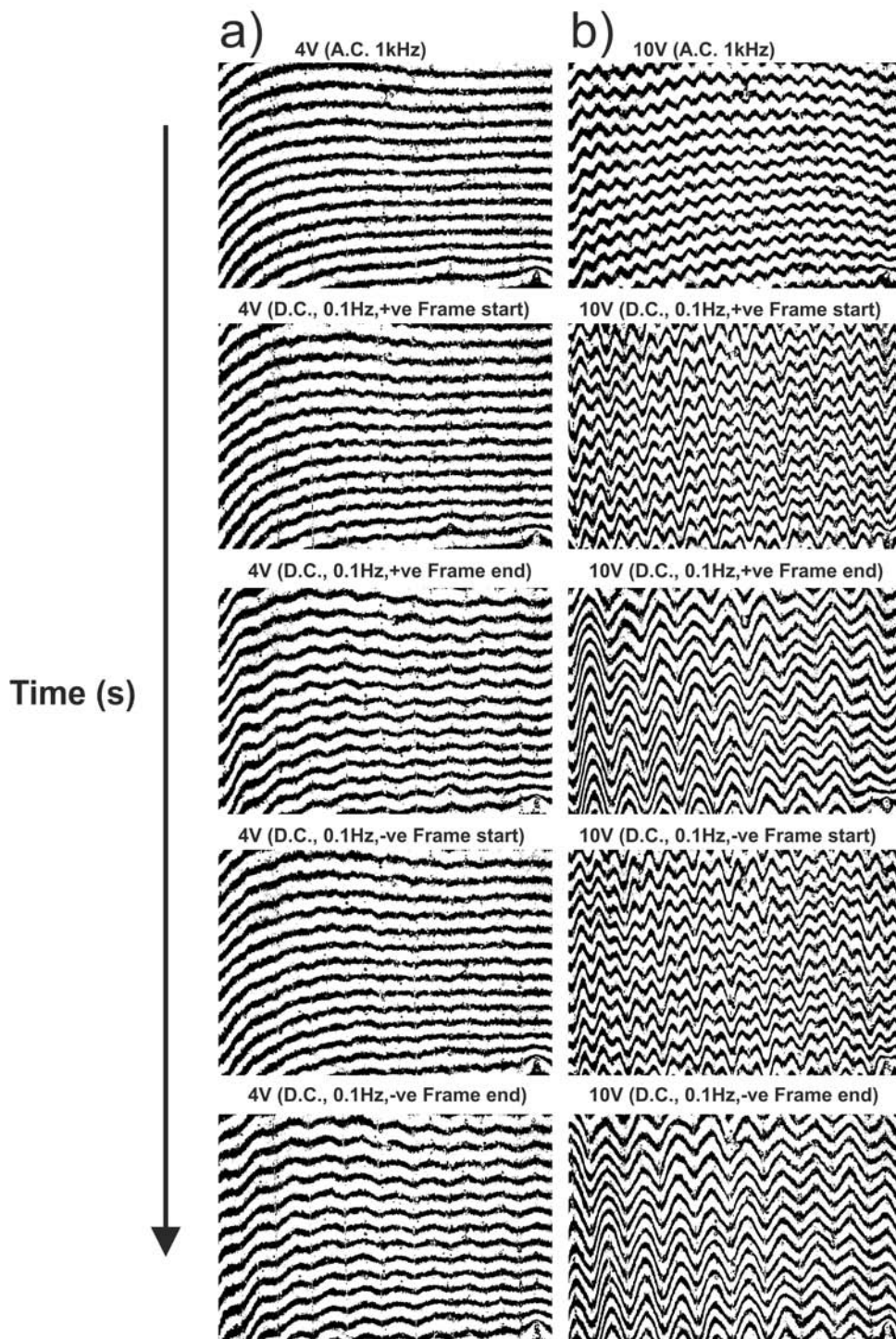
Figure 5.28: MDA 13-2167 film (d=10.08±1 μm), time-sequence images showing polarity dependent movement of surface wrinkle under different applied D.C. voltages, (a) voltage swapped from 4V A.C (1 kHz, square wave) to 4V D.C. (0.1 Hz, square wave). (b) Voltage swapped from 10V A.C (1kHz, square wave) to 10V D.C. (0.1 Hz, square wave).
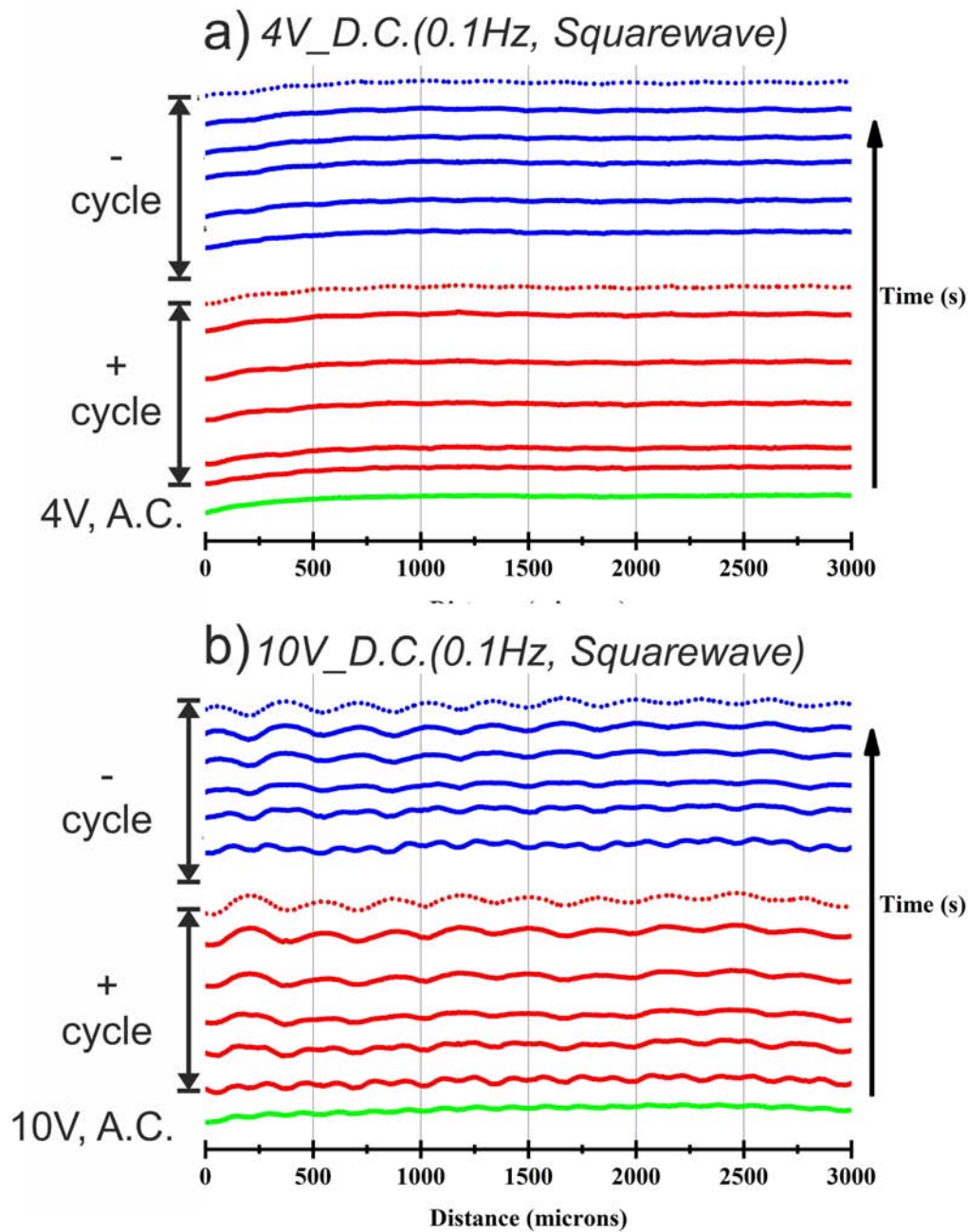
Figure 5.29: MDA 13-2167 film (d=10.08±1 μm), time-evolution of a surface wrinkle profile obtained from interferograms under different applied D.C. voltages, (a) voltage swapped from 4V A.C (1 kHz, square wave) to 4V D.C. (0.1 Hz, square wave). (b) Voltage swapped from 10V A.C (1kHz, square wave) to 10V D.C. (0.1 Hz, square wave)
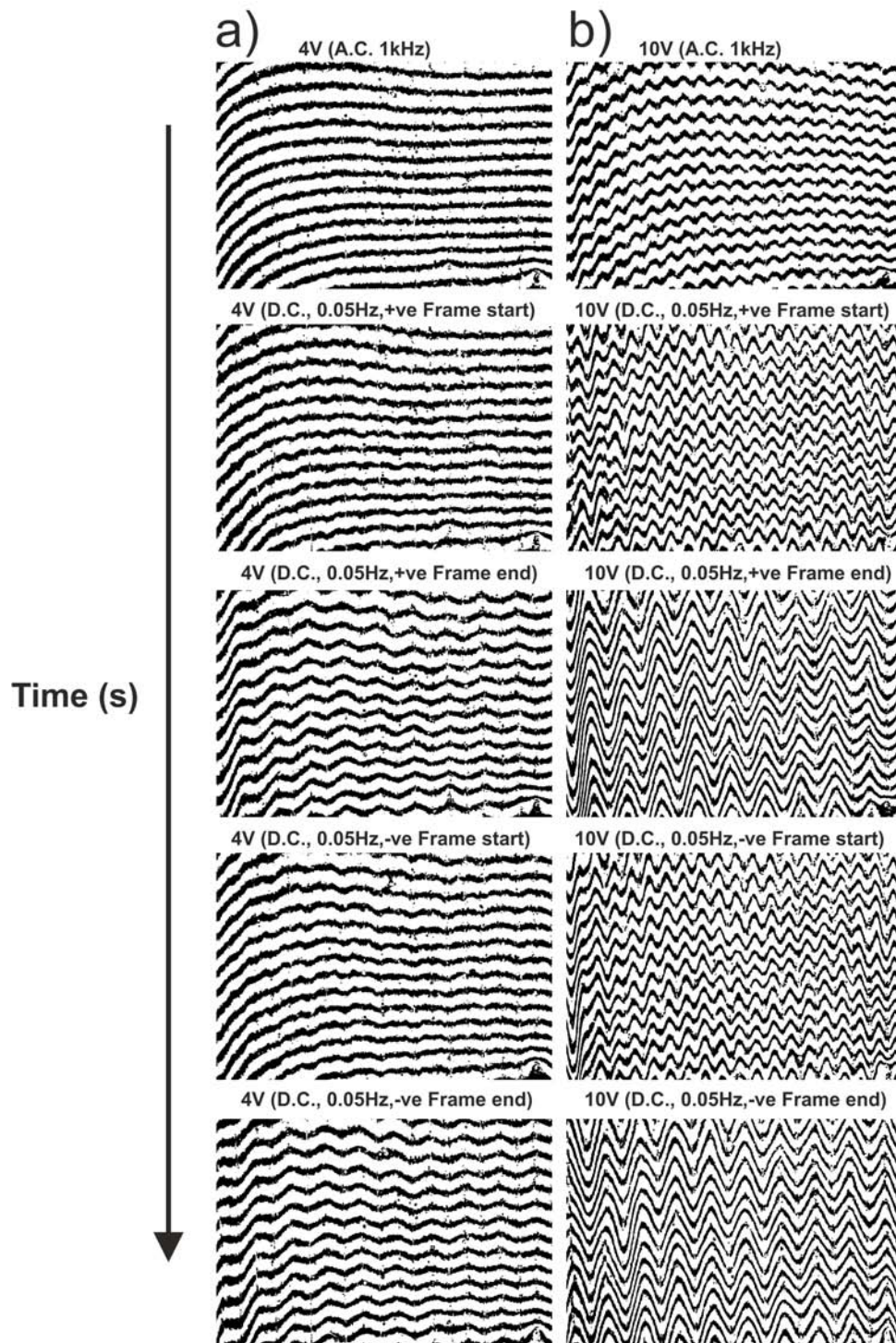
Figure 5.30: MDA 13-2167 film (d=10.08±1 μm), time-sequence images showing polarity dependent movement of surface wrinkle under different applied D.C. voltages, (a) voltage swapped from 4V A.C (1 kHz, square wave) to 4V D.C. (0.05 Hz, square wave). (b) Voltage swapped from 10V A.C (1kHz, square wave) to 10V D.C. (0.05 Hz, square wave).
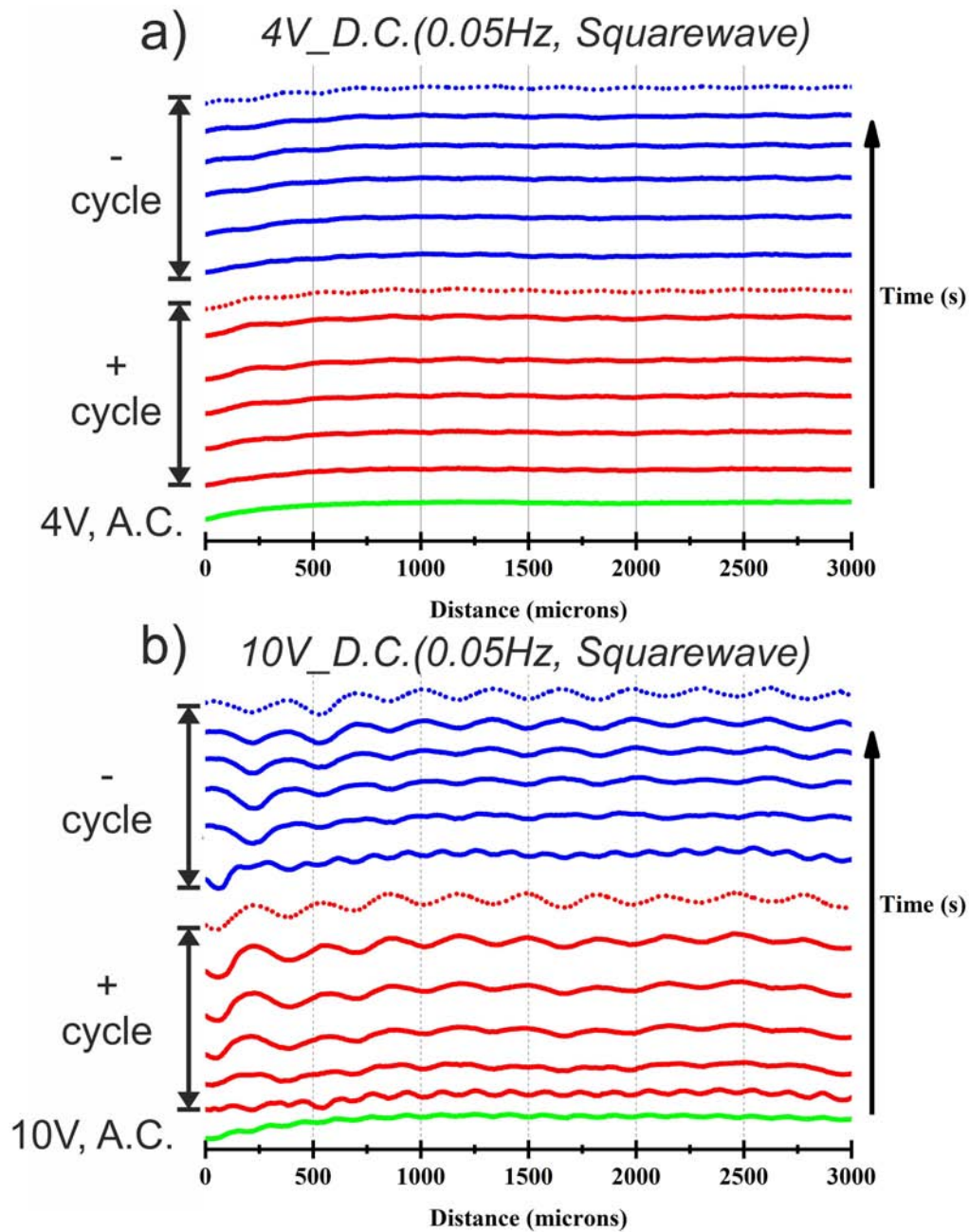
Figure 5.31: MDA 13-2167 film (d=10.08±1 μm), time-evolution of a surface wrinkle

profile obtained from interferograms under different applied D.C. voltages, (a) voltage

swapped from 4V A.C (1 kHz, square wave) to 4V D.C. (0.05 Hz, square wave). (b)

Voltage swapped from 10V A.C (1kHz, square wave) to 10V D.C. (0.05 Hz, square wave).
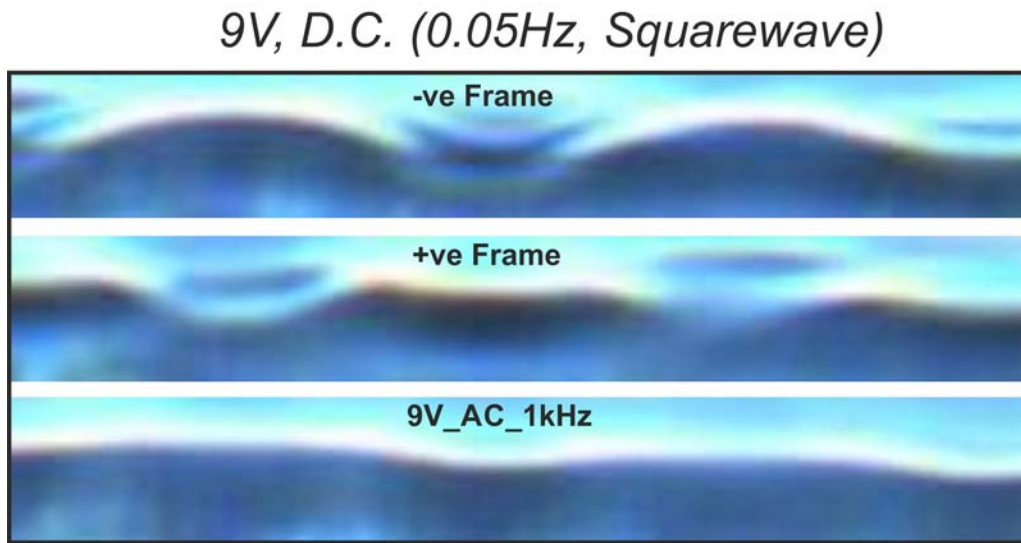
Figure 5.32: MDA 13-2167 film (d=10.08±1 µm), Optical micrographs (side view) of the actual film showing polarity dependent movement of surface wrinkle at 9V D.C. (0.05Hz, square wave).

5.4   Conclusion

We have thoroughly analysed the effect of flexoelectricity in hybrid aligned nematic liquid crystals layer consisting of alternating HAN domains. It was found that modulating the polarity of an applied D.C. electric field induce polarity dependent movement of the intervening tilt walls, as well as the accompanying topological defects, moving in the system as a result of electrostatic coupling to the flexoelectric polarisation. In addition to the polarity dependent response of the defect we also found that in case of the free nematic-air top surface, the periodic wrinkling deformation formed on the interface shows a polarity dependent phase changes at the free surface due to the flexoelectric polarisation in the layer. The novel method presented in this chapter can be applied to different types of nematic liquid crystal materials and can be extended to determine the flexoelectric coefficient of nematic materials.

Chapter 6

Summary and Future work

6.1 Summary

In the first results chapter, we performed experiments, theoretical analysis, and simulations that elucidate the complex nature of surface-flow-field-director coupling in a thin nematic layer. The electrodynamics of nematic director under pressure-driven Poiseuille flow is performed in rectangular microchannel flow cells having uniform planar and homeotropic alignment conditions. To investigate optofluidic and the electro-optofluidic response of n-director different experiments was performed on the flow cells under varying flow-field conditions. Results from the studies report that in case of planar layer of nematic liquid crystal with positive dielectric anisotropy the presence of orthogonal flow and electric field can significantly affect the stability of the different equilibrium director distortion modes associated with the electric Fréedericksz transition bifurcation diagram. In analogy to the $sin(n\pi z/d)$ director distortion modes in a zero-flow classic Fréedericksz transition perturbation analysis, we label these modes $n = 0, 1$. We found that Poiseuille flow parallel to the initial planar alignment direction can extend the $n = 0$ branch, and stabilize the flow distorted $n = 1$ branch at $V_{AC} > V_C$. We also found that that it is possible to

switch between the flow distorted $n = 1$ branch and the classic $n = 1$ branch via abrupt removal and re-application of externally driven flow. In case of a thin homeotropic nematic layer with negative dielectric anisotropy, n-director response to orthogonal flow and the electric field was studied in V-state, where n-director in the middle of the cell is aligned in initial homeotropic alignment. Preliminary results from the studies show that it is possible to switch flowing V-state below the critical threshold of classic Fréedericksz curve thus revealing contraction of $n = 0$ mode and the existence of flow-promoted Fréedericksz transition.

In the second results chapter of the thesis, we report an electrically controllable microcargo transportation device that employs a topological defect in a hybrid aligned (HAN) nematic layer for particle trapping and manipulation. We have created two stable coexisting equilibrium opposing HAN tilt orientation domains which are separated by an elastic wall that contains a line defect. Applying an A.C. voltage produces electrical confinement that distorts the shapes of the domains and evolves a tortuous intervening wall shape with high curvature tip regions. We quantitatively explain the time evolution of the shape of the wall using a nematic continuum theory model which has a soliton-like traveling wave solution since both opposing HAN states are equally possible. We have used this high curvature tip feature on the electric field confined domain wall to collect, trap, and move a microparticle. This provides straightforward precision A.C. voltage control of the positive and negative linear movement and placement of the particle, without any need for externally imposed flow, nor lateral confining walls or geometric or alignment texturing.

In the final chapter of the thesis, we investigate the effect of flexoelectricity in a hybrid aligned nematic layer. We found that the application of a spatially periodic in-plane A.C. electric field to the device creates an array of alternating hybrid aligned domains separated by topological defect lines. Results from that study show that modulating the polarity of an applied D.C. electric field in the device demonstrates the polarity dependent movement of the intervening tilt walls, as well as the accompanying topological defects as a result of electrostatic coupling to the flexoelectric polarisation. In case of the positive nematic layer with a free upper surface, we found that the polarity dependent movement of the topologically defects is accompanied by a polarity dependent phase changes in the periodic wrinkling deformation at the free surface

6.2   Liquid crystals microfluidics

6.2.1   Liquid crystals director dynamics during one drop filling

From the time of formulation of this work, we have investigated multiple numbers of conditions (nematic alignment, dielectric anisotropy, electrode geometry) presence of which can alter the internal orientational ordering of nematic liquid crystals under flow. Although, this provides insights into the fundamental understanding of the evolution of different director profiles under flow. For the wider applicability of the research, it would be interesting to investigate these director -reorientations during flow in the industrial display filling process.

As an extension of the work, much recently we started investigating the flow effect on the polymeric alignment layer during One-drop filling (ODF) technique. ODF is a newly adapted industrial display filling technique that enhances the device production rate as the filling process take usually 1-2 hr [134–136] compared to the traditional capillary filling

technique where it takes 1-2 days [134–136]. ODF method involves squeezing of an array of droplets (usually nanolitres (nL) volume) placed on one substrate (bottom) whilst being squeezed by the other substrate (top) moving at a velocity until the droplets coalesce into liquid crystals film. To further increase the production rate, an increase in the velocity of the top moving plate is required however, this may lead to detrimental effects due to director re-orientation at different regions of the display. Preliminary results shown below aim to investigate the effect of flow on the homeotropic polymeric alignment layer during the ODF process. Briefly, a single drop of liquid crystals (1-2 μl) is placed on the bottom homeotropic layer coated ITO substrate and is squeezed by the top moving plate to fill the display cell. Figure 6.1 shows the time-sequence of drop filling the cell area while the top plate is being moved by a velocity. After filing the device, we use electric field as a probe to investigate the effect of flow on the alignment layer. Preliminary results from studies are shown in figure 6.2. Conducted studies provide an important "proof of concept", namely we can see the alignment damage due to contact line (concentric circles in fig.6.2c) movement during fill.More detailed studies exploring the effect of different top plate velocity, change in defect textures on the application of electric field can provide a better understanding of the process. We are actively, collaborating with our industrial partners (Merck KGaA, Germany) and theoretical teams at the University of Strathclyde and University of Glasgow to explore these effects in detail.
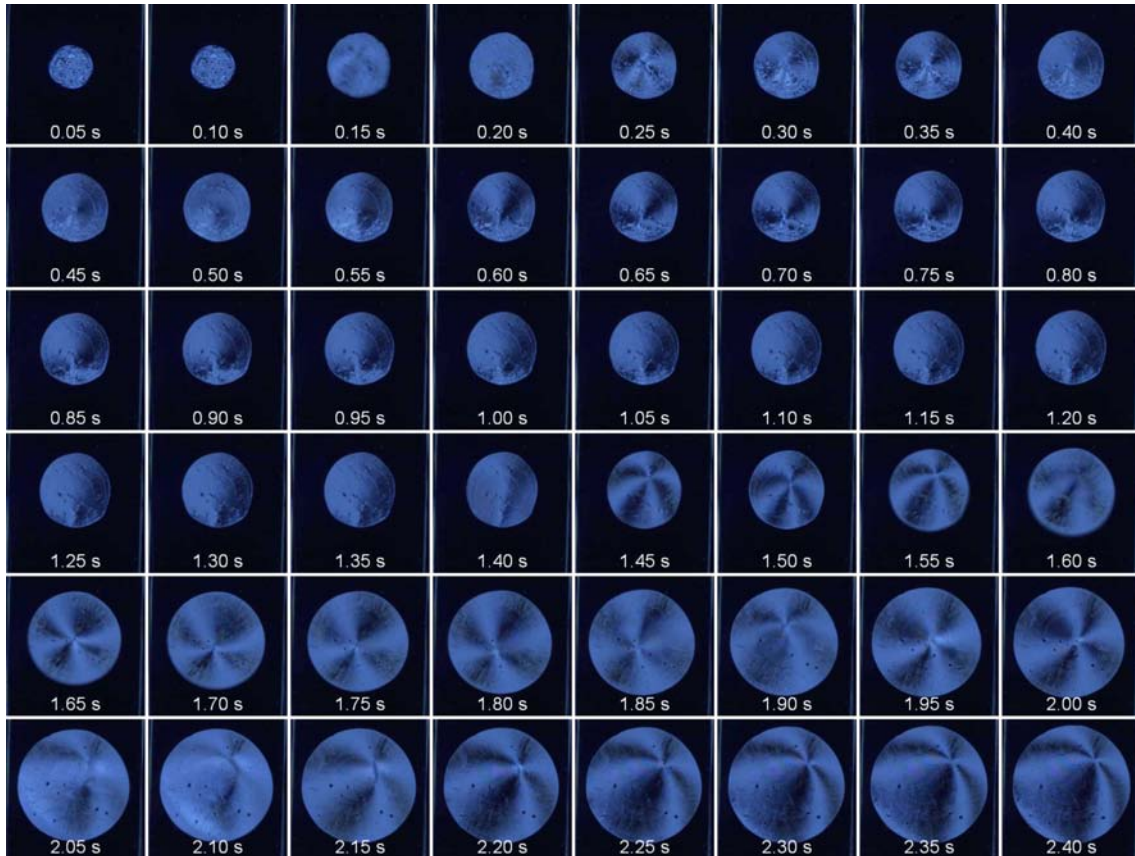
Figure 6.1: Time sequence showing a single drop of liquid crystals filling the display cell

polymeric homeotropic alignment layer. (Polarisers crossed at 45 degree)
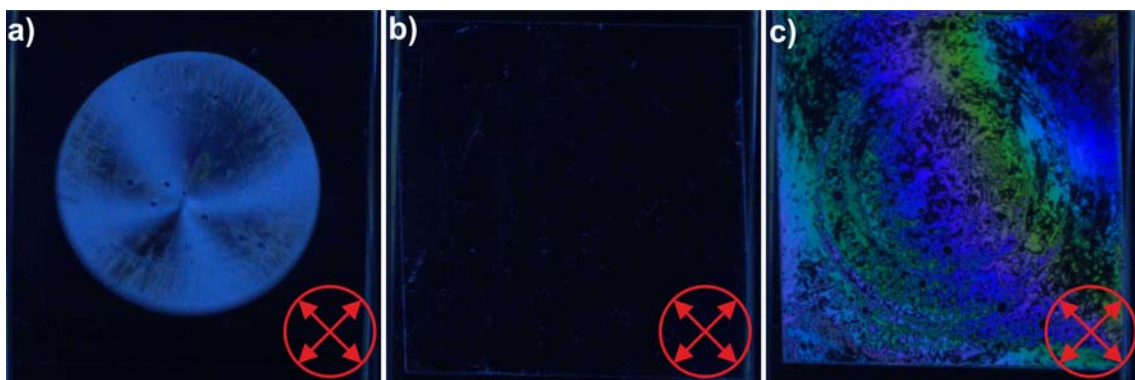
Figure 6.2: Image taken a) during one drop fill, b) after filling process is complete, and

c) on application of electric field to the filled sample.

207

6.2.2 Controlling the free surface of a rivulet using electric field
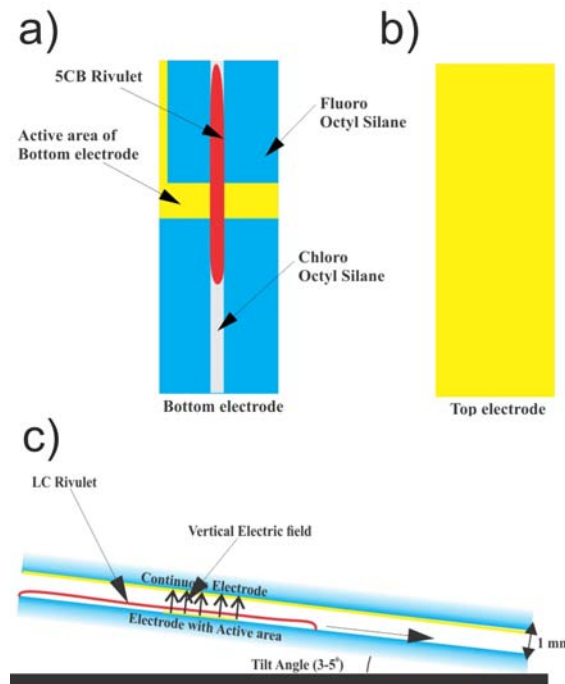
Figure 6.3: Rivulet experimental setup a) bottom substrate showing 5CB rivulet flowing along a specified path dictated by two different silane coatings on the substrate, yellow colour represents the electrode region, b) top substrate (continuous ITO electrode), and c) side-on view of the rivulet experimental setup.

The ability to actively control the internal ordering of nematic liquid crystals, using external fields, anchoring conditions also holds the potential to control the free-surface of flowing nematic liquid crystals layer. Take an example of a liquid crystals rivulet flowing on the homeotropic substrate in the direction of inclination of the plane, application of electric field orthogonal to the flow direction in a certain region of the sample will cause a viscosity change, as the director in this region aligns with the electric field. This will lead to variation in thickness of the rivulet, in the region where the electric field is applied, causing it to change its shape during flow. Figure 6.3 shows setup used for preliminary investigation of proposed hypothesis, in the study a nematic (5CB) rivulet is made to flow

in the direction of the inclination of the sample, and an electric field is applied between the bottom and the top substrate (not in contact with rivulet). Results from the experimental study (fig.6.4) demonstrate an important "proof of concept", namely that we are indeed able to observe significant changes in the free-surface profile due to field-induced changes in the viscosity of a liquid crystal (flow changes due to electric field along the rivulet stream direction for a positive dielectric anisotropy material, shown in Fig. 6.4).
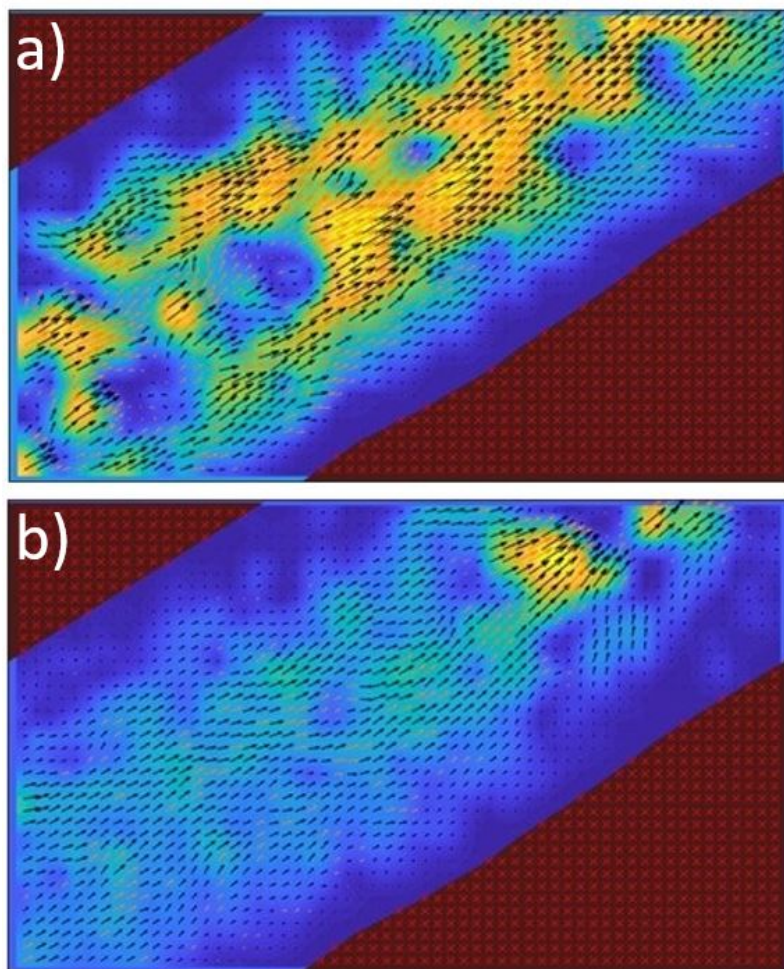
Figure 6.4: Preliminary experimental results. Flow diminution induced by applied electric field within a liquid crystal rivulet. a) Flow with field off, b) Flow with field on, in this case nematic liquid crystal align along the electric field direction thus reducing the velocity of the flow. (yellow= high flow rate, blue= low flow rate)

6.3 Dynamics of topological line defect in a HAN layer

The studies reported in chapter 4, utilise homeotropic anchoring conditions on the particle, which then get trapped in the defect line. A question that arises here is, how will the trapping efficiency of the system vary if the surface anchoring conditions is planar on the particle. Previous, reports have shown that particle with homeotropic alignment is found to be readily attracted to and trapped by the defect, whilst if the surface alignment on the particle is planar the situation is more complex. A repulsive interaction and energetic barrier can exist between the planar particle and disclination lines of strength $+1$ or $\frac{1}{2}$ and so an applied force is required to trap the particle [137]. In addition to the trapping efficiency, the presence of planar condition on the particle can also change the levitation of the particle in the system, because in this case both the planar bottom substrate and particle got director compatibility so particle may sediment in the system. It would be interesting to see how the system response to all these variations in the device. Furthermore, in the model results, we found that increasing the value of anchoring strength (W_0) increased the value of the critical stabilising voltage (V_C). So, the V_C value in our system can provide insight into the anchoring strengths at the surface. Since the strength of both planar and homeotropic anchoring, including on the particle, can be tuned [138–140]. We are interested in a systematic study, investigating V_c dependence on anchoring strength at the surface.

6.4 Flexoelectricity

In the future, we intend to perform the studies using different dielectric anisotropy materials and mixtures of different ionic and non-ionic nematic materials. At the moment present study involves the use of E1 ($\Delta\varepsilon$=12.3) and MDA 13-2167 ($\Delta\varepsilon$=400), using a medium permittivity materials MLC 6681 ($\Delta\varepsilon$=54) will help in establishing the flexo-electric polarisation dependence on dielectric anisotropy. Further to this, the influence of the ions can be systematically studied by making a mixture of non-ionic materials (TL-216) with ionic materials like E7 and E1. In addition to this, it would be interesting to see the effect of electrode spacing on flexoelectricity in the system. Previously, it has been shown that flexoelectricity and its resultant effect like image flickering can be eliminated in the fringe-field switching display cell by varying the electrode spacing [141].

We are also interested to extend this study to investigate whether the observed effect in hybrid geometry can be used to develop a new method for estimation of flexoelectric coefficients of nematic materials. The understanding generated and quantitative values for physical parameters obtained from all the proposed studies described above can also be used to elucidate the role of flexoelectricity in related geometries that are directly relevant to practical display technologies, i.e. FFS (Fringe Field Switching) and IPS (In-Plane Switching) modes.

References

[1]   E Reinitzer. In: *Physik Chemie* 4 (1889), pp. 462–472.

[2]   Pierre-Gilles De Gennes and Jacques Prost. *The physics of liquid crystals*. Vol. 83. Oxford university press, 1993.

[3]   Harry J. Coles and Stephen M. Morris. "Flexoelectro-Optic Liquid Crystal Displays". In: *Handbook of Visual Display Technology*. Ed. by Janglin Chen, Wayne Cranton, and Mark Fihn. Berlin, Heidelberg: Springer Berlin Heidelberg, 2012, pp. 1681–1694. URL: https://doi.org/10.1007/978-3-540-79567-4_100.

[4]   Philip W. Benzie and Steve J. Elston. "Optics of Liquid Crystals and Liquid Crystal Displays". In: *Handbook of Visual Display Technology*. Ed. by Janglin Chen, Wayne Cranton, and Mark Fihn. Berlin, Heidelberg: Springer Berlin Heidelberg, 2012, pp. 1365–1385. URL: https://doi.org/10.1007/978-3-540-79567-4_85.

[5]   Gorachand Ghosh. "Dispersion-equation coefficients for the refractive index and birefringence of calcite and quartz crystals". In: *Optics Communications* 163.1-3 (May 1999), pp. 95–102. DOI: 10.1016/S0030-4018(99)00091-7.

[6]   Carl V. Brown. "Physical Properties of Nematic Liquid Crystals". In: *Handbook of Visual Display Technology*. Ed. by Janglin Chen, Wayne Cranton, and Mark Fihn.

Berlin, Heidelberg: Springer Berlin Heidelberg, 2012, pp. 1343–1361. ISBN: 978-3-540-79567-4. URL: https://doi.org/10.1007/978-3-540-79567-4_84.

[7]   Zhang Ran et al. "Calculating the dielectric anisotropy of nematic liquid crystals: a reinvestigation of the Maier–Meier theory". In: *Chinese Physics B* 18.7 (July 2009), pp. 2885–2892. DOI: 10.1088/1674-1056/18/7/044. URL: https://doi.org/10.1088%2F1674-1056%2F18%2F7%2F044.

[8]   Haiqing Xianyu et al. "High birefringence and large negative dielectric anisotropy phenyl-tolane liquid crystals". In: *Liquid Crystals* 34.12 (2007), pp. 1473–1478.

[9]   Frank M Leslie. "Some constitutive equations for anisotropic fluids". In: *The Quarterly Journal of Mechanics and Applied Mathematics* 19.3 (1966), pp. 357–370.

[10]   Frank M Leslie. "Some constitutive equations for liquid crystals". In: *Archive for Rational Mechanics and Analysis* 28.4 (1968), pp. 265–283.

[11]   Jerald L Ericksen. "Continuum theory of liquid crystals of nematic type". In: *Molecular crystals and liquid crystals* 7.1 (1969), pp. 153–164.

[12]   O Parodi. "Stress tensor for a nematic liquid crystal". In: *Journal de Physique* 31.7 (1970), pp. 581–584.

[13]   M Miesowicz. "The three coefficients of viscosity of anisotropic liquids". In: *Nature* 158.4001 (1946), pp. 27–27.

[14]   M Miesowicz. "Influence of the magnetic field on the viscosity of liquids in the nematic phase". In: *Bulletin International de l'Academie Polonaise des Sciences et des Lettres,(5-6)* (1936), pp. 228–247.

[15] Ch Gähwiller. "Direct determination of the five independent viscosity coefficients of nematic liquid crystals". In: *Molecular crystals and liquid crystals* 20.3-4 (1973), pp. 301–318.

[16] Ludwig Pohl and E. MERCK. "Physical Properties of Liquid Crystals". In: *Liquid Crystals — Applications and Uses*, pp. 139–170. DOI: 10.1142/9789814368278_0004. URL: https://www.worldscientific.com/doi/abs/10.1142/9789814368278_0004.

[17] Viktor V Belyaev. "The viscosity of nematic liquid crystals". In: *Russian Chemical Reviews* 58.10 (1989), p. 917.

[18] Iain W Stewart. *The static and dynamic continuum theory of liquid crystals: a mathematical introduction*. Crc Press, 2004.

[19] Frederick C Frank. "I. Liquid crystals. On the theory of liquid crystals". In: *Discussions of the Faraday Society* 25 (1958), pp. 19–28.

[20] AS Bhadwal et al. "Electrically controlled topological micro cargo transportation". In: *Soft Matter* 16.12 (2020), pp. 2961–2970.

[21] Vsevolod Fréedericksz and V Zolina. "Forces causing the orientation of an anisotropic liquid". In: *Transactions of the Faraday Society* 29.140 (1933), pp. 919–930.

[22] S. Chandrasekhar. *Liquid Crystals*. 2nd ed. Cambridge University Press, 1992. DOI: 10.1017/CBO9780511622496.

[23] NJ Mottram et al. "Flow-induced delayed Freedericksz transition". In: *Physical Review E* 93.3 (2016), p. 030701.

[24] Kyogo Kawaguchi, Ryoichiro Kageyama, and Masaki Sano. "Topological defects control collective dynamics in neural progenitor cell cultures". In: *Nature* 545.7654 (2017), pp. 327–331.

[25] Thomas WB Kibble. "Topology of cosmic domains and strings". In: *Journal of Physics A: Mathematical and General* 9.8 (1976), p. 1387.

[26] James P Sethna. "Order parameters, broken symmetry, and topology". In: *arXiv preprint cond-mat/9204009* (1992).

[27] Bryan Gin-ge Chen. *Topological defects in nematic and smectic liquid crystals*. Citeseer, 2012.

[28] Anupam Sengupta. *Topological microfluidics: nematic liquid crystals and nematic colloids in microfluidic environment*. Springer Science & Business Media, 2013.

[29] Takuya Ohzono et al. "Uncovering different states of topological defects in schlieren textures of a nematic liquid crystal". In: *Scientific reports* 7.1 (2017), pp. 1–13.

[30] Agnes Buka and Nándor Éber. *Flexoelectricity in liquid crystals: theory, experiments and applications*. World Scientific, 2013.

[31] Kenji Uchino and Yukio Ito. "Ceramics, Transducers". In: *Encyclopedia of Smart Materials* (2002).

[32] Robert B Meyer. "Introduction to flexoelectricity: Its discovery and basic concepts". In: *Flexoelectricity in Liquid Crystals: Theory, Experiments and Applications*. World Scientific, 2013, pp. 1–8.

[33] Robert B Meyer. "Piezoelectric effects in liquid crystals". In: *Physical Review Letters* 22.18 (1969), p. 918.

[34] Jacques Prost and JP Marcerou. "On the microscopic interpretation of flexoelectricity". In: *Journal de Physique* 38.3 (1977), pp. 315–324.

[35] P Rudquist and ST Lagerwall. "On the flexoelectric effect in nematics". In: *Liquid crystals* 23.4 (1997), pp. 503–510.

[36] James T Jenkins. "Flows of nematic liquid crystals". In: *Annual Review of Fluid Mechanics* 10.1 (1978), pp. 197–219.

[37] Timothy J Sluckin, David A Dunmur, and Horst Stegemeyer. *Crystals that flow: classic papers from the history of liquid crystals*. CRC Press, 2004.

[38] PT Mather, DS Pearson, and RG Larson. "Flow patterns and disclination-density measurements in sheared nematic liquid crystals I: Flow-aligning 5CB". In: *Liquid crystals* 20.5 (1996), pp. 527–538.

[39] PT Mather, DS Pearson, and RG Larson. "Flow patterns and disclination-density measurements in sheared nematic liquid crystals II: Tumbling 8CB". In: *Liquid crystals* 20.5 (1996), pp. 539–546.

[40] Aman Kalsi and Nikhail Balani. *Physics for the Anaesthetic Viva*. Cambridge University Press, 2016.

[41] Patrick Oswald and Pawel Pieranski. *Nematic and cholesteric liquid crystals: concepts and physical properties illustrated by experiments*. CRC press, 2005.

[42] Harry J Levinson. *Principles of lithography*. Vol. 146. SPIE press, 2005.

[43] Ashok Chaudhary, Matvey Klebanov, and Ibrahim Abdulhalim. "Liquid crystals alignment with PbS nanosculptured thin films". In: *Liquid Crystals* 45.1 (2018), pp. 3–10.

[44]   I Kim et al. "Application of Magnesium Fluoride (MgF_2) Thin Films for Liquid Crystal Alignment Using Ion-Beam IrradiationApplication of Magnesium Fluoride (MgF_2) Thin Films for Liquid Crystal Alignment Using Ion-Beam Irradiation". In: *IEEE Electron Device Letters* 34.2 (2013), pp. 283–285.

[45]   Tae Uk Ryu et al. "Optical, mechanical and thermal properties of MgF2-ZnS and MgF2-Ta2O5 composite thin films deposited by coevaporation". In: *Optical Engineering* 39.12 (2000), pp. 3207–3214.

[46]   Sharon A Jewell et al. "Flow-driven transition and associated velocity profiles in a nematic liquid-crystal cell". In: *Physical Review E* 80.4 (2009), p. 041706.

[47]   Robert Allen Carlton. *Pharmaceutical microscopy*. Springer Science & Business Media, 2011.

[48]   Ivan I Smalyukh. "Confocal microscopy of director structures in strongly confined and composite systems". In: *Molecular Crystals and Liquid Crystals* 477.1 (2007), pp. 23–517.

[49]   Erik Meijering, Oleh Dzyubachyk, and Ihor Smal. "Methods for cell and particle tracking". In: *Methods in enzymology*. Vol. 504. Elsevier, 2012, pp. 183–200.

[50]   Caroline A Schneider, Wayne S Rasband, and Kevin W Eliceiri. "NIH Image to ImageJ: 25 years of image analysis". In: *Nature methods* 9.7 (2012), pp. 671–675.

[51]   Sotiria Kogou. "Investigation of the complementary use of non-invasive techniques for the holistic analysis of paintings and automatic analysis of large scale spectral imaging data". PhD thesis. Nottingham Trent University, 2017.

[52]   J Kalkman. "Fourier-domain optical coherence tomography signal analysis and numerical modeling". In: *International Journal of Optics* 2017 (2017).

[53] George H Heilmeier, Louis A Zanoni, and Lucian A Barton. "Dynamic scattering: A new electrooptic effect in certain classes of nematic liquid crystals". In: *Proceedings of the IEEE* 56.7 (1968), pp. 1162–1171.

[54] Eddy C Tam. "Smart electro-optical zoom lens". In: *Optics letters* 17.5 (1992), pp. 369–371.

[55] Michaël De Volder et al. "The use of liquid crystals as electrorheological fluids in microsystems: model and measurements". In: *Journal of Micromechanics and Microengineering* 16.3 (2006), p. 612.

[56] J Adrián Reyes, A Corella-Madueño, and Carlos I Mendoza. "Electrorheological response and orientational bistability of a homogeneously aligned nematic capillary". In: *The Journal of chemical physics* 129.8 (2008), p. 084710.

[57] Jay Fishers and AG Fredrickson. "Interfacial effects on the viscosity of a nematic mesophase". In: *Molecular Crystals* 8.1 (1969), pp. 267–284.

[58] Christopher J Holmes, Stephen Leslie Cornford, and J Roy Sambles. "Conoscopic observation of director reorientation during Poiseuille flow of a nematic liquid crystal". In: *Applied Physics Letters* 95.17 (2009), p. 171114.

[59] Christopher J Holmes, Stephen Leslie Cornford, and J Roy Sambles. "Small surface pretilt strikingly affects the director profile during poiseuille flow of a nematic liquid crystal". In: *Physical review letters* 104.24 (2010), p. 248301.

[60] Anupam Sengupta et al. "Liquid crystal microfluidics for tunable flow shaping". In: *Physical review letters* 110.4 (2013), p. 048303.

[61]   Zongdai Liu, Dan Luo, and Kun-Lin Yang. "Flow-driven disclination lines of ne-
       matic liquid crystals inside a rectangular microchannel". In: *Soft matter* 15.28
       (2019), pp. 5638–5643.

[62]   Simon Čopar et al. "Microfluidic control over topological states in channel-confined
       nematic flows". In: *Nature Communications* 11.1 (2020), pp. 1–10.

[63]   JL Ericksen. "Poiseuille flow of certain anisotropic fluids". In: *Archive for Ratio-
       nal Mechanics and Analysis* 8.1 (1961), p. 1.

[64]   RJ Atkin. "Poiseuille flow of liquid crystals of the nematic type". In: *Archive for
       Rational Mechanics and Analysis* 38.3 (1970), pp. 224–240.

[65]   Colin Denniston, Enzo Orlandini, and JM Yeomans. "Simulations of liquid crys-
       tals in Poiseuille flow". In: *Computational and Theoretical Polymer Science* 11.5
       (2001), pp. 389–395.

[66]   I Sh Nasibullayev et al. "Orientational instabilities in nematic liquid crystals with
       weak anchoring under combined action of steady flow and external fields". In:
       Physical Review E 72.5 (2005), p. 051706.

[67]   Judit Quintans Carou et al. "Shear-driven and pressure-driven flow of a nematic
       liquid crystal in a slowly varying channel". In: *Physics of Fluids* 18.2 (2006),
       p. 027105.

[68]   TG Anderson et al. "Transitions in Poiseuille flow of nematic liquid crystal". In:
       International Journal of Non-Linear Mechanics 75 (2015), pp. 15–21.

[69]   Vera MO Batista, Matthew L Blow, and Margarida M Telo da Gama. "The ef-
       fect of anchoring on the nematic flow in channels". In: *Soft Matter* 11.23 (2015),
       pp. 4674–4685.

[70] Shubhadeep Mandal and Marco G Mazza. "Multiparticle collision dynamics for tensorial nematodynamics". In: *Physical Review E* 99.6 (2019), p. 063319.

[71] Rajratan Basu and Germano S Iannacchione. "Dielectric hysteresis, relaxation dynamics, and nonvolatile memory effect in carbon nanotube dispersed liquid crystal". In: *Journal of applied physics* 106.12 (2009), p. 124312.

[72] JL Ericksen. "Archs Ration. Mech". In: *Archive for Rational Mechanics and Analysis* 4 (1959), p. 231.

[73] Jerald L Ericksen. "Conservation laws for liquid crystals". In: *Transactions of the Society of Rheology* 5.1 (1961), pp. 23–34.

[74] M Kaiser and W Pesch. "Amplitude equations for the electrohydrodynamic instability in nematic liquid crystals". In: *Physical Review E* 48.6 (1993), p. 4510.

[75] ND Mermin. "Topological point defects in nematic liquid crystals". In: *Rev. Mod. Phys* 51 (1979), pp. 591–648.

[76] Carl Rosenzweig and Ajit Mohan Srivastava. "Towards a qualitative understanding of the scattering of topological defects". In: *Physical Review D* 43.12 (1991), p. 4029.

[77] Thuan Beng Saw et al. "Topological defects in epithelia govern cell death and extrusion". In: *Nature* 544.7649 (2017), pp. 212–216.

[78] Mark J Bowick et al. "The cosmological Kibble mechanism in the laboratory: string formation in liquid crystals". In: *Science* 263.5149 (1994), pp. 943–945.

[79] Isaac Chuang et al. "Cosmology in the laboratory: Defect dynamics in liquid crystals". In: *Science* 251.4999 (1991), pp. 1336–1342.

[80] PE Cladis et al. "Dynamics of line defects in nematic liquid crystals". In: *Physical review letters* 58.3 (1987), p. 222.

[81] Lorenzo Marrucci, Carlo Manzo, and Domenico Paparo. "Optical spin-to-orbital angular momentum conversion in inhomogeneous anisotropic media". In: *Physical review letters* 96.16 (2006), p. 163905.

[82] Gabriel Molina-Terriza, Juan P Torres, and Lluis Torner. "Twisted photons". In: *Nature physics* 3.5 (2007), pp. 305–310.

[83] Sergei Slussarenko et al. "Tunable liquid crystal q-plates with arbitrary topological charge". In: *Optics express* 19.5 (2011), pp. 4085–4090.

[84] Yun Ho Kim et al. "Optically Selective Microlens Photomasks Using Self-Assembled Smectic Liquid Crystal Defect Arrays". In: *Advanced Materials* 22.22 (2010), pp. 2416–2420.

[85] Ahram Suh et al. "Controllable liquid crystal defect arrays induced by an in-plane electric field and their lithographic applications". In: *Journal of Materials Chemistry C* 7.6 (2019), pp. 1713–1719.

[86] Takahiro Yamamoto and Masaru Yoshida. "Viscoelastic and photoresponsive properties of microparticle/liquid-crystal composite gels: tunable mechanical strength along with rapid-recovery nature and photochemical surface healing using an azobenzene dopant". In: *Langmuir* 28.22 (2012), pp. 8463–8469.

[87] Igor Musevic et al. "Metamaterials and resonant materials based on liquid crystal dispersions of colloidal particles and nanoparticles". In: *E.P. Office* (2008), University of Ljubljana, Institut Jozef Stefan.

[88]   Jean-Baptiste Fleury, David Pires, and Yves Galerne. "Self-connected 3D architecture of microwires". In: *Physical review letters* 103.26 (2009), p. 267801.

[89]   Oleg D Lavrentovich, Israel Lazo, and Oleg P Pishnyak. "Nonlinear electrophoresis of dielectric and metal spheres in a nematic liquid crystal". In: *Nature* 467.7318 (2010), pp. 947–950.

[90]   Takuya Ohzono and Jun-ichi Fukuda. "Zigzag line defects and manipulation of colloids in a nematic liquid crystal in microwrinkle grooves". In: *Nature communications* 3.1 (2012), pp. 1–7.

[91]   Anupam Sengupta, Christian Bahr, and Stephan Herminghaus. "Topological microfluidics for flexible micro-cargo concepts". In: *Soft Matter* 9.30 (2013), pp. 7251–7260.

[92]   Yuji Sasaki et al. "Colloidal caterpillars for cargo transportation". In: *Soft matter* 10.44 (2014), pp. 8813–8820.

[93]   Chenhui Peng et al. "Control of colloidal placement by modulated molecular orientation in nematic cells". In: *Science advances* 2.9 (2016), e1600932.

[94]   Yimin Luo et al. "Tunable colloid trajectories in nematic liquid crystals near wavy walls". In: *Nature communications* 9.1 (2018), pp. 1–11.

[95]   M.Z Bazant. "Electrokinetic Motion of Heterogeneous Particles, in Encyclopedia of Microfluidics and Nanofluidics". In: *Springer* (2008), pp. 518–522.

[96]   Andrei S Dukhin and Stanislav S Dukhin. "Aperiodic capillary electrophoresis method using an alternating current electric field for separation of macromolecules". In: *Electrophoresis* 26.11 (2005), pp. 2149–2153.

[97]   DA Dunmur and WH Miller. "Volumetric studies of the homologous series of alkyl-cyano-biphenyl liquid crystals". In: *Le Journal de Physique Colloques* 40.C3 (1979), pp. C3–141.

[98]   GR Luckhurst, Atsuo Fukuda, and David A Dunmur. *Physical properties of liquid crystals: nematics*. 25. IET, 2001.

[99]   George William Gray, Kenneth J Harrison, and JA Nash. "New family of nematic liquid crystals for displays". In: *Electronics Letters* 9.6 (1973), pp. 130–131.

[100] Peter J Collings and John W Goodby. *Introduction to liquid crystals: chemistry and physics*. Crc Press, 1997.

[101] MJ Bradshaw and EP Raynes. "Electric permittivities and elastic constants of the cyano bi-cyclohexanes (CCH)". In: *Molecular Crystals and Liquid Crystals* 72.2-3 (1981), pp. 35–42.

[102] Gareth P Alexander et al. "Colloquium: Disclination loops, point defects, and all that in nematic liquid crystals". In: *Reviews of Modern Physics* 84.2 (2012), p. 497.

[103] C Tsakonas et al. "Multistable alignment states in nematic liquid crystal filled wells". In: *Applied physics letters* 90.11 (2007), p. 111913.

[104] CL Trabi et al. "Interferometric method for determining the sum of the flexo-electric coefficients (e 1+ e 3) in an ionic nematic material". In: *Applied Physics Letters* 92.22 (2008), p. 223509.

[105] N Éber, P Salamon, and Á Buka. "Electrically induced patterns in nematics and how to avoid them". In: *Liquid Crystals Reviews* 4.2 (2016), pp. 101–134.

[106] COMSOL Multiphysics. *3.4, COMSOL AB, Stockholm, Sweden*.

[107] D Voloschenko et al. "Effect of director distortions on morphologies of phase separation in liquid crystals". In: *Physical Review E* 65.6 (2002), p. 060701.

[108] Dong Ki Yoon et al. "Internal structure visualization and lithographic use of periodic toroidal holes in liquid crystals". In: *Nature materials* 6.11 (2007), pp. 866–870.

[109] Oleg D Lavrentovich. "Transport of particles in liquid crystals". In: *Soft Matter* 10.9 (2014), pp. 1264–1283.

[110] Philippe Poulin et al. "Novel colloidal interactions in anisotropic fluids". In: *Science* 275.5307 (1997), pp. 1770–1773.

[111] Guy Peter Bryan-Brown, Carl Vernon Brown, and John Clifford Jones. *Bistable nematic liquid crystal device*. US Patent 6,249,332. June 2001.

[112] JC Jones, SM Beldon, and EL Wood. "Gray scale in zenithal bistable LCDs: The route to ultra-low-power color displays". In: *Journal of the Society for Information Display* 11.2 (2003), pp. 269–275.

[113] J Cliff Jones. "The zenithal bistable display: from concept to consumer". In: *Journal of the Society for Information Display* 16.1 (2008), pp. 143–154.

[114] Pavlo Zubko, Gustau Catalan, and Alexander K Tagantsev. "Flexoelectric effect in solids". In: *Annual Review of Materials Research* 43 (2013).

[115] A Safari, B Jadidian, and EK Akdogan. "Piezoelectric composites for transducer applications". In: (2000).

[116] G Barbero and LR Evangelista. "Comment on "Optical determination of flexoelectric coefficients and surface polarization in a hybrid aligned nematic cell"". In: *Physical Review E* 68.2 (2003), p. 023701.

[117] M Buczkowska and G Derfel. "Role of flexoelectricity in electro-optical properties of hybrid aligned nematic layers". In: *Applied Physics Letters* 103.21 (2013), p. 211115.

[118] Stephen Leslie Cornford, TS Taphouse, and J Roy Sambles. "Analysis of the sign-dependent switching observed in a hybrid aligned nematic cell". In: *New Journal of Physics* 11.1 (2009), p. 013045.

[119] G Derfel and M Buczkowska. "Electro-optical effects in hybrid aligned flexoelectric nematic layers". In: *Journal of Applied Physics* 114.17 (2013), p. 173510.

[120] SA Jewell and JR Sambles. "Fully leaky guided mode study of the flexoelectric effect and surface polarization in hybrid aligned nematic cells". In: *Journal of applied Physics* 92.1 (2002), pp. 19–24.

[121] C Kischka, SJ Elston, and EP Raynes. "Measurement of the Sum (e 1+ e 3) of the Flexoelectric Coefficients e 1 and e 3 of Nematic Liquid Crystals using a Hybrid Aligned Nematic (HAN) cell". In: *Molecular Crystals and Liquid Crystals* 494.1 (2008), pp. 93–100.

[122] NV Madhusudana and Geoffroy Durand. "Linear flexo-electro-optic effect in a hybrid aligned nematic liquid crystal cell". In: *Journal de Physique Lettres* 46.5 (1985), pp. 195–200.

[123] A Mazzulla, F Ciuchi, and J Roy Sambles. "Optical determination of flexoelectric coefficients and surface polarization in a hybrid aligned nematic cell". In: *Physical Review E* 64.2 (2001), p. 021708.

[124] S Ponti et al. "Flexoelectro-optic effect in a hybrid nematic liquid crystal cell". In: *Liquid crystals* 26.8 (1999), pp. 1171–1177.

[125] TS Taphouse et al. "Time-resolved sign-dependent switching in a hybrid aligned nematic liquid crystal cell". In: *New Journal of Physics* 10.8 (2008), p. 083045.

[126] Chloe C Tartan and Steve J Elston. "Hybrid aligned nematic based measurement of the sum (e 1+ e 3) of the flexoelectric coefficients". In: *Journal of Applied Physics* 117.6 (2015), p. 064107.

[127] Chloe C Tartan and Steve J Elston. "Asymmetric Director Structures and Ions in the Measurement of the Flexoelectric Sum (e 1+ e 3)". In: *Molecular Crystals and Liquid Crystals* 610.1 (2015), pp. 77–88.

[128] W Helfrich. "Polarity-dependent electro-optical effect of nematic liquid crystals". In: *Applied Physics Letters* 24.10 (1974), pp. 451–452.

[129] Jacques Prost and Peter S Pershan. "Flexoelectricity in nematic and smectic-A liquid crystals". In: *Journal of applied Physics* 47.6 (1976), pp. 2298–2312.

[130] Kenneth S Cole and Robert H Cole. "Dispersion and absorption in dielectrics I. Alternating current characteristics". In: *The Journal of chemical physics* 9.4 (1941), pp. 341–351.

[131] NT Kirkman, T Stirner, and WE Hagston. "Continuum modelling of hybrid-aligned nematic liquid crystal cells: optical response and flexoelectricity-induced voltage shift". In: *Liquid crystals* 30.9 (2003), pp. 1115–1122.

[132] Gary George Wells. "Voltage programmable liquid optical devices". PhD thesis. Nottingham Trent University, 2009.

[133] Naresh Sampara. "Voltage induced spreading and liquid optical devices". PhD thesis. Nottingham Trent University, 2013.

[134] JRL Cousins et al. "Squeezing a drop of nematic liquid crystal with strong elasticity effects". In: *Physics of Fluids* 31.8 (2019), p. 083107.

[135] Kuang-Chao Fan et al. "Development of a drop-on-demand droplet generator for one-drop-fill technology". In: *Sensors and Actuators A: Physical* 147.2 (2008), pp. 649–655.

[136] Hiroyuki Kamiya et al. "56.3: Development of One Drop Fill Technology for AMLCDs". In: *SID Symposium Digest of Technical Papers*. Vol. 32. 1. Wiley Online Library. 2001, pp. 1354–1357.

[137] Ivan I Smalyukh et al. "Optical trapping, manipulation, and 3D imaging of disclinations in liquid crystals and measurement of their line tension". In: *Molecular Crystals and Liquid Crystals* 450.1 (2006), pp. 79–279.

[138] Yue Cui et al. "Alignment layers with variable anchoring strengths from Polyvinyl Alcohol". In: *Journal of Applied Physics* 111.6 (2012), p. 063520.

[139] Z Eskandari et al. "Particle selection through topographic templates in nematic colloids". In: *Soft Matter* 10.48 (2014), pp. 9681–9687.

[140] Sophie A Jones et al. "Method for tuneable homeotropic anchoring at microstructures in liquid crystal devices". In: *Langmuir* 34.37 (2018), pp. 10865–10873.

[141] Seung-Won Oh et al. "Effect of electrode spacing on image flicker in fringe-field-switching liquid crystal display". In: *Liquid Crystals* 43.7 (2016), pp. 972–979.

Appendix A

Appendix

A.1 Flow cell thickness measurement using UV-spectroscopy and OCT
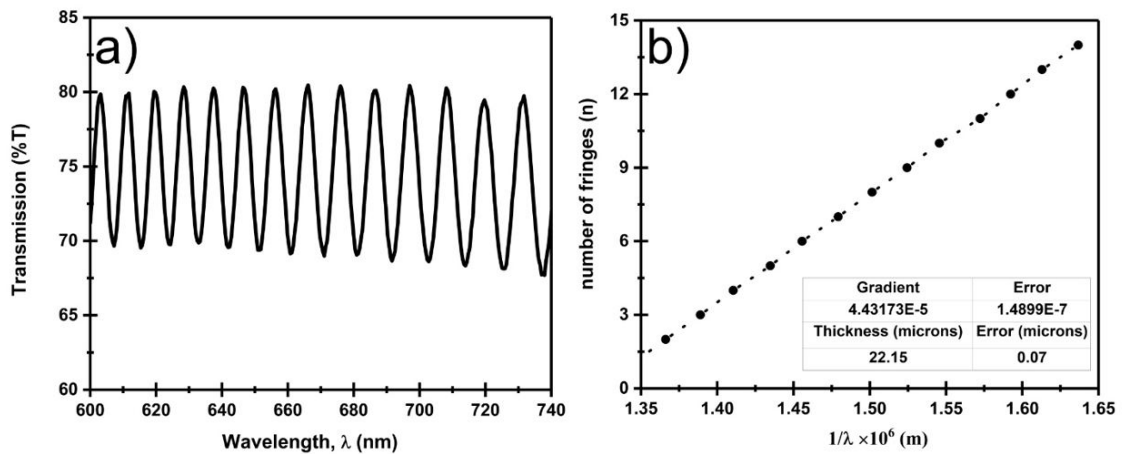
Figure A.1: Planar (MgF_2 alignment layer) lollipop electrode flow cell UV-results (a) % Transmittance as a function of wavelength (nm), b) n vs $1/\lambda$ plot for thickness determination.
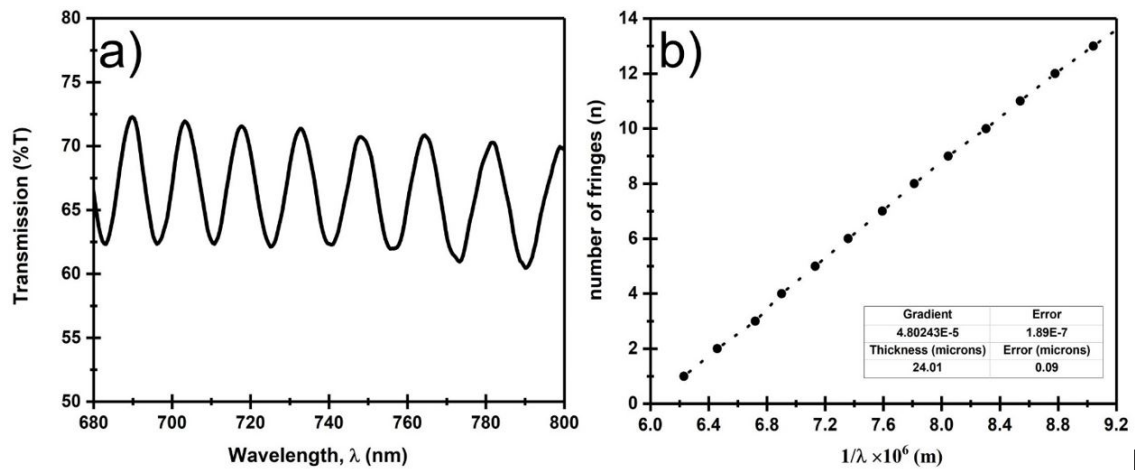
Figure A.2: Planar (MgF$_2$ alignment layer) rectangular electrode flow cell UV-results (a) %Transmittance as a function of wavelength (nm), b) n vs $1/\lambda$ plot for thickness determination.
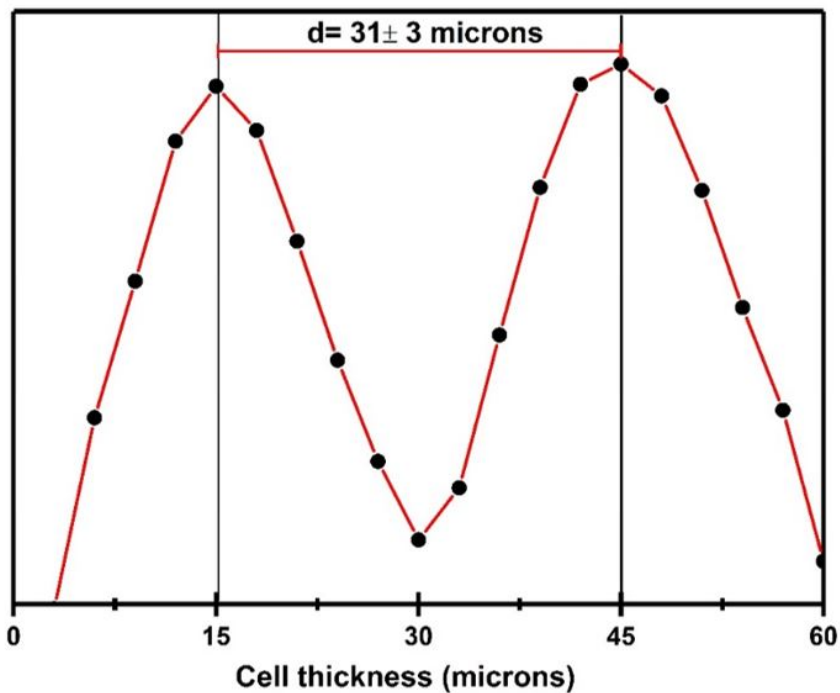
Figure A.3: Homeotropic lollipop electrode flow cell OCT thickness measurement.

A.2 Physical parameters of nematic liquid crystals used in the thesis

Material	Alignment condition	Thickness (d)	Frequency (kHz)	V_c (V)	$\epsilon_\perp$	$\epsilon_\parallel$	$\Delta\epsilon$	k_{11}(pN)	k_{33}(pN)
5CB (Single component LCs)	Planar	22 μm	1 kHz	0.75	6.2	20.4	14.2	7.2	10.0
E1 (5CB and 7CB Blend) (60:40 %w/w)	Planar	22 μm	1 kHz	0.76	5.9	18.2	12.3	6.4	59.5
MLC-6681	Planar	22 μm	1 kHz	0.35	11.3	65.4	54.1	5.9	20.0
MDA-13-2167 (High $\Delta\epsilon$)	Planar	22 μm	1 kHz	0.15	15.9	416.1	400.2	8.0	-
LCT-07-1132 (Negative $\Delta\epsilon$)	Homeotropic	22 μm	1 kHz	2.2	6.85	3.41	3.44	12	14.9

Figure A.4: Physical properties of nematic liquid crystals measured from Fréedericksz curve.

A.3   Matlab codes

A.3.1   Interferometer fringe extraction

The below mentioned MATLAB code is able to extract *xy*-coordinate of connected black pixels in local feature of a binary image. Before using the code, we need to convert our image into a binary image. This can be easily done using ImageJ (recommended) or MATLAB imbinarize command. Several local features that are represented by connected black pixels in an image can be extracted in a single run (make change to the for loop in the code). The output *xy*-coordinates of selected features is saved in an excel sheet in the order of the selection. In the example below (A.5) two fringes from an interferogram was extracted using the MATLAB code.
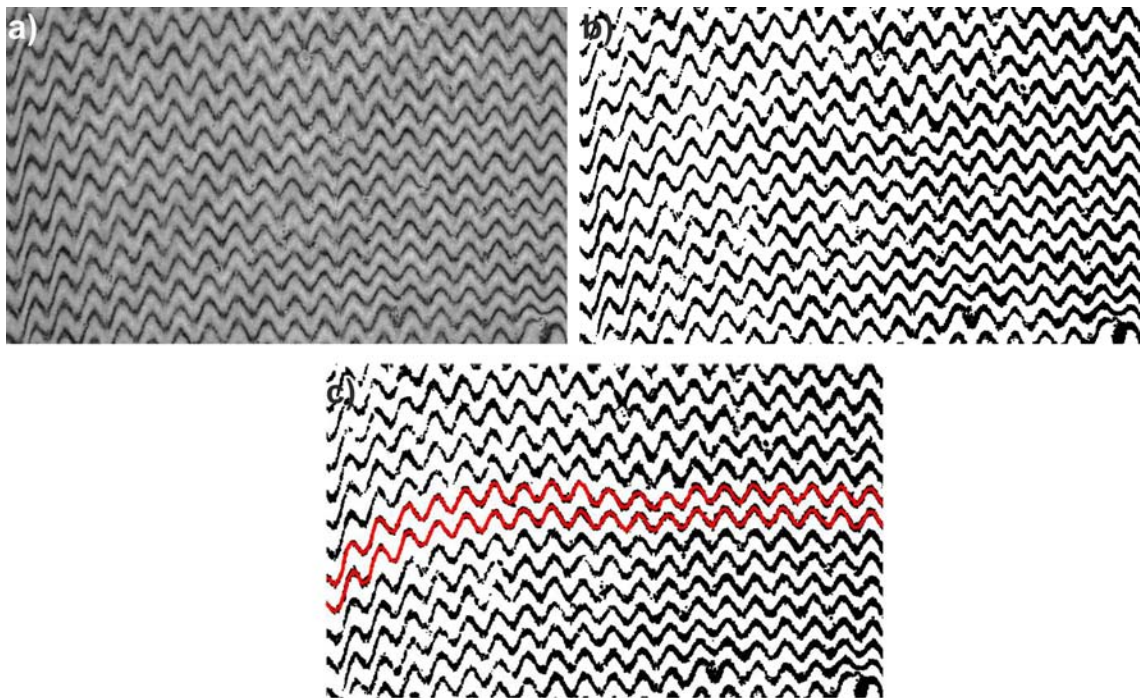
Figure A.5: a) Original image, b) Digitised image, and c) Extracted fringes (red-highlight) from the digitised image.

```matlab
1  clc
2  clear all
3  close all
4  set(0 'default text interpreter' 'latex')
5  mainim=imread('IMAGE HERE.jpg');
6  im = imcomplement(mainim);
7  h = fspecial('gaussian', 15);
8  im2 = imclose(im, ones(3)); % close
9  im2 = imfilter(im2, h); % smooth
10 im2 = imcomplement(im2);
11 %Invert Image to make Black fringes white and white
       background region Black from Original Image
12 inverti=imcomplement(im2);
13 black=im2bw(inverti);
14 %Morphological Tool to get rid of noise
15 clean=bwareaopen(black, 100);
16 %Fill the holes in the image
17 BW2 = imfill(clean,'holes');
18 figure,subplot(221),imshow(BW2),title('Image with all
       fringes')
19 % Find boundries of the image
20 [B,L,N,A] = bwboundaries(BW2);
21 BW = BW2;
22 imshow(imcomplement(BW)); hold on;
```

```matlab
23   % Create the csv file for all the fringes

24   fileID = fopen('myfile.csv','w');

25   % Iterate over all the detected boundaries

26   for k=1:length(B)

27     % Extract the boundary

28     boundary = B{k};

29     cordinate = [];

30     % Find the middle value of the upper bound and lower
          bound

31     for i = 1:length(boundary(:,2))

32        simy = find(boundary(:,2) == boundary(i,2));

33        simy = boundary(simy,1);

34        avgy = (min(simy) + max(simy))/2;

35        cordinate = [cordinate ; [boundary(i,2), avgy]];

36     end

37     % remove the repeated coordinate

38     tempcoordinate = unique(cordinate,'rows','stable');

39     % Extract the x-coordinate

40     strcordinate(k).x = tempcoordinate(:,1);

41     % Extract the y-coordinate

42     strcordinate(k).y = tempcoordinate(:,2);

43     % Write in the file

44     for temcoor = 1:length(tempcoordinate)
```

```matlab
45      nbytes = fprintf(fileID,'(%5d ; %5d),',tempcoordinate
            (temcoor,1),tempcoordinate(temcoor,2));
46    end
47    nbytes = fprintf(fileID,'\n');
48 %   cidx = mod(k,length(colors))+1;
49    % Plot the fringe in the image
50    plot(cordinate(:,1), cordinate(:,2),...
51        'r','LineWidth',2);
52 end
53 saveas(gcf,'fringes.jpg')
54 fclose(fileID);
55 %%
56 % Plot the original image
57 hax = subplot(222),imshow(mainim),title('Selected Fringe
       from Original Image');
58 for iteration = 1:2 %change interation here
       depedeninggupon number of fringes you wan tto select
       in am image
59 % Open the csv file for the fringe
60 fileID = fopen(['fringes',num2str(iteration),'.csv'],'w')
       ;
61 nbytes = fprintf(fileID,'%5s , %5s, %5s , %5s\n','x-
       coordinate',...
62        'y-coordinate',...
```

```matlab
63              'scaled-X', 'scaled-Y');
64 %select pixel value of fringe you want to trace using
     ginput
65 [x,y] = ginput(1);
66 x = round(x);
67 y = round(y);
68 cordinate = [x y];
69 minval = [];
70 minindex = [];
71
72 for i = 1: size(strcordinate,2)
73     x1 = strcordinate(i).x;
74     y1 = strcordinate(i).y;
75     Coordinate1 = [x1 y1];
76     Coordinate2 = repmat(cordinate,size(Coordinate1,1),1)
         ;
77     % Find the distance between the point clicked and the
           all fringes
78     distance = Coordinate1 - Coordinate2;
79     % Find the minimum of that distance
80     [icor,jcor] = min(sum(distance.^2,2));
81     % Find index as well as the index
82     minval = [minval icor];
83     minindex = [minindex i];
```

```matlab
84  end
85  [i,j] = min(minval);
86  hold on
87  %% Distance calculation
88  Dis.callibration= SCALE HERE; %in mm/pixel;
89  normalized.x = (strcordinate(j).x)/Dis.callibration;
90  normalized.y = (size(mainim,1) - strcordinate(j).y)/Dis.
        callibration;
91  %%
92  % Plot that minimum distanced fringe
93  plot(strcordinate(j).x, strcordinate(j).y,'r','LineWidth'
        ,2);
94  % Put the coordinate of the fringe
95  for temcoor = 1:length(strcordinate(j).x)
96      nbytes = fprintf(fileID,'%5d , %5d, %5d , %5d\n',
            strcordinate(j).x(temcoor),...
97          size(mainim,1)-strcordinate(j).y(temcoor),...
98          normalized.x(temcoor), normalized.y(temcoor));
99  end
100 nbytes = fprintf(fileID,'\n');
101 fclose(fileID);
102 end
103 %Plot Fringe
104 subplot(2,2,3);
```

```matlab
105  plot(normalized.x,normalized.y,'b','linewidth',2);

106  title('Selected Fringe Plot');

107  xlabel('x-Distance (mm)');

108  ylabel('y-Distance (mm)');

109  %save image with selected fringe marked

110  hfig = figure;

111  hax_new = copyobj(hax, hfig);

112  set(hax_new, 'Position', get(0, 'DefaultAxesPosition'));

113  % print(hfig);

114  saveas(gcf, 'selected fringes.jpg')
```

A.3.2 Tracking movement of the Domain wall

The below mentioned MATLAB code is able track movement of a selected white pixel along a specified straight line in the video file. The *xy*-coordinate of pixel movement is saved in an excel sheet after completion of the run.

```
1  clear all
2  close all
3  %Load Filename Parameters
4  InputVideoFilename = '4V-1';%Sets the name of the input
        video file does not require a file type extension
5  Video = VideoReader([InputVideoFilename '.avi']);%Fetches
         the video file - DO NOT EDIT THIS LINE
6  NoFrames = round(Video.Duration*Video.FrameRate);%
        Determines the total number of frames in the video
        file - DO NOT EDIT THIS LINE
7  Start =20;%Sets Start Image
8  ImageStep = 5;%Sets Image Step
9  End = NoFrames;%Sets Final Image
10 Threshold_Level = 0.2;%Sets Threshold Level - Must be
        between 0 & 1
11 Rotate_Offset = 270;%Sets Additional Rotation in degrees
12 % Videodata = read(Video,[Start End]);
13 % Videodata = Videodata(:,:,1,:);
14 % img_size = size(Videodata);
15 Framerate = 5; %In FPS
```

```matlab
16  Display_Wait_Time = 0.001; %In Seconds

17  Xcalibration = 1/850; %in mm/pixel

18  YCalibration = 1/850; %in mm/pixel

19  Time = (0:1/Framerate:(End-1)/Framerate);

20  Left_Y_Height = zeros(1,End);

21  Right_Y_Height = zeros(1,End);

22  Delta_Height = zeros(1,End);

23  accept = 0;

24  Start_Image = read(Video,End);

25  Start_Image = Start_Image(:,:,1);

26  Start_Image = imrotate(Start_Image,(Rotate_Offset));

27  img_size = size(Start_Image);

28  Left_Tube_Y = [1,img_size(1)];

29  Right_Tube_Y = [1,img_size(1)];

30  Left_Y_Store = [];

31  Right_Y_Store = [];

32  figure('units','normalized','outerposition',[0 0 1 1])

33   while accept~=1

34      imshow(Start_Image)

35      title('Select Left Defect')

36      hold on

37      [x,y] = ginput(1);

38      x = round(x);

39      y = round(y);
```

```matlab
40      Left_Tube_X = [x(1) x(1)];

41      plot(Left_Tube_X,Left_Tube_Y,'r');

42      title('Select Right Defect')

43      [x,y] = ginput(1);

44      x = round(x);

45      y = round(y);

46      Right_Tube_X = [x(1),x(1)];

47      plot(Right_Tube_X,Right_Tube_Y,'r');

48      accept = input('Are Points Okay?\n');

49   end

50 close

51 accept = 0;

52 figure('units','normalized','outerposition',[0 0 1 1])

53 for LoopNo=Start:ImageStep:End

54      Current_Image = read(Video,LoopNo);

55      Current_Image = Current_Image(:,:,1);

56      Current_Image = imrotate(Current_Image,(Rotate_Offset
            ));

57      %img_size = size(Current_Image);

58      if LoopNo == Start

59          while accept~=1

60              Difference_Image = imabsdiff(Start_Image,
                    Current_Image);
```

```matlab
61              Threshold_Image = im2bw(Difference_Image,
                    Threshold_Level);
62          subplot(2,3,[1 4])
63          imshow(Current_Image);
64          subplot(2,3,[2 5])
65          imshow(Threshold_Image);
66          hold on
67          plot(Right_Tube_X,Right_Tube_Y,'r');
68          plot(Left_Tube_X,Left_Tube_Y,'r');
69
70          accept = input('Is Threshold Level Okay?\n');
71          if accept ~=1
72              Threshold_Level = input('New Threshold Level
                    ?\n');
73          end
74          end
75      end
76      %Difference_Image = imabsdiff(Start_Image,
            Current_Image);
77      Threshold_Image = im2bw(Current_Image,Threshold_Level
            );
78      Left_Channel_Data = (Threshold_Image(:,Left_Tube_X(1)
            ))*255;
```

```matlab
79    Right_Channel_Data = (Threshold_Image(:,Right_Tube_X
          (1)))*255;
80    [Left_Y] = find(Left_Channel_Data == 255);
81    if size(Left_Y,1) > 1
82    Left_Y_Store = [Left_Y_Store Left_Y(1)];
83    Left_Y_Co = [Left_Y_Store(1) Left_Y_Store(end)];
84    Left_Y_Height(LoopNo) = (Left_Y_Store(end) -
          Left_Y_Store(1))*YCalibration;
85    end
86    [Right_Y] = find(Right_Channel_Data == 255);
87    if size(Right_Y,1) > 1
88    Right_Y_Store = [Right_Y_Store Right_Y(1)];
89    Right_Y_Co = [Right_Y_Store(1) Right_Y_Store(end)];
90    Right_Y_Height(LoopNo) = (Right_Y_Store(end) -
          Right_Y_Store(1))*YCalibration;
91    end
92    if (size(Right_Y,1) > 1 && size(Left_Y,1) > 1)
93    Delta_Height(LoopNo) = abs(Right_Y_Store(end)-
          Left_Y_Store(end))*YCalibration;
94    end
95    subplot(2,3,[1 4])
96    imshow(Current_Image);
97    hold on
98    plot(Left_Tube_X,Left_Tube_Y,'b');
```

242

```matlab
99      plot(Right_Tube_X,Right_Tube_Y,'b');
100     title(['Original Image at time: ',num2str(Time(LoopNo
            )),'s']);
101     hold off
102     subplot(2,3,[2 5])
103     imshow(Threshold_Image);
104     hold on
105     plot(Left_Tube_X,Left_Tube_Y,'b');
106     plot(Right_Tube_X,Right_Tube_Y,'b');
107     if size(Left_Y,1) > 1
108     plot(Left_Tube_X,Left_Y_Co,'r.');
109     end
110     if size(Right_Y,1) > 1
111     plot(Right_Tube_X,Right_Y_Co,'g.');
112     end
113     title('Thresholded Image');
114     hold off
115 %     subplot(2,4,[3 7])
116 %     imshow(Threshold_Image);
117 %     hold on
118 %     plot(Left_Tube_X,Left_Tube_Y,'b');
119 %     plot(Right_Tube_X,Right_Tube_Y,'b');
120 %     title('Thresholded Image');
121 %     hold off
```

```
122    subplot(2,3,3)
123    plot(Time,Left_Y_Height,'b.');
124    hold on
125    plot(Time,Right_Y_Height,'r.');
126    xlabel('Time (s)')
127    ylabel('Height (mm)')
128    hold off
129    subplot(2,3,6)
130    plot(Time,Delta_Height,'b.');
131    xlabel('Time (s)')
132    ylabel('Height (mm)')
133    pause(Display_Wait_Time)
134 end
135    Time(find(Left_Y_Height == 0)) = [];
136    Right_Y_Height(find(Left_Y_Height == 0)) = [];
137    Delta_Height(find(Left_Y_Height == 0)) = [];
138    Left_Y_Height(find(Left_Y_Height == 0)) = [];
139
140    Time(find(Right_Y_Height == 0)) = [];
141    Delta_Height(find(Right_Y_Height == 0)) = [];
142    Left_Y_Height(find(Right_Y_Height == 0)) = [];
143    Right_Y_Height(find(Right_Y_Height == 0)) = [];
144    Time = Time - Time(1);
```

```matlab
145  header = ('Time (s),Left Height (mm),Right Height (mm),
         Delta Height (mm)');
146          fileID = fopen([InputVideoFilename '.csv'],'w');
147          fprintf(fileID,header);
148          for i=1:1:size(Time,2)
149              fprintf(fileID,'\n%f,%f,%f,%f,',Time(i),
                     Left_Y_Height(i),Right_Y_Height(i),
                     Delta_Height(i));
150          end
151          pause(0.01);
152          fclose(fileID);
153          close all
```

List of Publications and Conferences

Journal articles

During Ph. D. studies

1. *"Flow and electric field stabilised nematic director modes in planar nematic microchannels"*, N.J.Mottram, **A.S. Bhadwal**, G. McKay, A.M.J. Edwards, I.C. Sage, C.V. Brown* *under preparation.*

2. *"Effect of line tension and nematic layer thickness on dynamics of topological defect line growth"*, **A.S. Bhadwal**, N.J. Mottram, I.C. Sage, C.V. Brown* *under preparation.*

3. *"Voltage-programmable dynamic surface topography of liquid crystals: A flexoelectric effect"*, **A.S. Bhadwal**, N.J. Mottram, A. Saxena, I.C. Sage, C.V. Brown* *under preparation.*

4. *"Electrically controlled topological micro cargo transportation"* **A.S. Bhadwal**, N.J. Mottram, A. Saxena, I.C. Sage, C.V. Brown*, *Soft matter*, **2020**, Accepted manuscript. `https://doi.org/10.1039/C9SM01956A`

5. *"Electrochemical detection and photocatalytic performance of MoS_2/TiO_2 nanocomposite against pharmaceutical contaminant:Paracetamol"* N. Kumar†*, **A. S. Bhadwal**†, S.Singh, C. Kranz, B. Mizaikoff*, *Sensing and Biosensing Research*, **2019**, 24, 100288. `https://doi.org/10.1016/j.sbsr.2019.100288`

6. *"A Comprehensive Review on Nano-Molybdenum Disulfide/DNA Interfaces as Emerging Biosensing Platforms"*, M. Kukkar, G.C. Mohanta, S.K. Tuteja, P. Kumar, **A.S. Bhadwal**, P. Samaddard, K.H. Kim*, A. Deep*, *Biosensors and Bioelectronics*, **2018**, 107, 244-258. `https://doi.org/10.1016/j.bios.2018.02.035`

7. *"A novel approach for amine derivatization of MoS_2 nanosheets and their application toward label-free immunosensor"*, M. Kukkar, S.K. Tuteja, P. Kumar, K.H. Kim*, **A.S. Bhadwal**, A. Deep*, *Analytical Biochemistry*, **2018**, 555, 1-8. `https://doi.org/10.1016/j.ab.2018.05.029`

8. *"Photocatalytic and Antibacterial Biomimetic ZnO Nanoparticles"*, N. Kumar†, **A.S. Bhadwal**†, M. Garg, R. Sharma, S. Singh*, B. Mizaikoff*, *Analytical Methods*, **2017**, 9, 4776-4782. `https://doi.org/10.1039/C7AY01468F`

During Bachelors and Masters research

9. *"Green synthesis of highly stable carbon nanodots and their photocatalytic performance"*, R. Gupta, <u>**A.S. Bhadwal**</u>, N. Kumar, M. Madhusudanan, R.N. Pudake, R.M. Tripathi*, *IET Nanobiotechnology*, **2017**, 11, 360-364. `http://dx.doi.org/10.1049/iet-nbt.2016.0025`

10. *"Catalytic degradation of methylene blue by biosynthesized copper nanoflowers using F.benghalensis leaf extract"*, M. Aggarwal, <u>**A.S. Bhadwal**</u>, N. Kumar, A. Shrivastav, B.R. Shrivastav, M.P. Singh, F. Zafar, R.M. Tripathi*, *IET Nanobiotechnology*, **2016**, 10, 321-325. `http://dx.doi.org/10.1049/iet-nbt.2015.0098`

11. *"Fungal biomolecules assisted biosynthesis of Au-Ag alloy nanoparticles and evaluation of their catalytic property"*, R. M.Tripathi*, R.K.Gupta, <u>**A.S. Bhadwal**</u>, P.Singh, A.Shrivastav, B.R.Shrivastav *IET Nanobiotechnology*, **2015**, 9, 178-183. `http://dx.doi.org/10.1049/iet-nbt.2014.0043`

12. *"Facile and rapid biomimetic approach for synthesis of HAp nanofibers and evaluation of their photocatalytic activity"*, R.M. Tripathi*, N.Kumar, <u>**A.S. Bhadwal**</u>, R. K. Gupta, A. Shrivastav, B.R. Shrivastav, *Materials Letters*, **2015**, 140, 64-67.`https://doi.org/10.1016/j.matlet.2014.10.149` `https://doi.org/10.1016/j.matlet.2014.10.149`

13. *"ZnO nanoflowers: Novel biogenic synthesis and enhanced photocatalytic activity"*, R.M. Tripathi*, <u>**A.S. Bhadwal**</u>, R.K. Gupta, P. Singh, A. Shrivastav, B.R. Shrivastav, *Journal of Photochemistry and Photobiology B*, **2014**, 141, 288-295. `https://doi.org/10.1016/j.jphotobiol.2014.10.001`

14. *"Ultra-sensitive detection of mercury (II) ions in water sample using gold nanoparticles synthesized by Trichoderma harzianum and their mechanistic approach"*, R.M. Tripathi*, R.K. Gupta, P. Singh, <u>**A.S. Bhadwal**</u>, A. Shrivastava*, N. Kumar, B.R. Shrivastav, *Sensors and Actuators B*, **2014**, 204, 637–646. `https://doi.org/10.1016/j.snb.2014.08.015`

15. *"Mechanistic aspects of biogenic synthesis of CdS nanoparticles using Bacillus licheniformis"*, R.M. Tripathi*, <u>**A.S. Bhadwal**</u>, P.Singh, A.Shrivastav, M.P.Singh and B.R.Shrivastav, *IOP Advances in Natural Sciences: Nanoscience and Nanotechnology*, **2014**, 5, 025006-0250010. `https://doi.org/10.1088/2043-6262/5/2/025006`

16. *"Biogenic synthesis and photocatalytic activity of CdS nanoparticles"*,<u>**A.S. Bhadwal**</u>, R.M. Tripathi*, R.K. Gupta, N. Kumar, R.P. Singh, and A. Shrivastav*, *RSC advances*, **2014**, 4, 9484-9490. `https://doi.org/10.1039/C3RA46221H`

Conference attended

1. Poster presentation, *2nD UK fluids Network ECR event*, **2019**, Nottingham, UK.

2. Poster presentation, *International Liquid crystals conference (ILCC)*, **2018**, Kyoto, Japan.

3. Oral presentation, *British Liquid crystal conference (BLCS)*, **2018**, Manchester, UK

4. Oral presentation, *Merck CASE conference*, **2018**, Southampton, UK.

5. Oral presentation, *Ist UK fluids Network ECR event*, **2018**, Northumbria, UK.

6. Oral presentation, *Merck CASE conference*, **2017**, Southampton, UK.

Check for updates

Electrically controlled topological micro cargo transportation†

A. S. Bhadwal, [ID] [a] N. J. Mottram, [ID] [b] A. Saxena, [ID] [a] I. C. Sage[a] and C. V. Brown [ID] *[a]

We demonstrate electrically controlled linear translation and precision positioning of a colloidal particle in a soft matter device. The basis of transportation is the time dependent electric field reconfiguration and manipulation of a topological line defect between two distinct hybrid aligned nematic liquid crystal domains having opposing tilt orientations. Deliberately tuning an applied voltage relative to a low threshold value (5.7 V at 1 kHz) permits defect trapping of the colloidal particle and allows subsequent control over the particle's velocity and bidirectional linear movement over millimeter distances, without the need for externally imposed flow nor for lateral confining walls.

1 Introduction

Transport of micrometer sized solid particles, liquid droplets or biological structures in carrier fluid systems is important in a diverse range of disciplines and applications including drug delivery, active matter, and lab-on-a-chip applications.[1] There has been intense recent interest in using anisotropic carrier fluids such as nematic liquid crystals[2–4] which offer a wide toolkit of potential particle manipulation techniques based on physical (voltage, light, temperature, flow), chemical (surface alignment, photoresponse, phase change), and geometrical (confinement, texturing and patterning) mechanisms. Some recent work includes nematic based micro cargo transportation and manipulation by electrophoresis and electrohydrodynamic convection utilising the asymmetric nematic distortions around an embedded particle,[5,6] by phase boundary movement of a particle trapped on a defect formed within a microgroove,[7] by flow within a microchannel with the particle trapped on a "soft rail" defect,[8] and by spatial gradients in the elastic distortion of the nematic produced *via* patterned substrate morphologies, *via* textured periodic surface alignment on the

substrate or *via* periodic patterning of the lateral walls of a confining channel.[9–11]

With long term goal of designing soft matter electronic devices, we report an electrically controllable micro cargo transportation device that employs a topological defect in a flat nematic liquid crystal layer for particle trapping and manipulation. Liquid crystals exhibit a range of different topological defects including monopoles and lines which can be embedded within textures and at domain walls[12,13] and which arise in general as a consequence of frustration and symmetry breaking in the system caused by geometric spatial confinement, alignment, and surface anchoring, electrostatic or magnetic confinement, and flow alignment.[14,15] Topological defects inevitably arise in the nematic director field surrounding a suspended micrometer scale colloidal particle.[2,16] We have used hybrid alignment of a nematic layer to create two stable coexisting equilibrium *n*-director tilt orientations which are separated by an elastic domain wall that contains a line defect. Previous work on the formation[17] of a topological defect line and its structural transformation[18–20] under hybrid alignment conditions has been reported for confinement in thin microchannels.

Here we use electrical confinement of the domain wall between opposing hybrid alignment states, without lateral confinement, to significantly distort the shapes of the domains and manipulate the domain wall to evolve a series of parallel intervening walls connected by high curvature tip regions. We have developed a nematic continuum theory model that duplicates the observed time evolution of the tortuous shape of the wall and which quantitatively reproduces the A.C. voltage controlled linear motion of the tip in the low-velocity range. We have used this high curvature tip feature on the electric field confined domain wall to collect, trap and move a micro particle. This provides straightforward precision A.C. voltage control of the positive and negative

[a] SOFT Group, School of Science and Technology, Nottingham Trent University, Nottingham NG11 8NS, UK. E-mail: carl.brown@ntu.ac.uk

[b] Department of Mathematics and Statistics, University of Strathclyde, Glasgow G1 1XH, UK

† Electronic supplementary information (ESI) available: File F1 provides additional experimental details; file F2 describes the development of the theoretical model; movie M1 shows electrohydrodynamic convection in response to a low frequency A.C. sinewave driving voltage (but no convection at 1 kHz); movie M2 shows the tip of a finger shaped domain wall moving at different speeds at different applied voltages; movie M3 shows theoretical dynamic domain wall evolution; movie M4 shows micro cargo collection; movie M5 shows micro cargo transport. See DOI: 10.1039/c9sm01956a

linear movement and placement of the particle, without any need for externally imposed flow, nor for lateral confining walls or geometric or alignment texturing.

2 Experimental

2.1 Device details and preparation

The device consisted of a nematic liquid crystal layer of thickness $d = 13$ μm sandwiched between two borosilicate glass substrates in the xy plane, Fig. 1. The lower substrate at $z = 0$ was patterned with an array of transparent co-planar interdigital stripe electrodes running parallel to the x-direction. The lower substrate was coated with a thin solid film which imparted low-pretilt planar nematic surface alignment with the easy alignment axis in the y-direction, orthogonal to the direction of the electrode lines. The opposing upper substrate at $z = d$ was coated with the amorphous fluorinated copolymer Teflon AF ("PTFE AF 2400", poly[4,5-difluoro-2,2-bis(trifluoromethyl)-1,3-dioxole-co-tetrafluoroethylene], dioxole 87 mol%), CAS 37626-13-4, Sigma-Aldrich/Merck KGaA, Darmstadt, Germany which imparted homeotropic nematic surface alignment (see also Supplementary file F1, ESI†).

The electrodes on the lower substrate were fabricated on indium tin oxide coated borosilicate glass slides using standard photolithography and etching techniques (ITO of 25 nm thickness and 100 Ω per square resistivity, Praezisions Glass and Optik GmbH, Germany). The electrode arrangement covered a square area of size 5 mm × 5 mm, whilst the electrode linewidth and the gaps between the electrodes were both equal to $w_e = w_g = 80$ μm. The entire lower substrate was coated with a magnesium fluoride on zinc sulphide mechanical alignment layer with a combined thickness of 300 nm. The magnesium fluoride layer was deposited with the plane of the substrate tilted at 45° to the evaporation direction. This provided mechanical nano-groove planar alignment of the nematic liquid crystal with a negligible pretilt angle.[21] Inorganic thin solid films, for example silicon dioxide and associated solid dielectrics, commonly provide a polar anchoring energy of the order of 10^{-5} J m^{-2} [22] similar to conventional polyimide[23] and polyvinyl alcohol alignment layers.[24] Magnesium fluoride thin films have previously been used to align twisted nematic cells in the literature, giving a comparable electro-optical performance to polyimide alignment layers.[21]

We used nematic liquid crystal material E1, which has a density of 1.01 ± 0.01 g cm^{-3} [25,26] and which is a two component mixture of 5CB and 7CB (4′-pentyl-4-biphenylcarbonitrile, CAS 40817-08-1, and 4′-heptyl-4-biphenylcarbonitrile, CAS 41122-71-8, Sigma-Aldrich/Merck KGaA, Darmstadt, Germany) in the proportion 60%:40% by weight. This mixture exhibits a stable room temperature nematic phase, and the mixture and its cyano-biphenyl components[27,28] are established and well characterised materials. We measured the value of the positive dielectric anisotropy, $\Delta\varepsilon = 12.3 \pm 0.4$, and also the values of the splay and bend elastic constants, $K_{11} = 7.2 \pm 0.5$ pN and
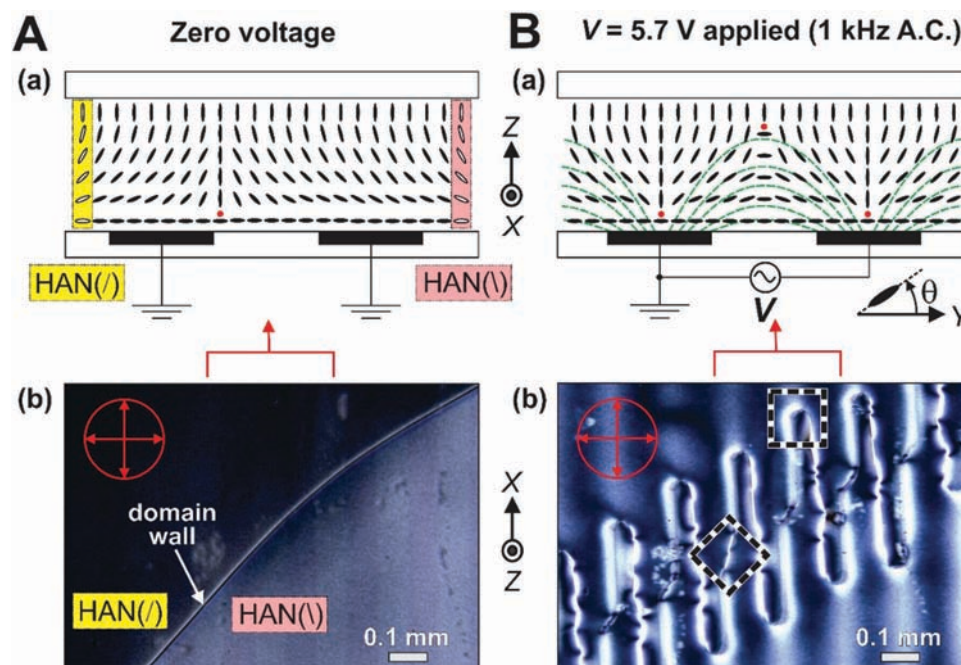
Fig. 1 (A) The nematic layer with no applied voltage: (a) illustration of the orientation of the nematic n-director in cross-section showing the coexisting HAN(/) and HAN(\) alignment states separated by a domain wall containing a topological line defect of strength $-\frac{1}{2}$ (note that the location of the line defect, the red dot, is arbitrary in the zero voltage state), (b) optical micrograph of the actual device under plane-polarised light with a crossed analyser showing two coexisting HAN regions separated by a diagonal domain wall. (B) The nematic layer under an applied voltage V, producing electrical confinement: (a) illustrating the nematic n-director configuration with the domain wall moved into the gap region between the electrodes. (b) The optical micrograph shows that electrical confinement has produced a tortuous domain wall shape with intercalated electric field distorted HAN(/) and HAN(\) regions. The crossed polariser and analyser orientations are shown by the arrows in the circle on the micrographs.

$K_{33} = 10.1 \pm 0.8$ pN respectively, for the E1 mixture that we used in our experiments using the A.C. voltage Fréedericksz effect[29,30] (see also Supplementary file F1, ESI†). The layer spacing in the device was maintained with polyethylene terephthalate strips (PET, 13 µm, Goodfellow, Cambridge, UK). The colloidal micro particles used in the micro cargo experiments were polymer microspheres of diameter 5.0 ± 0.1 µm (density 1.05 g cm^{-3}, Duke scientific Corp., USA) that were sparsely dispersed in the liquid crystal mixture before filling into the device. The particles were coated with trichloro(octyl)silane to impart homeotropic surface alignment, sonicated, and dispersed in the nematic E1 at 0.05% by weight.

2.2 Device addressing and polarising optical microscopy measurements

The nematic liquid crystal layer could be subjected to a spatially periodic electric field, **E**, by applying an A.C. voltage to alternate electrodes in the array whilst the interposed electrodes were held at earth potential. All experiments were performed on the open bench in a temperature controlled laboratory (21 ± 1 °C). The A.C. sinewave voltage (1 kHz, rms voltage values given in the text) was provided by a waveform generator (TGA1244, Thurlby Thander Instruments Limited, Cambridge, UK) combined with a voltage Amplifier (PZD700, Trek Inc., Medina, New York, USA). Videos and still images of the device under operation at different voltage values were recorded using a polarising microscope (BX51, Olympus, Essex, UK) fitted with a CMOS camera (EO-23121C, Edmund Optics Ltd, Yorkshire, UK). The polarisation was parallel to the planar easy-alignment axis, with the analyser crossed. Analysis of the video images, including feature and particle tracking, was performed using bespoke MATLAB programmes and the ImageJ plugin MTrackJ.[31,32]

3 Results and discussion

3.1 Creation and electrical distortion of a topological defect line

The nematic layer was subject to low-pretilt planar alignment at the lower substrate and to homeotropic alignment at the opposing upper substrate. This hybrid alignment arrangement leads to symmetry breaking and to two distinct, and equally energetically probable, equilibrium through-layer nematic n-director distortion profiles. These degenerate Hybrid Aligned Nematic HAN(/) and HAN(\) alignment states are illustrated in Fig. 1A(a) by the open ellipses in the left and right hand side highlighted boxes respectively. This schematic diagram represents a y–z cross section through the nematic layer, where the orientation of each ellipse indicates the out of plane tilt angle θ of the nematic n-director at that position. Consider the spatial variation in the n-director tilt orientation only in one dimension, the vertical z-direction. In the HAN(/) state the nematic n-director orientation changes smoothly and monotonically across the layer from horizontal planar at the lower surface ($z = 0$) to vertical homeotropic at the upper surface ($z = d$), with the tilt increasing by rotation in the anticlockwise sense as a function of the distance z from the

lower surface. In the HAN(\) state the orientation change is in the opposite, clockwise, sense as a function of z. Hence, towards the middle of the layer, $z \approx d/2$, the n-director tilt orientations in the HAN(/) and HAN(\) states will be orthogonal.

Uniform domains containing only HAN(/) or HAN(\) alignment states can co-exist within a hybrid aligned nematic layer, separated by domain walls. In Fig. 1A(a) a simplified representation of such a domain wall is shown, with HAN(/) on the left and HAN(\) on the right. The wall depicted runs along the x-direction, into the page, and is centred on a topological line defect of strength $-\frac{1}{2}$, shown by the filled circle (red). Away from the wall the one dimensional z-variation of tilt angle within each HAN state is undisturbed. In the vicinity of the wall there is a smooth and continuous distortion in the nematic tilt angle in both the y- and z-directions, of extent governed by the nematic elastic forces and the surface alignment. There is highly localised and abrupt spatial variation in the nematic n-director orientation close to the defect, associated with alignment induced frustration and symmetry breaking.[12,14]

Fig. 1A(b) shows an optical micrograph of the nematic liquid crystal device under plane-polarised light. At this stage the nematic layer does not contain colloidal particles. We have introduced a slight tilt to the device to provide optical contrast so that the two HAN domains are distinct in the optical micrograph. The HAN(/) domain covers the area in the top left half of the image, and the HAN(\) domain covers the area in the bottom right half of the image. Tilting the device further and rotating the device between crossed polarisers enabled identification of these states. The HAN(/) and HAN(\) opposing tilt domains were separated by a domain wall, visible as the light coloured, principally diagonal, line in the optical micrograph. The electrodes, visible as dark vertical bands in Fig. 1A(b) and depicted by the filled rectangles in Fig. 1A(a), were all held at earth potential and so they did not exert any influence over the position and orientation of the domain wall. Therefore, the actual position of the domain wall only depends on the x position of the zy cross section taken through the layer in Fig. 1A(b). Our stable two domain structure and diagonal domain wall geometry was intentionally achieved by careful placement of the homeotropic treated PET spacers, exploiting the fact that defects naturally occur at the corners of a laterally confined nematic layer and can provide defect line pinning points.[33] Additional thermal annealing applied to the device was also employed to avoid multiple HAN domains.

We then applied an A.C. voltage of 12.0 V to alternate electrodes. This started a dynamic evolution process, in which the domain wall was distorting in shape and continuously extending in length as a function of time. The wall shape became increasingly crenulated, due to the dominant growth direction along the edges of the electrodes, forming an array of roughly parallel fingers of each domain encroaching into the region previously occupied by the other domain. After 40 s the applied voltage was abruptly reduced to $V_C = 5.7$ V. The step down to this critical stabilising voltage V_C arrests any dynamic changes of the domain structures, halting significant domain wall movement. The resulting stationary optical texture of the nematic layer is shown in micrograph in Fig. 1B(b), in which the inter-penetrating
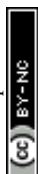
HAN(\) and HAN(/) regions have become intercalated, separated by a tortuous domain wall.

Fig. 1B(a) illustrates how electrical confinement of the nematic n-director can give rise to this alternating arrangement of opposite tilt domains in the intercalation region. The dashed lines (green) show the electric fields produced when a voltage is applied to the electrodes. The nematic material, E1, has a positive dielectric anisotropy and so electrostatic forces act to align the n-director orientation parallel to the local electric field direction. The tilt orientation of the HAN(/) state is commensurate with the direction of the electric field on the right hand edge of the electrode so this grows along that side at the expense of the HAN(\) state which is commensurate with the direction of the electric field on the left hand electrode edge. The walls between the resultant electric field distorted HAN domains are shown in the centre of the electrode (HAN(\)–HAN(/)) and in the centre of the gap (HAN(/)–HAN(\)) in Fig. 1B(a). In the micrograph of the actual device in Fig. 1B(b) the walls are observed to run along the sides of the electrode, just inside the cell gap, with a "kink" in the wall connecting across the centre of the electrode gap, highlighted in the figure by the dashed diamond. The domain wall crosses each electrode with a high curvature cusp at the tip of each inter-penetrating finger-shaped domain, highlighted in the dashed square in Fig. 1B(b). The orientation of the diagonal domain wall before the voltage was applied drives an asymmetry in shape about x at the tip of each finger. This zero voltage diagonal domain wall between the HAN(/) and HAN(\) alignment states is labelled in Fig. 1A(b).

When the applied voltage was removed from the device, and all electrodes were held at earth potential, the optical texture was found to revert back to the state shown in Fig. 1A(b). With no electric field, the inter-penetrating domains retracted, and the domain wall distortion relaxed. After a period of time (of order 80 s) the domain structure returned back to the zero voltage equilibrium arrangement of Fig. 1A(b), in which opposite tilt domains were separated by an undistorted diagonal wall. The domain wall contains elastic energy due to the spatial distortion of the n-director as well as energy associated with a reduction in nematic order at the core of the topological defect. Hence in the absence of an applied voltage, the system returns to the state where the length of the domain wall is minimised by being substantially straight.

3.2 Frequency dependence of the response of the nematic liquid crystal layer

As discussed in Section 3.1, applying an A.C. sinewave voltage V that is equal to the critical stabilising voltage V_C arrests the motion of the dynamically changing domain structures and halts any further significant domain wall movement whilst the voltage is being applied. The frequency dependent value of the critical stabilising voltage is shown by the open circles in Fig. 2. To within experimental scatter of ± 0.2 V, the value of V_C remains constant over the frequency range f = 40 Hz to 10 000 Hz. However, for frequencies below 40 Hz the value of V_C increases, and this rise becomes more prominent as the frequency is further lowered to 10 Hz. This increase can be attributed to ionic

migration and shielding effects that have been previously observed in nematic devices with interdigital electrodes.[34] The characteristic timescale of ionic response are governed by many factors including dissociation and recombination, surface trapping, and drift.[35–37] Transit of ionic species between electrodes is limited by the drift time, of order $\tau \sim w_g^2/(\mu V)$, where μ is the ionic mobility. At low frequencies, $\tau \ll 1/(2f)$, ionic species traverse across the inter-electrode gap between voltage polarity reversals and can partially or fully shield the charge on the electrodes. However, at high frequencies, $\tau \gg 1/(2f)$, ionic species remain relatively static in the time between voltage polarity reversals and so do not act to shield the liquid crystal from the electrode voltage.

At low frequencies we can observe electrohydrodynamic (EHD) convection in our device due to the finite resistivity of the nematic liquid crystal,[15,38] and it is important to distinguish EHD effects from those that are the subject of this paper. In our device EHD convection produces periodic circulating flow of the nematic liquid crystal in the y-direction, perpendicular to the electrode stripes. The frequency–voltage regime in which EHD flow occurs is indicated by the cross hatched region of Fig. 2. The open circles indicate the minimum A.C. voltage for the onset of the EHD instability at different frequencies, which exhibits the sharp frequency dependency typical of the phenomenon.[15,38] Supplementary movie M1 (ESI†) demonstrates the effect of this flow on a single polymer microsphere of diameter 5.0 ± 0.1 μm. This micro particle sits within the nematic fluid in a region of the device that is far from any domain walls. In the movie, 20 second videos of the device under plane-polarised light with a crossed analyser are shown under an applied A.C. sinewave voltage of 15 V, at three different frequencies. At 10 Hz the system is within the region of EHD instability shown in Fig. 2 and the micro particle exhibits rapid circulatory motion in a direction perpendicular to the electrodes.
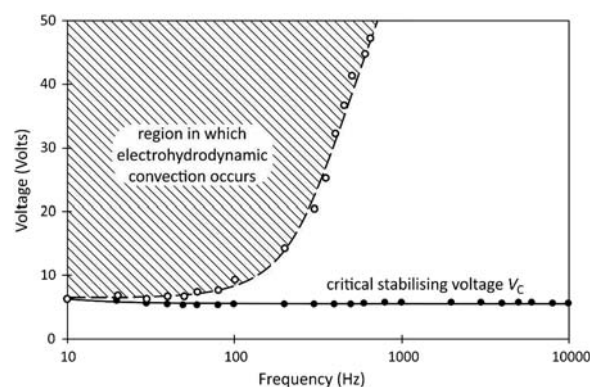
Fig. 2 An A.C. sinewave voltage V was applied between adjacent interdigital electrodes on the lower bounding substrate of the nematic layer. At a critical stabilising voltage, $V = V_C$, the domain wall movement was halted and the prevailing domain structure was held static. The filled circles show the variation of the value of V_C with the sinewave voltage frequency. On the same plot, the open circles show the frequency variation of the minimum voltage at which the onset of electrohydrodynamic convection occurs. The cross hatched region shows the frequency–voltage regime within which electrohydrodynamic convection is observed in the layer. The solid line and the dotted line are guides for the eye.
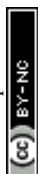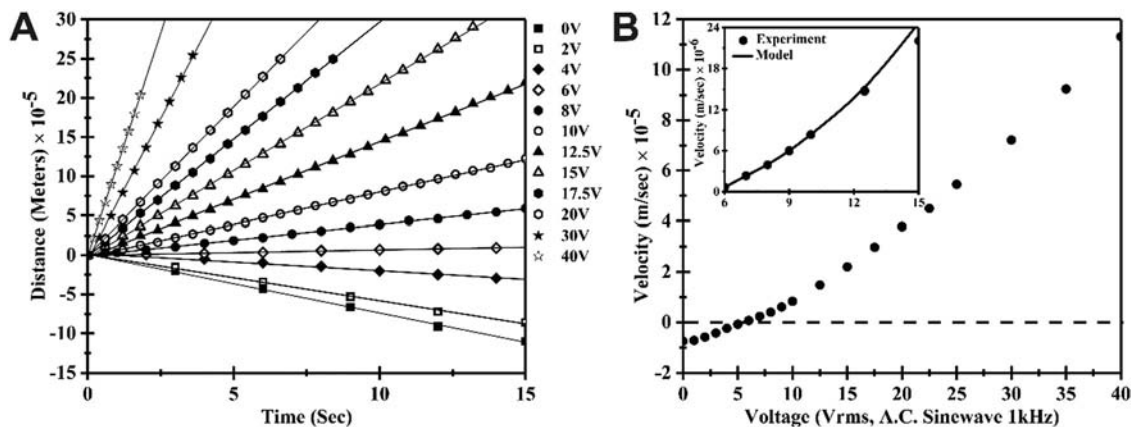
Fig. 3 (A) The distance moved *versus* time by the tip of a finger-shaped electrically confined domain (dashed box in Fig. 1B(b)) in the *x*-direction for a range of applied different voltages. Linear fits to the data, shown by the solid lines, show that the tip moves at constant velocity. (B) The velocity *versus* voltage for the movement of the tip obtained from linear fits to the distance *versus* time data. The inset shows a theoretical fit to the data for low tip movement velocities.

At 200 Hz the system is close to but below the critical frequency for EHD onset and micro particle moves slowly, perpendicular to the electrodes. At 1 kHz there is no electrohydrodynamic convection and the particle remains stationary. We emphasise that all the results described on micro cargo transport in the remainder of this paper are obtained under 1 kHz drive and at voltages up to 40 V, where no EHD induced flow occurs.

3.3 Dynamical properties of the topological defect line

We now describe the results of the study of the voltage dependence of the linear motion of the tip of a finger-shaped HAN domain that was produced by electrical confinement. The domain texture shown in Fig. 1B(b) was used as the starting point for each different applied voltage used in the study. This texture was reproducibly re-established after each voltage measurement ready for the next voltage using the steps described in Section 3.1, *i.e.* first allowing the domain wall to relax back to its zero voltage equilibrium arrangement, then applying 12 V for 40 s, and then abruptly changing the voltage to V_C = 5.7 V to stabilise and immobilise the texture. This resetting procedure created the required high curvature cusp, as highlighted in the dashed square in Fig. 1B(b), enabling the investigation of both retraction and growth of the intercalated domain structure, and allowing quantitative comparison between the tip translation recorded at different voltages.

The time dependent position of the domain tip (dashed box in Fig. 1B(b)) was measured from video images of the nematic layer between crossed polarisers under an optical microscope. The voltage controlled domain tip movement was in the *x*-direction, orthogonal to the direction of the electric fields produced by the interdigital electrodes. The time when the applied voltage was abruptly changed from the critical stabilising voltage V_C = 5.7 V to a new voltage V was taken as t = 0 s. The distance moved by the tip in the *x*-direction from its position at t = 0 s is plotted in Fig. 3A, with data shown for a range of applied voltages, between V = 0 and V = 40 V (R.M.S., 1 kHz, A.C. sinewave). Supplementary movie M2 (ESI†) shows the tip of a finger shaped domain wall moving at

different speeds at three different applied voltages, in the negative *x* direction at 0 V, in the positive *x* direction at 7 V which is just above V_C, and at a higher velocity in the positive *x* direction at 15 V.

The data taken at all of the different voltages exhibit a linear dependence of the distance on the time, demonstrated by the solid straight line regression fits through each set of data points in Fig. 3A. A negative gradient is found for applied voltages below V_C, with the data for V = 0 V showing the largest negative gradient and the highest negative velocity. As described in Section 3.1, the energy of elastic distortion around the domain wall and the energy cost of the defect line within the wall leads to a torque that acts to straighten the wall and retract the intercalated domains, pulling the tip in the negative direction when the electric field confinement is removed. The gradient increases monotonically as the voltage is increased, changing from negative to just positive when V = 6.0 V. This increase results from the torque on the nematic *n*-director due to electrical confinement becoming increasingly dominant at higher voltages over the torque that acts to straighten the domain wall, creating a more tortuous domain wall shape at higher voltages with a faster positive movement of the tip of the penetrating electrically confined domain.

Fig. 3B shows the velocity *versus* voltage dependence for the movement of the tip obtained from linear fits to the distance *versus* time data. The velocity increases monotonically in the voltage range from V = 0 V to V = 40 V, and exhibits a super linear dependence on voltage. The inset shows a theoretical fit to the data for low tip movement velocities, which will be discussed in Section 3.4. Hence the key observations are that the electric field constrained domain tip is held stationary at a critical stabilising voltage V_C = 5.7 V, it moves with a constant velocity along a line in the negative *x*-direction under a lower applied voltage $\Delta V = V - V_C < 0$, and it moves with a constant velocity in the positive *x*-direction under a higher voltage when $\Delta V = V - V_C > 0$, where $|\Delta V|$ determines the velocity in the range -7.5×10^{-6} m s^{-1} to 113×10^{-6} m s^{-1}. The tip can therefore be moved and positioned on demand, controlled by the magnitude of the applied voltage.

3.4 Theoretical description of the topological defect line dynamics

A nematic continuum theory-based dynamic model was developed which reproduces all of the key features of electrically confined domain evolution that have been observed in the experiments. We provide a summary here of the theory, further details are given in Supplementary file F2 (ESI†). The orientation of the nematic n-director was described by a tilt angle $\theta(x,y,z,t)$ relative to the y direction, and a nematic director of the form $\mathbf{n} = (0,\cos\theta,\sin\theta)$, as illustrated in Fig. 1. The HAN alignment states were then described by a linear variation of the tilt angle in the z-direction,

$$\theta(x,y,z,t) = \left(\theta_0(x,y,t) + \left(\frac{\pi}{2} - \theta_0(x,y,t)\right)\frac{z}{d}\right), \quad (1)$$

which corresponds to the situation with strong elastic effects in the single elastic constant approximation, $K = K_{11} = K_{22} = K_{33}$ and in the absence of a significant flexoelectric polarisation. This method of prescribing a z-dependence of the tilt angle enables a two-dimensional model to be created. The key physical contributions to the energy of the system will originate from elasticity (E_f), the electric polarisation of the nematic n-director (E_e), and the surface alignment anchoring (E_a), and will now be considered in turn.

The Frank elastic energy E_f is given by,

$$E_f = \int_0^L \int_0^{2\pi n/\lambda} \int_0^d \frac{K}{d}\left(\left(\frac{\partial\theta}{\partial x}\right)^2 + \left(\frac{\partial\theta}{\partial y}\right)^2 + \left(\frac{\partial\theta}{\partial z}\right)^2\right) dz\, dy\, dx \quad (2)$$

The integration from $z = 0$ to $z = d$ in eqn (2) can be performed after substitution of eqn (1). The x-extent of the cell is taken to be $0 \leq x \leq L$, and the y-integration is over an integer n number of periods of the electrode pitch $\lambda = w_e + w_g$.

The periodic electric field produced by the interdigital electrodes is modelled by the function

$$\mathbf{E} = E(y,z)\left(0, \cos\left(\frac{\pi}{2} - \frac{\pi}{\lambda}y\right), \sin\left(\frac{\pi}{2} - \frac{\pi}{\lambda}y\right)\right), \quad (3)$$

which describes an electric field direction that is a function of y only, and a field strength that $E(y,z)$ decays into the cell in the z-direction with the y-periodicity imposed by the electrodes. The electrostatic energy E_e is then simplified through an integration in the z-direction to give

$$E_e = -\int_0^L \int_0^{2\pi n/\lambda} \int_0^d \frac{\varepsilon_0 \Delta\varepsilon}{2}(\mathbf{E}\cdot\mathbf{n})^2 dz\, dy\, dx$$

$$= -\int_0^L \int_0^{2\pi n/\lambda} \frac{\varepsilon_0 \Delta\varepsilon d}{2} E(y)^2 \sin^2\left(\theta_m + \frac{\pi}{\lambda}y\right) dy\, dx, \quad (4)$$

where $\theta_m(x,y,t)$ is the tilt angle of the director in the middle of the cell, at $z = d/2$, so that $\theta_m = ((\pi/4) + (\theta_0/2))$ rad.

Assuming that the electric field reorientation is stronger closest to the electrodes, we include a surface energy effect only at the lower surface, so that the surface energy is

$$E_a = \int_0^L \int_0^{2\pi n/\lambda} \frac{W_0}{2}\sin^2(\theta_0) dy\, dx, \quad (5)$$

where the lower surface anchoring strength, W_0, expresses the amount of energy required to break the lower surface planar anchoring to transform from a HAN(\) to a HAN(/) state.

The rate of dissipation due to n-director rotation, parameterised by a phenomenological viscosity γ that is related to the nematic rotational viscosity, γ_1, is

$$D = -\int_0^L \int_0^{2\pi n/\lambda} \int_0^d \gamma\left(\frac{\partial\theta}{\partial x}\right)^2 dz\, dy\, dx = -\int_0^L \int_0^{2\pi n/\lambda} \frac{\gamma d}{3}\left(\frac{\partial\theta_0}{\partial x}\right)^2 dy\, dx. \quad (6)$$

The Rayleigh dissipation principle and the above equations and definitions are then used to derive the governing equation (see also Supplementary file F2, ESI†) for the tilt angle of the director in the middle of the cell, namely

$$\frac{2\gamma d}{3}\frac{\partial\theta_m}{\partial t} = K\left(\frac{2d}{3}\left(\frac{\partial^2\theta_m}{\partial x^2} + \frac{\partial^2\theta_m}{\partial y^2}\right) + \frac{(\pi - 2\theta_m)}{d}\right)$$
$$+ \frac{W_0}{2}\sin(4\theta_m) - \frac{\varepsilon_0 \Delta\varepsilon}{2}E(y)^2\sin\left(2\left(\theta_m + \frac{\pi}{\lambda}y\right)\right). \quad (7)$$

We have then used eqn (7). to model spatial variations of the mid-layer tilt angle $\theta_m(x,y,t)$ in the xy plane, as a function of time, to provide a description of the dynamic evolution of the domain wall shape. The electric field $E(y)$ was prescribed using numerical finite element simulations[39] (see Supplementary file F2, ESI†). With no applied voltage, and well away from the distortion associated with a domain wall, hybrid alignment leads to two stable orthogonal mid-layer tilt directions at equilibrium, $\theta_{me} = (\pi/4)$ rad for the HAN(/) alignment state and $\theta_{me} = (3\pi/4)$ rad for the HAN(\) alignment state.

Dynamic simulations results produced by solving eqn (7) are shown in Fig. 4 (see also Supplementary movie M3, ESI†). Eqn (7) is non-linear in θ_m and there is a large spatial variation of θ_m across the nematic layer, particularly across the domain wall since the two equilibrium mid-layer orientations are separated by $\Delta\theta_{me} = \pi/2$ rad. If we consider the behaviour at a single point, and perturb eqn (7) about one of the long-time equilibrium states, that would result in a solution that is exponential in time.[40] However, here we are concerned with the nonlocal motion of the wall as a forced travelling wave. Due to the bistability, i.e. both HAN states being possible, the full non-local dynamic solution of eqn (7) is of a soliton-like travelling wave form.[41] Time dependent solutions for $\theta_m(x,y,t)$ were produced with the aid of a commercial finite element partial differential equation solver[39] using the following parameters: $\gamma = 2.49$ N s m^{-2}; $W_0 = 55 \times 10^{-5}$ J m^{-2}; $d = 13 \times 10^{-6}$ m; $K = 7.5 \times 10^{-12}$ N; $\Delta\varepsilon = 12.3$; and $\lambda = 160 \times 10^{-6}$ m. The colours in Fig. 4 indicate the value of the tilt angle of the director in the middle of the cell, $\theta_m(x,y,t)$, as a function of position. The boundary lines of abrupt change in colour correspond to highly localised jumps in the values of the tilt angle on crossing the domain walls between the two possible opposing tilt domains. The boundary conditions were selected to produce a diagonal domain wall separating two opposing HAN states as the initial zero voltage equilibrium state in the simulation,
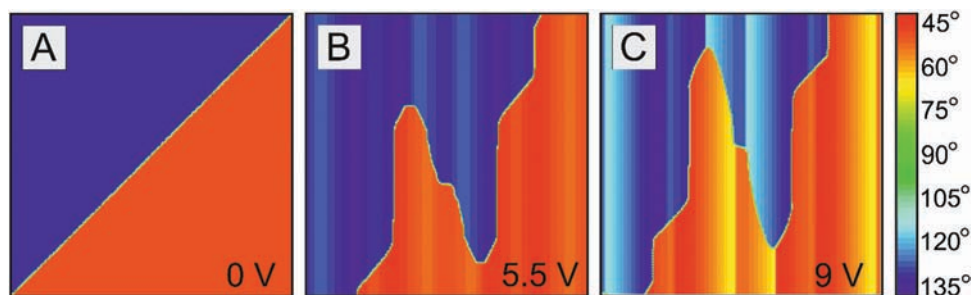
Fig. 4 Numerical simulations of the time evolution of the domain wall (solid line) between two opposing HAN domains under the application of different voltages. The colours indicate the value of the tilt angle of the director in the middle of the cell, $\theta_m(x,y,t)$, according to the legend given to the right of the figure. (A) Zero volt equilibrium state. (B) The distorted static domain wall shape obtained after a period of dynamic deformation with 9 V applied, followed by abruptly changing the voltage to 5.5 V which arrested the dynamic domain evolution. This shows a close resemblance to the experimental optical texture in Fig. 1B(b). (C) A snapshot of the domain wall during dynamic extension after voltage had been again increased to 9 V.

shown in Fig. 4A. This emulated the experimental situation previously shown in the optical micrograph in Fig. 1A(b). Voltages were then applied in the simulation as in a similar sequence to that described at the beginning of Section 3.3, *i.e.* 9 V for 16.8 s, followed by changing the voltage to V = 5.5 V for 16.8 s. The value of the energy barrier W_0 was adjusted to ensure that the value of the critical stabilising voltage in the model of 5.5 V was close to the value of V_C found in the experiments. This procedure resulted in the static domain wall structure shown in Fig. 4B, which reproduces all the key features observed experimentally in the optical micrograph in Fig. 1B(b), including the kink across the region between electrodes, and the tips of the finger shaped domains where the domain wall crosses above the electrodes. The voltage in the simulation was increased back to 9 V which caused the tip regions to move again in the *x*-direction. This was accompanied by further domain wall deformation and encroachment of the electrically confined finger shaped domains into the regions initially occupied by the oppositely tilted HAN domain. Fig. 4C shows a snapshot of the domain wall during this dynamic extension process.

The inset velocity *versus* voltage graph in Fig. 3B demonstrates an excellent fit between the theoretical model and the experiment results at low voltages when $V \geq V_C$, using only the values of γ and W_0 in eqn (7). as the adjustable fitting parameters. The quality of fit deteriorates at higher voltages, above 12 V, where the highly distorted regions localised around the defects embedded in the domain wall move closer to the substrates (see also Supplementary file F1, ESI†). This cannot be described in our model which neglects the *z*-direction. Hence the model reproduces a critical stabilising voltage, it also quantitatively describes the observed linear distance *versus* time behaviour and super-linear voltage dependence of the velocity for applied voltages immediately above this value, and also accurately reproduces the observed domain structures and domain wall shapes. This level of agreement provides confidence that we have captured the key physical nematic *n*-director structures and switching mechanisms produced *via* electrical confinement of the *n*-director, in our model and our interpretation of the experimental observations.

3.5 Electrically controlled topological micro cargo transportation

We now demonstrate how a colloidal micro particle can be collected and transported on demand *via* the voltage controlled motion of the domain wall. Polymer microspheres of density 1.05 g cm^{-3} and diameter 5.0 ± 0.1 μm were dispersed within the nematic carrier fluid. These had been treated with
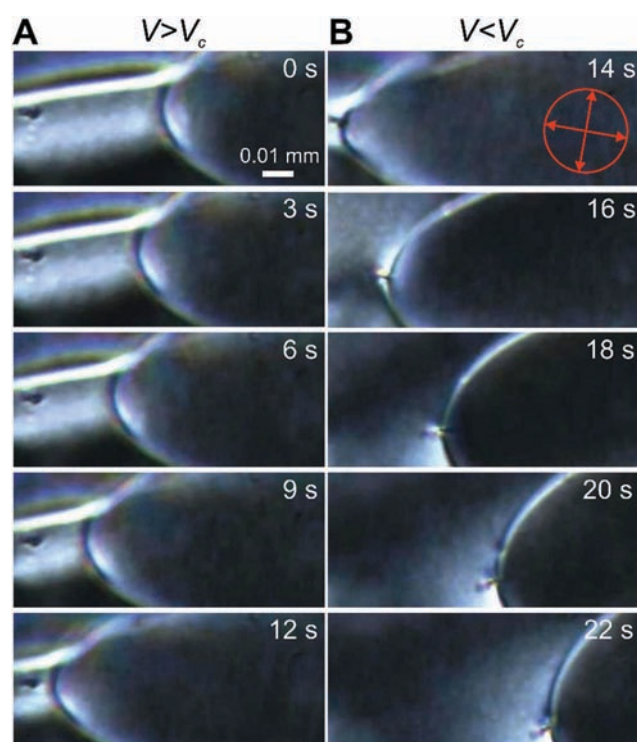
Fig. 5 Optical micrograph of the nematic layer under plane-polarised light with a spherical micro particle towards the left hand side of the images. A domain wall is shown trapping and collecting the particle: (A) the wall dynamically extends and moves to the left under applied voltage 7 V, above V_C (where V_C = 5.7 V), overlapping the position of the particle. (B) At time 14 s the voltage is abruptly reduced to 1 V, below V_C, and the domain wall retracts whilst transporting the adhered particle at its tip. The crossed polariser and analyser orientations are shown by the arrows in the circle on the micrograph.

trichloro(octyl)silane to impart homeotropic alignment of E1 at the surface of the particle. Since the particles have homeotropic surface treatment, whilst the lower substrate of our device has planar nematic alignment, the uniform director field near the wall is incompatible with the director distortions around the sphere. The balance between the elastic repulsion from the wall and the gravity force driving sedimentation is expressed by eqn (6) of ref. 2, which gives the equilibrium height $z_{elastic}$ of an elastically levitating particle. The parameters for our system (K = 7.5 pN, R = 2.5 μm, $\Delta\rho$ = 40 kg m^{-3}) predict that $z_{elastic}$ = 17 μm. Hence elastic forces are more than sufficient to prevent sedimentation in our device which has a layer thickness of d = 13 μm and so micro particles are located within the layer and away from surfaces (see also Supplementary file F1, ESI†).

Fig. 5 shows a series of snapshots of the device under a polarising microscope that follow the dynamic process of a moving domain wall interacting with one of the particles, including collection, trapping, and transporting the particle.

In Fig. 5A, a voltage of 7 V is applied to the device, which is above the critical stabilising voltage, V_C = 5.7 V. This causes the domain wall to elongate, moving in the positive x-direction and also towards the nearest electrode edge in the negative y-direction where it connects with an initially separate micro particle. The micro particle is static under an applied voltage for 12 seconds, up until the point at which the wall and the particle connect, indicating an absence of significant thermally or electrically driven flow in the sample. The bright line that is visible in the optical micrograph to the top left of Fig. 5A corresponds to director reorientation close to the edge of the electrode under the action of a voltage. This reorientation is also reproduced in the results of the numerical simulations, Fig. 4C. The applied voltage is then abruptly reduced to 1 V at 14 s, below V_C, which causes the domain wall to retract and move in the negative x direction. Fig. 5B shows how the particle has adhered to the domain wall and moves with the retracting wall, remaining at the high curvature tip as it moves in the negative x direction. Hence
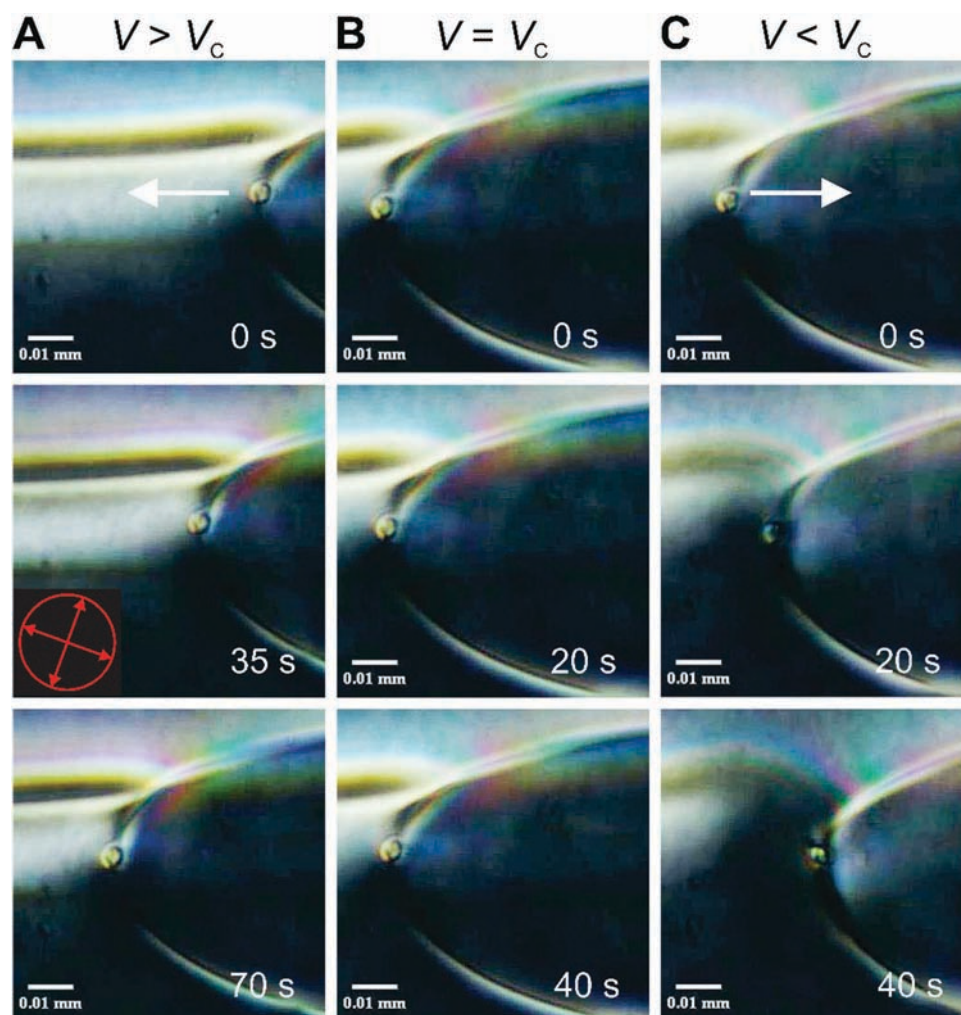

Fig. 6 Optical micrographs showing transportation of a colloidal micro particle by the high curvature tip of the electrically confined finger shaped domain: (A) the particle was moved in the negative x-direction when the applied voltage was 6.5 V, above the critical stabilising voltage ($V > V_C$). (B) The particle is held stationary when $V = V_C$ = 5.7 V. (C) The particle is moved in the positive x-direction when the applied voltage was 4 V, below the critical stabilising voltage ($V < V_C$). The crossed polariser and analyser orientations are shown by the arrows in the circle on the micrograph.

the micro sphere has been attracted to and trapped at the region of strong elastic deformation at the domain wall.[42,43] A video demonstrating particle collection is given in Supplementary movie M4 (ESI†).

Fig. 6 shows a series of snapshots of the device under a polarising microscope that follow the dynamic process of a moving domain wall transporting and positioning a micro particle. In Fig. 6A the particle was moving in the negative x direction when the applied voltage is 6.5 V, above the critical stabilising voltage V_C, in Fig. 6B the particle stopped when the applied voltage was set exactly to $V_C = 5.7$, and in Fig. 6C the particle was moving in the positive x direction when the applied voltage was decreased to 4 V. In each case the images show that the particle remained located to the region of the high curvature tip of a finger-shaped electrically confined domain. A video demonstrating this controlled micro particle movement is given in Supplementary movie M5 (ESI†).

Hence, voltage control of the distortion and extent of the domain wall using the magnitude of voltage relative to the critical stabilising voltage, $\Delta V = V - V_C$ provides both positive and negative precision bidirectional movement of the micro particle along a line. At any point, setting the voltage abruptly to V_C stops the particle movement and holds the particle at the position that it has reached, providing the capability to reversibly place the trapped micro particle on demand.

4 Conclusion

We have created and demonstrated the time dependent electric field reconfiguration and manipulation of a wall containing a topological line defect between two opposing hybrid aligned nematic liquid crystal domains. A high curvature tip region of the wall can be moved with constant velocity on demand in both positive or negative directions, or held stationary at any position during its travel, simply by tuning the value of a low applied voltage. We have elucidated the important physical processes acting within the layer within a theoretical model that accurately reproduced the observed time and voltage dependent shapes of the meandering domain wall.

In the model the anchoring strength parameter, W_0, expresses the amount of energy required to break surface anchoring and transform from one hybrid aligned state to the opposing state. Increasing the value of W_0 in the model increased the value of the critical stabilising voltage V_C. Hence the value of the parameter V_C in our system can provide insight into the anchoring strengths at the surface. Future work will investigate how V_C depends systematically on the surface anchoring since the strength of both planar and homeotropic anchoring, including on the particle, can be tuned.[24,44,45] In previous work a particle with homeotropic alignment has been shown to be readily attracted to and trapped by the defect, whilst if the surface alignment on the particle is planar the situation is more complex. A repulsive interaction and energetic barrier can exist between the planar particle and disclination lines of strength +1 or $\frac{1}{2}$ and so an applied force is required to trap the particle.[46]

We have exploited these domain manipulation capabilities in a technological micro cargo transport application, providing electrically controlled linear translation and precision positioning of a colloidal particle in a soft matter device. Our system avoids the requirement for externally imposed and controlled flow, and also avoids the requirement for alignment patterning or lateral confinement walls and structures within the liquid layer. Our technique offers the opportunity to transport either neutral or charged particles, whilst the use of an A.C. voltage avoids electrochemical degradation effects that can be associated with D.C. electric fields. The research has potential relevance to the design of the next generation of micromachines and lab-on-chip devices, providing the possibility of using voltage actuated defect wiring or collection and movement of individual particles to regions where self-assembly occurs.[47–50] This opens up avenues for the voltage assisted assembly of functional materials for soft matter electronically controlled sensing and opto-electronic devices.

Conflicts of interest

There are no conflicts to declare.

Acknowledgements

References

1 G. M. Whitesides and B. Grzybowski, *Science*, 2002, **295**, 2418–2421.

2 O. D. Lavrentovich, *Soft Matter*, 2014, **10**, 1264–1283.

3 I. Mušević, *Liquid Crystal Colloids*, Springer International Publishing, Springer Nature Switzerland AG, 2017.

4 Ivan I. Smalyukh, *Annu. Rev. Condens. Matter Phys.*, 2018, **9**, 207–226.

5 O. D. Lavrentovich, I. Lazo and O. P. Pishnyak, *Nature*, 2010, **467**, 947–950.

6 Y. Sasaki, Y. Takikawa, V. S. R. Jampani, H. Hoshikawa, T. Seto, C. Bahr, S. Herminghaus, Y. Hidaka and H. Orihara, *Soft Matter*, 2014, **10**, 8813–8820.

7 T. Ohzono and J. I. Fukuda, *Nat. Commun.*, 2012, **3**, 701–707.

8 A. Sengupta, C. Bahr and S. Herminghaus, *Soft Matter*, 2013, **9**, 7251–7260.

9 H. Yoshida, K. Asakura, J. Fukuda and M. Ozaki, *Nat. Commun.*, 2015, **6**, 7180–7807.

10 C. Peng, T. Turiv, Y. Guo, S. V. Shiyanovskii, Q.-H. Wei and O. D. Lavrentovich, *Sci. Adv.*, 2016, **2**, e1600932.

11 Y. Luo, D. A. Beller, G. Boniello, F. Serra and K. J. Stebe, *Nat. Commun.*, 2018, **9**, 3841–3851.

12 N. D. Mermin, *Rev. Mod. Phys.*, 1979, **51**, 591–648.

13 M. V. Kurik and O. D. Lavrentovich, *Phys.-Usp.*, 1988, **31**, 196–224.

14 G. P. Alexander, B. G. G. Chen, E. A. Matsumoto and R. D. Kamien, *Rev. Mod. Phys.*, 2012, **84**, 497–514.

15 S. Chandrasekhar, *Liquid Crystals*, Cambridge University Press, Cambridge, 1992.

16 P. G. De Gennes and J. Prost, *The physics of liquid crystals*, Clarendon Press, Oxford, 1993.

17 A. Sengupta, S. Herminghaus and C. Bahr, *Liq. Cryst. Rev.*, 2014, **2**(2), 73–110.

18 H. Agha and C. Bahr, *Soft Matter*, 2016, **12**(18), 4266–4273.

19 H. Agha and C. Bahr, *Soft Matter*, 2018, **14**(4), 653–664.

20 A. Sengupta, B. Schulz, E. Ouskova and C. Bahr, *Microfluid. Nanofluid.*, 2012, **13**(6), 941–955.

21 H. P. Kim, J. Park, J. Han, J. Han and D. Seo, *IEEE Electron Device Lett.*, 2013, **34**(2), 283–285.

22 H. Yokoyama and H. A. V. Sprang, *J. Appl. Phys.*, 1985, **57**, 4520–4526.

23 P. Kumar, S. Y. Oh, V. K. Baliyan, S. Kundu, S. H. Lee and S. W. Kang, *Opt. Express*, 2018, **26**(7), 8385–8396.

24 Y. Cui, R. S. Zola, Y.-C. Yang and D.-K. Yang, *J. Appl. Phys.*, 2012, **111**(6), 063520.

25 D. Dunmur and W. Miller, *J. Phys., Colloq.*, 1979, **40**(C3), 141–146.

26 D. A. Dunmur and G. R. Luckhurst, *Physical properties of liquid crystals: nematics*, Institution of Engineering and Technology, London, 2007.

27 G. W. Gray, K. J. Harrison and J. A. Nash, *Electron. Lett.*, 1973, **9**, 130–131.

28 P. J. Collings and M. Hird, *Introduction to Liquid Crystals: Chemistry and Physics*, CRC Press, USA, 1997.

29 M. J. Bradshaw and E. P. Raynes, *Mol. Cryst. Liq. Cryst.*, 1981, **72**(2–3), 35–42.

30 V. Fréedericksz and V. Zolina, *Trans. Faraday Soc.*, 1933, **29**(140), 919–930.

31 E. Meijering, O. Dzyubachyk and I. Smal, in *Methods in Enzymology*, ed. P. M. Conn, Academic Press, 2012, vol. 504, pp. 183–200.

32 C. A. Schneider, W. S. Rasband and K. W. Eliceiri, *Nat. Methods*, 2012, **9**, 671–675.

33 C. Tsakonas, A. J. Davidson, C. V. Brown and N. J. Mottram, *Appl. Phys. Lett.*, 2007, **90**, 111913.

34 C. L. Trabi, C. V. Brown, A. A. T. Smith and N. J. Mottram, *Appl. Phys. Lett.*, 2008, **92**, 223509.

35 K. H. Yang, *J. Appl. Phys.*, 1990, **67**, 36–39.

36 S. Takahashi, *J. Appl. Phys.*, 1991, **70**, 5346–5350.

37 H. Y. Chen, K. X. Yang and Z. Y. Lin, *J. Phys. D: Appl. Phys.*, 2010, **43**(31), 315103.

38 N. Éber, P. Salamon and Á. Buka, *Liq. Cryst. Rev.*, 2016, **4**(2), 101–134.

39 COMSOL Multiphysics® v. 5.4, www.comsol.com, COMSOL AB, Stockholm, Sweden.

40 I. W. Stewart, *The Static and Dynamic Continuum Theory of Liquid Crystals A Mathematical Introduction*, Taylor and Francis, London, New York, 2004.

41 N. V. Madhusudana, J. F. Palierne, Ph. Martinot-Lagarde and G. Durand, in *Solitons in Liquid Crystals*, ed. L. Lam and J. Prost, Springer-Verlag, New York, 1991, ch. 8.

42 P. Poulin, H. Stark, T. C. Lubensky and D. A. Weitz, *Science*, 1997, **275**, 1770–1773.

43 D. Voloschenko, O. P. Pishnyak, S. V. Shiyanovskii and O. D. Lavrentovich, *Phys. Rev. E: Stat., Nonlinear, Soft Matter Phys.*, 2002, **65**, 060701.

44 S. A. Jones, J. Bailey, D. R. E. Walker, G. P. Bryan-Brown and J. C. Jones, *Langmuir*, 2018, **34**, 10865–10873.

45 Z. Eskandari, N. M. Silvestre, M. M. Telo da Gamaa and M. R. Ejtehadi, *Soft Matter*, 2014, **10**, 9681–9687.

46 I. I. Smalyukh, B. I. Senyuk, S. V. Shiyanovskii, O. D. Lavrentovich, A. N. Kuzmin, A. V. Kachynski and P. N. Prasad, *Mol. Cryst. Liq. Cryst.*, 2006, **450**, 279–295.

47 T. Yamamoto and M. Yoshida, *Langmuir*, 2012, **28**, 8463–8469.

48 I. Muševič, M. Škarabot, U. Tkalec, M. Ravnik and S. Žumer, *Science*, 2006, **313**, 954.

49 I. Muševič, M. Škarabot, S. Žumer and M. Ravnik, EP1975656, Priority date 1 Oct., 2018.

50 J. B. Fleury, D. Pires and Y. Galerne, *Phys. Rev. Lett.*, 2009, **103**, 267801.